Ensemble de centres azote-lacune dans le diamant pour l'analyse de signaux radiofréquences

Simone Magaletti

université
PARIS-SACLAY

Ensemble of nitrogen-vacancy centers in diamond for radiofrequency signal analysis

Thèse de doctorat de l'Université Paris-Saclay

École doctorale n° 572, École Doctorale Ondes et Matière - EDOM
Spécialité de doctorat: Physique
Unité de recherche: Université Paris-Saclay, ENS Paris-Saclay, CNRS, LuMIn, 91190, Gif-sur-Yvette, France.
Référent: : ENS Paris-Saclay

Thèse présentée et soutenue à Paris-Saclay, le 15 décembre 2021, par

Simone MAGALETTI

Composition du jury:

Pascale Sénellart Directrice de recherche, CNRS - Centre de Nanoscience et de Nanotechnologies	Présidente
Jocelyn Achard Professeur, Laboratoire des Science, Procédés et Matériaux, Université Paris XIII	Rapporteur & Examinateur
Isabelle Robert-Philip Directrice de recherche, CNRS - Université de Montpellier	Rapporteure & Examinatrice
Elke Neu-Ruffing Professeure, University of Kaiserslautern	Examinatrice

Direction de la thèse:

Thierry Debuisschert Ingénieur de recherche, Thales Research & Technologies	Directeur
Jean-François Roch Professeur, ENS Paris Sacaly	Co-encadrant

Thèse de doctorat

NNT: 2021UPASP114

Acknowledgements

This manuscript summarizes the work I realized during the last three years at the Laboratoire Micro et Nano Physique (LMNP) at Thales Research & Technology with the professional and personal help of many people that I would like to thank.

First of all, I would like to thank the members of the jury, the president Pascale Sénellart, the two rapporteurs and examiners Jocelyn Achard and Isabelle Robert-Philip, and the examiner Elke Neu-Ruffing, for the careful reading of the manuscript, their comments and suggestions, and the fruitful discussion during the thesis defense.

I would like to express my deepest gratitude to my supervisor Thierry Debuisschert, who gave me the opportunity to discover the world of NV centers. Thierry, you guided me during my Ph.D. providing me with a solid scientific basis and a methodology that allowed me to reach excellent scientific goals and a remarkable professional growth.

I also had the opportunity to have, as co-supervisor, Jean-François Roch, who contributed with fruitful discussions and clear ideas to make me achieve the results presented in this manuscript. Jean-François, your passion for science, your kindness, and your cheerfulness make you a role model in my scientific growth.

I would like to sincerely thank Ludovic Mayer, who taught me the techniques and tricks of experimental work in the laboratory. Ludo, you guided me daily by sharing your experience and helped me, professionally and personally, with great patience and commitment. For the continuous encouragement and the long time spent together, thank you.

I take this opportunity to express gratitude to Arnaud Brignon and Daniel Dolfi, who respectively lead the LMNP and the Physics group of Thales. Arnaud and Daniel, your very human leadership is a model for me and allowed me a complete integration in the Physics group of Thales since the beginning.

During the three years of my Ph.D., I have bonded, discussed, and had a lot of fun with so many people working at Thales Research & Technology in Palaiseau. I would like to thank all the interns, doctoral students, and permanent staff at Thales and Jean-François Roch's team at LuMIn for creating a healthy and stimulating work environment.

My Ph.D. thesis has been realized in the frame of the European Marie-Curie project QuSCo, a challenging project involving fifteen doctoral students, their supervisors, and some of their team members. Some of them hosted me for short periods at their university, with many of them I had the opportunity to deepen my knowledge in physics, and with all of them I had a good time. To them goes my thanks.

Finally, I would like to dedicate a few lines of these acknowledgements to all my friends, in Italy and France, to my girlfriend and to my family, to all those who have been close to me in these years and that, with their more varied personalities, contribute to my personal growth and make me happy.

Résumé

Le centre azote-lacune est un défaut de spin du diamant constitué d'un atome d'azote et d'une lacune de carbone dans deux positions adjacentes du réseau cristallin. Il existe dans deux états de charge: l'état neutre (NV^0), qui a un spin 1/2, et l'état négatif (NV^-), qui a un spin 1. Dans le présent manuscrit nous nous intéressons uniquement au centre NV^- qui possède de remarquables propriétés optiques dépendant du spin et que nous appelons dorénavant centre NV par soucis de simplicité. En effet, suite à une excitation optique par un laser émettant dans le vert (532 nm), le centre NV émet de la photoluminescence dans le rouge dont l'intensité dépend de l'état de spin du système: elle est plus élevée quand le centre NV est dans l'état de spin $m_s = 0$ (état brillant) que lorsqu'il est dans les états de spin $m_s = \pm 1$ (états sombres). De plus, le pompage optique du centre NV permet la polarisation de son spin électronique dans l'état de spin $m_s = 0$ et donc l'initialisation du système.
L'état de spin du centre NV peut être manipulé par un champ magnétique radiofréquence (RF) en résonance avec l'une des deux transitions de spin autorisées ($m_s = 0 \rightarrow m_s = -1$ ou $m_s = 0 \rightarrow m_s = +1$). La fréquence de résonance de ces transitions peut être manipulée par un champ magnétique statique (effet Zeeman).
La possibilité d'initialiser et lire optiquement l'état de spin du centre NV ainsi que sa manipulation par un champ magnétique, font de ce défaut du diamant une piste prometteuse pour les applications en information quantique ou comme capteur quantique.

Dans le présent manuscrit, deux applications pour l'analyse de champs radiofréquence (RF) basées sur un ensemble de centres NV dans le diamant sont étudiées: un analyseur de spectre radiofréquence ainsi qu'une technique de microscopie à champ large pour l'imagerie en champ proche du rayonnement émis par des dispositifs RF.

L'analyse spectrale RF en temps réel à large bande est un sujet d'intérêt pour de nombreux domaines technologiques tels que la communication, la médecine et la navigation. Les réseaux radio cognitifs, l'analyse de la compatibilité électromagnétique (EMC), les radars, les communications sans fil, etc, sont quelques-unes des nombreuses applications qui requièrent une détection spectrale en temps réel sur une large bande de fréquences (plusieurs dizaines de GHz). La solution commerciale actuellement disponible est l'analyseur de spectre à transformée de Fourier (FFT) où le signal RF est numérisé par un convertisseur analogique-numérique (ADC) et puis traité par une analyse de Fourier au moyen d'un FPGA. Cette solution permet l'analyse spectrale sur une bande spectrale instantanée de quelque centaine de MHz et elle est essentiellement limité par la vitesse d'échantillonnage et la puissance nécessaire à ses composants électroniques. Pour surmonter la limite imposée par l'électronique et donc analyser, en temps réel, une bande de fréquences plus large (dizaines de GHz), nous proposons une approche alternative basée sur l'utilisation des centres NV du diamant à température ambiante.

L'imagerie en champ proche RF est un outil important pour l'étude et l'analyse du fonctionnement de dispositifs RF. La petite taille de ceux-ci exige des techniques qui offrent à la fois une sensibilité magnétique élevée et une excellente résolution spatiale. Une solution à ce problème est offerte par les SQUIDs (superconducting quantum in-

terference devices) à balayage, qui permettent la mesure des champs RF avec une haute sensibilité ($\mathrm{fT}/\mathrm{Hz}^{1/2}$ à basse fréquence proche du continu) et une résolution spatiale de l'ordre de quelques micromètre. Toutefois, la sensibilité de SQUIDs se dégrade rapidement avec l'augmentation de la fréquence et, en plus, ils nécessitent de travailler à température cryogénique. Dans les années récentes, une approche basée sur les oscillations de Rabi des systèmes atomiques a été proposée et démontrée avec les atomes froid, les cellules à vapeur atomique et les centres NV afin d'effectuer des mesures directes de l'amplitude du champ RF sans nécessité d'une calibration. Dans ce manuscrit nous étudions, à l'aide de simulations, le comportement d'un ensemble de centres NV quand il est utilisé pour l'imagerie en champ proche du rayonnement émis par des dispositifs RF. Par rapport aux SQUIDs, cette technique fonctionne à température ambiante, ne nécessite pas de balayage du capteur ni de l'échantillon et peut atteindre une résolution spatiale inferieure au micromètre.

Le manuscrit est organisé comme suit. Le premier chapitre expose les propriétés des centres NV du diamant ainsi que les motivations des deux applications basées sur celles-ci. En particulier, les solutions existantes et l'état de l'art des techniques pour l'analyse spectrale RF et l'imagerie en champ proche RF sont passées en revue.

Dans le deuxième chapitre, nous présentons un montage expérimental permettant la détection optique en champ large de la résonance de spin des centres NV et nous l'utilisons pour étudier les principales propriétés de ce défaut du diamant. Cette technique, appelée ODMR (optically detected magnetic resonance), consiste à suivre l'intensité de photoluminescence du centre NV en faisant varier la fréquence d'un champ RF qui lui est appliqué. Une réduction de photoluminescence correspond à une transition du centre NV de l'état de spin $m_s = 0$, l'état brillant, à l'un des deux états sombres, $m_s = \pm 1$, et permet de mesurer la fréquence de résonance du système. A l'aide de la technique ODMR, les résonances de spin électronique des centres NV sont détectées sur une large bande de fréquences (plus de 10 GHz) et différents phénomènes sont étudiés: le comportement d'un ensemble de centres NV auquel on applique un champ magnétique statique, les propriétés de polarisation de la photoluminescence émise par les centres NV et comment elles peuvent être exploitées pour reconnaître les orientations des centres NV dans le diamant, et la polarisation du spin nucléaire de l'azote des centres NV sur une large gamme de fréquences (plus de 2 GHz).

Le troisième chapitre est consacré à la mise en œuvre d'un analyseur de spectre RF basé sur un ensemble de centres NV et à l'étude des principales caractéristiques physiques d'un ensemble de centres NV considéré comme un détecteur radiofréquence. Le principe de l'analyse spectrale avec un ensemble de centres NV repose sur l'encodage spatial de leurs fréquences de résonance par un gradient de champ magnétique statique. La photoluminescence de l'ensemble des centres NV est mesurée par une caméra. Etant donné la distribution du champ magnétique statique, chaque pixel de la caméra image des centres NV dont la fréquence de résonance est connue. Quand le signal RF à analyser est envoyé en proximité du diamant, une réduction de photoluminescence est détectée par les pixels qui imagent les centres NV en résonance avec les composantes spectrales du signal. En regardant la position de ces pixels il est donc possible de mesurer le spectre du signal RF. Nous avons mis en œuvre une architecture expérimentale qui permet une analyse spectrale RF en temps réel sur une gamme de fréquence accordable (10 MHz – 25 GHz), une largeur de bande jusqu'à 4 GHz, une résolution en fréquence jusqu'à 1 MHz et une résolution temporelle allant jusqu'à la milliseconde. La mise en place de ce dispositif a nécessité une analyse du comportement d'un ensemble de centres NV sous fort gradient de champ magnétique (plusieurs dizaines de Tesla par mètre) qui est aussi détaillée dans le chapitre.

Le quatrième et dernier chapitre traite de l'imagerie en champ large des champs RF basée sur un ensemble de centres NV. Deux techniques sont proposées. La première

est basée sur l'élargissement en puissance RF de la résonance de spin des centres NV et la seconde utilise la détection en champ large des oscillations de Rabi des centres NV. Ces deux techniques ont permis de reconstruire le champ proche radiofréquence émis par une antenne boucle. La première technique nécessite une calibration pour retrouver l'amplitude du champ RF alors que la seconde permet sa mesure directe. La détection en champ large des oscillations de Rabi des centres NV a été étudiée à la fois expérimentalement et par des simulations. Cette technique a permis de mesurer des amplitudes de champ magnétique dans la gamme [10 µT ; 100 µT] et d'avoir une mesure précise de la distribution du champ RF produit par l'antenne avec une résolution spatiale de l'ordre du micromètre sur une zone d'environ 350 µm. Afin d'expliquer la forme asymétrique des oscillations de Rabi observées expérimentalement, nous avons modélisé le comportement du centre NV pendant la séquence d'impulsions utilisée pour le piloter. Nous avons tenu compte du fait que la lecture de l'état de spin est effectuée par un système d'imagerie champ large et non par une photodiode, comme c'est le cas, le plus souvent, dans la littérature. Les résultats des simulations, en accord avec les résultats expérimentaux, permettent ainsi d'avoir une meilleure compréhension de la polarisation optique et de la lecture du spin du centre NV pendant la séquence. Plus généralement, le modèle peut être utilisé pour étudier la dynamique d'un ensemble de centres NV en présence de séquences complexes d'impulsions laser ou micro-onde, ce qui ouvre des perspectives intéressantes en ce qui concerne les applications des centres NV en régime impulsionnel.

En conclusion, dans ce travail de thèse nous avons employé un ensemble de centres NV pour réaliser deux applications pour l'analyse de signaux RF qui répondent à des besoins concrets de la communauté des radiofréquences et qui, étant donné leur compacité et simplicité d'utilisation, montrent un réel potentiel de développement avancé. De plus, l'étude approfondie de ces techniques a permis de mieux comprendre le comportement des centres NV dans des conditions de fonctionnement rarement explorées (fort champs magnétique, fort gradient de champ magnétique, imagerie en champ large des centres NV en régime impulsionnel) et de développer des outils de travail qui ouvrent des perspectives nouvelles et intéressantes dans le domaine de la magnétométrie et de l'analyse des signaux RF.

Contents

Introduction

The first quantum revolution gave us new rules that govern physical reality. The second quantum revolution will take these rules and use them to develop new technologies.
With these words, J. P. Dowling and G. J. Milburn started almost twenty years ago a very positive review paper on the opportunities and potential of quantum technologies [1]. Since then, many steps have been taken towards the realization of real-world quantum technologies. In this manuscript we are interested in one branch of quantum technology, which is quantum sensing.
In strict analogy and inspired by the DiVincenzo criteria for quantum computation [2], Degen et al. [3] defined four criteria to consider a quantum system eligible for quantum sensing:

- The system has quantized and resolvable energy levels
- The system can be initialized in a well-defined state and its state can be readout
- The system can be coherently manipulated
- The system interacts with the physical quantity to be detected and the interaction induces a state transition of the system or a shift in the system's energy levels.

The nitrogen-vacancy (NV) center in diamond, fulfilling these criteria, is a good candidate to become a building block of the second quantum revolution.

The NV center is a spin-defect in diamond consisting of a nitrogen atom and a carbon vacancy in two adjacent positions of the diamond lattice. It is a solid-state spin defect that can work at room temperature and an extremely photostable single photon source with remarkable spin-dependent optical properties. The opportunity to optically polarize and optically readout its electronic spin, together with the incredible development and mastering of its fabrication techniques, make this defect suitable for various applications such as magnetometers [4], gyroscopes [5], thermometers [6], high-pressure sensors [7], electrometers [8], etc. At present, some companies already offer on the market ready-to-use devices based on NV centers.

In the present manuscript, two applications involving an ensemble of NV centers in diamond are investigated: a radio frequency (RF) spectrum analyzer and a widefield imaging technique of the RF radiation emitted in near field by microwave devices. Considering the fast development of RF-based technologies, both applications find a real interest and offer new opportunities for several and various domains such as telecommunications, medicine, science, space, radars, etc. [9].

At present, the principal and most common solution for the real-time spectral analysis of microwave (MW) signals is the electronic FFT spectrum analyzer [10]. Like several electronic signal analysers, its performances are finally limited by the electronic nature of its components (the so-called electronic bottleneck). For this reason, several photonics-based approaches have been developed in the last decades to the point that a new research field called microwave photonics has been developed [11]. The general idea behind photonics-based RF spectrum analyzers is to transpose a MW signal in

the optical domain and then process it to retrieve the spectral information. Here we propose a new method [12] which exploits the quantum spin properties of electrons to directly detect MW signals with neither analog-to-digital conversions nor optical processing modules.

Concerning the widefield imaging of the radiation emitted in the near-field by RF devices, the present solutions essentially consist in electric scanning probes, which tend to perturb the measurement, or SQUIDs, which require cryogenic working temperature and are not suitable for high frequency fields. Here we investigate a different approach, inspired by previous works both with NV centers [13] and other atomic sensors [14], which exploits the widefield detection of the Rabi oscillations of an ensemble of NV centers to retrieve directly the amplitude of the RF field, at room temperature and in a non-invasive way.

The two applications proposed in this manuscript give the opportunity to investigate the properties of an ensemble of NV centers and to carry out a more general analysis whose results may contribute not only to the improvement of the two techniques proposed in this manuscript but also to the development of new NV centers-based applications.

Outline of the thesis

The thesis consists of four chapters.

In the first chapter, the physics of the NV center in diamond, its properties and its applications are introduced and some diamond and NV centers fabrication techniques are described. The available solutions and the state-of-the-art for both RF spectral analysis and near field imaging of RF radiation are reviewed; the motivations and the general ideas behind each of the two applications considered in this manuscript are detailed and discussed.

In the second chapter, the spin resonances of an ensemble of NV centers are investigated both theoretically, introducing the Hamiltonian formalism, and experimentally. The experimental set-up, the acquisition procedure and the signal processing used to optically detect the NV center resonance frequencies in the continuous wave regime are detailed. Several phenomena are investigated such as the behaviour of an ensemble of NV centers under a static magnetic field, the polarization properties of the NV center photoluminescence and how they can be exploited to characterize the NV centers orientations, and the NV's nitrogen nuclear spin polarization.

The third chapter is dedicated to the implementation of a real-time RF spectrum analyzer based on an ensemble of NV centers. The main physical features of NV centers considered as MW detectors are investigated, an experimental architecture is proposed and its performances are studied.

The fourth and last chapter deals with the widefield imaging of the RF field amplitude based on an ensemble of NV centers. Two techniques are proposed. The first one is based on the RF power broadening of the NV center spin resonances in continuous pumping regime while the second one is based on the widefield detection of NV centers Rabi oscillations in pulsed regime. The experimental set-up and the acquisition procedure used to drive Rabi oscillations in an ensemble of NV centers and to detect them using a widefield imaging system is described. It is then compared to the more classical procedure implemented when an avalanche photodiode (APD) is employed as detector. A model to simulate the widefield detection of NV centers Rabi oscillations is proposed and exploited to have a better insight of the NV centers dynamics during the pulse sequence. Finally optically detected magnetic resonance (ODMR) spectrum of an ensemble of NV centers is measured in pulsed regime using a widefield detection scheme and the technique is compared to the classical pulsed-ODMR acquisition

procedure performed when APDs are used as detectors.

Chapter 1

Nitrogen-vacancy center and its applications

1.1 The diamond

Diamond is a crystalline allotropic form of carbon. Carbon is a chemical element belonging to the IV group of the periodic table of elements. Its electron configuration is $1s^2 2s^2 2p^2$ and thus the valence shell is half-filled by four valence electrons. In diamond, carbon atoms are covalently bonded by means of sp^3 orbitals, forming a tetrahedral structure. Carbon bonds are oriented, according to the crystallographic notation, along the crystallographic directions $\{111\}$, $\{11-1\}$, $\{1-11\}$, $\{1-1-1\}$ (fig. 1.1a).
The lattice structure and the strength of the chemical bonds make diamond a material with extraordinary and interesting properties: it is the hardest material existing in nature, it has an extremely high thermal conductivity and it is a good electrical insulator. The energy band structure of diamond is characterized by an energy gap of 5.5 eV and thus diamond is transparent in the visible region of the electromagnetic spectrum. These features make diamond an attractive material for several applications in various fields: electronics, thermal management, high-pressure physics, optics, etc. [15].
Diamond properties (both optical, mechanical and electrical) can be altered by the presence of defects. Among the hundreds of existing diamond defects [16], in the framework of this thesis we are interested in the so-called colour centers and, more specifically, in one of them: the nitrogen-vacancy center, which is considered a very promising tool for quantum sensing applications. Colour centers are defects in which one or more unpaired electrons occupy a lattice vacancy [17]. The presence of this kind of defect alters the diamond electronic band structure adding discrete energy levels in the bandgap. The energy gap between these new energy levels falls in the visible part of the electromagnetic spectrum making diamond not transparent anymore, and that is why these defects are called colour centers. Before introducing the nitrogen-vacancy center and its properties (section 1.2), it is interesting to say a few words on the different techniques to synthesize diamonds.

1.1.1 Synthetic diamond growing techniques

The attractive properties of diamond and its defects have led to further development and improvement of diamond fabrication techniques.

The first technique implemented to synthesise diamond was the high-pressure high-temperature (HPHT) synthesis [18]. Miming the natural formation process, diamond is synthesized using carbon-containing materials (e.g. graphite) that are exposed to high temperature (1500 °C) and high pressure ($>$ 5 GPa), where diamond is the most

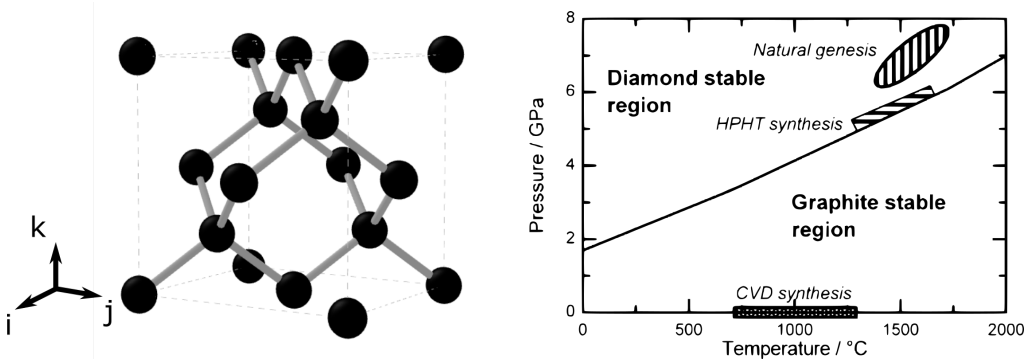

(a) (b)

Figure 1.1: (a) Diamond unit cell. Carbon atoms, represented by black spheres, are arranged in a tetrahedral lattice. In grey the sp^3 bonds oriented along the four diamond crystallographic axis $\{111\}$, $\{11-1\}$, $\{1-11\}$, $\{1-1-1\}$. (b) Pressure-temperature phase diagram of carbon showing the different formation regimes. Figure taken from [19].

favourable allotropic form of carbon (fig. 1.1b).

A second technique to synthesize diamond is based on chemical vapour deposition (CVD) [19, 20]. In this case, the synthesis happens at low pressure and high temperature (1000 °C), under thermodynamic conditions that would favour the graphite formation (fig. 1.1b). Diamond is thus produced exploiting the kinetics and not the thermodynamics of the synthesis. During the CVD process, a hydrocarbon gas source (usually methane plus hydrogen) is injected into a reaction chamber where a diamond substrate was previously included. The gas is then transformed in plasma to activate the deposition, layer by layer, of carbon atoms on the diamond substrate. CVD growth enables a better control of diamond impurities at the cost of a longer and more complex procedure with respect to the HPHT method.

A third technique is the detonation of carbon-based materials. During the detonation high pressure and high temperature are reached thus enabling the formation of diamond [21]. This technique is largely used for the synthesis of nano-size diamond crystals which are extremely appealing for biomedical applications. In fact, the inertness and bio-compatible nature of diamond, in addition to its optical and mechanical properties, make nano-diamonds superior to any other nano-material for biomedical applications [22].

1.2 The nitrogen-vacancy center

The nitrogen-vacancy (NV) center consists of a nitrogen atom and a carbon vacancy in two adjacent positions of the diamond lattice. It has a C_{3V} symmetry[1] with respect to the axis connecting the nitrogen and the vacancy lattice positions, usually called NV center axis [23].

According to the geometry of the diamond lattice, the NV center axis can be oriented along one of the four diamond crystallographic axis ($\{111\}$, $\{11-1\}$, $\{1-11\}$, $\{1-1-1\}$). NV centers oriented along the same crystallographic axis are usually said to belong to the same NV centers family.

NV centers exist in two stable charge states: the neutral charge state (NV^0) and the negative charge state (NV^-) (fig. 1.2a and **????**. NV^0 has five valence electrons: the

[1]The system is invariant under rotation of $2\pi/3$ around its axis

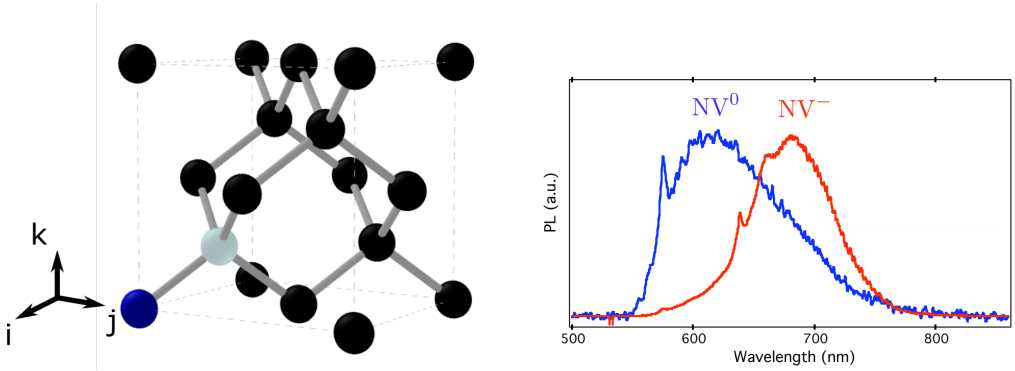

(a) (b)

Figure 1.2: (a) NV center in the diamond lattice. The blue sphere represents a nitrogen atom, the white sphere a carbon vacancy and the black spheres the carbon atoms. (b) Photoluminescence spectra of the NV^0 (blue) and the NV^- (red).

three valence electrons of the three carbon atoms surrounding the vacancy and the two unpaired valence electrons of the nitrogen atom. The ground state spin of the system is equal to 1/2 [26]. NV^- has six valence electrons, two of which forming a lone pair, which induces a total spin equals to 1.
The two charge states present a different absorption and emission spectrum enabling their optical identification. The emission spectra of NV^0 and NV^- are reported in fig. 1.2b. They both are characterised by a large phonon band. The NV^0 zero phonon line (ZPL), which is the spectral line associated to an optical transition not mediated by the lattice phonons, is at 575 nm. The NV^- ZPL is at 637 nm. In this manuscript we are interested in the negatively charged NV center, which from now on will be simply called NV center. In fact, differently from NV^0, NV^- shows remarkable spin-dependent optical properties which make it apt to sensing applications.

The orbitals structure and the energy levels of the NV center can be deduced using a group theory approach [23, 27, 28] and ab-initio calculations based on density functional theory (DFT) [29, 30, 31]. Without entering into the details of the calculation, we just report here the main results for an NV center at room temperature (fig. 1.3). Due to the C_{3V} symmetry of the defect, the NV center axis forms an intrinsic spin quantization axis. Both ground state and excited state are spin triplets ($|m_s = 0, \pm 1\rangle$). The ground state (excited state) zero-field splitting [2] (ZFS) between the $|0\rangle$ state and the two degenerate $|\pm 1\rangle$ states is equal to 2.87 GHz (1.42 GHz). The degeneracy between the $|\pm 1\rangle$ can be removed by applying a static magnetic field (Zeeman effect). The metastable state consists of three singlet states, two of which are degenerate. The energy gap between the singlet states is 1042 nm [32, 33], in the infrared region of the electromagnetic spectrum. This transition can be exploited for sensing protocol [34, 35], but it is out of the scope of this manuscript. Therefore the structure of the metastable state is neglected and it is approximated to a single energy level [36].

1.2.1 Spin dependent optical properties: optical spin polarization and optical spin readout

The NV center presents spin-dependent optical properties which make possible the optical polarization and the optical readout of its spin state. The optical cycle of the NV center is depicted in fig. 1.3. At room temperature, the three ground state spin

[2] The Energy gap between the $|0\rangle$ level and the two degenerate $|\pm 1\rangle$ levels when no external static field is applied

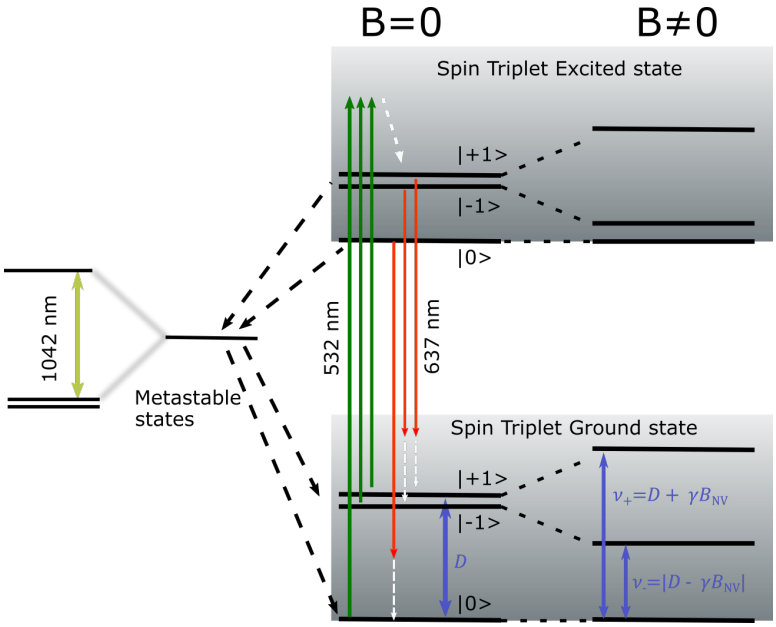

Figure 1.3: NV center energy level diagram. The ground state triplet and the excited state triplet are represented by grey blocks to take into account the coupling with the lattice mediated by phonons. At zero static magnetic field, the $|\pm1\rangle$ states are degenerate. The degeneracy can be removed applying a static magnetic field. The green arrows represent the optical excitation process. The red arrows and the black dashed arrows respectively represent the radiative decay process (the frequency reported, 637 nm corresponds to the ZPL) and the inter-system crossing through the metastable state. The decay processes are usually mediated by phonons (white dashed arrow). The metastable state consists of three singlet states, two of which are degenerate, separated by an energy gap of 1042 nm (light green arrow). Since the infrared (IR) transition between the metastable states is not considered in this manuscript, the metastable states are grouped in a single metastable state to simplify the NV center dynamics description.

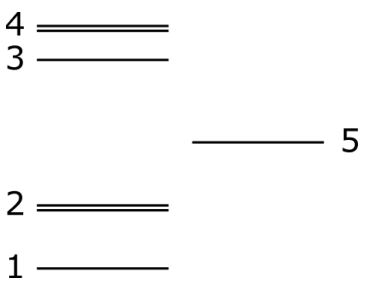

Transition	Transition rate (μs^{-1})
$k_{31} = k_{42}$	64.9
k_{35}	10.6
k_{45}	80
k_{51}	2.6
k_{52}	3

Figure 1.4: Room temperature NV center transition rates. Since the behaviour of the $|\pm1\rangle$ states is the same, the NV center energy structure is approximate to a five-level system (left). The transition rate from the i level to the j level is denoted as k_{ij} and reported in the table (right). The values are taken from [36].

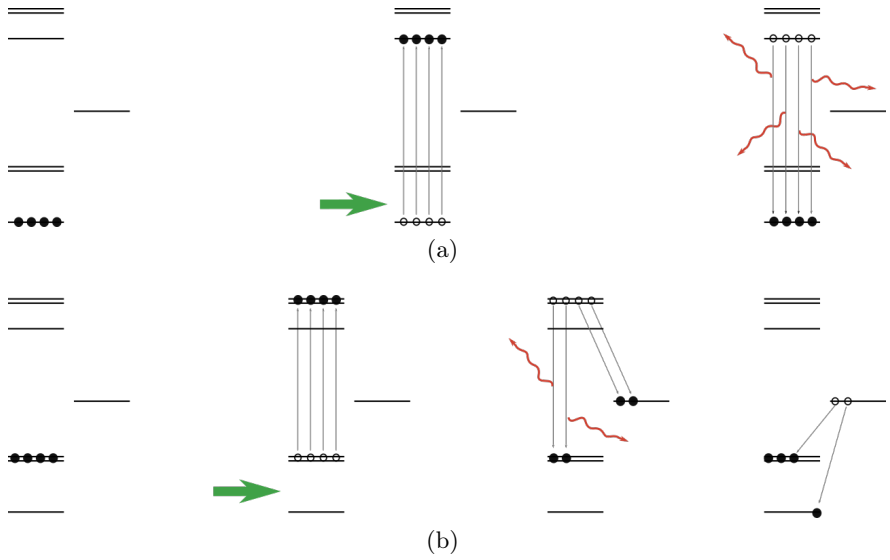

Figure 1.5: Schematic of the NV center optical cycle assuming that the NV centers are initially in $|0\rangle$ (a) and in $|\pm1\rangle$ (b). An ensemble of four NV centers is considered. Each NV center is represented by a black circle. The green arrow represents the laser optical pumping, the red lines represent photons. The schematic is inspired by [38].

levels are equally populated due to thermal excitation. The NV center is excited from the ground state to the excited state by a non-resonant laser excitation. Usually a 532 nm optical pumping is used in order to efficiently excite the NV center and reduce the probability of photo-ionization [37].
Once the NV center is excited, two decay processes are possible: a radiative spin-conserving process and a non-radiative inter-system crossing (ISC) process through the metastable state. According to the transition rates reported in fig. 1.4, the probability to undergo an ISC process when the NV center is in $|\pm1\rangle$ (k_{45}) is higher than the probability to follow the same path when the NV center is in $|0\rangle$ (k_{35}). As a consequence, the NV center emits more photoluminescence when it is in $|0\rangle$ than when it is in $|\pm1\rangle$, allowing the optical readout of its spin state. The $|0\rangle$ state is usually called bright state and the $|\pm1\rangle$ states are called dark states. It is important to stress that even if the $|\pm1\rangle$ states are called dark states, they are still photoluminescent states, but their photoluminescence (PL) rate is lower than the PL rate of the NV center when it is in the $|0\rangle$ state. The transition rate from the metastable state to the ground state is almost spin-independent ($k_{51}/k_{52} = 1.15$). Therefore, since the passage through the metastable state is more probable when the NV center is in $|\pm1\rangle$ than when it is in $|0\rangle$ ($k_{45}/k_{35} = 7.6$), after some optical cycles the NV center results polarized in $|0\rangle$.

A schematic of the NV center optical cycle is represented in fig. 1.5. In order to graphically represent more than one optical cycle, an ensemble of four NV centers (each circle represents an NV center) is considered. In fig. 1.5a all the NV centers are initially in $|0\rangle$. Once excited by the laser (green arrow), they preferentially decay through a radiative process, emitting therefore four photons (red arrows). In fig. 1.5b all the NV centers are initially in $|+1\rangle$ or $|-1\rangle$. Once excited, they have almost the same probability to undergo a radiative de-excitation process or an ISC process. Therefore only two photons will be emitted. The other two NV centers in the metastable state have the same probability to decay in $|0\rangle$ or $|\pm1\rangle$. Therefore, at the end of the optical cycle, a part of NV centers initially in $|\pm1\rangle$ is in $|0\rangle$. This simple scheme explains both the optical spin readout process and the optical polarization process.

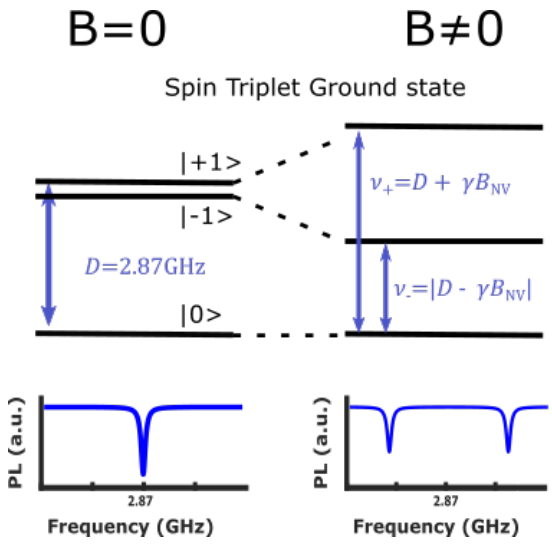

Figure 1.6: NV center ground state ODMR spectrum without (left) and with (right) an external static magnetic field applied.

1.2.2 Optical detection of the NV center magnetic resonances

The NV center spin state can be manipulated by means of a radiofrequency (RF) or microwave (MW) field [3]. According to the magnetic-dipole selection rules [39], transitions are possible between states which verify the condition: $\Delta m_s = \pm 1$, where Δm_s is the difference between the spin quantum number of the initial and final state. Thus, for NV centers, two RF spin transitions are allowed: $|0\rangle \rightarrow |+1\rangle$ and $|0\rangle \rightarrow |-1\rangle$. Due to the spin-dependent optical properties of the NV centers, these two transitions can be optically detected. The optical detection of the electron spin resonance (ESR) is called ODMR (optically detected magnetic resonance). The simplest ODMR experiment consists in monitoring the PL emitted by the NV centers while the frequency of a RF field is swept. When the RF field is on resonance with the NV center spin transition, the NV center initially polarized in $|0\rangle$ moves to $|\pm 1\rangle$ and therefore a drop of PL is observed. Figure 1.6 shows the ground state ODMR spectrum of an NV center without and with an external static magnetic field. In the first case, the two spin transitions are degenerate in correspondence of the ground state ZFS (2.87 GHz). In the second case, two resonance peaks are visible. When the static magnetic field (B) is applied along the NV center axis, the two resonance frequencies are

$$\nu_{\pm} = |D \pm \gamma B| \tag{1.1}$$

where γ is the NV center gyromagnetic ratio (28 GHz/T) and D is the ground state zero-field splitting. Therefore, simply measuring the frequency distance (Δf) between the two resonance peaks ($\Delta f = 2\gamma B$) it is possible to retrieve the amplitude of the static magnetic field and therefore operate NV centers as magnetometers.
The amplitude of the ODMR peaks with respect to the baseline is called ODMR contrast and it is defined as:

$$C = \frac{PL_{OFF} - PL_{ON}}{PL_{OFF}} \tag{1.2}$$

where PL_{OFF} is the NV center PL intensity when it is off resonance with the RF field and PL_{ON} is the NV center PL intensity when it is on resonance with the RF field.

[3] In this text the appellations RF and MW are used almost interchangeably to denote a frequency range from 1MHz to approximately 30 GHz.

The Zeeman interaction between a spin-system and a static magnetic field is described by the well known Zeeman Hamiltonian:

$$H = h\gamma \vec{B} \cdot \vec{S} \tag{1.3}$$

where γ is the gyromagnetic ratio of the system (in Hz/T) and $\vec{S} = (S_x, S_y, S_z)$ is the spin operator[4]. Taking into account the ground state zero-field splitting (D = 2.87 GHz) of the NV center, the Hamiltonian of an NV center interacting with a static magnetic field can be written, in first approximation, as:

$$H = h(DS_z^2 + \gamma \vec{B} \cdot \vec{S}) \tag{1.4}$$

where z is the NV center axis and $\gamma = 28$ GHz/T is the NV center gyromagnetic ratio. A more detailed discussion about the NV center Hamiltonian and the Zeeman interaction is developed in chapter 2. Here it is interesting to observe that, for low static magnetic field and using a secular approximation, the only component that affects the Zeeman interaction is the one parallel to the NV center axis. Therefore eq. (1.1) can be generalized to

$$\nu_{\pm} = |D \pm \gamma B_{NV}| \tag{1.5}$$

where B_{NV} is the magnetic field component parallel to the NV axis.
This discussion about the Zeeman interaction is useful to understand the ODMR spectrum of an ensemble of NV centers homogeneously oriented along the four diamond crystallographic axis. Applying a static magnetic field B to the NV centers ensemble, each NV center family undergoes a different Zeeman shift because of the different projection of the magnetic field along the NV center family axis. Thus the ODMR spectrum of an ensemble of NV centers shows eight ODMR peaks, two for each NV center family. The contrast for each peak is now defined as:

$$C_i = \frac{PL_i(RF_{OFF}) - PL_i(RF_{ON})}{\sum_{i=1}^{4} PL_i(RF_{OFF})} \tag{1.6}$$

where the subscripts $i = [1, 4]$ identify the NV center family. The ODMR of an ensemble of NV centers is the subject of chapter 2.

1.2.3 Coherent control of a two-level system

The NV center can be considered as a two-level system when only one of the two spin transitions is considered: $|0\rangle \rightarrow |-1\rangle$ or $|0\rangle \rightarrow |+1\rangle$. This approximation is quite reasonable under certain hypothesis. Indeed, applying a static magnetic field well oriented along the NV center quantization axis, it is possible to sufficiently shift the $|-1\rangle$ and $|+1\rangle$ ground state sublevels and thus address only one of the two NV center ground state transitions (secular approximation). The interaction between the NV center and the RF field can be studied in a very general way considering a generic two-level system. As an example we discuss now the case of spin-1/2 system driven by an external oscillating field.
The Hamiltonian of the system has the general form :

$$H = \hbar(\omega_0 S_z + 2\pi\gamma \vec{B} \cdot \vec{S}) \tag{1.7}$$

[4]We define: $S_x = \frac{1}{\sqrt{2}} \begin{pmatrix} 0 & 1 & 0 \\ 1 & 0 & 1 \\ 0 & 1 & 0 \end{pmatrix}$; $S_y = \frac{1}{\sqrt{2}i} \begin{pmatrix} 0 & 1 & 0 \\ -1 & 0 & 1 \\ 0 & -1 & 0 \end{pmatrix}$; $S_z = \begin{pmatrix} 1 & 0 & 0 \\ 0 & 0 & 0 \\ 0 & 0 & -1 \end{pmatrix}$.

where ω_0 is the Larmor angular frequency of the system, $\vec{S}$ is the spin operator, S_x, S_y, S_z are the 1/2 spin projection operator along x,y,z (where z is the spin quantization axis and x and y are arbitrarily chosen to obtain a Cartesian coordinate system), $\vec{B}$ is the driving oscillating magnetic field and γ is the gyromagnetic ratio expressed in Hz/T. We remind here the 1/2 spin operators:

$$S_x = \frac{1}{2}\begin{pmatrix} 0 & 1 \\ 1 & 0 \end{pmatrix} \qquad S_y = \frac{1}{2i}\begin{pmatrix} 0 & 1 \\ -1 & 0 \end{pmatrix} \qquad S_z = \frac{1}{2}\begin{pmatrix} 1 & 0 \\ 0 & -1 \end{pmatrix} \tag{1.8}$$

According to eq. (1.7), the magnetic field component along the spin quantization axis does not contribute to the level transition but only affects the energy of the two levels. Therefore, B_z is set to zero and, without losing of generality [39], the oscillating magnetic field is assumed to be circularly polarized in the xy plane:

$$B = B_1 \left(\cos(\omega t)\,\vec{x} + \sin(\omega t)\,\vec{y}\right). \tag{1.9}$$

Developing the scalar product of eq. (1.7), we obtain:

$$H = \hbar\omega_0 S_z + \hbar\Omega_R \left(\cos(\omega t) S_x + \sin(\omega t) S_y\right) \tag{1.10}$$

where

$$\Omega_R = 2\pi\gamma B_1 \tag{1.11}$$

is called Rabi angular frequency. Considering as a basis the eigenvectors of the S_z operator, which are denoted as $|+\rangle = \begin{pmatrix} 1 \\ 0 \end{pmatrix}$ and $|-\rangle = \begin{pmatrix} 0 \\ 1 \end{pmatrix}$, the matrix representation of H is:

$$H = \frac{\hbar}{2}\begin{pmatrix} \omega_0 & \Omega_R e^{-i\omega t} \\ \Omega_R e^{i\omega t} & -\omega_0 \end{pmatrix} \tag{1.12}$$

The state vector of the system at a generic instant of time (t) has the general form:

$$|\psi(t)\rangle = c_+(t)\,|+\rangle + c_-(t)\,|-\rangle \tag{1.13}$$

where the time-dependent coefficients $c_+(t)$ and $c_-(t)$ can be evaluated solving the Schrödinger equation for the system [39]. Assuming the system is initially in $|+\rangle$ (that is $|\psi(0)\rangle = |+\rangle$), it is interesting to evaluate the probability to find the system in the state $|-\rangle$ at a generic instant of time (t) and for a generic angular frequency (ω) of the driving field. This probability is given by [39]:

$$P(t,\omega) = |\,\langle -|\psi(t)\rangle\,|^2 = \frac{\Omega_R^2}{\Omega_R^2 + (\Delta\omega)^2}\sin^2\left(\sqrt{\Omega_R^2 + (\Delta\omega)^2}\,\frac{t}{2}\right) \tag{1.14}$$

where $\Delta\omega = \omega - \omega_0$ is the detuning between the angular frequency of the driving field and the Larmor frequency of the system. According to eq. (1.14), the probability to find the system in $|-\rangle$ oscillates at frequency $\Omega_R^* = \sqrt{\Omega_R^2 + (\Delta\omega)^2}$. These oscillations are known as Rabi oscillations and Ω_R^* is called generalized Rabi angular frequency .
When the driving system is on resonance with the two-level system ($\Delta\omega = 0$ and $\Omega_R^* = \Omega_R$), eq. (1.14) becomes:

$$P(t,\omega_0) = \sin^2\left(\Omega_R \cdot \frac{t}{2}\right) \tag{1.15}$$

In this case, the probability to find the system in $|-\rangle$ oscillates between 0 and 1 or, in other words, the system oscillates between the $|+\rangle$ and the $|-\rangle$ states at the Rabi angular

frequency (fig. 1.8a). The shortest driving field pulse which enables to completely reverse the spin of the system ($P(t, \omega_0) = 1$) has duration $t = \frac{\pi}{\Omega_R}$ and it is called π pulse.
When the driving field is detuned with respect to the resonance frequency of the system, the probability to find the system in $|-\rangle$ oscillates at a higher angular frequency, the generalized Rabi angular frequency, without never being equal to 1 (fig. 1.8a). The maximum probability of finding the system in $|-\rangle$ is:

$$P(t = \frac{\pi}{\Omega_R^*}, \omega) = \frac{\Omega_R^2}{\Omega_R^2 + (\Delta\omega)^2} < 1. \tag{1.16}$$

and therefore a complete spin-inversion is impossible.
Looking at the dependence of the probability from the detuning (eq. (1.14)) it is possible to recognise the phenomenon of resonance. The spectral lineshape of the resonance is a Lorentzian with a full width at half maximum (FWHM) proportional to the Rabi frequency. This proportionality is called power broadening effect.

Moving now to the NV center, according to (eq. (1.4)), the interaction with a RF field ($B^{RF} = B\left(\cos(\omega t) + \sin(\omega t)\right)$) circularly polarized in a plane perpendicular to the NV center axis (z) is given by

$$H = 2\pi\hbar D S_z^2 + 2\pi\hbar(B_z^{DC} \cdot S_z) + 2\pi\hbar\gamma B\left(\cos(\omega t)S_x + \sin(\omega t)S_y\right) \tag{1.17}$$

where D is the NV center ZFS expressed in Hz, B_z^{DC} is a static magnetic field aligned to the NV center axis and $\vec{S}$ is the spin-1 operator whose components are defined as [40]:

$$S_x = \frac{1}{\sqrt{2}}\begin{pmatrix} 0 & 1 & 0 \\ 1 & 0 & 1 \\ 0 & 1 & 0 \end{pmatrix} \qquad S_y = \frac{1}{\sqrt{2}i}\begin{pmatrix} 0 & 1 & 0 \\ -1 & 0 & 1 \\ 0 & -1 & 0 \end{pmatrix} \qquad S_z = \begin{pmatrix} 1 & 0 & 0 \\ 0 & 0 & 0 \\ 0 & 0 & -1 \end{pmatrix} \tag{1.18}$$

The static magnetic field (B_z^{DC}) removes the degeneracy between the $|+1\rangle$ and $|-1\rangle$ states. Defining ω_1 and ω_2 as the two NV center resonance frequencies ($|0\rangle \to |+1\rangle$ and $|0\rangle \to |-1\rangle$ respectively), the Hamiltonian of the system can be written as:

$$H = \hbar\begin{pmatrix} \omega_1 & \frac{2\pi\gamma}{\sqrt{2}}Be^{-i\omega t} & 0 \\ \frac{2\pi\gamma}{\sqrt{2}}Be^{+i\omega t} & 0 & \frac{2\pi\gamma}{\sqrt{2}}Be^{-i\omega t} \\ 0 & \frac{2\pi\gamma}{\sqrt{2}}Be^{+i\omega t} & \omega_2 \end{pmatrix} \tag{1.19}$$

As discussed at the beginning of this paragraph, we can limit our discussion to only one NV center transition (for example $|0\rangle \to |+1\rangle$), and therefore we can rewrite the Hamiltonian of the system as:

$$H = \hbar\begin{pmatrix} \omega_1 & \frac{2\pi\gamma}{\sqrt{2}}Be^{-i\omega t} \\ \frac{2\pi\gamma}{\sqrt{2}}Be^{+i\omega t} & 0 \end{pmatrix} \tag{1.20}$$

Comparing this Hamiltonian to eq. (1.12), we can define the angular Rabi frequency of the system as:

$$\Omega_R = \sqrt{2} \cdot 2\pi\gamma B \tag{1.21}$$

which differs from the angular Rabi frequency defined for a 1/2-spin system (eq. (1.11)) by a factor of $\sqrt{2}$. Redefining the zero of the energy axis at the middle of the energy gap between the $|0\rangle$ and the $|+1\rangle$ levels, eq. (1.20) reads exactly as eq. (1.12). Therefore we can use the results achieved for a spin-1/2 system to study the behaviour of an NV center interacting with a RF field. Considering the $|0\rangle \to |-1\rangle$ transition and a RF field

clockwise circularly polarized leads to the same result.
Another interesting case concerns a RF field which is linearly polarized in a plane perpendicular to the NV axis. It can always be written as the sum of a clockwise and anti-clockwise components:

$$B = B_0 cos(\omega t)\vec{x} = \frac{B_0}{2}(cos(\omega t) - sin(\omega t)) + \frac{B_0}{2}(cos(\omega t) + sin(\omega t)) \tag{1.22}$$

Since the NV center transitions are driven by the circularly polarized components of the RF field, whose amplitudes are $B_c = \frac{B_0}{2}$, the Rabi angular frequency (eq. (1.21)) associated with each of the two NV center transitions is related to the amplitude of the linear polarized field by the equation [43]:

$$\Omega_R = \sqrt{2} \cdot 2\pi\gamma B_c = \frac{\sqrt{2}}{2} \cdot 2\pi\gamma B_0 \tag{1.23}$$

1.2.4 Relaxation processes and Bloch equations

A real quantum system (e.g. the NV center), differently from the simple model described above, interacts with its environment. As a result of these interactions, (also called relaxation processes) the system loses its coherence. The characteristic time scale of the spin relaxation processes fixes an upper bound for the characteristic time of quantum manipulations and measurements.
The two main spin-relaxation processes are the spin-lattice (or longitudinal) relaxation process, whose characteristic time is denoted as T_1, and the spin-spin (or transverse) relaxation process, whose characteristic times are denoted as T_2 and T_2^*. The spin-lattice relaxation process accounts for the interaction between the NV center spin and the lattice phonons whose effect is to restore the thermodynamic equilibrium. Typical T_1 times for NV centers are of the order of some ms. The spin-spin relaxation process accounts for the interaction between the NV center spin and the other spins which surround it (paramagnetic environment). Therefore the T_2 time strongly depends on the diamond quality. Indeed, the higher is the number of paramagnetic impurities (e.g. ^{14}N, ^{13}C,...), the lower is T_2. T_2^* characterizes the inhomogeneous relaxation processes of an ensemble of quantum systems. It accounts both for the different environment surrounding each quantum system and for any other source of decoherence such as spatial inhomogeneity of the electromagnetic field, temperature fluctuations, etc.
The relaxation processes depend on the NV center environment and therefore on the diamond and NV center fabrication technique (see section 1.4). In fig. 1.7 typical values of T_2 and T_2^* for NV center obtained under different growing conditions are reported. As explained in section 1.1, diamonds grown using the HPHT technique usually present more impurities than CVD diamonds. For this reason, NV centers embedded in HPHT diamonds have a lower coherence time. In the case of CVD diamonds, one way to improve the coherence time is to prefer the ^{12}C carbon isotope (nuclear spin equal to 0) to the ^{13}C carbon isotope (nuclear spin equals to 1/2) in order to reduce the spin-impurity in the material.

Adding the relaxation phenomena to the mathematical model described in the previous paragraph leads to the well known Bloch equations for a closed two-level system. The relaxation phenomena are taken into account using the formalism of the Lindbald equation [45], according to which the time evolution of the density matrix can be written as:

$$\frac{d\varrho}{dt} = \frac{1}{i\hbar}[H, \varrho] + \left\{\frac{d\varrho}{dt}\right\}_{relaxation} \tag{1.24}$$

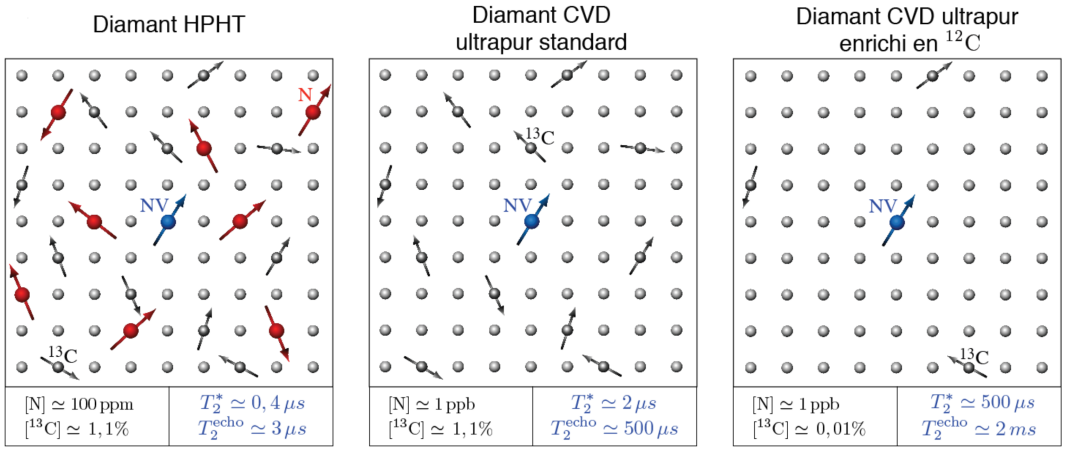

Figure 1.7: Typical relaxation time for NV centers embedded in diamonds grown by using different techniques and under different conditions. NV centers are represented by blue arrows, ^{13}C by grey arrows and other paramagnetic impurities by red arrows. Image taken from [44].

where H is the Hamiltonian in eq. (1.10), ϱ is the density matrix of the system

$$\varrho = \begin{pmatrix} \varrho_{00} & \varrho_{01} \\ \varrho_{10} & \varrho_{11} \end{pmatrix} \tag{1.25}$$

and $\left\{\frac{d\varrho}{dt}\right\}_{relaxation}$ is the contribution of the relaxation processes which is defined as:

$$\left\{\frac{d\varrho}{dt}\right\}_{relaxation} = \begin{pmatrix} \Gamma_1(\varrho_{11} - \varrho_{00}) & -\Gamma_2 \\ -\Gamma_2 & -\Gamma_1(\varrho_{11} - \varrho_{00}) \end{pmatrix} \tag{1.26}$$

where $\Gamma_1 = 1/T_1$ and $\Gamma_2 = 1/T_2$ are the spin-lattice and spin-spin relaxation rates. Γ_1 brings the system to the thermodynamic equilibrium ($\varrho_{11} = \varrho_{00}$), while Γ_2 tends to suppress the quantum coherence ($\varrho_{01} = \varrho_{10} = 0$).
Replacing eq. (1.10) and eq. (1.26) in eq. (1.24), it results [46]:

$$\frac{d\varrho_{11}}{dt} = i\left(\frac{\Omega_R}{2}\left(\varrho_{10}e^{i\omega t} - \varrho_{01}e^{-i\omega t}\right) - \Gamma_1\left(\varrho_{11} - \varrho_{00}\right)\right) \tag{1.27a}$$

$$\frac{d\varrho_{00}}{dt} = -\frac{d\varrho_{11}}{dt} \tag{1.27b}$$

$$\frac{d\varrho_{01}}{dt} = i\omega_0\varrho_{01} - i\frac{\Omega_R}{2}e^{i\omega t}\left(\varrho_{11} - \varrho_{00}\right) - \Gamma_2\varrho_{01}e^{-i\omega t} \tag{1.27c}$$

$$\frac{d\varrho_{10}}{dt} = -\frac{d\varrho_{01}^*}{dt} \tag{1.27d}$$

In order to make the coefficients of the Bloch equations time-independent, we define:

$$\varrho'_{10} = \varrho_{10}e^{i\omega t} \tag{1.28a}$$

$$\varrho'_{01} = \varrho_{10}e^{-i\omega t} \tag{1.28b}$$

$$\varrho'_{00} = \varrho_{00} \tag{1.28c}$$

$$\varrho'_{11} = \varrho_{11} \tag{1.28d}$$

Using these new variables, eq. (1.27) become:

$$\frac{d\varrho'_{11}}{dt} = i\frac{\Omega_R}{2}\left(\varrho'_{10} - \varrho'_{01}\right) - \Gamma_1\left(\varrho'_{11} - \varrho'_{00}\right) \tag{1.29a}$$

$$\frac{d\varrho'_{00}}{dt} = -\frac{d\varrho'_{11}}{dt} \tag{1.29b}$$

$$\frac{d\varrho'_{01}}{dt} = -i\Delta\omega\varrho'_{01} - i\frac{\Omega_R}{2}\left(\varrho'_{11} - \varrho'_{00}\right) - \Gamma_2\varrho'_{01} \tag{1.29c}$$

$$\frac{d\varrho'_{10}}{dt} = -\frac{d\varrho'^{*}_{01}}{dt} \tag{1.29d}$$

Using the density matrix property ($\varrho'_{01} = \varrho'^{*}_{10}$) and removing the superscript from the density matrix elements ($\varrho'_{ij} = \varrho_{ij}$), it is possible to write:

$$\frac{d\varrho_{11}}{dt} = \Gamma_1\left(\varrho_{00} - \varrho_{11}\right) + \Omega_R\Im\left[\varrho_{01}\right] \tag{1.30a}$$

$$\frac{d\varrho_{00}}{dt} = -\Gamma_1\left(\varrho_{00} - \varrho_{11}\right) - \Omega_R\Im\left[\varrho_{01}\right] \tag{1.30b}$$

$$\frac{d\Im\left[\varrho_{01}\right]}{dt} = -\frac{\Omega_R}{2}\left(\varrho_{11} - \varrho_{00}\right) - \Gamma_2\Im\left[\varrho_{01}\right] - \Delta\omega\Re\varrho_{01} \tag{1.30c}$$

$$\frac{d\Re\left[\varrho_{01}\right]}{dt} = +\Delta\omega\Im\varrho_{01} - \Gamma_2\Re\varrho_{01} \tag{1.30d}$$

where $\Re\left[\varrho_{01}\right]$ and $\Im\left[\varrho_{01}\right]$ are respectively the real and imaginary part of ϱ_{01} [47].

The effect of the relaxation processes are shown in fig. 1.8, where the Rabi oscillations for a non-dissipative and a dissipative system are compared.

1.2.5 Modelling the NV center as a two-level system

In the previous paragraph both the dynamics of an isolated two-level system interacting with an oscillating driving field (section 1.2.3) and the effect of the interaction between the system and its environment (section 1.2.4) have been discussed. Now, we report a model that, using the Lindbald formalism, describes a dissipative two-level system under optical pumping [48]. This model is useful to describe the NV center behaviour under continuous optical pumping. For this reason, the two levels of the model are called $|0\rangle$ and $|1\rangle$ and it is assumed that the $|0\rangle$ level corresponds to the $|m_s = 0\rangle$ NV center ground state sublevel, and $|1\rangle$ to the $|m_s = +1\rangle$ or $|m_s = -1\rangle$ NV center ground state sublevel.
The optical pumping influences the spin dynamics in two different ways. First, it tends to polarize the system in $|0\rangle$. This contribution is taken into account adding a transition from $|1\rangle$ to $|0\rangle$. Since the pumping process is a saturation process, the transition rate related to the optical polarization process is written in the form:

$$\Gamma_P = \Gamma_P^{\infty}\frac{s}{1+s} \tag{1.31}$$

where s is the optical pumping saturation parameter and it is defined as the ratio between the laser power used to polarize the NV center during the experiment and the NV center optical saturation power: $s = P_{opt}/P_{sat}$. Γ_P^{∞} is the polarization rate at saturation and is related to the lifetime of the metastable state ($\approx$ 200 ns) (fig. 1.4). Thus Γ_P^{∞} is set to $5 \cdot 10^6$ s^{-1}.
Second, the optical pumping, exciting the NV center from the ground state to the excited state, acts as a source of decoherence. The decoherence rate (Γ_c) induced by

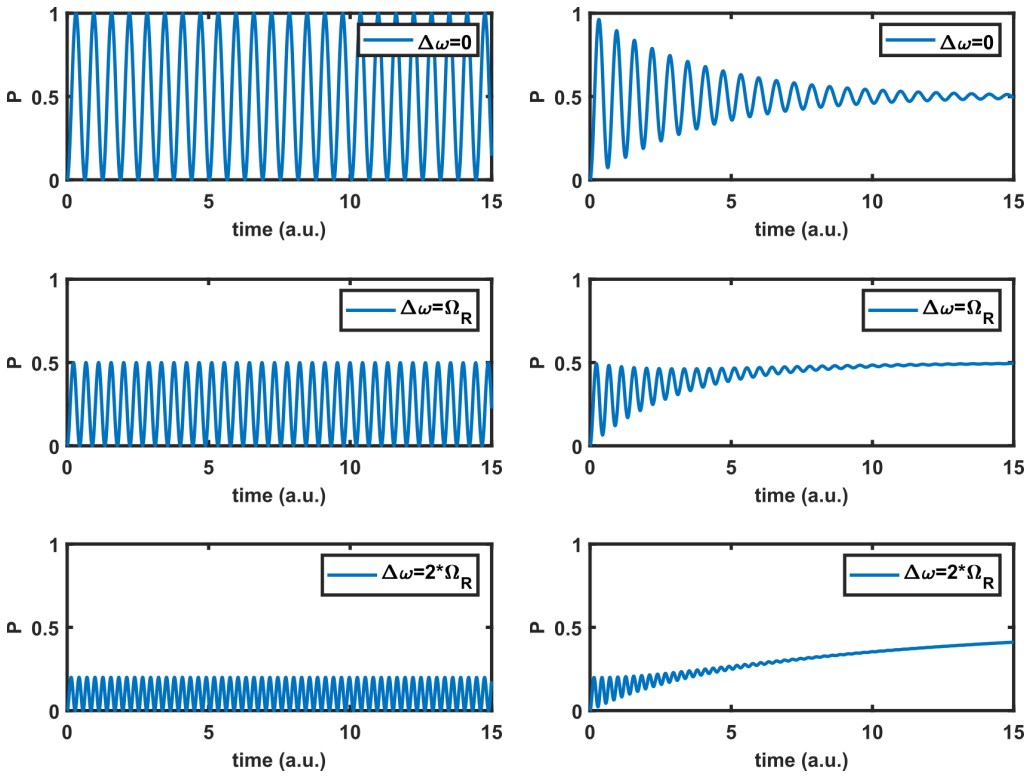

(a) (b)

Figure 1.8: Rabi oscillations of a two-level system without considering (a) and considering (b) the relaxation processes. P is the probability of finding the system in $|-\rangle$ assuming it was initially in $|+\rangle$. Both for (a) and (b), starting from the top, the case of no detuning, a detuning equal to the Rabi angular frequency and a detuning equal to twice the Rabi angular frequency is considered. (b) For the simulation it is assumed $\Gamma_2 = \Omega_R/20 >> \Gamma_1$.

the optical pumping is also modelled as a saturation law:

$$\Gamma_c = \Gamma_c^{\infty} \frac{s}{1+s} \tag{1.32}$$

In this case, the decoherence rate at saturation (Γ_c^{∞}) is related to the excited state lifetime (13 ns) (fig. 1.4) and it is set to $8 \cdot 10^7$ s^{-1}.

Taking into account these two relaxation rates, the Bloch equations of the system become:

$$\frac{d\varrho_{11}}{dt} = i\frac{\Omega_R}{2}(\varrho_{10} - \varrho_{01}) - \Gamma_1(\varrho_{11} - \varrho_{00}) - \Gamma_p \varrho_{11} \tag{1.33a}$$

$$\frac{d\varrho_{00}}{dt} = -\frac{d\varrho_{11}}{dt} \tag{1.33b}$$

$$\frac{d\varrho_{01}}{dt} = -i\Delta\omega\varrho_{01} - i\frac{\Omega_R}{2}(\varrho_{11} - \varrho_{00}) - (\Gamma_2 + \Gamma_c)\varrho_{01} \tag{1.33c}$$

$$\frac{d\varrho_{10}}{dt} = -\frac{d\varrho_{01}^*}{dt} \tag{1.33d}$$

This model can now be employed to study the continuous-wave optically detected magnetic resonance (CW-ODMR) spectrum of an NV center. In the CW-ODMR spectroscopy the laser and the RF field are always on. This is equivalent to considering the steady-state solution (ϱ^{st}) of the system in eq. (1.33). The NV center PL rate for a given value of detuning between the RF field and the NV resonance frequency (that is nothing more than the CW-ODMR spectrum) is given by:

$$R(\Delta\omega) = PL_0 \varrho_{00}^{st}(\Delta\omega) + PL_1 \varrho_{11}^{st}(\Delta\omega) \tag{1.34}$$

where PL_0 and PL_1 are the PL rate of the NV center when it is respectively in $|0\rangle$ and $|\pm1\rangle$ state and ϱ_{11}^{st} and ϱ_{00}^{st} are the steady-state solutions of the Bloch equations.
A complete discussion of this model and the outbuildings calculations can be found in [44]. Here we are interested in reporting the expression for the contrast and the linewidth of the CW-ODMR spectrum in the case of a saturation parameter $s > 0.02$, that is the common working regime of NV centers. Under this approximation (s > 0.02), the intrinsic relaxation processes are neglected with respect to the pumping relaxation processes ($\Gamma_1 << \Gamma_p$ and $\Gamma_2 << \Gamma_c$). The ODMR linewidth (FWHM of the spectrum) results:

$$\Delta\nu = \frac{\Gamma_c^{\infty}}{\pi}\sqrt{\left(\frac{s}{s+1}\right)^2 + \frac{\Omega_R^2}{\Gamma_p^{\infty}\Gamma_c^{\infty}}} \tag{1.35}$$

and the contrast results:

$$C = \Theta\frac{\Omega_R^2}{\Omega_R^2 + \Gamma_p^{\infty}\Gamma_c^{\infty}\left(\frac{s}{s+1}\right)^2} \tag{1.36}$$

where $\Theta = \frac{PL_0 - PL_1}{2PL_0}$.

Concerning the ODMR linewidth, it is possible to observe both the well-known RF power broadening effect and an additional broadening contribution due to the optical pumping. Concerning the contrast, it depends both on the RF power and on the laser power. It follows a saturation law with respect to the RF power and, in the limit $\Gamma_p^{\infty}\Gamma_c^{\infty}\left(\frac{s}{s+1}\right)^2 >> \Omega_R^2$ it scales linearly with the RF power.

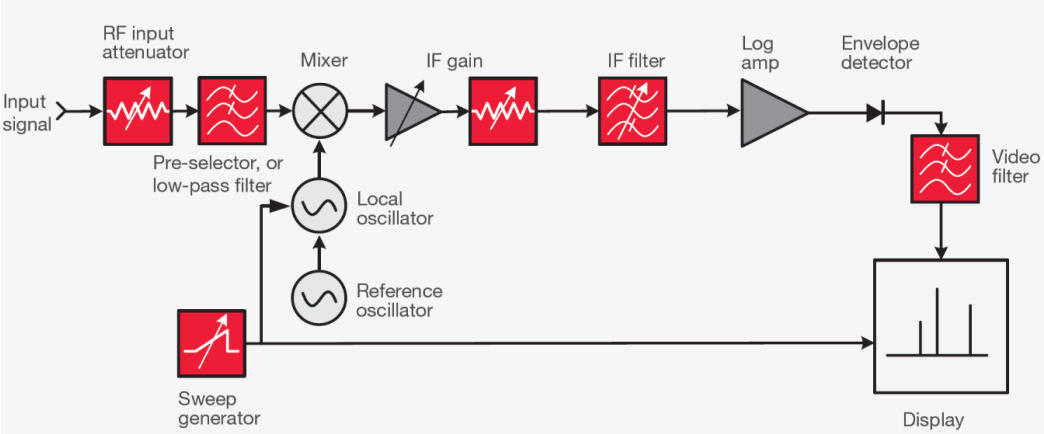

Figure 1.9: Schematic of a swept-tuned spectrum analyzer. The signal to be detected (input signal) is firstly attenuated to fall in the working area of preselector filters, which cut off all the frequency components outside the frequency band set for the analysis. A local oscillator, whose frequency can be swept, downconverts the input signal. The downconverted signal is then filtered by a very fine intermediate filter and finally its amplitude is detected by an envelope detector and displayed. The amplitude detection is done at the central frequency of the intermediate filter with the frequency resolution of the filter. Scanning the frequency of the local oscillator over a proper frequency range, the input signal is analysed over the desired bandwidth. Image taken from [66]

1.3 NV centers applications

In the last decades, NV centers have been an attractive tool for the quantum information and the quantum sensing community. Its spin-dependent optical properties, the long coherence time, the room-temperature working point, the single-photon source nature, the excellent photostability and the atomic size make this defect an extremely good quantum sensor for magnetic, electric and temperature fields and a very promising qubit. Several applications exploiting single NV centers and NV centers ensemble in both nanodiamonds or bulk crystals have been proposed, implemented and commercialized [49] [50] in several different domains such as neuroscience and biosensing ([51] [52] [53]), high-pressure physics ([7] [54] [55]), geology ([56] [57]), condensed matter physics ([58] [59] [60]), quantum information [61] [62], quantum computing ([63] [64] [65]), etc.

In this manuscript, two NV center applications are proposed and investigated: a radiofrequency spectrum analyzer and a widefield imaging system to map the near field microwave radiation emitted by a RF device.

1.3.1 Radiofrequency spectral analysis using an ensemble of NV centers

The real-time detection and the broadband spectral analysis of microwave signals is a subject of interest for many technological domains such as communication, medicine and navigation. Cognitive radio networks, electromagnetic compatibility (EMC) analysis, radars, wireless communications, etc. are some of the many applications that require a real-time spectral detection over a broad frequency band (tens of GHz) [9].

At present, the principal and most common solutions to measure RF spectra are electronic spectrum analyzers. They are essentially grouped in two categories: the swept-tuned spectrum analyzers [66] and the fast Fourier transform (FFT) spectrum analyzers [10].

The swept-tuned spectrum analyzer is a heterodyne spectrum analyzer (fig. 1.9). A frequency-sweeping local oscillator downconverts the MW signal we want to detect in

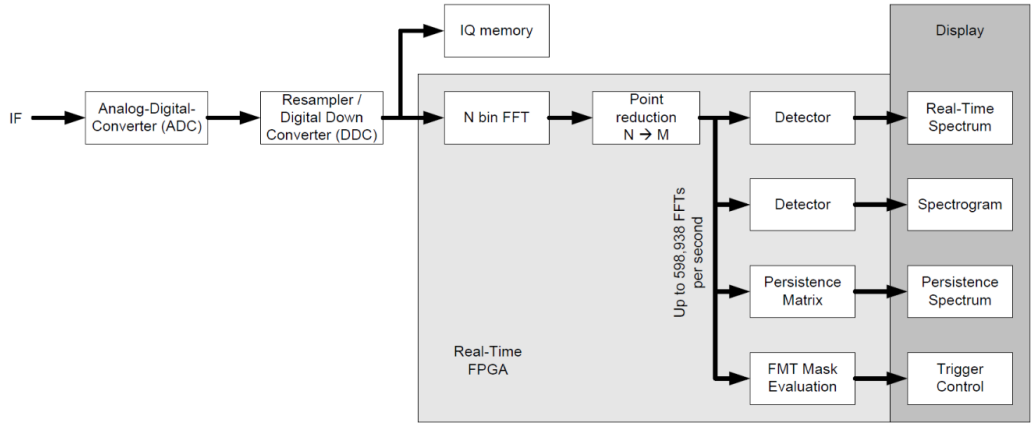

Figure 1.10: Schematic of an FFT spectrum analyzer. The input signal (IF) is digitalized by an ADC and downconverted in the digital baseband of the spectrum analyzer. An FPGA computes the FFT of the digitalized signal which is then displayed. Image taken from [10].

the frequency band of a very narrow filter (intermediate filter), which sets the frequency resolution of the spectrum analyzer. The frequency of the local oscillator is swept over the desired bandwidth and an envelope detector measures the amplitude of the signal at the output of the intermediate filter. This method enables to acquire spectra with a high frequency resolution (given by the intermediate filter) over a wide frequency band (given by the frequency range over which the frequency of the local oscillator is swept). However, due to the sweeping of the local oscillator, fast-changing signals or signals shorter than the time needed by the local oscillator to cover the entire bandwidth may be lost. In order to overcome this problem, an FFT-based approach is used to simultaneously detect all the frequencies in the frequency bandwidth; from now on we will refer to this property saying that the device has a 100% probability of intercept (POI).

In an FFT spectrum analyzer the MW signal is digitalized by an analog-to-digital (ADC) converter and then processed through a Fourier analysis using an FPGA (fig. 1.10). The sampling of the signal and the FFT calculation are made in parallel in order not to lose any signal because of dead times. However, since both the ADC conversion and the FFT calculation are based on electronic devices, the performances of FFT spectrum analyzers are strictly related to the performances of the electronic components. In particular, when a large number of channels combined with a large dynamics are necessary, the sampling rate and the power consumption of the ADCs constitute a limitation to the improvement and the use of this kind of electronic spectrum analyzers which are thus typically limited to a real-time analysis over several hundreds of MHz.

The need for large bandwidth and large dynamics can be provided by analog solutions. In the last decades new photonics-based approaches for the microwave spectral analysis have been proposed [11, 68]. The general idea behind these approaches is to transpose the MW signal into the optical domain and then use optics to process it and retrieve its spectrum (fig. 1.11). The main advantages of optics with respect to electronics are the larger real-time bandwidth and frequency range, the reduction of losses especially at high MW frequencies and the immunity to electromagnetic interference during the measurement process.
Several photonics-based techniques have been proposed for many and different microwave applications: frequency scanning spectrum analyzer [69], instantaneous fre-

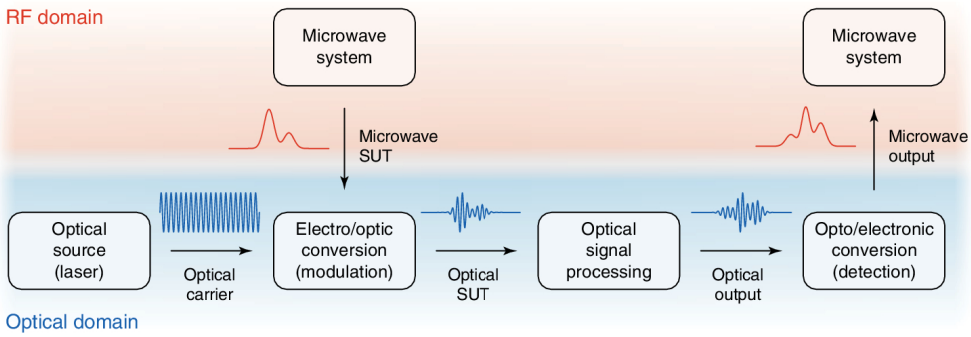

Figure 1.11: Schematic of a microwave photonics device. An optical signal is modulated by the RF signal by means of an electro-optical modulator. The optical signal is then processed and analysed by means of optical modules in order to retrieve the required information about the RF signal. Image taken from [67].

quency measurements [70], Doppler frequency shift measurements [71], angle of arrival measurements [72], etc. In this manuscript, particular attention is given to the photonics-based real-time spectrum analyzers. They are also called photonics-based MW channelizers since the general idea behind their working principle is to first transpose the MW signal in the optical domain and then divide the optical signal in several channels. Each channel is associated to a MW bandwidth, which corresponds to the frequency resolution of the photonics-based MW channelizer, and for each channel the amplitude of the MW signal is measured with high sensitivity.
An example of this technique is the MW spectral analysis based on the spectral hole burning in rare-earth ion-doped crystals at cryogenic temperature [73]. Rare-earth ion-doped crystals are characterized by several hosting defects which, shifting the resonance lines of the rare-earth atoms, are responsible of the broad inhomogeneous absorption spectrum of the material. Pumping the crystal on resonance with one of the rare-earth atoms transition, it is possible to saturate the transition thus creating (burning) a hole in the absorption spectrum of the crystal. This technique is called spectral hole burning (SHB). The depth of the hole depends on the pumping power while the linewidth depends on the homogeneous spectral linewidth of the rare-earth atoms which, at cryogenic temperature, can be smaller than 1 MHz. Spatially modulating the pump, it is possible to engrave a Bragg diffraction grating in the crystal. Once the Bragg diffraction grating is engraved for a given frequency, a probe beam at that frequency propagating in the material will be deflected according to the Bragg diffraction rules. Engraving different Bragg gratings for different frequencies, the SHB material works as an optical spectrum analyzer, where the spectral information is encoded in the angle of diffraction of the incident beam. The number of channels of the spectrum analyzer depends on the number of holes burned in the absorption spectrum of the material.

Once the SHB material has been prepared to work as an optical spectrum analyzer, it can be exploited for the MW spectral analysis after having transposed the MW signal into the optical domain (fig. 1.12).

This technique enables to reach an instantaneous real-time bandwidth of several tens of GHz, a large dynamic range ($>$ 50 dB) and a frequency resolution of hundreds of kHz at cryogenic temperatures. [75]. However, although cooling technique has made impressive progress with closed cryocoolers now available, there is a need for complementary solutions that are compact, work at room temperature and require low power consumption, in particular for onboard components.

One possible technique investigated in this manuscript involves exploiting the spin properties of NV centers to directly detect MW signals without analog-to-digital conver-

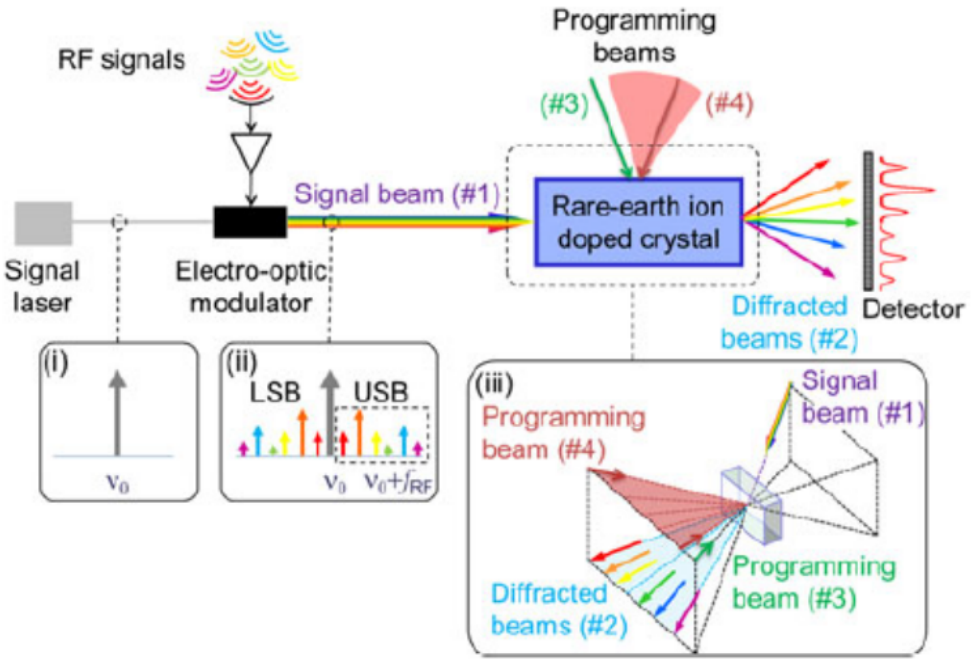

Figure 1.12: Schematic of the experimental set-up proposed in [74] for the spectral analysis of MW signal based on the SHB in rare-earth ion-doped crystals. A monochromatic laser is modulated by the RF signal whose information is then coded in the laser sidebands. The signal beam is then sent on a rare-earth ion doped crystal where, previously, several Bragg gratings were engraved using the SHB. In this architecture the Bragg gratings are created exploiting the interference between two programming beams. The different spectral components of the signal beam, passing through the crystal, are diffracted in different directions. A widefield detector is used to detect the optical spectrum of the signal which enables to retrieve the spectral components of the RF field.

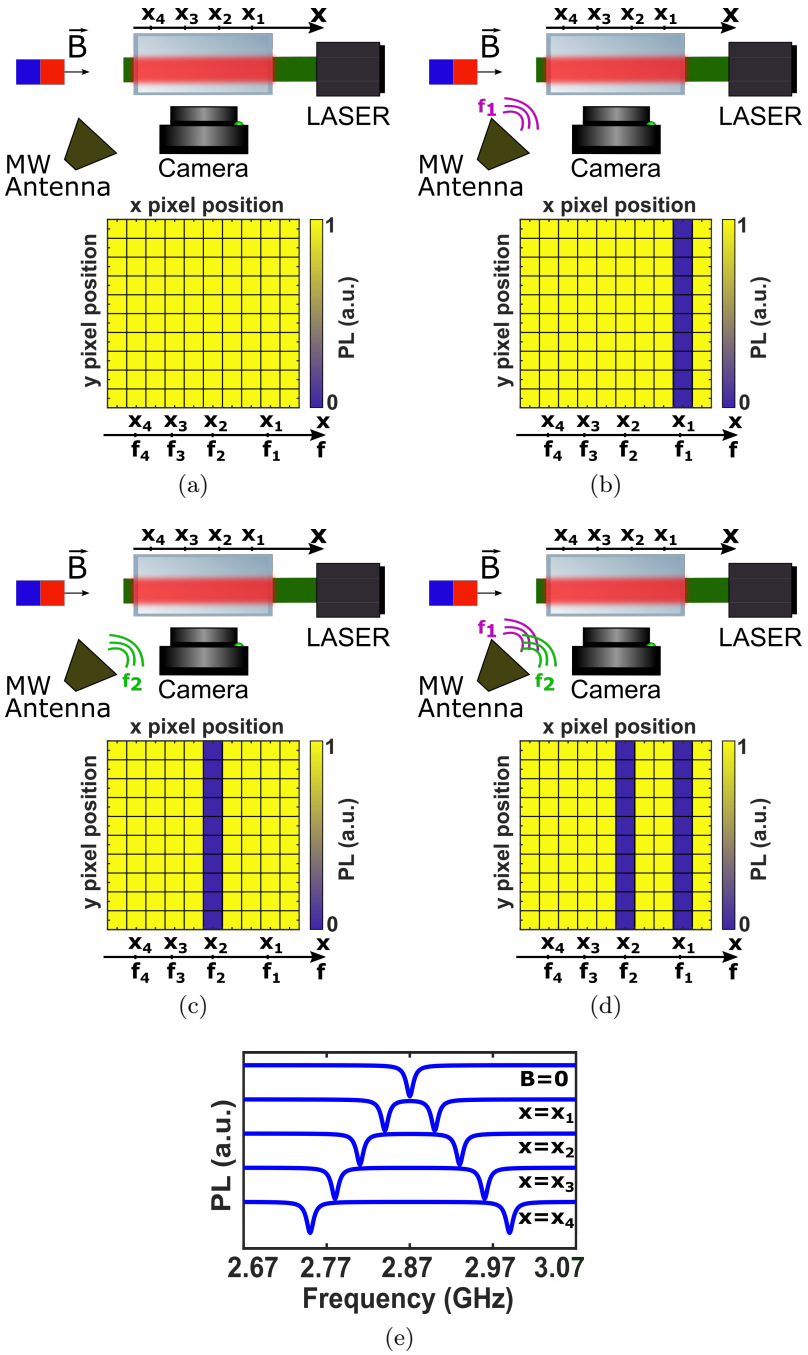

Figure 1.13: Schematic of the experimental set-up for the NV center-based spectral analysis. Four different cases are represented: (a) no signal resonant with the NV centers, (b-c) monochromatic RF signal resonant with NV centers, (d) complex RF signal resonant with NV centers. (e) Spatial encoding of the NV center resonance frequencies. NV centers located in different position undergo a different Zeeman shift and thus resonate at different frequencies.

sions or optical processing modules. The working principle of the MW spectral analysis based on an ensemble of NV centers relies on the spatial encoding of the NV centers resonance frequencies by means of a controlled magnetic field gradient. The schematic is reported in fig. 1.13. A continuous-wave pumping laser polarises the ensemble of NV centers embedded in the diamond in the $|0\rangle$ state (bright state). The PL emitted by the NV centers is collected by means of an imaging system and detected by a camera. The resonance frequencies of the NV centers are spatially controlled through a controlled static magnetic field gradient. NV centers located at different positions undergo a different Zeeman shift and resonate at different MW frequencies. The MW signal to be analysed is sent on the diamond through an antenna. If no component of the MW signal is resonant with any NV center, the PL intensity is equally distributed over the entire diamond area. If some components of the MW signal are resonant with NV centers, a drop of the PL intensity is detected on the camera in correspondence of the pixels which image the NV centers resonant with the MW signal. Due to the correspondence between the pixel position and the NV center resonance frequency, the spectral components of the signal are measured instantaneously, simultaneously and without any signal processing, by taking a picture of the diamond.
The proof of principle of the RF spectral analysis using an ensemble of NV centers has been demonstrated by Chipaux et al. [12]. In this manuscript (chapter 3) we investigate the main physical features of NV centers considered as MW detectors in order to extend the frequency range, the spectral resolution, the power detection threshold and the time resolution of the spectral analysis.

1.3.2 Imaging of MW field using an ensemble of NV centers

Mapping the near-field microwave radiation generated by an electromagnetic device is something of interest for several scientific domains from classical engineering to quantum technologies. Function and failure analysis [76], materials characterization [77, 78], quality assurance of integrated circuits [79] , devices characterization [80], comparison with the simulation and debugging are some of the several applications which need to measure, with high spatial resolution and high sensitivity, the spatial distribution of a RF field. In our particular case, the imaging of RF radiation is a useful tool to characterize the source of the RF field which is used to manipulate the NV centers spin.

The most classical way to study the performance of a RF device is by measuring the scattering parameters using a vector analyser [81]. The scattering parameters contain information about the global transmission and global reflection properties of the device under test (DUT) and thus this method of analysis, really useful to study the performances of microwave emitters, receivers and antennas in the far-field regime, is less efficient for near-field analysis, where instead of the global reflection and transmission performance of the device, the interest is in the local distribution of the MW field.
In the last decades, several electronic techniques have been developed [82, 83] to study the near-field properties of RF devices. The more intuitive of them consists in scanning an antenna close to the DUT [84] . According to the shape of the antenna, and after a proper calibration, both the electric and the magnetic field can be measured. The spatial resolution depends on the size of the antenna and it can reach the order of tens of µm. By properly engineering the antenna, broadband (20 GHz [85]) measurements are possible. The main drawback of this kind of system is the need of approaching the antenna close to the DUT, risking coupling effects between the two.
Another interesting technique is based on scanning superconducting quantum interference devices (SQUIDs). SQUIDs are extremely interesting because of their extremely high sensitivity ($\frac{fT}{\sqrt{Hz}}$ for dc-SQUID [86]) and µm spatial resolution. Although SQUIDs-based detection of MW fields up to 200 GHz has been demonstrated [87, 88], their per-

formance fast deteriorate for frequencies above about 200 MHz [89]. Moreover, SQUIDs working temperature (typically 77 K) limits their application to electromagnetic devices which are resistant at those temperatures.
A different approach to mapping microwave fields consists in atomic sensors. Different platforms have been investigated in the last years: vapor cells [90], ultracold atoms [14] and NV centers [91]. The common idea behind the different platforms is to exploit the Rabi oscillations induced by the interaction between the atomic system and the electromagnetic field to retrieve the amplitude of the electric or magnetic field. The main advantage of this method is that it does not require any calibration procedure since the Rabi frequency is related to the amplitude of the electromagnetic field by physical constants well-known with a high level of accuracy. In this regard, it has been proposed to use Rabi oscillations as an alternative microwave power standard to the classical calorimeters [92, 93].
Two main techniques have been investigated to measure the RF radiation emitted by a RF device in the near-file region using an atomic sensor. The first consists in scanning an atomic sensor in the proximity of the DUT and, for each point of the scan, measuring the amplitude of the MW field [94]. The second, which is the one investigated in this manuscript, consists in the widefield detection of an ensemble of atomic sensors (in our case NV centers) which are close to the DUT [13]. Interestingly, several of the works about the implementation of an atomic sensor for microwave field mapping were driven by the need to find a method to characterize the RF chain of an atom-based experimental set-up [95]. Our work is moved by the same motivation as well. This aspect confirms the need for new and alternative techniques to measure with high spatial resolution and high sensitivity the near-field MW radiation generated by electromagnetic devices.

The working principle of the widefield imaging of a MW field using an ensemble of NV centers

Solving the NV center rate equations (see chapter 4), it is possible to obtain the time evolution of the NV center PL assuming it is initially polarized in $|0\rangle$ or $|\pm1\rangle$. The results are reported in fig. 1.14a. As expected, the PL intensity depends on the NV center spin state until the steady-state condition is reached and, independently from its initial state, the system is polarized in $|0\rangle$. The difference between the PL emitted when the NV center is in $|0\rangle$ and $|\pm1\rangle$ (yellow curve of fig. 1.14a) has a maximum for a given laser pulse duration and then decreases till to be equal to zero when the system reaches the steady-state condition.
Looking at this plot, we can understand the classical pulse scheme used for the detection of the NV center Rabi oscillations (fig. 1.14b). A first laser pulse polarizes the NV center in $|0\rangle$. After a waiting time of approximately 1 μs which enables a complete decay of the metastable state, a MW pulse of duration τ is applied to manipulate the NV center spin. Finally a second laser pulse is used to readout the spin state of the system. The PL detection is performed by means of an avalanche photo-diode (APD). In order to optimize the contrast, the APD is open for a small time (usually some hundreds of ns) at the beginning of the laser pulse (fig. 1.14b). It is open again, for the same amount of time, just before the end of the laser pulse, when the NV center is completely polarized, to take a reference signal. The contrast is then calculated as the ratio between the difference of PL collected at the beginning and the end of the laser pulse, and the reference signal. This procedure is repeated several times to increase the SNR of the measurement. Repeating the experiment for different MW pulse durations allows retrieving Rabi oscillations.
Using this acquisition procedure, a scanning diamond cantilever with a single NV center at its apex has been employed to map the MW near-field of an electromagnetic device,

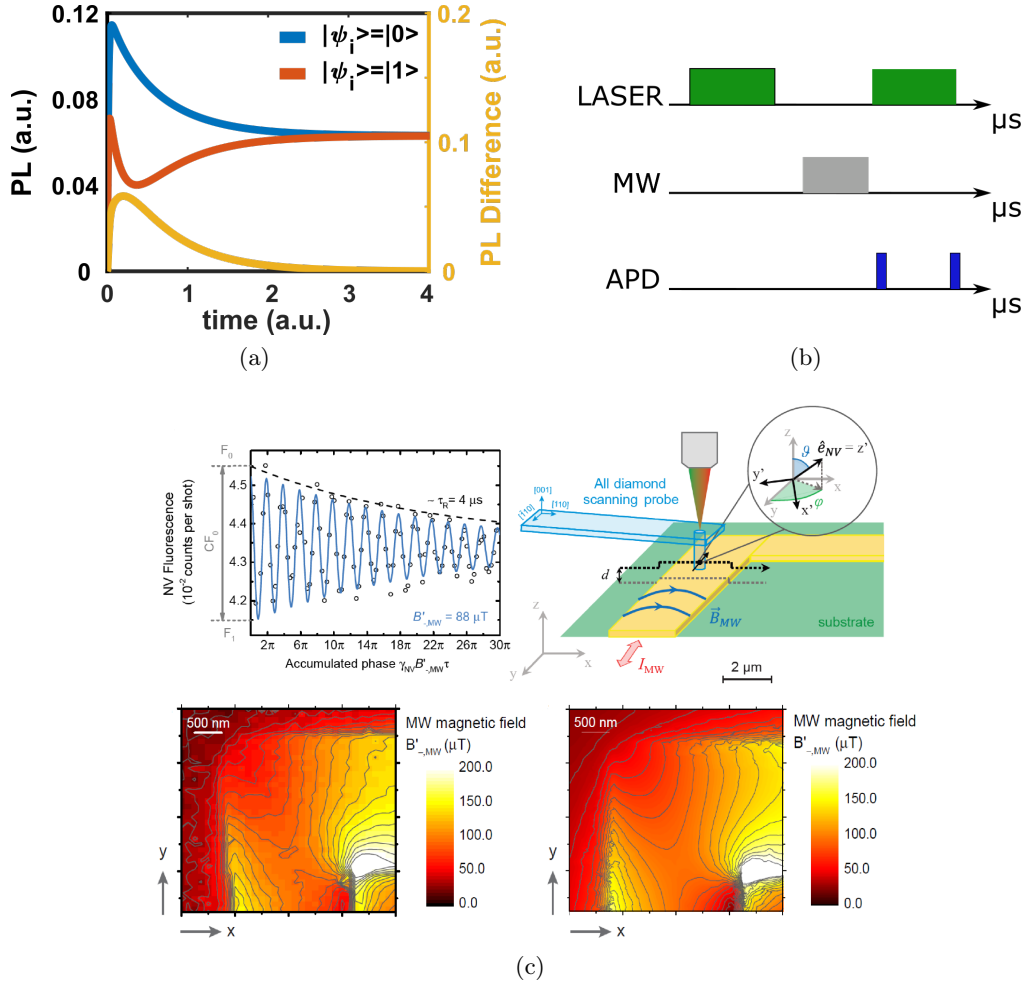

Figure 1.14: Imaging of MW field amplitude using a scanning NV center. (a) Time dependent PL intensity emitted by an NV center initially in $|0\rangle$ (blue) and $|\pm1\rangle$ (orange). The origin of the time scale corresponds to the moment the laser is turned on. The yellow curve is the difference between the blue and the orange plot. (b) Pulse sequence for the detection of Rabi oscillations using an avalanche photodiode. (c) Map of the RF near-field emitted by a RF device realized using a single NV center at the apex of a diamond cantilever. The results are compared to the simulations showing a good agreement. The work is reported in [94].

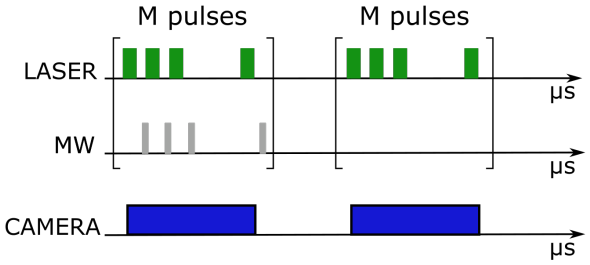

(a)

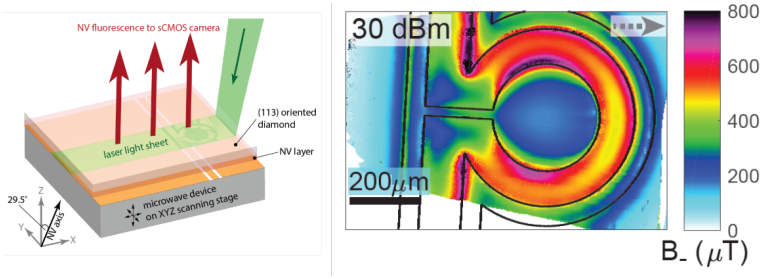

(b)

Figure 1.15: Widefield imaging of MW field amplitude using an ensemble of NV centers. (a) Pulse sequence for the detection of Rabi oscillations using a camera as detector. (b) Map of the RF near-field emitted by a RF device realized using a widefield microscope and an ensemble of NV centers. On the left the experimental setup and on the right the experimental results. Images from [13].

as shown in fig. 1.14c [94].

In order to avoid the NV center scanning, a widefield imaging system and an ensemble of NV centers can be employed to map the RF field radiated by a RF device [96, 97]. Since in this case a camera is used instead of an APD, the acquisition procedure needs to be changed to take into account the characteristic time of the detector. The acquisition procedure proposed by [13] is reported in fig. 1.15a. During a single exposure of the camera, several laser pulses and MW pulses are sent on a diamond containing an ensemble of NV centers. The same procedure is then repeated with the MW field turned off to acquire a reference image. Repeating this procedure for different MW pulse durations, the Rabi oscillations of NV centers located in different positions are simultaneously measured enabling the mapping of the MW field (fig. 1.15b).
In chapter 4, the acquisition procedure for the widefield detection of Rabi oscillations is detailed with the help of simulations and some preliminary results concerning the mapping of a MW field using our experimental set-up are presented.

1.4 NV center fabrication

The development of NV center-based applications is strictly related to the advancement of NV centers fabrication processes. In fact, each application requires specific performance from both the diamond and NV centers: some applications are based on single NV center, some on large and dense NV centers ensemble, some need low concentrations of paramagnetic impurities, etc... Several efforts have been made in order to be able to engineer both the concentration, the orientation, the position and the paramagnetic environment of NV centers. The main techniques devoted to the fabrication of NV centers are discussed in this paragraph [98].

A first approach to creating NV centers is by irradiating a diamond sample with an ion or electron beam. The irradiation process creates vacancies inside the diamond lattice. A subsequent annealing process ($\approx$ 850 K) enhances the movement of vacancies in the diamond sample until they are trapped by nitrogen atoms. Since the NV bond is energetically favourable with respect to a nitrogen atom and a carbon vacancy far apart, the NV center which has been created is stable. The irradiation method is usually performed on diamond samples rich in nitrogen atoms, in order to reach high NV centers concentrations [99].
A second method to control the NV centers formation consists in implanting nitrogen atoms in diamond samples which have a very low intrinsic nitrogen concentration. The nitrogen atoms are implanted by means of a N^+ ion beam and then an annealing process enables the localized formation of NV centers. In this way it is possible to control, carefully choosing the implantation parameters, both the position and the concentration of the NV centers [100]
A third method consists in doping diamond with nitrogen atoms during the CVD growth. In this case, nitrogen-containing gases are injected into the vacuum chamber during the diamond CVD growth. Engineering the CVD parameters and the gases used during the growth of the sample, it is possible to control both the NV centers concentration in the diamond (from a single NV to a high density ensemble) [101] [102] and its paramagnetic environment, for example using ^{12}C instead of carbon ^{13}C isotope.

Another interesting point concerning the formation of NV centers is the opportunity to control their orientation during the growth process [103]. As a general rule, during a CVD process, the NV center formation is favourable for NV centers oriented along the growth direction and it is adverse for NV centers laying in the growth plane. The growth direction is defined by diamond substrate properties. For instance, in samples grown on [111]-oriented substrates, it has been demonstrated a preferential orientation along the growing direction of 99% [104]. However, this kind of sample presents a high level of nitrogen impurity. For diamond sampled grown on [110]-oriented substrates [105], NV centers oriented along the [111] and $[1-11]$ directions (the two directions pointing out of the [110] plane) represent almost the 100% of the NV concentration, and therefore the sample shows a 50% of preferential orientation. To overcome the high level of nitrogen impurity of [111]-oriented diamonds and at the same time to preserve a high level of preferential orientation, CVD diamond films have been grown on [113]-oriented substrates showing a preferential orientation of 73% [106].
The main interest in diamond samples presenting preferential orientation is for NV center applications that use only one NV center family, as it is, for example, for the spectral analysis of RF field. In fact, in this way, it is possible to naturally suppress the PL emitted by NV centers belonging to families different from the one we are interested in and thus reduce the background noise and increase the contrast (eq. (1.6)) of the measurement.

Chapter 2

Widefield ODMR of an ensemble of NV centers in diamond

The aim of this chapter is to investigate the spin resonances of an ensemble of NV centers under different static magnetic field conditions. This is a preliminary and fundamental step for the two NV center-based applications proposed in this manuscript: a RF spectrum analyzer (chapter 3) and the widefield imaging of RF fields (chapter 4). In fact, both of these applications exploit the NV center electron spin resonances to sense the RF field and measure its properties.
The technique adopted to analyse the NV center magnetic resonances is the CW-ODMR technique (or simply ODMR), whose working principle has already been explained in the previous chapter (section 1.2.2). In this chapter we present the experimental setup (section 2.1) and the acquisition procedure (section 2.2) implemented to measure the ODMR spectrum of an ensemble of nitrogen-vacancy centers. In section 2.3, the ODMR technique is used to characterize the diamond sample used all along this manuscript. A theoretical analysis of the NV center spectrum is conducted in section 2.4, where the general Hamiltonian of the NV center is discussed. A particular attention is given to the interaction between the NV center and both the static magnetic field (section 2.5) and the nitrogen nuclear spin (section 2.6). Two main effects are illustrated: the level anti-crossing at the NV center ground state and excited state, and the optical polarization of the NV's nitrogen nuclear spin. In particular it is shown that the optical polarization of the nitrogen nuclear spin is possible, with a sufficiently high efficiency, over a large range of magnetic field amplitude (section 2.7). Finally, the CW-ODMR spectrum of an ensemble of NV centers is measured over a large frequency range (several GHz) to investigate both the NV ground state and the NV excited state spin resonances (section 2.8). These measurements show an unknown positive-contrasted resonance line, to our knowledge never reported in literature, that is discussed at the end of the chapter.

2.1 The experimental setup

The schematic of the experimental set-up is reported in fig. 2.1. The NV centers are optically excited by means of a 532 nm continuous wave laser beam which is focused, with a waist of $(38 \pm 3)\ \mu m$, into the diamond plate. The photoluminescence is collected by an optical microscope objective (20x, 0.33 NA) and focused by means of a 75 mm lens on a commercial CMOS camera (UI-5240CP-M, IDS). A band-pass filter (FF01-697/75, Semrock) is interposed between the objective and the lens in order to suppress the diffracted laser light and reduce the photoluminescence of the NV^0 (fig. 2.2). A polarizer mounted after the microscope objective makes the imaging system sensitive to the polarization of the emitted photoluminescence (section 2.1.6). The RF signal used

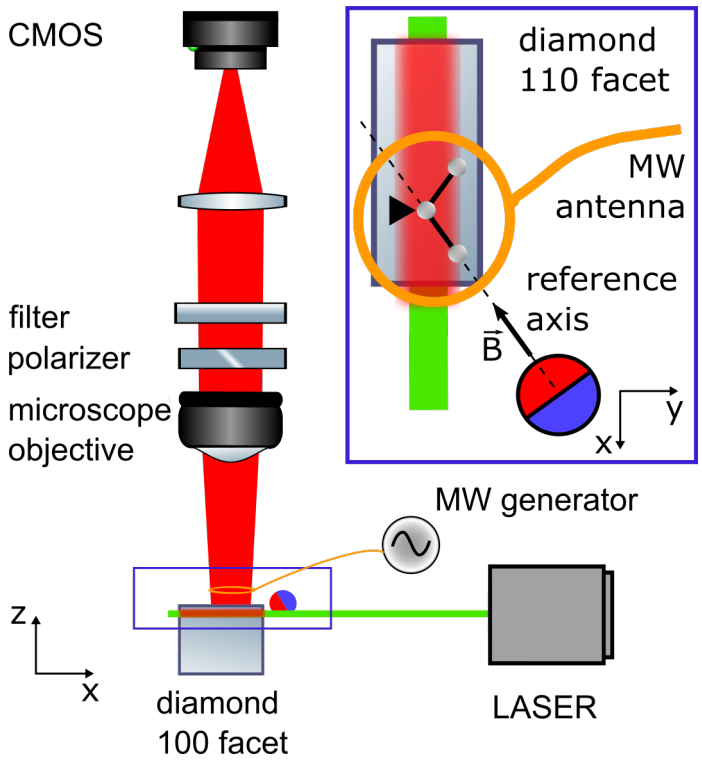

Figure 2.1: Experimental set-up. The diamond is pumped by a green laser as near as possible to the 110 top facet, which is the focal plane of the imaging system used to collect the NVs PL. The inset shows the top view of the diamond. The magnet is aligned with one of the NV centers families laying in the [110] plane. A homemade loop antenna brings the RF signal generated by a RF generator close to the diamond surface.

to drive the spin transitions of the NV centers is generated by a RF signal generator and carried close to the diamond by a homemade loop antenna (section 2.1.2). Neodymium magnets are employed to generate the static magnetic field which, through the Zeeman interaction, shifts the NV resonance frequencies (section 2.1.3).
The different components of the experimental system are detailed in the following paragraphs.

2.1.1 The diamond sample

The diamond is a commercially available 4.5 x 4.5 x 0.5 mm^3 single-crystal, CVD diamond plate (elementsix [107]). The nitrogen concentration is lower than 1 ppm (10^{-6}) and approximately the 0.1% of nitrogen atoms are naturally converted in NV centers, whose concentration is, therefore, of some ppb (10^{-9}) .
The two main faces of the diamond plate are [100] planes and the four lateral facets are [110] planes. The orientation of the four NV centers families with respect to these crystallographic planes is reported in fig. 2.3. A plane [110] is characterized by two in-plane families forming an angle of 109° with each other and two out-of-plane families symmetrically tilted by 54° with respect to the plane [110]. A [100] plane is characterized by four out-of-plane NV centers families tilted by 35° with respect to the [100] axis.
The diamond is glued on a goniometric stage with one of the four [110] facets in the focal plane of the microscope objective. This facet is also called, from now on, the top facet and it is the facet from which the PL is collected. The laser beam is focused into the diamond plate parallel to and as close as possible to the [110] top facet (fig. 2.1).

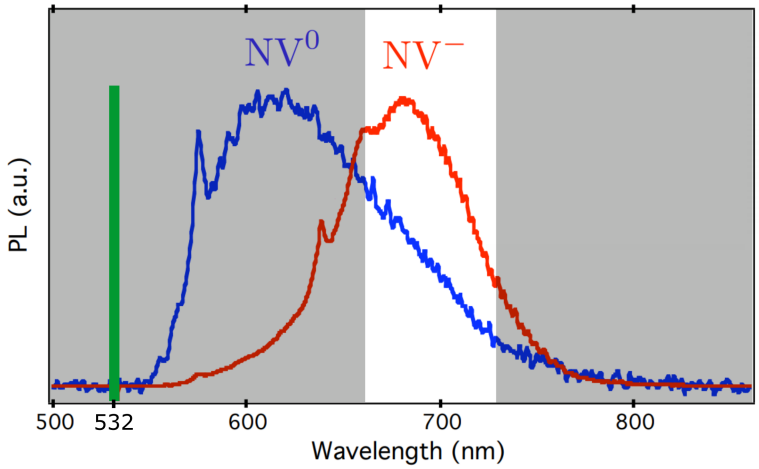

Figure 2.2: Bandpass filter. The laser (green curve), the NV^0 PL (blue curve) and NV^- PL (red curve) spectra are superposed on the same plot. The white region corresponds to the frequency bandpass of the filter which, thus, completely suppress the laser light and partially suppress the NV^0 PL.

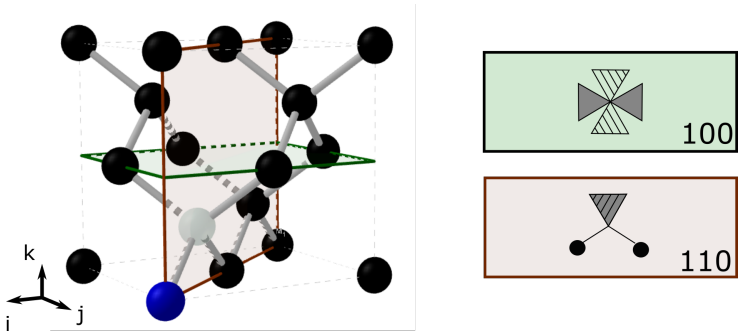

Figure 2.3: Diamond crystallographic planes. On the left, the diamond lattice: the black spheres represent carbon atoms, the blue sphere represents the nitrogen and the white sphere represents the carbon vacancy. In red and green an example of [110] and [100] planes. On the right, the NV center orientations with respect to the diamond crystallographic plane. The black circles define the in-plane bonds, the grey triangles represent the chemical bonds pointing outside the plane of the page, the striped triangles represent the out-of-plane chemical bonds pointing inside the plane of the page.

2.1.2 The RF antenna

The RF antenna is a homemade 1 mm-diameter loop antenna realized short-circuiting a coaxial cable with a copper wire. The magnetic field (B_{MW}) generated by the short-circuit current is focused at the center of the loop and it is oriented perpendicularly to the plane of the antenna. The amplitude of the magnetic field, which is almost homogeneous inside the loop, can be mathematically calculated using the Bio-Savart law:

$$B_{MW} = \frac{\mu_0 I_{MW}}{2R} \tag{2.1}$$

where I_{MW} is the current flowing in the loop, μ_0 is the vacuum permeability and R is the radius of the loop [1].
According to eq. (2.1), the smaller the radius of the loop is, the stronger the magnetic field generated at the center of the antenna is. Outside the loop, in the plane of the antenna, the magnetic field decreases approximately like $\propto 1/(\ell\text{-R})$, where ℓ is the distance from the center of the antenna. In order to work with an intense homogeneous magnetic field, the diamond area useful for sensing applications is the one inside the loop. We find a 1 mm-diameter loop antenna a good compromise between the strength of the magnetic field eq. (2.1) and the size of the sensing area.
The Bio-Savart law also allows calculating the magnetic field along the rotation axis of the loop antenna, at a given distance r from its center; it results:

$$B_{MW}(r) = \frac{\mu_0 I_{MW} R^2}{2(R^2 + r^2)^{3/2}} \tag{2.2}$$

Since the magnetic field amplitude decreases when the distance from the plane of the antenna increases (r), we place the antenna in contact with the diamond so that r is of the order of the depth of focus of the microscope objective ($\approx 10\mu$m), and therefore small compared to the radius of the antenna. As a consequence, eq. (2.1) is a good approximation for the magnetic field felt by the NV centers in the sensing area (r<<R).
As discussed in section 1.2.3 the NV spin transitions are induced by the RF magnetic field components perpendicular to the NV axis and thus the experimental configuration adopted optimizes the coupling between the RF field and the two NV center families laying in the [110] plane parallel to the diamond top facets.

2.1.3 The static magnetic field source

The static magnetic field sources are permanent Neodymium magnets (NdFeB). They are the strongest room-temperature permanent magnets commercially available, with a remanent magnetization of approximately 1.3 T. Depending on the shape and the size of the magnet, magnetic fields of the order of 1 T can be reached close to the magnet surface.
In this manuscript we will essentially consider three magnetic architectures: a single cylindrical magnet (radius 6 mm, height 6 mm), a single spherical magnet (radius 6.3 mm) and two cylindrical magnets (radius 6 mm, height 6 mm) with the opposite poles facing each other. For each architecture, the flux density, the longitudinal (B_z) and the transverse (B_r) magnetic field components along the magnetization axis (z) are calculated using the software $femm$ [108] and the results are reported in fig. 2.4. For all of the three configurations, the transverse magnetic field component is zero along

[1] The Bio-Savart law is valid for a continuous current. However, since the size of the loop (R$\approx$ 0.5 mm) is small compared to the wavelength of the RF radiation employed ($\nu = 3$ GHz $\rightarrow \lambda = 10$ cm) we assume that the Bio-Savart law is a good approximation to evaluate the magnetic field generated by the current flowing in the loop

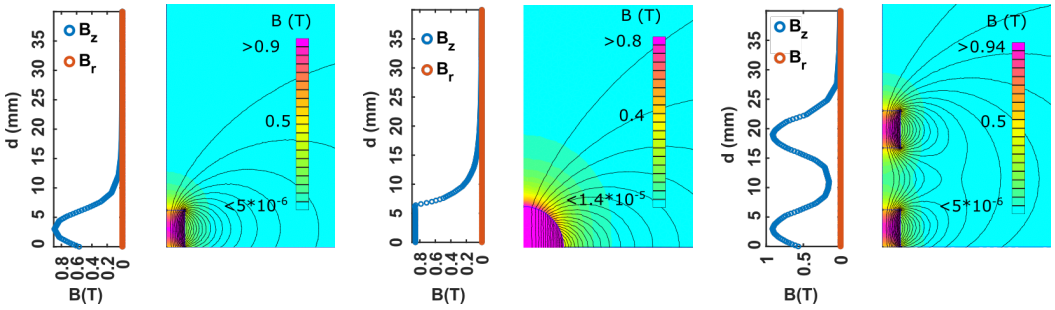

(a) (b) (c)

Figure 2.4: Magnets configurations. (a) Single cylindrical magnet. (b) Single spherical magnet. (c) two cylindrical magnets. The flux density of the three magnetic architectures is simulated using the finite element methods performed by the free software *femm* ([108]). The three architectures are axisymmetric with respect to the magnet magnetization axis, which is the vertical axis of the color map. The amplitude of the flux density is reported in the colormaps and the direction of the magnetic field is indicated by the contour plot. On the left of each map, both the longitudinal and the transverse component of the magnetic field along the magnetization axis (d) are plotted.

the magnetization axis, but not in the other spatial positions, as shown by the contour plots. The longitudinal magnetic field component follows a decreasing behaviour for a single-magnet configuration and a U-shape behaviour for the two-magnet configuration. The main difference between the single-magnet and the two-magnet (or more generally several magnets) configuration is that in the first case the magnetic field amplitude and the magnetic field gradient are strictly related, while in the second case they can be tuned almost independently changing the magnets relative positions. For example, in the two-magnet configuration, a zero magnetic field gradient along the magnetization axis is achieved at the center of the two magnets, regardless of the magnetic field amplitude (section 2.7). The magnetic field gradient plays a key role in the application of NV centers for the RF spectral analysis and its contributions to the ODMR spectrum are discussed in chapter 3.
The magnets are mounted on three axis translation stages in order to fine control their position and their orientation with respect to the NV centers families. In particular, using this assembly, one can easily align the magnet magnetization axis along one of the two NV center families laying in the [110] plane and preserve the alignment while the magnet is translated along its magnetization axis (section 3.2).

2.1.4 The CMOS camera

The camera is a CMOS camera with a 1280×1024 pixel resolution. The physical pixel size is 5.30 µm× 5.30 µm which, considering the magnification (8×) and the depth of field (6 µm) of the imaging system, corresponds to a diamond area of 0.66 µm × 0.66 µm and a diamond volume of 2.6 μm^3. Therefore, considering the NV center concentration in the diamond sample, some hundreds of NV centers are imaged per pixel.
In the full-frame image acquired by the camera (fig. 2.5a) the diamond, the antenna and the laser beam are clearly visible. The diamond area useful for sensing is limited by the beam waist in the y direction and the size of the antenna in the x direction. Therefore, after having used the full frame of the camera to place the antenna at the contact of the diamond, the area of interest (AOI) of the camera is set to the useful area for sensing. A picture of the AOI is reported in fig. 2.5b. We can clearly observe on the image the presence of some striations that are more photoluminescent than the rest of

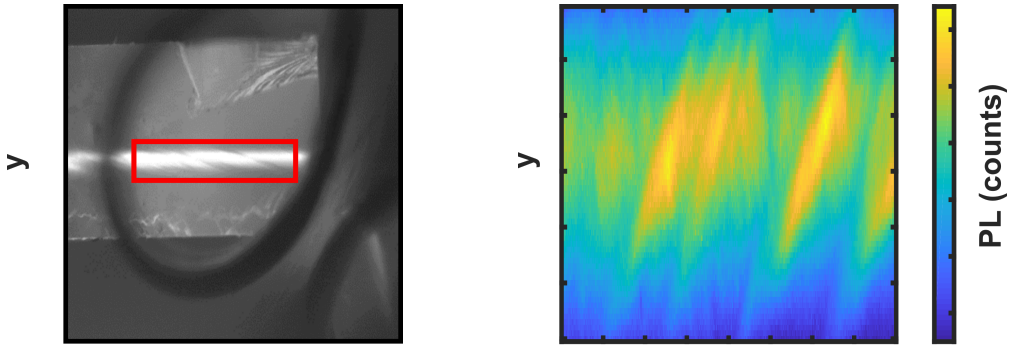

(a) (b)

Figure 2.5: Comparison between the full-frame image (a), useful for the alignment procedure, and the AOI image (b), useful for sensing. In (a) the diamond is the light grey rectangle on focus. The laser beam is the white line at the center of the diamond. On the right-bottom corner it is visible the shadow of the spherical magnet. The black quasi-circular shape is the antenna, which is placed at the contact of the diamond and thus it is in focus as well. The red rectangle defines the camera AOI useful for sensing applications.

the diamond. We attribute this effect to an inhomogeneous NV center concentration within the sample.

2.1.5 The signal-to-noise ratio

Any imaging system is affected by some common sources of noise [109, 110]. They are usually grouped into two classes: temporal noise sources and spatial noise sources.
The three main sources of temporal noise are dark current of the camera, readout noise of the camera and photon shot-noise. The first two noise sources are related to the camera while the third is related to the PL source.
Dark current is the signal obtained on the camera pixels in absence of photons and is caused by thermally generated electrons in the silicon structure of the camera sensor. Readout noise is the electrical noise related to the internal analog-to-digital conversion process of the camera. Photon shot-noise is the intrinsic limit of a photon-collecting system and it is caused by the intrinsic Poissonian distribution of the emitted photons. As the number of photons collected by the camera in a single exposure increases, photon shot-noise becomes the dominant source of noise for the imaging system. The signature of photon shot-noise is in the signal-to-noise ratio (SNR) of the measurement. Indeed, for an emission process governed by a poissionian distribution of mean value $\mu = \alpha$ and variance $\sigma^2 = \mu = \alpha$, the SNR of a photon counting measurement is given by $SNR = \mu/\sigma = \sqrt{\alpha}$. In the specific case of NV centers PL, the mean value of photons emitted in a time interval T (the integration time of the detector) is given by $\alpha = RT$, where R is the NV photoluminescence rate; thus the SNR of the measurement is equal to $SNR = \sqrt{RT}$ and scales as the square root of the integration time of the camera.
The SNR^2 versus the exposure time of the camera is reported in fig. 2.6a. The measurement consisted in acquiring 100 pictures for each exposure time; the SNR is evaluated, pixel by pixel, as the ratio between the mean value and the standard deviation of the PL of the 100 acquisitions. In fig. 2.6a the results for one pixel are reported. They show that the system is essentially shot-noise limited until the camera starts saturating. Since the system is shot-noise limited, a useful technique to increase the SNR is to

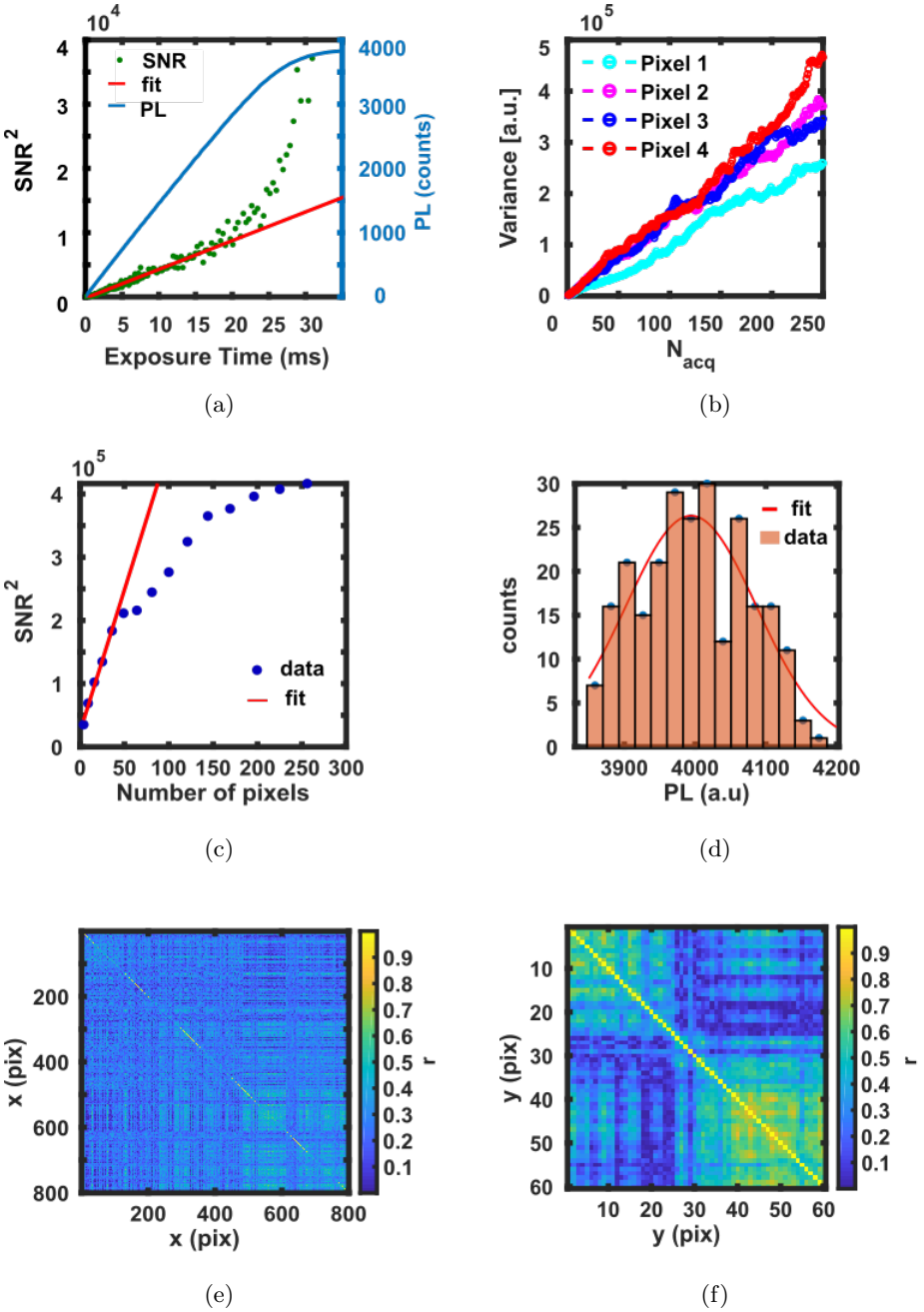

Figure 2.6: SNR. (a) PL and SNR for different camera exposure times. (b) PL temporal variance versus the number of acquisitions. (c) SNR versus the number of pixels. (d) PL spatial distribution of the pixels summed in (c). (e-f) Linear correlation coefficient maps.

increase the integration time of the measurements, or equivalently, to sum the signal of several consecutive acquisitions. This is shown in fig. 2.6b, where the temporal variance of the PL versus the number of acquisitions is reported. The measurement consisted in acquiring, for M times (cycles), N images. The variance is evaluated among the different cycles after having summed the signal over the first N_{acq} measurements of each cycle:

$$\sigma^2(N_{acq}) = \frac{\sum_{i=1}^{M}\left(\sum_{j=1}^{N_{acq}} PL(i,j) - \frac{\sum_{i=1}^{M}\sum_{j=1}^{N_{acq}} PL(i,j)}{M}\right)}{M} \tag{2.3}$$

As expected, the variance scales linearly with the number of acquisitions confirming that the system is shot-noise limited. The pixel dependence of the variance, which can be observed in fig. 2.6b, is caused by the spatial noise of the measurement.
The spatial noise has both an intrinsic contribution from the camera and a contribution from the light source. The former is caused by the inhomogeneity of the pixels dark current and of the pixels photo-response. However, we did not investigate these parameters since, in our case, the main source of spatial noise is clearly the inhomogeneity of the PL source (fig. 2.5). This inhomogeneity is caused by both a spatial-dependent NV center concentration in the diamond sample (the PL striations of fig. 2.5) and the gaussian distribution of the laser intensity, which results in different pumping conditions for NV centers differently located along the direction perpendicular to the beam propagation axis (y axis in fig. 2.5).
This inhomogeneity limits the improvement of the SNR achievable by integrating the signal from several pixels of the camera, which is one of the main advantages of a wide-field imaging system. In fact, for a set of N uncorrelated pixels with the same PL temporal distribution P(μ, σ), where μ is the mean value of the distribution and σ^2 its variance, the signal integrated over the ensemble of pixels has mean value $\mu_N = \mu$ and variance $\sigma_N^2 = \sigma^2/N$. In this ideal case, the SNR scales proportionally to the square root of the number of pixels: $SNR = \frac{\mu_N}{\sqrt{\sigma_N}} \propto \sqrt{N}$.
In our case, the SNR scales linearly with the square root of the number of pixels only when the sum is limited at around 50 pixels (fig. 2.6c). In fig. 2.6c the SNR has been evaluated as the ratio between the temporal average and the standard deviation of the PL summed over concentric squares of pixels of increasing side. To figure out the behaviour of the SNR with the number of pixels, the temporal average of each pixel considered in fig. 2.6c is plotted in fig. 2.6d and the variance of these values is calculated. It is approximately 8000 counts and corresponds to the PL spatial noise. This value must be compared to the PL temporal noise of each pixel, which, assuming to be shot-noise limited, corresponds to the PL temporal average (≈ 4000 counts). Since the spatial noise is higher than the temporal noise, the hypothesis of considering the PL temporal distribution identical for all pixels is false. As a consequence, the SNR does not scale linearly with the square root of the number of pixels.
The second hypothesis necessary to state that the SNR scales linearly with the square root of the number of pixels is that pixels are not correlated. This hypothesis is investigated by looking at the correlation maps of the PL temporal distribution for the different pixels of the camera (fig. 2.6f and fig. 2.6e). In fig. 2.6e each point $P(i,j)$ of the map is the Pearson's linear correlation coefficient (r_{ij}) between the temporal signal acquired at two different pixel positions (x_i and x_j) after a sum over ten rows of pixels in the y direction:

$$r_{ij} = \frac{\sum_{t=t_0}^{t_{end}}\left(PL_i(t) - \overline{PL_i}\right)\left(PL_j(t) - \overline{PL_j}\right)}{\left[\sum_{t=t_0}^{t_{end}}\left(PL_i(t) - \overline{PL_i}\right)^2 \sum_{t=t_0}^{t_{end}}\left(PL_j(t) - \overline{PL_j}\right)^2\right]^{\frac{1}{2}}} \tag{2.4}$$

where:

$$PL_i = \sum_{y=y_0}^{y_0+10} PL(x_i, y) \tag{2.5}$$

and $\overline{PL_i}$ is the temporal mean of PL_i. PL_j and $\overline{PL_j}$ are defined in the same way considering the pixel position (x_j). Figure 2.6f shows the Pearson's linear correlation coefficient for different y positions after a sum over 30 rows in the x direction. The values of the linear correlation coefficient (r»0) indicates that the pixels are correlated and therefore our initial hypothesis was false.
Although the SNR does not increase linearly with the square root of the number of pixels, there is still a SNR improvement in integrating over multiple pixels, and for this reason we will use this procedure several times in the following of this dissertation.

2.1.6 The Polarizer

The NV center radiative emission process is governed by two electric dipoles laying in the plane perpendicular to the NV center axis [111, 112]. Each dipole emits an electromagnetic field whose expression, in the far field region [113], is:

$$\vec{E}(\vec{r}) = \frac{E_0}{r} e^{-i\omega t + ikr} (\vec{n} \times \vec{p}) \times \vec{n} \tag{2.6}$$

where, assuming as the origin of the reference frame the center of the dipole (fig. 2.7), $\vec{n}$ is a unit vector along the vector position direction $\vec{r}$, $\vec{p}$ is a unit vector along the electric dipole moment direction and E_0, k and ω are respectively the amplitude, the wave vector and the angular frequency of the electric field. Two different cases are considered: $\vec{n} \perp \vec{p}$ and $\vec{n} \parallel \vec{p}$. In the first case, that is when we are looking in a direction perpendicular to the dipole axis, the amplitude of the electric field is maximal ($|(\vec{n} \times \vec{p}) \times \vec{n}| = 1$) and the electric field is polarized along the dipole axis ($(\vec{n} \times \vec{p}) \times \vec{n} = \vec{p}$). In the second case the electric field is null.

At room temperature, the two NV center dipoles are coupled and both can emit independently of the one that is excited. For this reason, one can discuss the polarization of the emitted PL without considering the polarization of the laser[2]. In our experimental configuration, the two NV families laying in the [110] plane are perpendicular to the optical axis (here defined as z). We consider one of these two families and define its NV center axis as the x axis. $\vec{d_1}$ and $\vec{d_2}$ are the two electric dipoles associated with the NV center and they lay in the yz plane. According to eq. (2.6), the electric field emitted by the NV center along the optical axis z is given by:

$$\vec{E} \propto (\vec{z} \times \vec{d_1}) \times \vec{z} + (\vec{z} \times \vec{d_2}) \times \vec{z} \tag{2.7}$$

Considering the first dipole, but the discussion is identical for the second, the cross product $\vec{z} \times \vec{d_1}$ is a vector along the x axis and thus the cross product $(\vec{z} \times \vec{d_1}) \times \vec{z}$ is a vector along the y axis. As a consequence, assuming that only the light propagating along the optical axis is detected by the camera, photons emitted by NV centers oriented in a plane perpendicular to the optical axis are polarized perpendicularly to the NV center axis. Therefore, using a polarizer in our imaging system, it is possible to completely suppress the PL emitted by one of the two NV families laying in the [110] plane. This is not the case for the two families that do not lay in the [110] plane, because the PL they emit along the optical axis is not completely polarized in the [110] plane (fig. 2.8).

These observations illustrate that a polarizer in the PL detection chain is a useful

[2]Since the interaction between the laser and the NV center is mediated by the same two dipoles, also the NV center pumping process depends on the polarization of the laser light.

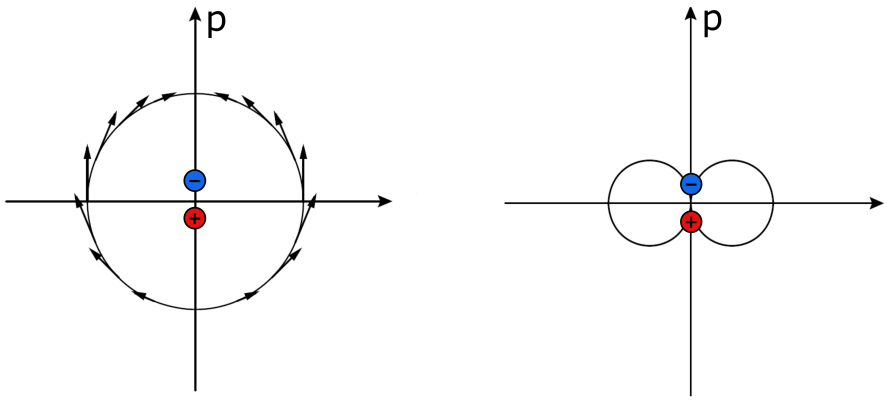

(a) (b)

Figure 2.7: Far field electromagnetic field emitted by an oscillating dipole. The images are taken from [113]. The dipole is simply represented by a positive and a negative electric charge along the dipole axis p. Since the dipole emission is symmetric with respect to the dipole axis (p), the reference frame reported in this figure represents a generic plane containing the dipole. (a) Direction of the electric field for different radial direction (n). (b) Relative amplitude of the electric field for different radial direction. It is maximum in the direction perpendicular to the dipole axis and it is null in the direction parallel to the dipole axis.

tool to increase the ODMR contrast of some NV center families. In fact, according to eq. (1.6), the contrast of an NV center family depends not only on the ratio between the PL emission rate when the NV center is on resonance and out of resonance, as it is for a single NV center, but also on the PL of the other families. Therefore, properly orienting the polarizer, it is possible to reduce the PL of some families to increase the contrast of some others (fig. 2.8).
This is advantageous for NV center applications which exploit only one NV center family, such as the two applications proposed in this manuscript: RF spectral analysis and imaging of the MW field amplitude.

2.2 The ODMR acquisition procedure

The continuous wave ODMR acquisition procedure consists in sweeping the frequency of the RF field while the camera detects, for each frequency, the PL emitted by the NV centers. During the acquisition, the laser and the RF field are always on (fig. 2.9a).
The RF frequency (f) is scanned in a range $[f_{min}; f_{max}]$ with a frequency resolution of Δf, which results in $N_{seq} = (f_{max} - f_{min})/\Delta f$ frequency steps (fig. 2.9b). In order to increase the SNR of the measurement, the frequency ramp is repeated N_{cycle} times; for each frequency step, the signal acquired by the camera is summed to the signal acquired during the previous ramps at the same frequency (fig. 2.9b). A theoretically equivalent procedure is to take N_{cycle} images for each frequency (f) and sweep the frequency only once. However, the latter procedure is more sensitive to PL fluctuations, which in the former are averaged throughout the acquisition.

During the acquisition, the data are stocked in a three dimensional matrix of size $[w, h, N_{cycle}]$, where w and h are respectively the width and the height of the camera AOI (fig. 2.9c). The data can be extracted in four different ways:

- as a photoluminescence map in the x-y plane at a given frequency position (f),

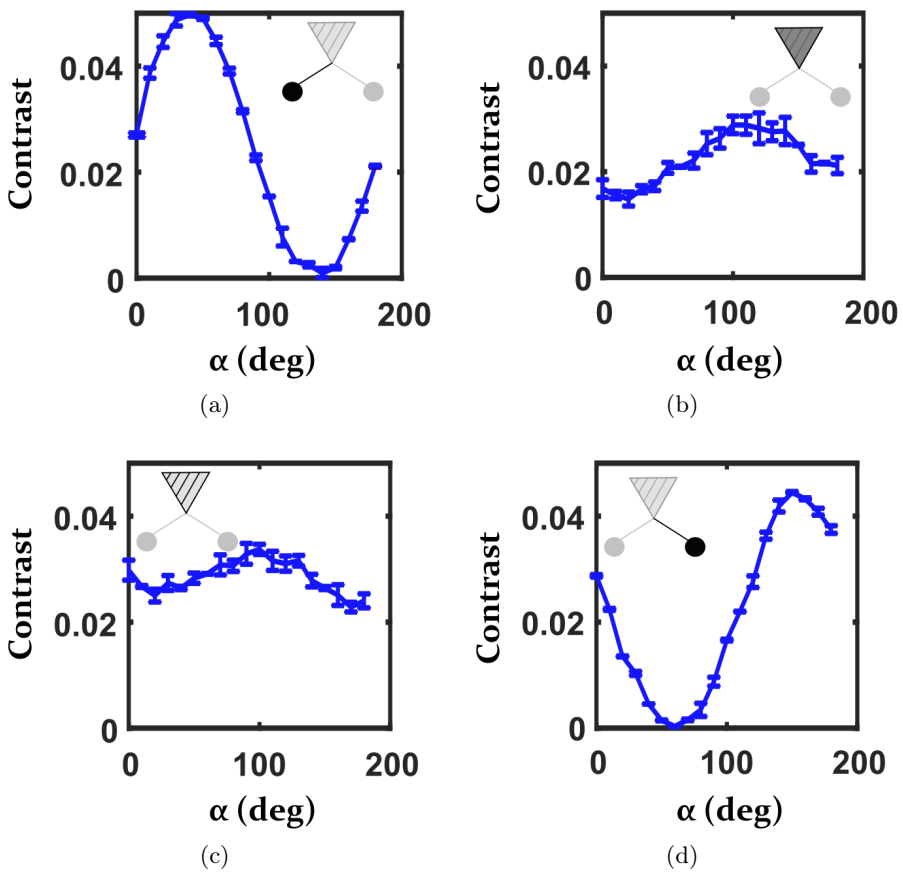

Figure 2.8: Contrast variation of the four NV center families turning the polarizer angle. The measurement is realized using a classical confocal set-up. The optical excitation and the optical readout are realized through the [110] diamond facet. The orientation of the investigated NV centers family with respect to the [110] plane from which the PL is collected is reported in the wedge-dash diagrams on the top of each plot. Solid lines represent in-plane bonds; dashed lines represent bonds pointing outside the plane, towards the viewer; wedge-shaped lines represent bonds pointing inside the plane.(a)-(d) are the contrast of the two NV center families laying in the [110] plane. Rotating the polarizer axis it is possible to completely suppress their contrast. (b-c) are the contrast of the two NV center families which do not lay in the [110] plane.

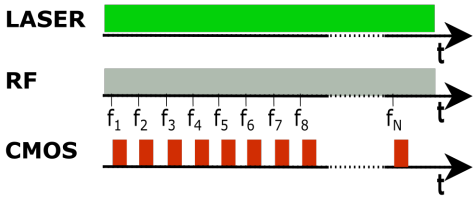

(a)

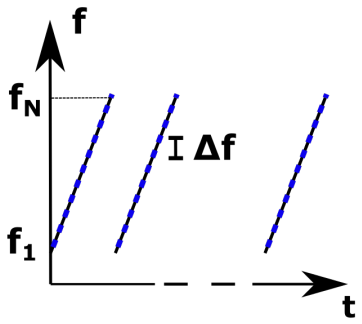

(b)

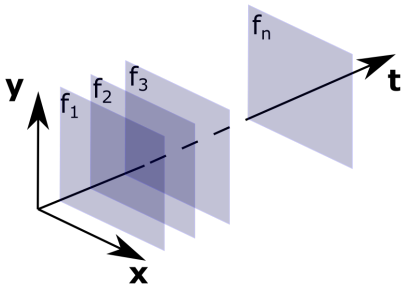

(c)

Figure 2.9: CW-ODMR acquisition procedure. (a) The laser and the RF field are always on. The camera acquires one image per frequency during each frequency sweep. (b) During the acquisition the frequency ramp is repeated several times and one picture per frequency is acquired for each ramp. (c) The data are stocked in a 3D matrix. For each frequency, the signal consists in a 2D matrix obtained by summing all the images taken at that frequency during the measurement.

to retrieve the spatial position of the NV centers resonating at f;

- as a photoluminescence map in the x-f plane to retrieve a 2D ODMR spectrum at a given y position;
- as a photoluminescence map in the y-f plane to retrieve a 2D ODMR spectrum at a given x position;
- as a photoluminescence spectrum at a given pixel (x-y) position.

As an example, we report the ODMR spectrum acquired when no static magnetic field is applied (fig. 2.10). Figure 2.10a shows the PL map in the x-y plane when the MW field is off resonance (top) and on resonance (down) with the NV centers spin transition. We can clearly observe the position of the laser beam and, as already shown in fig. 2.5, the PL striations. Although at first glance there is no difference between the two images, looking closely at the colour bar it is possible to observe a higher level of PL for the image taken with the RF field out of resonance. However, since the difference in the PL level is small compared to the PL fluctuations due to the striations, no immediate difference is visible when comparing the two images. Figures 2.10b and 2.10c show respectively the 2D ODMR spectrum in the x-f and y-f planes. In both cases we can guess the presence of a resonance line around 2.87 GHz characterized by a drop of PL. Since in absence of a static magnetic field all the NV centers resonate at the same frequency, the resonance line in the x-f and y-f plane is a vertical line perpendicular to the frequency axis. Finally, fig. 2.10d shows a single pixel ODMR spectrum where the spin resonance at 2.87 GHz is easily identifiable.

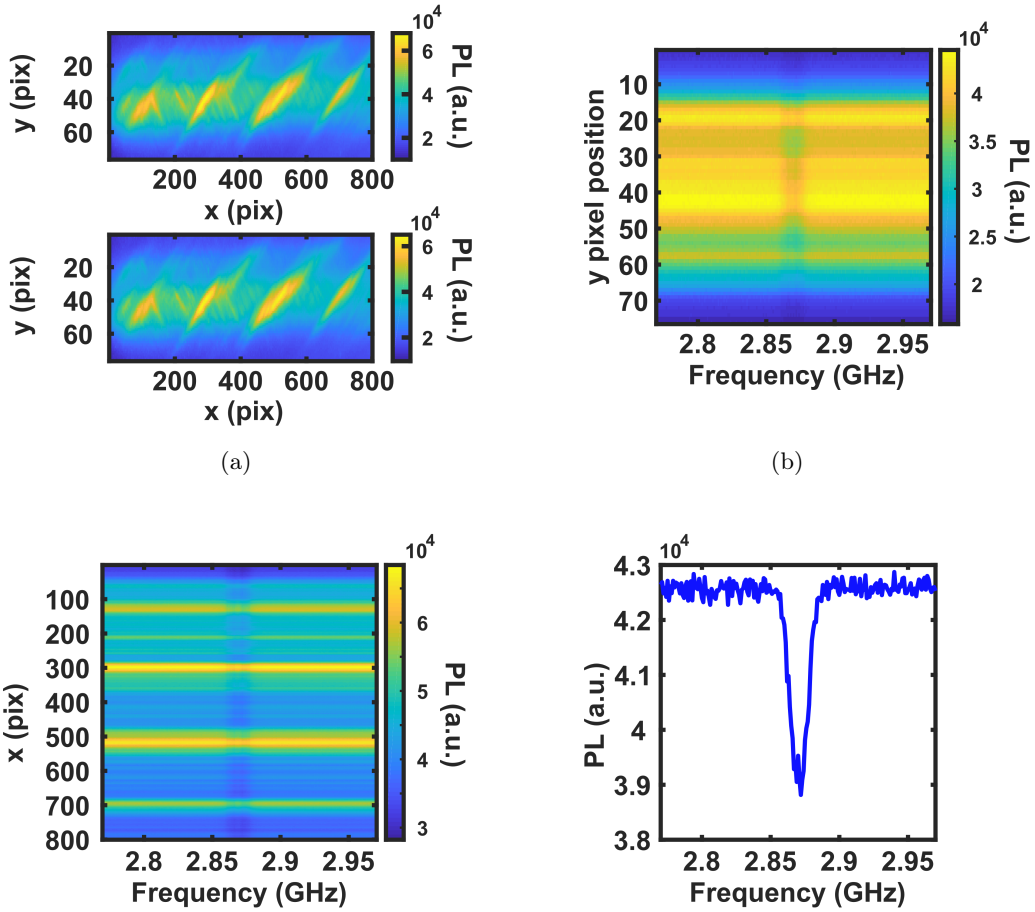

(a) (b)

(c) (d)

Figure 2.10: Raw data for a zero field CW-ODMR measurement. The nominal power of the RF field is 25dBm. (a) xy plane at $f = 2.7GHz$ (top) and at $f = 2.87GHz$(down). (b) yf plane at $x = 400$. (c) xf plane at $y = 50$, at the center of the laser beam. (d) Single pixel spectrum at $x = 400$ and $y = 50$

The bad visibility of the resonance line in the y-f and x-f plane is mainly due to the PL striations and it can be overcome by normalizing the data with respect to the PL acquired by the camera when the NV centers are out of resonance with the RF field or, equivalently, when no RF field is applied. Two different procedures are possible.
The first is a simple normalization procedure performed at the end of the measurement; it consists in dividing each single-pixel spectrum by the value of its baseline. This procedure does not alter the acquisition process described before.
The second procedure consists in acquiring for each image with the RF on (signal image), a reference image with the RF field off which is then subtracted to the signal image.
The advantage of the second procedure is both the suppression of the noise whose temporal scale is shorter than the time needed to complete a frequency scan (laser fluctuation, light fluctuation due to mechanical vibrations,...) and the suppression of the dark current and readout current of the camera. Moreover, summing over several cycles, the spectra acquired at the different cycles are equally weighted even in the case of laser power fluctuations, while this is not the case of the first normalization procedure. The drawback of the second procedure is that it requires a longer acquisition time (twice the time required using the first acquisition procedure) and, in the case of a shot-noise limited measurement, the noise of the measurement is doubled. Assuming the laser intensity is sufficiently stable and the dark current and readout current of the camera are negligible with respect to the photon shot-noise, in this manuscript the first normalization method is preferred to the second one. Moreover, it is less time-consuming.

In practice, the normalization procedure has been implemented dividing the data matrix (D) for the mean value of the PL in the first m and the last m steps of the frequency ramp, checking that all the NV centers in the AOI are out of resonance for those frequency values. The normalized data matrix (N) can be written as:

$$N_{xyf} = \frac{2m * D_{xyf}}{\sum_{f=f_{min}}^{f=f_{min}+m\Delta f} D_{xyf} + \sum_{f=f_{max}-m\Delta f}^{f=f_{max}} D_{xyf}} \tag{2.8}$$

and it is directly related to the ODMR contrast (eq. (1.6)) by the formula:

$$C_{xyf} = 1 - N_{xyf} \tag{2.9}$$

The results of the normalization process are shown in fig. 2.11. The normalized PL in the x-y plane when the RF field is set to f=2.87 GHz (fig. 2.11a bottom), compared to the one acquired out of resonance (fig. 2.11a top), clearly shows the presence of NV centers resonating at that frequency. In the PL map acquired out of resonance the PL striations are not visible anymore, while this is not the case for the PL map at 2.87 GHz, which shows a pixel-dependent contrast. This phenomenon is attributed to an unexpected presence of an NV centers preferential orientation in the sample and it will be better investigated in section 2.3. The visibility in the x-f and y-f plane (figs. 2.11b and 2.11c) is extremely better than the one obtained without the normalization and a very well contrasted resonance line is visible. The spectrum at a given pixel position is not modified by the normalization fig. 2.11d. However, in the case of a sum over many pixels to increase the SNR of the measurement, the normalization procedure allows equally weighting the spectra acquired by different pixels.

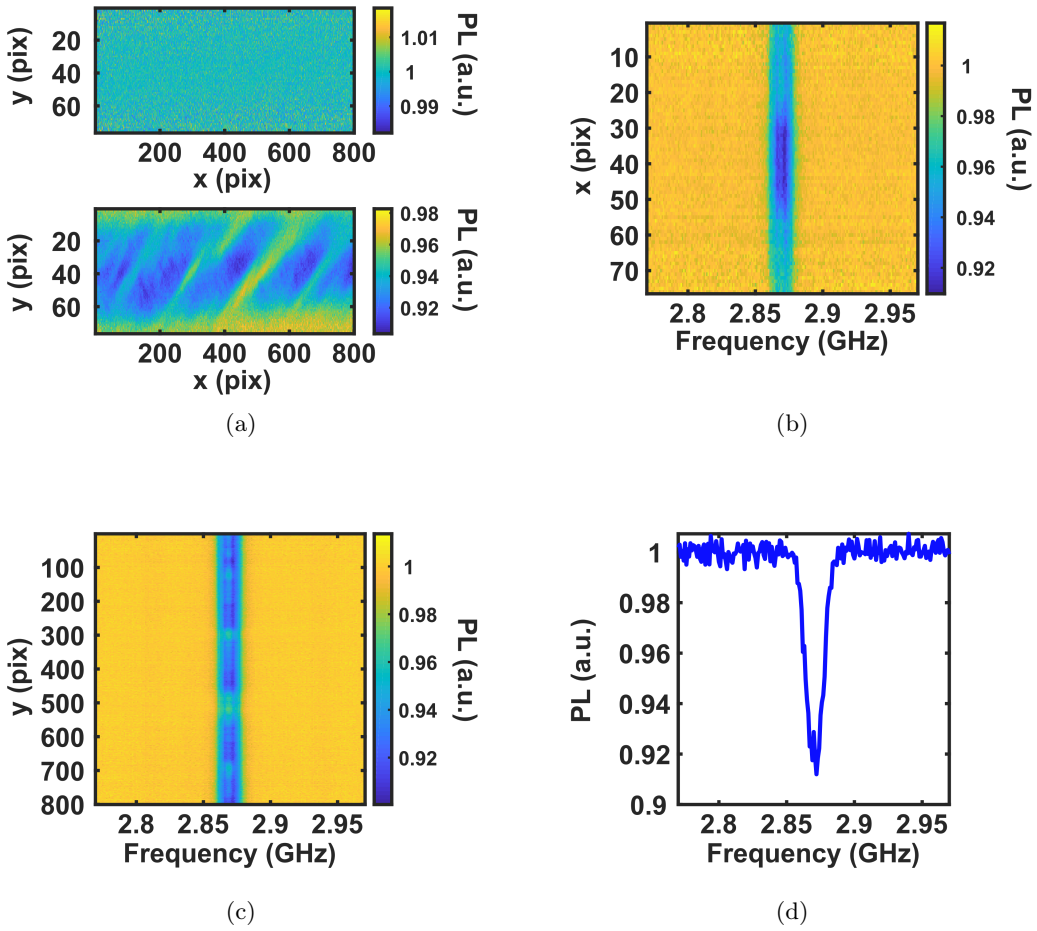

Figure 2.11: Normalized data for a zero field CW-ODMR measurement. The nominal power of the RF field is 25dBm. (a) xy plane at $f = 2.7$ GHz (top) and at $f = 2.87$ GHz (down). (b) yf plane at $x = 400$. (c) xf plane at $y = 50$, at the center of the laser beam. (d) Single pixel spectrum at $x = 400$ and $y = 50$

2.3 Sample characterization under a low static magnetic field

In the previous section the ODMR of an ensemble of NV centers in absence of any static magnetic field has been investigated. The four NV center families resonated at the same frequency and the two NV center ground state spin transitions were degenerate. In order to remove both the degeneracy between the two ground state spin transitions and the degeneracy between the four NV center families, a low static magnetic field is applied in proximity of the diamond. According to eq. (1.5), the ground state resonance frequencies for each NV center family are:

$$f_{0\rightarrow\pm1} = D \pm \gamma B \cos\vartheta \tag{2.10}$$

Where ϑ is the angle between the static magnetic field and the NV center axis. If ϑ is different for the four NV center families, as it is in our case, the NV center ensemble presents eight spin resonance frequencies[3], two for each NV center orientation, symmetrically placed with respect to D=2.87 GHz (fig. 2.12).

Differently from fig. 2.11, the ODMR lines in the x-f and y-f plane (fig. 2.12b) are tilted with respect to the frequency axis. This is the signature of a magnetic field gradient along the x and y axes which induces NV centers located in different positions to resonate at different frequencies. This property is the key idea of a spectrum analyzer based on an ensemble of NV centers and will be discussed in chapter 3.
To simplify the discussion, in this paragraph the NV center families are named A,B,C,D starting from the one that resonates at the lowest frequency and moving toward 2.87 GHz. Figure 2.12c shows the ODMR spectrum acquired by two different pixels, whose positions are reported on fig. 2.12a. As expected, the eight resonance lines and the dependence of the resonance frequency on the diamond position are well visible. However, depending on the pixel position, the ratio of the contrast of the four families changes. This unexpected effect is also visible in the x-f and y-f plane, where the contrast of the ODMR lines is not homogeneous over the entire image. The dependence of the contrast on the position is investigated in the x-y plane by looking at the images acquired when the RF field is resonant with each of the different NV center families (figs. 2.12d to 2.12g). Comparing these images with the PL image acquired out off resonance (fig. 2.12a), families C and D show a better contrast in correspondence of PL striations, while it is the contrary for families A and B. According to the definition of contrast of one NV center family in an ensemble of NV centers (eq. (1.6)), the contrast inhomogeneity may be due to a localized preferential orientation.

The preferential orientation can be explained considering the diamond growing process. The sample used in this manuscript is grown along a {100} axis and then cut along four [110] perpendicular planes (fig. 2.13). Although no preferential orientation is expected for diamonds grown along the [100] direction (section 1.4), during the growing process it is possible that, due to some interstitial defects, the growing axis changes and becomes the 110 axis [114]. Under this growing condition, NV centers will be preferentially oriented along crystallographic directions which do not lay in the growing plane (pink plane in fig. 2.13). As a consequence, the [110] facet we are investigating (the green plane in fig. 2.13) shows a preferential orientation for one family laying in the plane and one family pointing out of the plane.

To figure out which ODMR line corresponds to each NV family, the polarization of the emitted photoluminescence is analysed with the help of the polarizer, as discussed in section 2.1.6. The ODMR spectra are acquired for different angles of the polarizer axis (fig. 2.14). By turning the polarizer axis, it is possible to suppress the contrast of family C ($\alpha = 70° \pm 10°$) and family A ($\alpha = 135° \pm 10°$), but not the one of families B

[3]We are considering only the NV center ground state spin resonances.

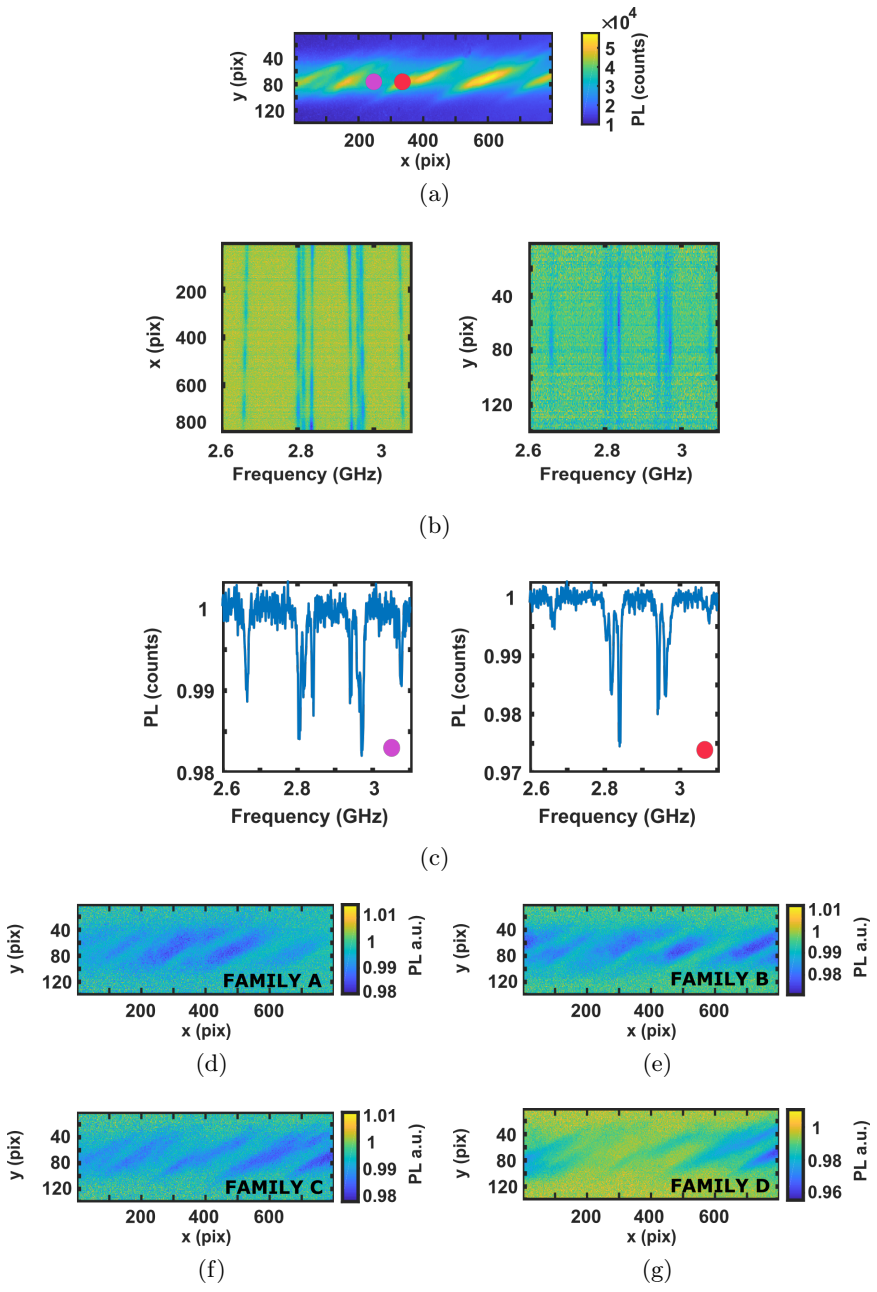

Figure 2.12: Low static magnetic field CW-ODMR measurement. (a) xy plane raw data. (b) xf and yf planes normalized data. (c) Single pixel ODMR spectra. The position of the pixel is defined by the position of the coloured circles in the xy plane (a). These positions are chosen in order to be at the same y position but at a different x position, in the first case on a dark PL striation and in the second case on a bright PL striation. (d-g) xy plane normalized data when the RF field is on resonance with the NV center family indicated in the right bottom corner of each image. The families are named $A - B - C - D$ starting from the one which resonates at the lowest frequency and moving toward the center of the spectrum.

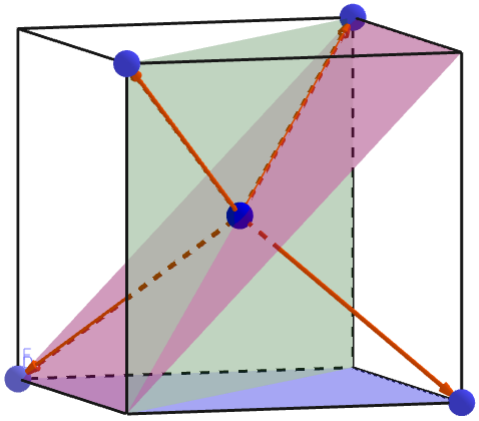

Figure 2.13: Growing process and preferential orientation. The blue spheres represent carbon atoms, while the red lines are the chemical bonds along the [111] crystallographic axis. The blue plane is a [100] plane, the pink and the green plane are two different [110] planes.

and D. Therefore A and C are the two NV center families laying on the [110] plane from which the PL is collected. This result is in agreement with the previous explanation about the preferential orientation in the diamond sample: the families which show a preferential orientation in a certain diamond area are either families A and B or families C and D, i.e., one in-plane and one out-of-plane family with respect to the diamond top facet.

Regarding the two NV center applications discussed in this manuscript, the presence of PL striations and localized preferential orientation limits the performance of the experimental set-up but not at all the explanation of the proof of principle, the real purpose of this thesis. Therefore, considering the explanation that the drop of contrast is detected due to spatial-dependent preferential orientation as sufficient, the nature of this effect is not investigated further.

In the next sections the interaction between a static magnetic field and an ensemble of NV centers is investigated both mathematically, looking at the Hamiltonian of the system, and experimentally, using the experimental set-up, the acquisition procedure and the normalization method described until now in this chapter.

2.4 Hamiltonian of an ensemble of NV centers

At room temperature, the ground state and the excited state Hamiltonian of an NV center interacting with a static magnetic field have the same general expression, which is [115]:

$$H = h\left(DS_z^2 + E(S_x^2 + S_y^2) + \gamma\vec{B}\vec{S} + \gamma_N\vec{B}\vec{I} + \vec{I}\mathbf{A}\vec{S} + Q_N I_z^2\right) \tag{2.11}$$

$\vec{S}$ and $\vec{I}$ are respectively the NV center electron spin operator and the NV center's nitrogen nuclear spin operator. Depending on the nitrogen isotope present in the sample, I=1 in the case of ^{14}N and I=1/2 in the case of ^{15}N. Since the sample considered in this manuscript contains ^{14}N, only the case I=1 will be considered from now on.

In the absence of any external static magnetic field, given the NV center C_{3V} symmetry, the NV center axis is the most natural spin quantization axis, here denoted with z. The x and y axis are arbitrarily chosen in order to obtain a Cartesian coordinate system.

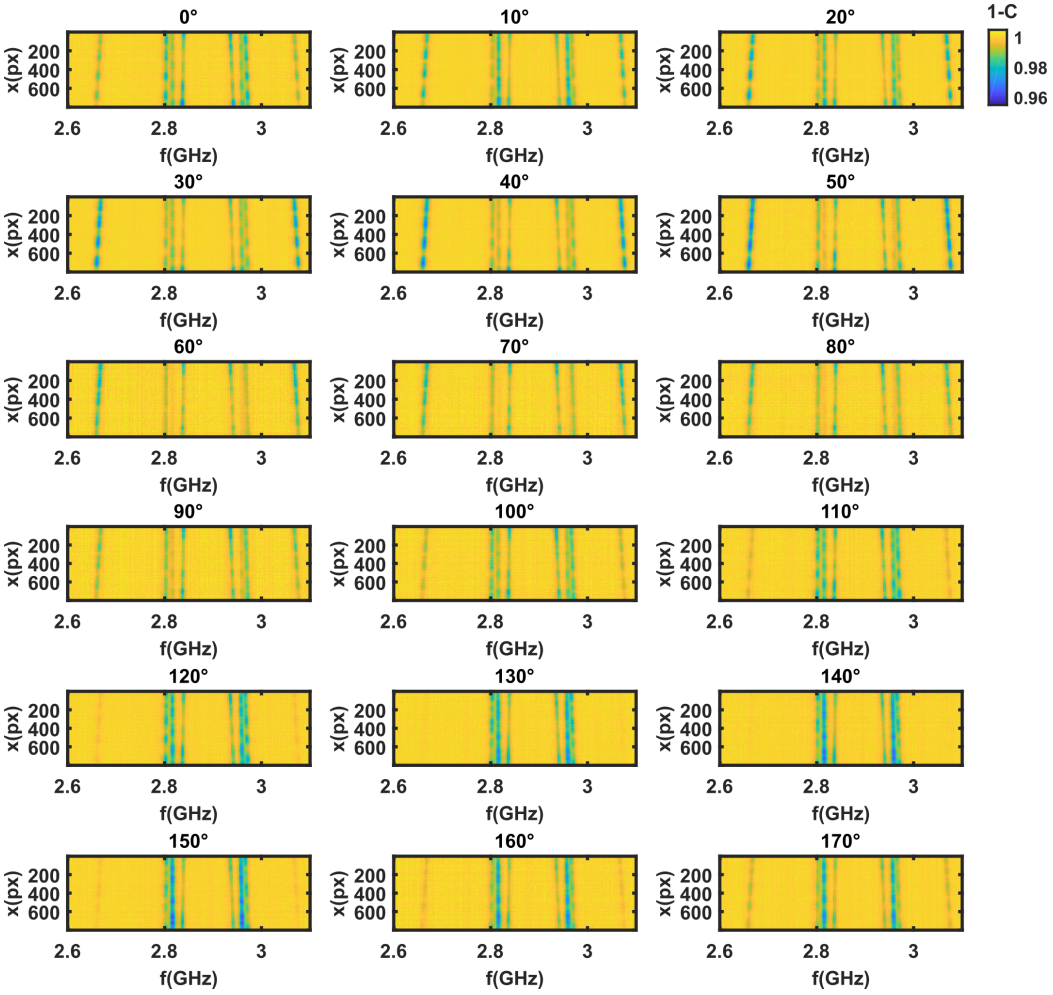

Figure 2.14: ODMR spectra in the xf plane acquired for different angles of the polarizer axis, reported as the title of each subplot. The zero is arbitrarily chosen. The signal is summed over 20 pixels along y in order to increase the SNR.

S_x, S_y, S_z and I_x, I_y, I_z are thus the components of the electronic and nuclear spin operators along these axis. The eigenvector of $[S^2, S_z]$ and $[I^2, I_z]$ are respectively denoted by $|m_s = 0, \pm 1\rangle$, $|m_i = 0, \pm 1\rangle$, where m_s and m_i are the electronic and nuclear spin quantum numbers. According to the spin sum rules, the phase space of the system described by eq. (2.11) is the Hilbert space which results from the tensor product between the NV center electronic spin phase space and the nitrogen nuclear spin phase space. A basis of this new Hilbert space is $|m_s\rangle \otimes |m_i\rangle$ that in the following will be abbreviated as $|m_s, m_i\rangle$. Since the spin-dependent optical properties of the NV center are related only to its electronic spin, in the following we will use the notation $(|0\rangle, |+1\rangle, |-1\rangle)$ to refer to the spin states manifolds characterized by electronic spin quantum numbers $m_s = 0, \pm 1$.

The first two terms of eq. (2.11) constitute the zero field NV center Hamiltonian. D=2.87 GHz (D=1.42 GHz) is the ground state (excited state) axial zero field splitting and it corresponds to the energy gap between the $|m_s = 0\rangle$ state and the two degenerate $|m_s = \pm 1\rangle$ states when no external field is applied. In the following, we will use the notation D_{GS} and D_{ES} to identify the zero field splitting frequency at the ground state and the excited state. If the subscript is omitted, we refer to the ground state zero field splitting. E is the non axial zero field term and it depends on the diamond lattice strain. It is sample dependent and since in CVD bulk diamonds it is usually of the order of hundreds of kHz, it is usually negligible compared to other interactions. Its contribution to the NV center energy levels structure consists in removing the degeneracy between the $|m_s = -1\rangle$ and $|m_s = +1\rangle$ state in absence of static magnetic field. A complete discussion about the effect of the strain on the NV center energy levels can be found in [116].

The third and the fourth terms of eq. (2.11) are related to the Zeeman interaction between the magnetic field and the electronic and nuclear spins; $\gamma_N = 3$ MHz/T and $\gamma = 28$ GHz/T are respectively the nuclear and electronic gyromagnetic ratios. Due to the very small value of γ_N with respect to γ, the Zeeman shift of the nuclear spin levels is usually neglected. The interaction between a static magnetic field and the NV center electronic spin is the subject of section 2.5.

The last two terms of eq. (2.11) account for the hyperfine coupling between the NV center electronic spin and the NV center's nitrogen nuclear spin [117]. $\mathbf{A}$ is the hyperfine tensor and $Q_N = -5$ MHz is the electric quadrupolar interaction term[4] [118]. The hyperfine tensor A is diagonal in the $|m_s, m_i\rangle$ basis. Denoting the hyperfine tensor components parallel and perpendicular to the NV center axis as $A_\parallel$ and $A_\perp$, and introducing the raising and lowering spin operators $I_\pm = \frac{I_x \pm j I_-}{\sqrt{2}}$ and $S_\pm = \frac{S_x \pm j S_-}{\sqrt{2}}$, the hyperfine Hamiltonian can be written as:

$$H_{hyp} = h\left(Q_N I_z^2 + \vec{I}\mathbf{A}\vec{S}\right) = h\left(Q_N I_z^2 + A_\parallel S_z I_z + A_\perp (I_+ S_- + I_- S_+)\right) \tag{2.12}$$

For the ground state, it results $A_\parallel = -2.3$ MHz and $A_\perp = 2.1$ MHz, while for the excited state $A_\parallel = -40$ MHz and $A_\perp = -23$ MHz [119]. The main contribution of the first two terms of the hyperfine interaction consists in removing the degeneracy between energy levels having the same electronic spin but different nuclear spin (fig. 2.15). The last two terms, which are the transverse components of the hyperfine interaction, couple energy states with the same total angular momentum ($m_j = m_I + m_s$) and nuclear and electronic spin such that $\Delta m_s = -\Delta m_I$. They have a main role in the optical polarization of the nitrogen nuclear spin which is discussed from a theoretical point of view in section 2.6 and from an experimental point of view in section 2.7.

[4]This term is null for nuclear spin $I \leq 1/2$, namely for the ^{15}N nitrogen isotope

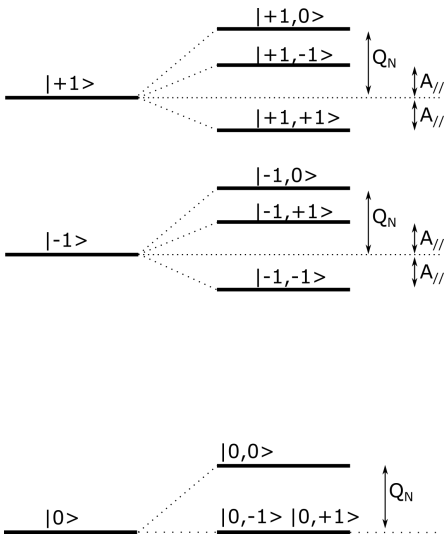

Figure 2.15: Ground state NV center hyperfine structure. On the left, the fine structure whose levels are labelled using the notation $|m_s\rangle$. On the right, the hyperfine structure whose levels are labelled using the notation $|m_s, m_i\rangle$.

2.5 The Zeeman interaction

The Zeeman interaction between an NV center and a static magnetic field can be studied, in first approximation, neglecting the contribution of the nuclear spin ($\gamma_N << \gamma$) and considering only the interaction between the magnetic field and the electron spin of the NV center. The Hamiltonian of the system is:

$$H = h(DS_z^2 + \vec{B}\vec{S}) = h(DS_z^2 + B_z S_z + B_x S_x) \tag{2.13}$$

where the x axis is chosen parallel to the magnetic field component perpendicular to the NV axis, so that $\vec{B} = (B_x, 0, B_z)$.

The eigenvalues of the ground state Hamiltonian are numerically evaluated and plotted in fig. 2.16a for four different cases:

- a magnetic field perfectly aligned with the NV center axis ($B_x = B_y = 0$);
- a magnetic field slightly misaligned (2°) with respect to the NV axis;
- a magnetic field highly misaligned (71°) with respect to the NV axis;
- a magnetic field perpendicular to the NV axis.

The reason why an angle of 71° (or equivalently of 109°) has been chosen for the simulation is that when the static magnetic field is well aligned with one NV center family, the other three NV families form an angle of this amplitude with respect to the static magnetic field (see section 2.8). The color of each data point of fig. 2.16 is expressed in the RGB scale, defining the components of the RGB three-dimensional vector as:

$$R = |\langle +1|\psi\rangle|^2; G = |\langle 0|\psi\rangle|^2; B = |\langle -1|\psi\rangle|^2 \tag{2.14}$$

where $|\psi\rangle$ is the state vector of the system and $|0, \pm 1\rangle$ are the $[S_z, S^2]$ eigenstates. Using this color scale, the plot contains also information about the eigenvectors of the system. In fact, a red point means that the system eigenstate associated with that eigenvalue is $|+1\rangle$, a green point means that the system eigenstate associated with that eigenvalue is $|0\rangle$ and a blue point means that the system eigenstate associated with that

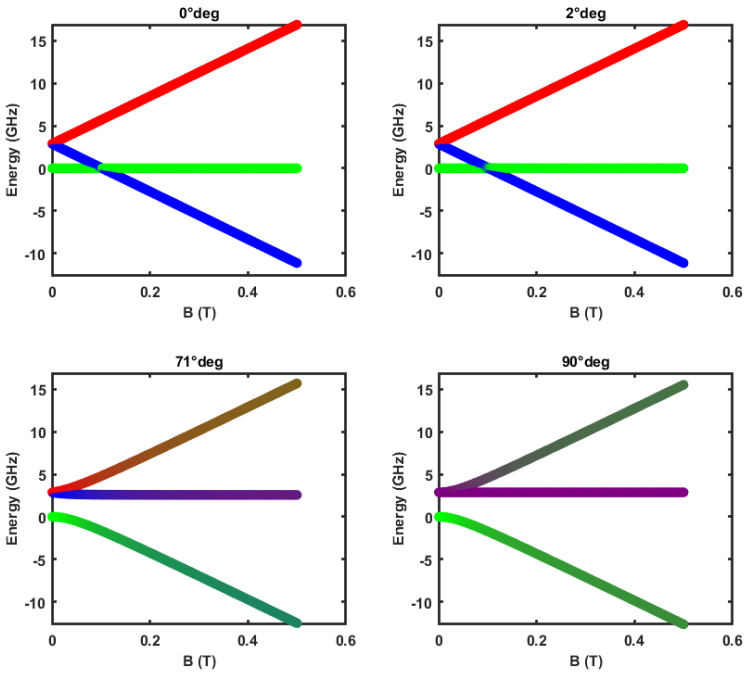

(a)

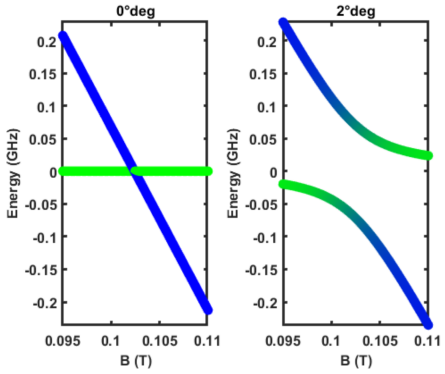

(b)

Figure 2.16: Zeeman effect. (a) The eigenvalues of the Zeeman Hamiltonian are evaluated for four different angles between the NV center axis and the static magnetic field. The angles are reported in the title of each subplot. (b) Zoom in proximity of the level crossing for a well-aligned static magnetic field and for a static magnetic field tilted of 2° with respect to the NV center axis. In the second case the level crossing is avoided.

eigenvalue is $|-1\rangle$.
In the case of a magnetic field parallel to the NV center axis, the eigenvectors of the system are the eigenvectors of the spin operator S_z, for any value of static magnetic field. Moreover, for a magnetic field value B=D/γ[5] the energy of the $|-1\rangle$ state equals the energy of the $|0\rangle$ state and the two levels become degenerate. This phenomenon is known as level crossing.
For a magnetic field slightly misaligned with respect to the NV center axis, the level crossing is avoided due to the coupling between the $|-1\rangle$ and the $|0\rangle$ state by means of the transverse component of the Zeeman Hamiltonian (the last term of eq. (2.13)). This phenomenon is known as level anticrossing and it is a well-known phenomenon of two-level systems [39]. The ground state level anticrossing (GSLAC) is achieved at $B \approx \frac{D_{GS}}{\gamma} \approx 102$ mT while the excited state levels anticrossing (ESLAC) at $B \approx \frac{D_{ES}}{\gamma} \approx 51$ mT. Assuming that the coupling between the $|0\rangle$ state and the $|+1\rangle$ state is negligible with respect to the energy gap of the transition ($B_x << D/\gamma + B_z$), the $|+1\rangle$ state is an eigenvector of the system. Therefore we can discuss the effect of the transverse component of the static magnetic field considering the NV center as a two-level system $[|0\rangle, |-1\rangle]$. The Hamiltonian of this system, in the matrix representation of basis $|0\rangle = [1;0]$ and $|1\rangle = [0;1]$ is:

$$H = h \begin{bmatrix} 0 & \gamma B_x \\ \gamma B_x & D - \gamma B_z \end{bmatrix} \tag{2.15}$$

The eigenvalues of eq. (2.15), in frequency unity, are:

$$E_{1,2} = \frac{D - \gamma B_z \pm \sqrt{(D - \gamma B_z)^2 + 4(\gamma B_x)^2}}{2} \tag{2.16}$$

and the eigenvectors are:

$$|+\rangle = \cos(\vartheta/2)\,|0\rangle + \sin(\vartheta/2)\,|-1\rangle \tag{2.17}$$

$$|-\rangle = \sin(\vartheta/2)\,|0\rangle + \cos(\vartheta/2)\,|-1\rangle \tag{2.18}$$

where

$$\tan(\vartheta) = \frac{2\gamma B_x}{\gamma B_x - D} \tag{2.19}$$

In eqs. (2.16) to (2.18) we found mathematically the same results plotted in fig. 2.16a. When B_x=0, the eigenvectors of the system are the S_z eigenvectors and the energy levels are degenerate for B=D/γ. When $B_x \neq 0$, the two eigenvectors are a linear combination of $|0\rangle$ and $|-1\rangle$ and their eigenvalues are never degenerate, giving rise to a level anticrossing, that is an energy gap ($|E_2\text{-}E_1|$) between the eigenvalues. The amplitude of the energy gap depends on the transverse component of the static magnetic field (fig. 2.16b).
When B_x is comparable with D/γ+ B_z, as it is in the case of a magnetic field tilted of 71° or 90° with respect to the NV center axis, the $|+1\rangle$ state is not an eigenstate of the system anymore. In this case the previous approximation is not valid and the eigenstates of the system are a linear combination of the three S_z eigenstates as shown by the colour scale of fig. 2.16a.
The mixing of the S_z eigenstates has two main consequences: a drop of PL and a drop of the ODMR contrast with respect to the system whose eigenstates are the S_z eigenstates [120]. This effect is shown in section 2.8.

[5] In the simulation we considered the NV center gournd state zero field splitting, that is D=2.87 GHz

Since according to eq. (2.16) the energy gap and the levels mixing at the level anti-crossing depend on the angle between the static magnetic field and the NV axis (fig. 2.17a), both the drop of contrast and the amplitude of the energy gap can be exploited to properly align the static magnetic field to the NV center axis. As an example, we show the NV ODMR spectra near the GSLAC in the case of a well aligned (fig. 2.17b) and a slightly misaligned (fig. 2.17c) static magnetic field. Both the decrease in contrast and the increase in the energy gap are visible when comparing the two spectra.

It is important to notice that, even for a well aligned static magnetic field, the NV center level crossing is avoided because of the coupling between the $|0\rangle$ and the $|-1\rangle$ states induced by the lattice strain or other residual traverse fields eq. (2.11). In this case, the energy gap at the level anti-crossing becomes comparable with the strength of the hyperfine coupling and therefore the contribution of the nuclear spin cannot be neglected anymore, as explained in the next paragraph.

2.6 All optical polarization of the nitrogen nuclear spin: theory

The all optical polarization of the NV's nitrogen nuclear spin (also called dynamic hyperpolarization or dynamic polarization or simply DNP) has been firstly investigated for a single NV center in [121].
At room temperature, according to the Boltzmann distribution, the three hyperfine levels associated with each electron spin level are equally populated (fig. 2.15). Close to level anti-crossing, where the Zeeman shift compensates for the zero-field splitting, the hyperfine interaction, in combination with the optical polarization of the NV center electron spin, induces the polarization of the nuclear spin.
In this paragraph we describe the DNP in proximity of the ESLAC. However a similar argument can be used to explain the DNP in proximity of the GSLAC. Moreover in this paragraph the subscript GS and ES will be used to identify respectively the NV center ground state and the NV center excited state.
The excited state NV center Hamiltonian under a well aligned static magnetic field is:

$$H = h\left(D_{es}S_z^2 + \gamma B_z S_z + Q_N I_z^2 + A_{\parallel} S_z I_z + A_{\perp}(I_+ S_- + I_- S_+)\right) \tag{2.20}$$

The strain term and the nuclear spin Zeeman interaction are neglected because small with respect to the hyperfine interaction terms. The last term of the eq. (2.20),that is the transverse component of the hyperfine interaction, is usually neglected when the energy gap between the $|m_s = 0, m_i\rangle_{ES}$ and $|m_s = -1, m_i\rangle_{ES}$ state is larger with respect to $A_{\perp}$; in that case the eigenstates of the system are $|m_s, m_i\rangle_{ES}$. However, in proximity of the ESLAC, the energy gap between the $|m_s = 0, m_i\rangle_{ES}$ and $|m_s = -1, m_i\rangle_{ES}$ tends to zero, and the transverse component of the hyperfine interaction cannot be neglected anymore. The transverse component of the hyperfine interaction is however still negligible between the $|m_s = 0\rangle_{ES}$ and $|m_s = +1\rangle_{ES}$ manifolds, and therefore, as already done in the previous paragraph, we limit our discussion only to the $|m_s = 0\rangle_{ES}$ and $|m_s = -1\rangle_{ES}$ manifolds.
Using the formalism of lowering and rising operators[6], it easy to observe that the transverse component of the hyperfine interaction couples the energy states which have same total angular momentum ($m_j = m_I + m_s$) and nuclear and electronic spin such that $\Delta m_s = -\Delta m_I$: $|0, -1\rangle_{ES}$ is coupled with $|-1, 0\rangle_{ES}$ and $|-1, +1\rangle_{ES}$ is coupled with $|0, 0\rangle_{ES}$. The state $|-1, -1\rangle_{ES}$ is not coupled to any other state by the hyperfine in-

[6] $\langle m_j|S_-|m_k\rangle \neq 0$ if k=j+1.
$\langle m_j|S_+|m_k\rangle \neq 0$ if k=j-1.
$\langle m_j|S_z|m_k\rangle \neq 0$ if k=j. Where m_j and m_k are the NV center spin quantum number. The same rules are valid for $I_{\pm}$

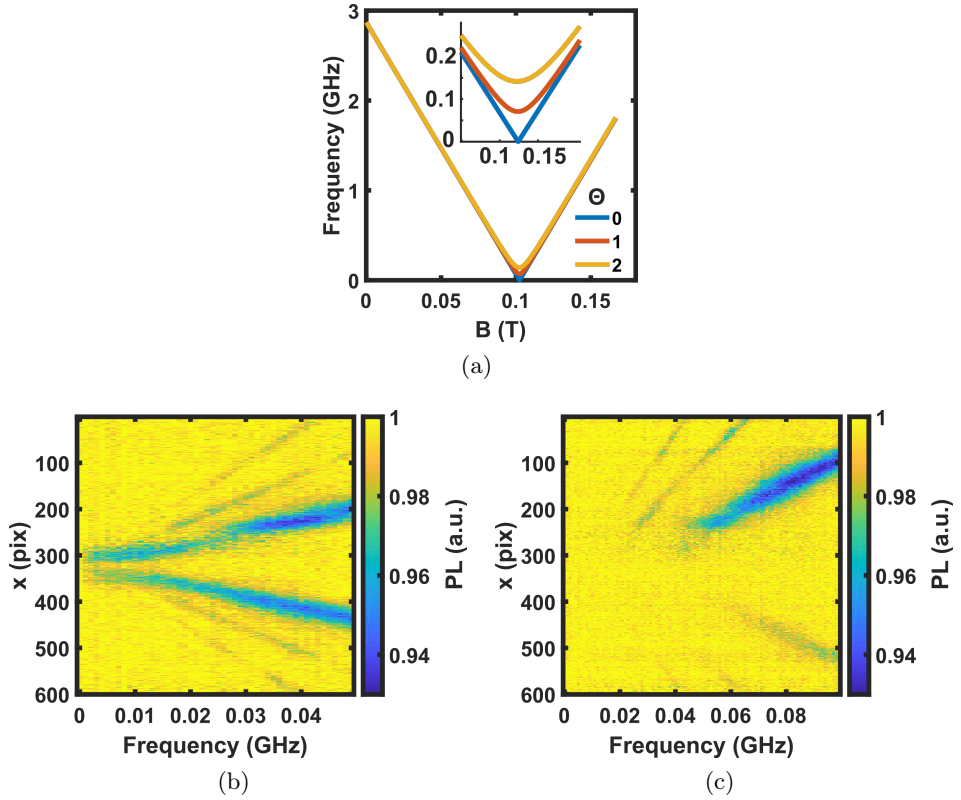

(a)

(b)

(c)

Figure 2.17: ODMR spectra at the GSLAC in the case of a well aligned and misaligned static magnetic field. (a) Resonance frequency of the $|0\rangle_{GS} \rightarrow |-1\rangle_{GS}$ transition in proximity of the GSLAC for different angles of misalignement. The small plot inside the main plot is a zoom in proximity of the GSLAC. The GSLAC is easy to recognize looking at the slope variation of the resonance line. (b) ODMR spectrum in the xf plane at the GSLAC in the case of a well-aligned static magnetic field. The lowest detectable frequency is of the order of some MHz. (c) ODMR spectrum in the xf plane at the GSLAC in the case of a misaligned static magnetic field. The lower detectable frequency is of the order of $50MHz$. The ODMR contrast is better at the top of the image than at the bottom because the static magnetic field is better aligned with the NV centers placed around $x = 200$ than the NV centers placed around $x = 600$. This is caused by the non-homogeneous spatial distribution of the static magnetic field generated by the spherical magnet. Since at the GSLAC the system is extremely sensitive to the magnetic field alignment, even a small angle of misalignment can drastically reduce the ODMR contrast.

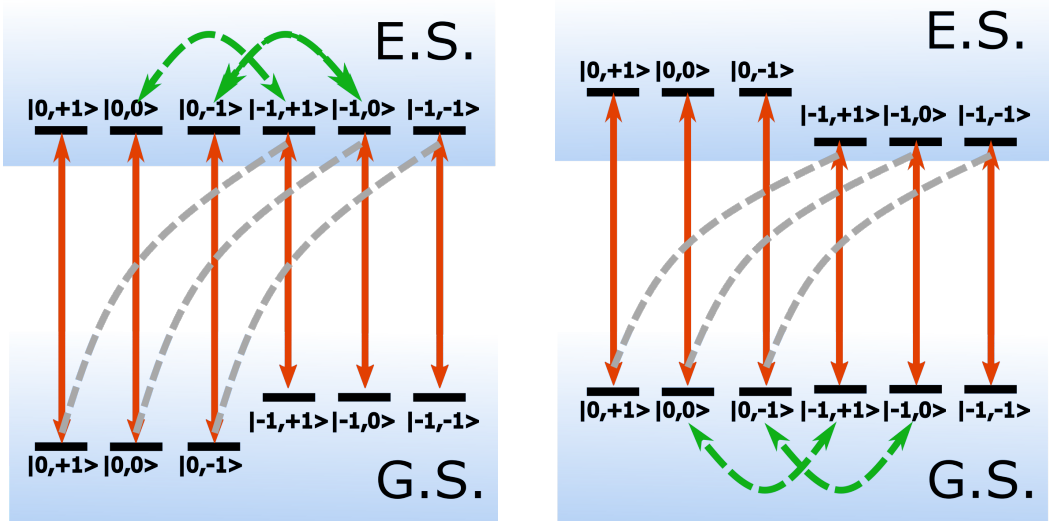

(a) *ESLAC* (b) *GSLAC*

Figure 2.18: All optical nuclear spin polarization at the ESLAC (a) and the GSLAC (b). The energy levels are named using the notation $|m_s, m_I\rangle$. The red arrows represent the spin conserving transitions between the ground state and the excited state, that is both the optical excitation and the radiative decay. The grey dashed arrows represent the ISC decay process, which therefore preserves the nuclear spin changing the electronic spin. The green arrows link the states which are coupled by the hyperfine interaction and therefore represent the possible spin flip-flop transitions. Image inspired by [121].

teraction while the state $|0,+1\rangle_{ES}$ is coupled with $|+1,0\rangle_{ES}$ but the strength of the coupling ($\approx$ 23 MHz) is negligible with respect to the energy gap between the two states ($\approx$ 4 GHz) [7].

The excited state decay rate ($\approx$ 80 MHz) is comparable with the strength of the transverse hyperfine coupling ($\approx$ 40 MHz). When the NV center is in the excited state, an electron-nuclear spin flip-flop can occur, which is a transition between energy levels that are coupled by the hyperfine interaction. This mechanism and how it generates the polarization of the nitrogen nuclear spin is depicted in fig. 2.18a. An NV center initially in the $|0,-1\rangle_{GS}$ state is optically excited by a spin preserving transition in $|0,-1\rangle_{ES}$. By means of the hyperfine coupling, the NV center can flip in $|-1,0\rangle_{ES}$ and decay in the $|0,0\rangle_{GS}$ state through an ISC process. Comparing this state to the initial state ($|0,-1\rangle_{GS}$) the nuclear spin of the nitrogen changed. Repeating the same argument, it is possible for the NV center initially in $|0,0\rangle_{GS}$ to decay in $|0,+1\rangle_{GS}$ state. Since the $|0,+1\rangle_{ES}$ is not coupled with any other state by the hyperfine interaction, once the nuclear spin is in the $|m_I = 1\rangle$ state, it will remain in this state. Since the nuclear spin relaxation time (T_1) is extremely large with respect to the NV center optical cycle duration, the ensemble of NV centers is polarized in $|m_I = 1\rangle$ state after some optical cycles.

The same polarization process is possible at the GSLAC (fig. 2.18b). The main difference between the nuclear polarization at the GSLAC and the ESLAC is the strength of the hyperfine coupling, which is lower at the ground state $A_{\parallel}^{GS} = -2.16$ MHz $A_{\perp}^{GS} = -2.70$ MHz than at the excited state $A_{\parallel}^{GS} = -40$ MHz $A_{\perp}^{GS} = 23$ MHz. Therefore we can expect the nuclear spin polarization to be more sensitive to the transverse magnetic

[7] this approximation falls in the more general case of the secular approximation, where the coupling between two systems is neglected when the time constant of the coupling are much more slower than the characteristic time of the system

field and the strain field at the GSLAC than at the ESLAC [117].

In [121] it has been demonstrated that, even for magnetic fields lower than the one required for the ESLAC, the nitrogen nuclear spin is partially polarized. In the next section, we experimentally investigate the DNP of an ensemble of NV centers for static magnetic fields up to 200mT, showing that the nitrogen nuclear spin is partially polarized over the entire magnetic field range.

2.7 All optical polarization of the nitrogen nuclear spin: experiment

The nuclear spin optical polarization is investigated using the experimental set-up described in section 2.1 and two cylindrical magnets as magnetic field source. The magnets are placed equidistant from the diamond and aligned with one of the two NV center families laying on the top [110] diamond facet (fig. 2.19b). Using this magnetic architecture, the magnetic field is almost homogeneous inside the AOI. A comparison between the single-magnet and the two-magnet configuration is reported in fig. 2.19. We can clearly observe that in the two-magnet configuration the magnetic field gradient is weaker than in the single magnet configuration and almost all the NV centers resonate at the same frequency, allowing the sum over several pixels to increase the SNR of the measurement. Changing the magnet-diamond distance while preserving the symmetry of the magnets with respect to the center of the diamond AOI, it is possible to tune the static magnetic field amplitude preserving a low magnetic field gradient (section 2.1.3).

The experimental signature of the nuclear spin polarization is in the hyperfine structure of the NV center. When the nuclear spin is not polarized, the three hyperfine levels are equally populated and three equally contrasted hyperfine peaks are visible on the ODMR spectrum (fig. 2.20a). On the contrary, when the nuclear spin is completely polarized, only one of the three hyperfine peaks is visible on the ODMR spectrum (fig. 2.20b).

In this thesis, the nuclear spin polarization is investigated for different values of static magnetic field, from 51 mT (ESLAC) to 200 mT; the upper limit is due to the impossibility of approaching the magnets without touching the diamond. Some of the spectra acquired are reported in fig. 2.21.

As a consequence of the level anti-crossing, before the GSLAC the most contrasted peak is the one at the highest frequency, while after the GSLAC it is the one at the lowest frequency.

In order to quantify the nuclear spin polarization, the spectra are fitted by a fit function defined as the weighted sum of three Lorentzians, frequency shifted of $A_{\parallel}^{GS} = 2.14$ MHz:

$$f(\nu) = w_1 * \frac{a^2}{a^2 + (\nu - b - A_{\parallel}^{GS})^2} + w_0 * \frac{a^2}{a^2 + (\nu - b)^2} + w_{-1} * \frac{a^2}{a^2 + (\nu - b + A_{\parallel}^{GS})^2} + c \tag{2.21}$$

The degree of polarization is calculated, according to [122], as:

$$P = \frac{\sum_I m_I * w_I}{\sum_I m_I} \tag{2.22}$$

The results are reported in fig. 2.22, where the detuning corresponds to the energy difference, in frequency units, between the $|0\rangle_{GS}$ and the $|-1\rangle_{GS}$ energy levels. We can observe that the hyperfine polarization is preserved after the ESLAC (Detuning $= -1.42$ GHz) over the entire frequency range investigated. It is, as expected, highest near the level anti-crossing (better than 80% both at the ESLAC and GSLAC) and

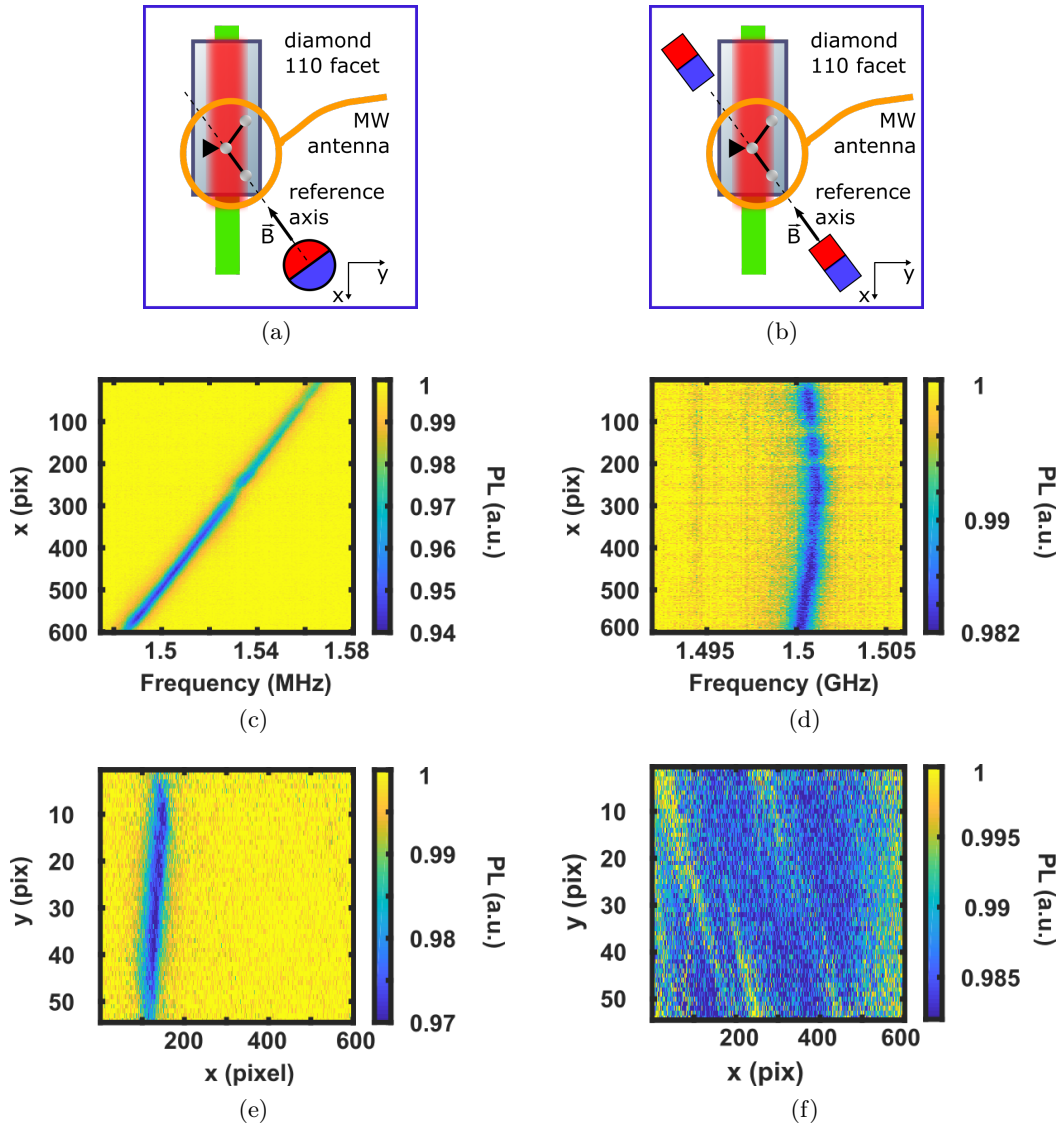

Figure 2.19: Comparison between the single-magnet and the two-magnet configuration. (a) Schematic of the single-magnet architecture with a spherical magnet. (b) Schematic of the two-magnet architecture with two cylindrical magnets facing each other and placed equidistant from the diamond. (c) ODMR spectra in the xf plane for the single-magnet architecture. (d) ODMR spectra in the xf plane for the two-magnet architecture. The different slope of the ODMR line in (c) and (d) shows that in the first case the magnetic field gradient is stronger than in the second case, where it is almost negligible. (e) ODMR spectra in the xy plane for the single-magnet architecture. (f) ODMR spectra in the xy plane for the two-magnets architecture. As effect of the magnetic field gradient, in (e) only a small number of pixels resonate at the same frequency; in (f) almost all the pixels resonate at the same frequency

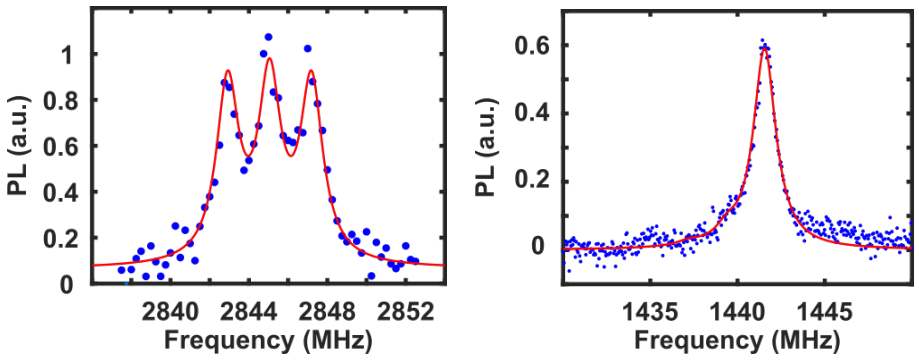

(a) *Low field* (b) *ESLAC*

Figure 2.20: Comparison between the ODMR spectra acquired under a low static magnetic field (a) and at the ESLAC (b). In the first case the three peaks of the NV center hyperfine structure are well visible. In the second case only one peak of the hyperfine structure is visible. This is the signature of the polarization of the nitrogen nuclear spin.

however better than 50% over the entire frequency range.

Previous works showed that the degree of polarization is extremely sensitive to the alignment of the static magnetic field and that even a small misalignment can depolarize the system. This effect has been investigated at the ESLAC by voluntarily misaligning the magnets with respect to the NV center axis. They have been displaced in the plane perpendicularly to the NV center axis in opposite directions one with respect to the other (inset fig. 2.22b). The degree of polarization for different angles of misalignment is reported in (fig. 2.22b) and shows that even small angles of misalignment induce a loss of nuclear spin polarization.
This effect must be taken into account in the analysis of the experimental results concerning the degree of polarization (fig. 2.22a). In fact, our way to tune the NV center resonance frequency is to translate the two magnets simultaneously and in the same direction. This procedure does not ensure to strictly preserve the same alignment over the entire frequency range investigated because the magnets' magnetization axis may not exactly be the translation axis of the translation stages used to displace the magnets (section 3.2.1). Therefore it is possible that the values of the degree of polarization reported in eq. (2.22) underestimate the real degree of polarization, which may be better than the one measured. A deeper study about the dynamic polarization of the nitrogen nuclear spin in an ensemble of NV center has been conducted by Bausaite et al. [122] using an electromagnet and evaluating the degree of polarization of the $|0\rangle \rightarrow |+1\rangle$ transition. Their results confirm our experimental observations and in particular the strong sensitivity of the polarization to the magnetic field alignment.

One point to note is the dependence of the ODMR linewidth on the static magnetic field amplitude. In fig. 2.21 we can observe that the ODMR line increases as the static magnetic field amplitude increases. This effect is caused by mechanical vibrations of the experimental set-up that induce an additional magnetic field gradient in the measurement. In fact, although the magnetic field gradient generated by the two magnets is weak at the center of the AOI, mechanical vibrations of the magnets can induce magnetic field fluctuations of the same order of magnitude as in a single-magnet configuration. In this case, NV centers still all resonate at the same frequency, but this one fluctuates throughout the measurement, broadening the ODMR line (section 3.5). As described in section 2.1, the magnetic field gradient along the magnetization axis of a cylindrical magnet increases with the amplitude of the static magnetic field, therefore

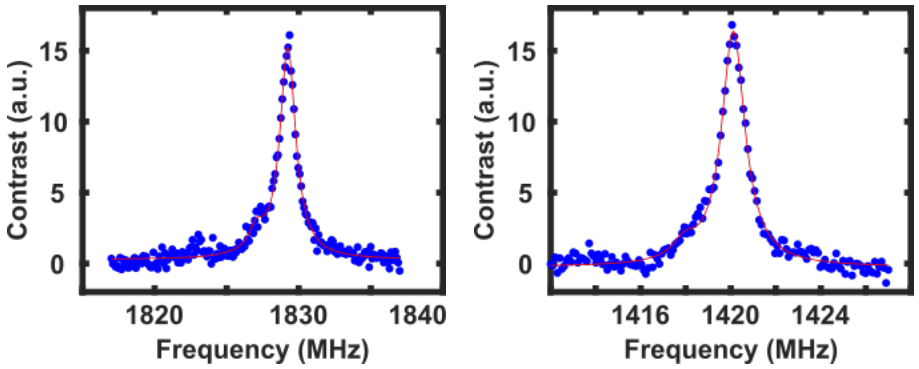

(a) *37 mT*

(b) *51 mT*

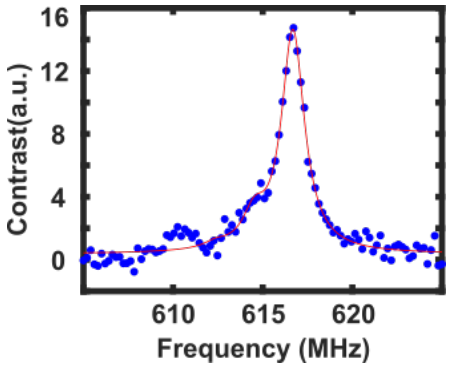

(c) *80 mT*

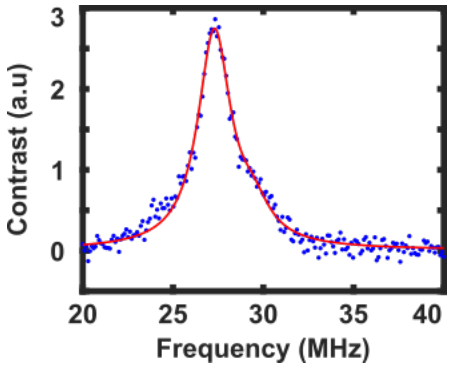

(d) *102 mT*

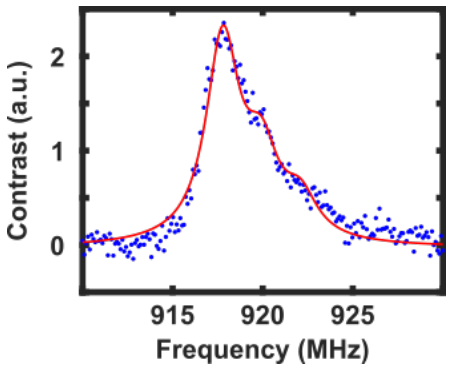

(e) *135 mT*

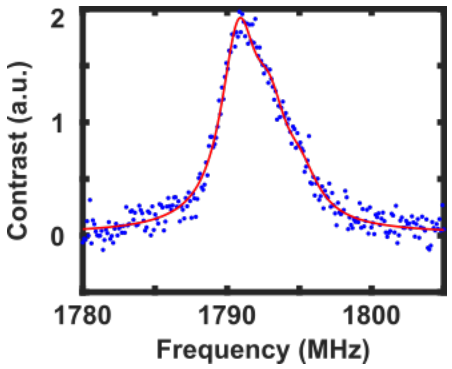

(f) *167 mT*

Figure 2.21: Dynamic hyper-polarization. The spectra acquired for different values of magnetic field show that the nuclear spin of the NV centers is polarized, with an efficiency that depends on the value of the static magnetic field. The magnetic field values are reported in the caption of each sub-figure. They are simply evaluated reversing eq. (2.10).

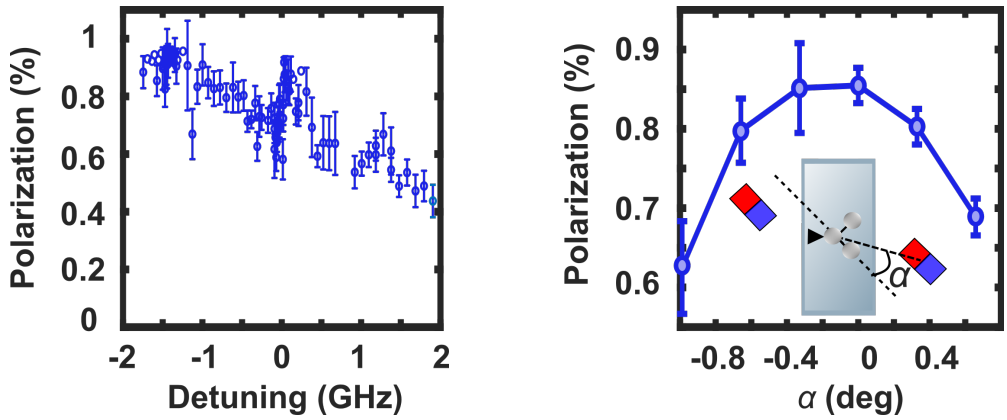

(a) (b)

Figure 2.22: Degree of the nuclear spin polarization for different values of static magnetic field (a) and different angles between the static magnetic field and the NV axis (b). (a) The frequency axis is defined considering the 0 at the GSLAC. (b) The measurement is done at the ESLAC. The angle is changed displacing the two magnets perpendicularly to their magnetization axis in opposite direction. After having arbitrarily fixed the zero, the angle is evaluated as the arctangent of the ratio of the displacement to the distance between the magnet and the diamond. This distance is the magnet-diamond distance necessary to have a magnetic field of 51 mT along the magnet magnetization axis when the two magnets are well-aligned. 51 mT is the amplitude of the static magnetic field at the ESLAC. Therefore the measurements of the angle may be affected by some errors that are difficult to estimate. For this reason, instead of the absolute value, it is interesting to consider the order of magnitude. Thee degree of polarization starts decreasing for angles of misalignment smaller than 1 degree.

a larger FWHM is observed for higher static magnetic field. In order to suppress this source of broadening, it is necessary to implement a different and more stable magnetic architecture (e.g. bigger magnets, electromagnets...).

In this paragraph we demonstrated the opportunity to optically polarize the NV center nuclear spin over a large frequency range using a simple and compact room-temperature system. The DNP of the nuclear spin is interesting for the two NV center applications presented in this manuscript. As it will be described in chapter 3, the frequency resolution of a RF spectrum analyzer based on an ensemble of NV centers is related to the linewidth of the ODMR spectrum. Therefore, nuclear spin polarization is advantageous to increase the frequency resolution of the spectrum analyzer because it suppresses or partially suppresses two of the three hyperfine peaks. Concerning the widefield imaging of the RF field amplitude (chapter 4), the DNP makes the NV center a real two-level system ($|0,+1\rangle, |-1,+1\rangle$). Consequently, the Rabi oscillations protocol is easier to implement.

2.8 Widefield broadband ODMR of an ensemble of NV centers

A comprehensive knowledge of the spin resonance spectrum of an ensemble of NV centers is of relevant importance for the application of NV centers to the RF spectral analysis. For this reason, in this paragraph, we investigate the ODMR spectra of an ensemble of NV centers over a broad frequency range (several GHz).
The experimental set-up is the one described in section 2.1. The static magnetic field is generated by the spherical magnet and aligned with one of the two NV center families laying on the [110] diamond top facet. The other three NV center families are tilted of 71° with respect to the static magnetic field and therefore undergo the same Zeeman shift (section 2.5).

The 2D normalized spectra in the xf plane for three different values of the static magnetic field are reported in figs. 2.23 to 2.25. The magnetic field increases along the x direction. In order to improve the SNR of the measurement the PL signal is integrated along the direction perpendicular to the laser beam. For each 2D spectrum the data are displayed using two different colour scales to bring out the less contrasted resonance lines.

In the three cases, the two most contrasted lines corresponds to the $|0\rangle_{GS} \rightarrow |-1\rangle_{GS}$ and (lower frequency) and the $|0\rangle_{GS} \rightarrow |+1\rangle_{GS}$ (higher frequency) transitions. The difference in contrast between these two resonance lines is caused by the transmission efficiency of the RF chain, which works better at low frequency than at high frequency (section 3.6). According to section 2.5, before the GSLAC (figs. 2.23a and 2.23b), increasing the static magnetic field, the $|0\rangle_{GS} \rightarrow |-1\rangle_{GS}$ resonance frequency decreases while the $|0\rangle_{GS} \rightarrow |+1\rangle_{GS}$ resonance frequency increases. After the GSLAC (figs. 2.25a and 2.25b), increasing the static magnetic field, both the $|0\rangle_{GS} \rightarrow |-1\rangle_{GS}$ and the $|0\rangle_{GS} \rightarrow |+1\rangle_{GS}$ resonance frequencies increase. For a magnetic field of 102mT (Figures 2.24a and 2.24b), the ground state level anticrossing is well visible and easily identifiable by the changing in the slope of the $|0\rangle_{GS} \rightarrow |-1\rangle_{GS}$ resonance line.

The frequency gap between the $|0\rangle_{GS} \rightarrow |+1\rangle_{GS}$ and the $|0\rangle_{GS} \rightarrow |-1\rangle_{GS}$ transitions gives information about the state of the alignment between the static magnetic field and the NV centers axis. In fact, in the case of a perfectly aligned static magnetic field, from eq. (2.10) it results:

$$\Delta f = f_{0\rightarrow+1} + f_{0\rightarrow-1} = 2D = 5.74GHz \qquad if \qquad B < 102mT \tag{2.23}$$

$$\Delta f = f_{0\rightarrow+1} - f_{0\rightarrow-1} = 2D = 5.74GHz \qquad if \qquad B > 102mT \tag{2.24}$$

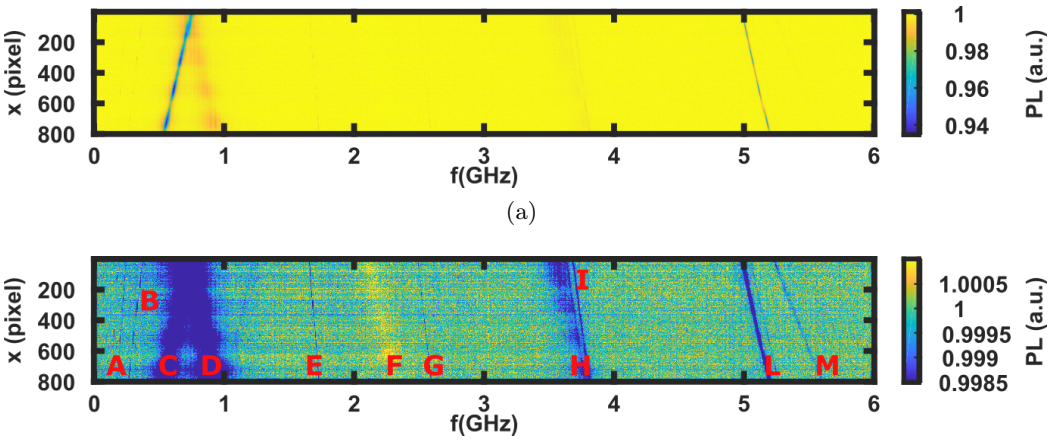

Figure 2.23: Large frequency scan at B≈ 80 mT. (a) and (b) show the same data using a different color scale. For this reason, the resonance lines in (b) seem much broader than the respective resonance lines in (a). (b) A and B correspond to the $|0\rangle_{GS} \rightarrow |-1\rangle_{GS}$ transition excited by the MW generator harmonics. C is the $|0\rangle_{GS} \rightarrow |+1\rangle_{GS}$ transition. E and G correspond to the $|0\rangle_{GS} \rightarrow |-1\rangle_{GS}$ transition excited by the generator harmonics. L is the $|0\rangle_{GS} \rightarrow |+1\rangle_{GS}$. D and H are the $|0\rangle_{ES} \rightarrow |-1\rangle_{ES}$ and $|0\rangle_{ES} \rightarrow |+1\rangle_{ES}$ transitions. I ad M are the transitions associated with the not aligned NV center families. F is the unknown positive contrasted line.

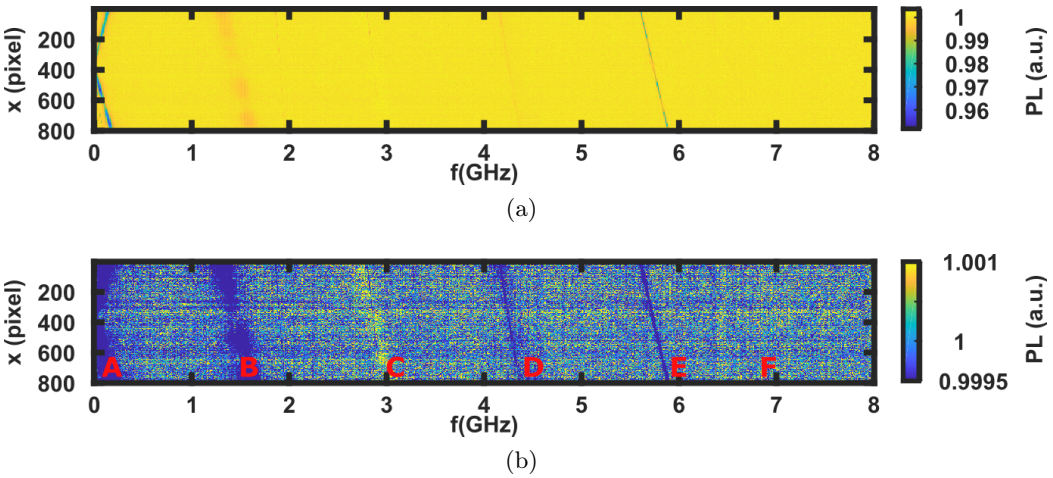

Figure 2.24: Large frequency scan at $B \approx 102$ mT. (a) and (b) show the same data using a different color scale. For this reason the resonance lines in (b) seems much broader than the respective resonance lines in (a). (b) A and E are the $|0\rangle_{GS} \rightarrow |-1\rangle_{GS}$ and $|0\rangle_{GS} \rightarrow |+1\rangle_{GS}$ transitions. B and D are the $|0\rangle_{ES} \rightarrow |-1\rangle_{ES}$ and $|0\rangle_{ES} \rightarrow |+1\rangle_{ES}$ transitions. The thin lines near D and F (really hard to see) are the transitions associated with the not aligned NV center families. C is the unknown positive contrasted line. Near C and around 2 GHz it is possible to observe the $|0\rangle_{GS} \rightarrow |+1\rangle_{GS}$ transition excited by the MW generator harmonics.

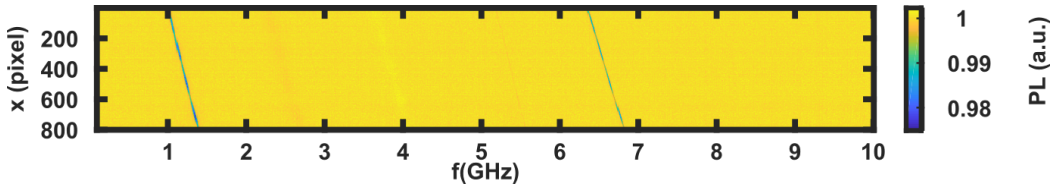

(a)

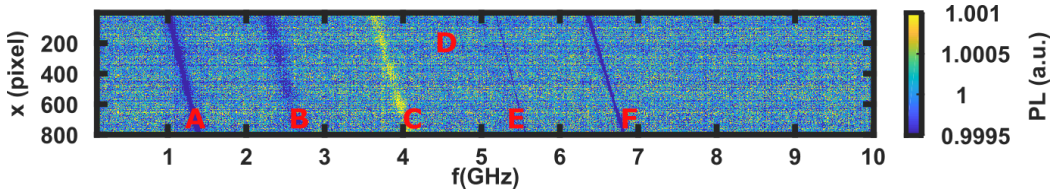

(b)

Figure 2.25: Large frequency scan at B ≈ 140 mT. (a) and (b) show the same data using a different color scale. For this reason, the resonance lines in (b) seem much broader than the respective resonance lines in (a). (b) A and F are the $|0\rangle_{GS} \rightarrow |-1\rangle_{GS}$ and $|0\rangle_{GS} \rightarrow |+1\rangle_{GS}$ transitions. B is the $|0\rangle_{ES} \rightarrow |-1\rangle_{ES}$ transition. D (very difficult to see) and E are the transitions associated with the not-aligned NV center families. C is the unknown positive contrasted line.

Magnetic field (mT)	Frequency gap (GHz)
80	$\Delta f = f_{0\rightarrow+1} + f_{0\rightarrow-1} = 5.74$
102	$\Delta f = f_{0\rightarrow+1} + f_{0\rightarrow-1} = 5.74$
140	$\Delta f = f_{0\rightarrow+1} - f_{0\rightarrow-1} = 5.35$

Table 2.1: Frequency gap between the NV center ground state resonance transitions.

The frequency gaps (Δf) for the three different measurements are reported in Table 2.1 and show that the system is well aligned in the first two cases (B=80 mT and B=102 mT) and a little bit misaligned in the last case (B=140 mT).
The angle of misalignment can be estimated by solving the Hamiltonian of a single NV center interacting with a static magnetic field tilted of ϑ with respect the to NV axis. The Δf at the frequency of the $f_{0\rightarrow-1}$ transition is reported in fig. 2.26. According to this simple simulation, the angle of misalignment is approximately 8°. This method, even if does not permit to reconstruct the spatial direction of the static magnetic field, is a useful tool to have an idea about the status of the alignment. The detailed procedure to measure the 3D vector magnetic field using an ensemble of NV centers is described in [123].
The large resonance lines visible in the xf spectra are the ODMR lines of the NV center excited state. Their resonance frequencies are reported in Table 2.2. They are shifted of approximately 1.45 GHz with respect to the respective spin transitions at the ground state, according to the difference in the zero field splitting term between the ground state and the excited state. Due to the short lifetime of the excited state (≈ 13 ns), the excited state transitions resonance lines are less contrasted than the ground state transitions resonance lines and have a larger FWHM. In figs. 2.24a and 2.25a only one of the two excited state transitions is clearly visible, the $|0\rangle_{ES} \rightarrow |-1\rangle_{ES}$ transition. The low contrast of the resonance peak as well as the frequency dependent performance of the RF chain, make difficult the detection of the $|0\rangle_{ES} \rightarrow |+1\rangle_{ES}$ transition which can nevertheless be guessed carefully looking at the right frequency position.

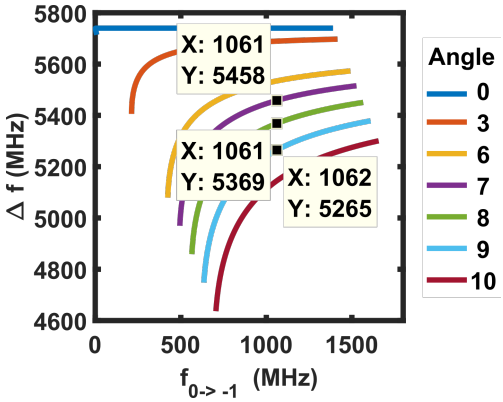

Figure 2.26: Frequency gap between the $f_{0\to-1}$ and the $f_{0\to+1}$ transition for different angles between the NV center axis and the static magnetic field when $f_{0\to-1} \approx 1$ GHz .

Magnetic field (mT)	$f_{0\to+1}(GHz)$	$f_{0\to-1}(GHz)$
80	0.84	3.67
102	4.19	1.35
140	5.23	2.33

Table 2.2: Excited state frequency transition for the well-aligned NV center family. For $B = 80mT$ the frequencies are evaluated at x=400. For $B = 102mT$ and $B = 140mT$ the frequencies are evaluated at x=100.

The several thin resonance lines visible on the xf spectra (for example at 2.6 GHz and 1.8 GHz in fig. 2.23b) do not correspond to any NV center resonance frequency. They are the ODMR lines of NV centers transitions exited by the harmonics of the MW generator at the frequencies reported on the spectra. For example, considering fig. 2.23b, the resonance lines at 2.6 GHz and 1.8 GHz result from the excitation of the $|0\rangle_{GS} \to |+1\rangle_{GS}$ transition at 5.2 GHz by respectively the first and the second harmonics of the MW generator. For this reason, their slope is respectively twice and three times the slope of the main NV center resonance line, and, by the way, this is the signature they are the NV center resonance lines excited by the harmonics of the generator. The effect of the harmonics of the RF generator is visible, on the same figure, for both the ground state and excited state $|0\rangle \to |-1\rangle$ transition, and in fig. 2.24b for the $|0\rangle_{GS} \to |-1\rangle_{GS}$ transition.

Another interesting class of magnetic resonances which is possible to observe on the large scan images are the ground state transitions of the three non-aligned NV center families. They are very little contrasted because of the strong transverse component of the static magnetic field with respect to the NV center axis. The resonance frequencies are reported in Table 2.3. The slope of the resonance lines associated with these transitions differs from the slope of the resonance line associated with the transitions of the well aligned family because under strong transverse field the Zeeman shift is not linear anymore (section 2.5). In the last configuration (fig. 2.25b) it is possible to observe two lines associated with the $|0\rangle_{GS} \to |-1\rangle_{GS}$ transition because, due to the misalignment between the static magnetic field and the main NV center family, the other three NV center families do not undergo the same Zeeman shift.

The last line we want to report is the positive-contrasted line which is possible to observe in the three configurations and whose nature is, at the moment, still unknown. In the next paragraph some additional measurements and their results are discussed in

Magnetic field (mT)	$f_{0\to+1}(GHz)$	$f_{0\to-1}(GHz)$
80	3.75	5.42
102	4.19	6.34
140	$[4.72; 5.23]$	not detectable

Table 2.3: Not-aligned NV center families. For $B = 80mT$ the frequencies are evaluated at x=400. For $B = 102mT$ and $B = 140mT$ the frequencies are evaluated at x=100.

order to acquire some information about this line.

Finally, it is interesting to notice that the widefield imaging mode and the presence of a magnetic field gradient considerably help the detection and the identification of the NV centers resonance lines. In fact, the slope of the resonance lines is a useful tool to recognize the NV center transitions since it enables to visualize the evolution of the energy levels with respect to the magnetic field amplitude and, moreover, it is a hint to distinguish the presence of a resonance from noise. For example, both the identification of the resonance frequencies of the NV center families not aligned with the static magnetic field, and the contribution of the MW generator harmonics to the NV centers excitation, have been realized exploiting the slope of the resonance lines. They would have been probably harder to identify using a confocal system, which does not allow an immediate visualization of the dependence of the NV centers resonance frequencies on the static magnetic field.

2.8.1 A positive-contrasted unknown line

The positive-contrasted line displayed in the previous section has, according to our knowledge, never been reported in the literature. Out first hypothesis to explain this line was a phenomenon of dark resonance [124] between the three ground state levels. In order to verify this hypothesis and better understand the behaviour of this line, several measurements have been conducted and the main experimental observations are here discussed.

- The frequency position of the positive-contrasted line depends on the strength of the static magnetic field, as observed in the previous section. Since its slope in the xf ODRM spectra is the same as the NV center resonance lines slope, we can assume that the gyromagnetic ratio associated with this positive line is similar to the NV center gyromagnetic ratio, which is, in first approximation, the electron gyromagnetic ratio.

- The positive-contrasted line in not homogeneously contrasted (figs. 2.23 to 2.25) and its contrast is higher on diamond regions where striations are present.

- The contrast of the positive-contrasted line depends both on the MW power (fig. 2.27b) and the laser power (fig. 2.27a), suggesting that the line is associated with an optically detectable process of magnetic resonance.

- Misaligning the static magnetic field with respect to the NV center axis, the positive-contrasted line is still visible, while this is not the case for the resonance lines associated with the NV center $|0\rangle_{GS} \to |\pm1\rangle_{GS}$ transitions, as displayed in fig. 2.28. The contrast of the $|0\rangle_{GS} \to |\pm1\rangle_{GS}$ resonance lines are reduced by the magnetic field component perpendicular to the NV center axis, while the contrast of the positive-contrasted line is almost unchanged. Looking at the frequency gap between the $|0\rangle_{GS} \to |\pm1\rangle_{GS}$ transitions, we can roughly estimate that the angle

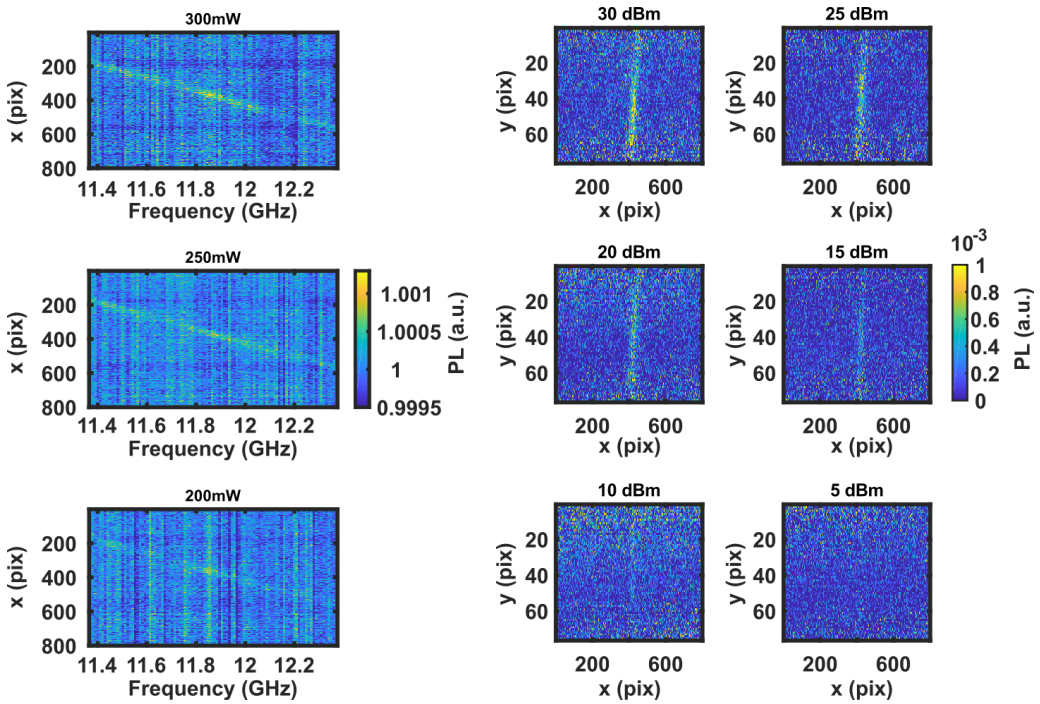

(a) (b)

Figure 2.27: Frequency scan around the positive contrasted line for different laser powers (a) and MW nominal powers (b). Both the laser powers and the MW powers are reported in the title of each subplot.

between the static magnetic field and the NV center axis is of approximately 25°. According to this angle, the frequency position of the positive-contrasted line is equal to $f = \gamma B$, where γ is the gyromagnetic ratio of the NV center and B is the amplitude of the static magnetic field.

- The contrast of the positive-contrasted line is independent of the angle of the polarizer axis.

- No remarkable difference has been observed neither in the PL spectra of the sample nor in the ODMR spectra using a bandpass optical filter which allows the collection of the NV^0 PL.

The measurements presented in this paragraph, and in particular the fact that no difference is observed turning the polarizer axis, suggest that this resonance line is probably not related to the well aligned NV center family, ruling out our hypothesis of dark resonance. Other possible hypotheses may concern diamond defects other than the NV center, which a more sensitive PL spectral analysis could detect, or an effect related to the presence of PL striations or something related to the three not-aligned NV families. At the moment, we do not have an explanation for this positive-contrasted line and further experiments need to be conducted in order to understand its physical nature. Moreover, it is interesting to observe that NV centers based experiments usually do not explore such large frequency range. That can explain why there is no report of this line in the literature.

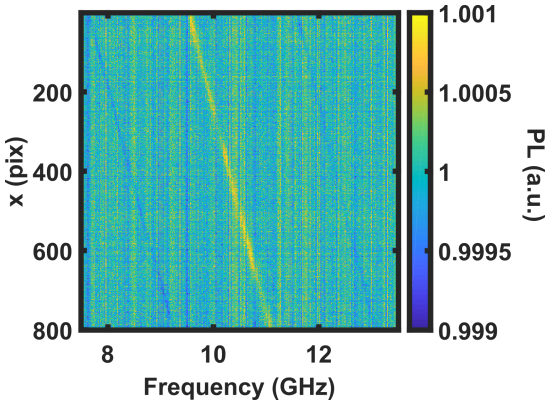

Figure 2.28: Frequency scan in proximity of the positive contrasted line when the static magnetic field is misaligned with respect to the axis of the NV center family which shows the strongest Zeeman shift.

2.9 Conclusion and perspectives

In this chapter, we studied the interaction between an ensemble of NV centers and a static magnetic field from both a theoretical and experimental point of view. We introduced the NV center Hamiltonian and used this formalism to investigate the effects of a static magnetic field on the NV center energy structure. We discussed the energy level anticrossing and the role it plays, together with the hyperfine interaction, in the NV DNP. We described the experimental setup and the acquisition procedure to detect the ODMR of an ensemble of NV centers over a broad frequency range. We obtained three main results.

First, we showed the interest in using a polarizer in the PL imaging system. In particular, we demonstrated the opportunity to identify the NV centers families and their eventual preferential orientation looking at the polarization of the emitted PL. Moreover, we showed the opportunity to increase the ODMR contrast properly orienting the direction of the polarizer axis. This result is of great interest for the two NV center applications proposed in this manuscript since, in both cases, only one of the four possible NV center orientations is exploited. More generally, several NV center applications may benefit of these results to increase the ODMR contrast and thus the magnetic field sensitivity.

Second, we demonstrated the opportunity to optically polarize the NV's nitrogen nuclear spin of an ensemble of NV centers over a large frequency range (more than 4 GHz for each NV center transition) with a high polarization efficiency: better than 80% in proximity of the GSLAC and ESLAC and however better than 50% over the entire frequency range. This result is interesting for the two applications presented in this manuscript because by suppressing the hyperfine structure of the NV center we reduce the ODMR spectral linewidth, which now consists in a single peak, and make easier the spin manipulation of the system, which now behaves as a true two-level system.

Third, we demonstrated the great advantage of working with a widefield imaging system and a magnetic field gradient. In fact, they make possible the visualization of the NV centers energy levels under a static magnetic field and help to identify the several NV center spin resonances that can be detected, with a high spectral resolution, scanning a broad frequency range. In particular, using this technique we managed to detect a positive-contrasted line whose physical origin is, at the moment, still unknown.

This chapter opens up two perspectives. The first concerns the opportunity to improve the ODMR detection using a polarizer not only in the imaging system but also in the excitation one. The second concerns the positive-contrasted line, for which new

experiments are needed to figure out its physical nature.

Chapter 3

Radiofrequency spectrum analyzer based on an ensemble of nitrogen-vacancy centers

The fast development of radiofrequency-based technologies increases the need for compact, low consumption, broadband and real-time RF spectrum analyzers (section 1.3.1). To overcome the electronic bottleneck encountered by electronic solutions, which limits the real-time bandwidth to hundreds of MHz, we propose a new approach that exploits the quantum properties of NV centers in diamond. The general idea behind the RF spectral analysis based on an ensemble of NV centers has been introduced in section 1.3.1 and it is shortly summarized in section 3.1, where the first experimental architecture employed for its proof of principle is also presented. In section 3.2, a new experimental architecture is proposed to investigate the main physical features of NV centers considered as MW detectors. After having discussed the calibration procedure of the system (section 3.3), its key parameters are investigated: frequency range and real-team bandwidth (section 3.4), frequency resolution (section 3.5), dynamic range and power detection threshold (section 3.6), and temporal resolution (section 3.7). Finally, in section 3.8, we propose an architecture based on a heterodyne technique to remove frequency ambiguities from the NV center based RF spectral analysis and extend the frequency range of the system.

3.1 The proof of principle

3.1.1 The general idea

The working principle of a RF spectrum analyzer based on an ensemble of NV centers relies on the spatial encoding of the NV centers resonance frequencies by means of a controlled magnetic field gradient (section 1.3.1).
The schematic of the principle is reported in fig. 3.1. The NV centers are continuously pumped by a green laser and their PL is continuously detected by a widefield imaging system. A controlled static magnetic field gradient induces a different Zeeman shift on NV centers located in different positions of the diamond (fig. 3.1b). In this way, it is established a correspondence between the spatial position of the NV centers and the RF frequencies at which they resonate. The RF signal to be detected is sent close to the diamond by means of RF chain. Exploiting the spatial encoding of the RF frequencies, the spectral components of the signal are retrieved by looking at the diamond areas where a drop of PL is detected.

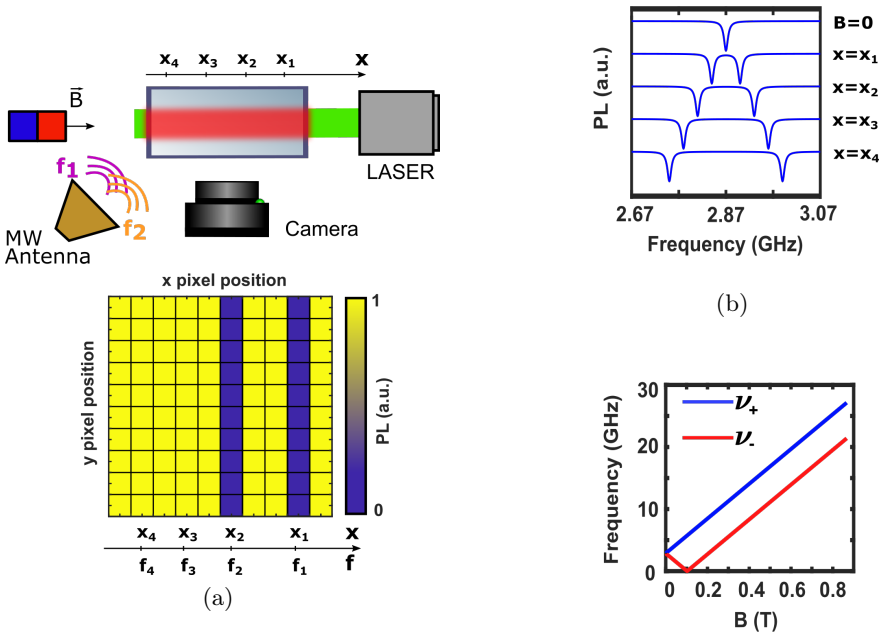

Figure 3.1: Working principle of a spectrum analyzer based on an ensemble of NV centers. (a) Scheme of principle. A green laser continuously pumps the diamond which contains an ensemble of NV centers. The PL emitted by the NV centers is continuously collected by a camera. A magnetic field source induces a static magnetic field which spatially encodes the NV center resonance frequencies. The signal to be detected is sent in proximity of the NV centers by means of a RF antenna. The PL collected by the camera is, in absence of any RF field, uniformly distributed on the image. If RF components of the signal are on resonance with some NV centers embedded in the diamond, a drop of PL is detected on the image. By observing the pixel positions where a drop of PL is detected, the spectrum of the RF field is retrieved. (b) The magnetic field gradient induces a spatial dependent Zeeman shift of the NV center resonance frequencies. (c) Frequencies shift due to the Zeeman interaction between the NV center and the static magnetic field.

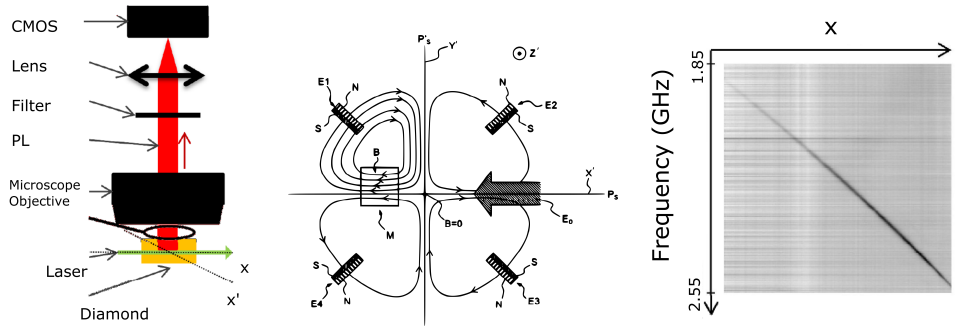

(a) *Experimental Set-Up* (b) *Four magnets architecture* (c) *Spatial encoding of the RF frequencies*

Figure 3.2: Proof of principle of RF spectral analysis using an ensemble of NV centers. (a) Experimental architecture employed for the proof of principle [12]. A green laser is focused into the diamond through a 110 facet. The beam propagation axis is the x axis. The PL is collected by means of an imaging system from the diamond 100 face. The imaging system is composed of a microscope objective, a filter to suppress the laser diffracted light and the NV^0 PL, and a CMOS camera. The static magnetic field is aligned along one of the NV centers families (x' axis), that is 35° tilted with respect to the x axis. The RF signal is brought in proximity of the NV centers by means of a loop wire employed as antenna. (b) Four-magnet architecture to generate a magnetic field gradient along the x' axis. The small square on the left of the image is the diamond. (c) ODMR of an ensemble of NV centers in the x-f plane. The RF frequencies are spatially encoded in the diamond by means of a magnetic field gradient along the x axis. The colour scale represents the normalized PL level.

3.1.2 The four magnets architecture

The proof of principle of RF spectral analysis based on an ensemble of NV centers was provided by Chipaux et al. [12] using the experimental architecture shown in fig. 3.2 and it is the object of a patent [125]. The diamond employed was the same described in section 2.1.1, a CVD, optical grade diamond plate with two [100] main faces and four [110] facets. The NV center concentration is of some ppb and it results a good compromise between the sensitivity of the device, which scales with the square root of the number of NV centers [123], and its spectral resolution, which depends on the NV center intrinsics linewidth and is usually better at low NV center concentrations (section 1.2). The laser beam is focused on the diamond through one of the four [110] facets and the PL is collected from a [100] face by means of a CMOS camera. The four NV centers families are thus tilted of 35° with respect to the focal plane (section 2.1.1), which is the [100] face from which the PL is collected. In this experimental architecture, the static magnetic field gradient is generated by four rectangular neodymium magnets ($6 \times 5 \times 2$) mm^3 placed at the corners of a square of side 8 mm (fig. 3.2b). This geometry, inspired by the cold atom magneto-optical traps, generates a homogeneous static magnetic field gradient along the square's medians , x' and y' axis in fig. 3.2. The static magnetic field is aligned with one of the four NV centers families tilting the magnets in order to have an angle of 35° between the x' axis and the laser beam propagation axis (x axis in fig. 3.2a).
The spatial encoding of the RF frequencies along the x axis is reported on fig. 3.2c. Using this four-magnet experimental architecture, the RF spectral analysis based on an ensemble of NV centers has been demonstrated over a bandwidth of 700 MHz at a central frequency of 2.2 GHz.

One of the main purposes of this thesis is to increase the RF frequency range of the spectral analysis based on an ensemble of NV centers. That can be achieved by increasing the static magnetic field seen by the NV centers in order to increase their resonance frequencies (fig. 3.1c). Using the four-magnet experimental architecture described before (fig. 3.2b), the magnetic field can be increased by approaching the magnets to the diamond while preserving the overall symmetry of the system. This procedure, however, is experimentally hard to realize because four magnets need to be displaced, with high accuracy (to preserve the alignment), in a plane tilted of 35° with respect to the optical table. In addition, since the strongest magnetic field generated by this magnetic architecture is close to the surface of the magnets, the physical size of the diamond limits, at a certain point, the possibility of approaching the magnets to the sensing diamond area, thus limiting the maximum static magnetic field applicable to the NV centers.

In order to overcome these experimental difficulties and investigate the behaviour of an ensemble of NV centers under strong static magnetic fields, in this manuscript a new experimental single-magnet architecture is proposed for the spectral analysis of RF signals based on an ensemble of NV centers.
The feasibility of the NV CW-ODMR under strong static magnetic fields has been investigated and demonstrated by [126, 127] using a confocal system and a homogeneous static magnetic field of some Tesla. In this manuscript, the ensemble of NV centers is instead investigated under strong static magnetic fields and magnetic field gradients using a widefield imaging system.

3.2 Single-magnet architecture

The single-magnet experimental architecture has already been described in section 2.1. In this paragraph, we want to emphasizes the advantages of having a single magnet architecture and the experimental procedure to align the static magnetic field to one of the NV center families.

Compared to the four-magnet architecture, the single-magnet architecture is easier to handle and more compact. The main drawback is the impossibility of controlling, simultaneously, the amplitude and the gradient of the static magnetic field, which are strictly related (section 2.1.3). The static magnetic field generated by a single magnet depends on the magnet features: material (neodymium in our case), shape and size. As an example, the mathematical expressions of the magnetic field generated by a spherical and a cylindrical magnet along their magnetization axis are reported:

$$B_{Sphere} = \frac{2}{3} B_R \frac{R^3}{(R+d)^3} \tag{3.1}$$

$$B_{Cylinder} = \frac{B_R}{2} \left(\frac{H+d}{\sqrt{R^2+(H+d)^2}} - \frac{d}{\sqrt{R^2+d^2}} \right) \tag{3.2}$$

where B_R is the remanent magnetization (1.3 T for neodymium), R is the radius of the sphere and of the cylinder, H is the height of the cylinder and d the distance from the magnet surface along the magnet magnetization axis.

The magnetic field along the magnetization axis of magnets having different shapes and sizes are plotted in fig. 3.3. Independently of the radius of the sphere, the static magnetic field at the surface ($d = 0$) of spherical magnets is equal to $\frac{2}{3}B_R$ and it is stronger than the one generated at the surface of cylindrical magnets $\frac{B_R}{2}\left(\frac{H}{\sqrt{R^2+H^2}}\right)$. Therefore, a spherical magnet is preferred in our experimental architecture in order to achieve a stronger static magnetic field. It must be noticed that the static magnetic

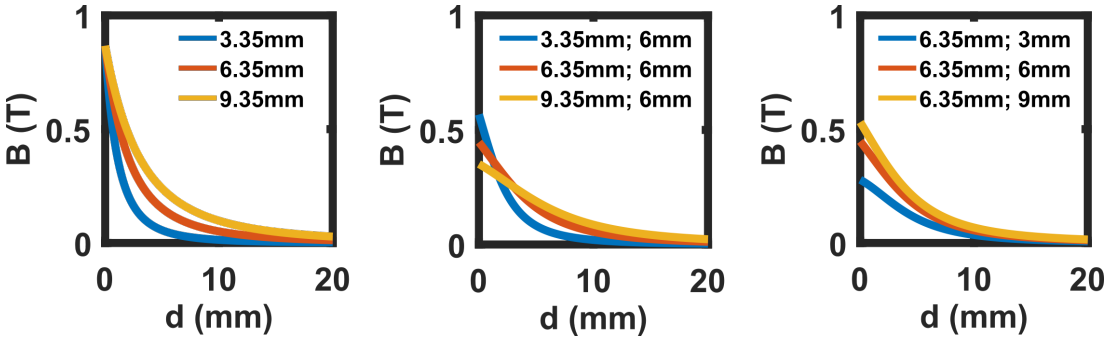

Figure 3.3: Static magnetic field generated by magnets of different shape and size. Left: magnetic field profile along the magnet magnetization axis for three different spherical magnets whose radii are reported in the legend of the figure. Center and right: magnetic field profile along the magnet magnetization axis of different cylindrical magnets whose radii and heights are reported, in this order and separated by a semicolon, in the legend of the figures.

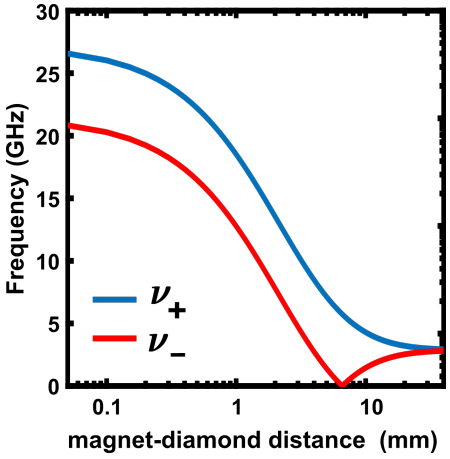

Figure 3.4: Zeeman shift of the NV center resonance frequencies ($|0\rangle \rightarrow |-1\rangle$ in red, $|0\rangle \rightarrow |+1\rangle$ in blue) at different distances from the surface of a spherical magnet of radius 6.35 mm. The distance is evaluated along the magnet magnetization axis. The resonance frequencies are calculated considering the Zeeman shift (eq. (1.5)) induced by the static magnetic field generated by the spherical magnet (eq. (3.1)).

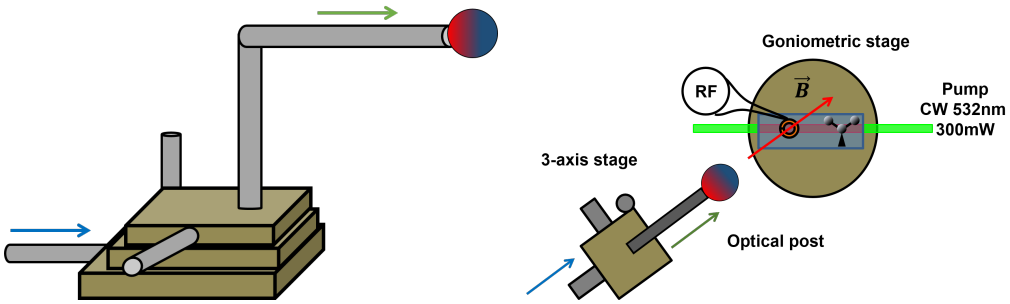

(a) (b)

Figure 3.5: Magnetic architecture. (a) The magnet is glued on an L-shaped optical post assembly which is then fixed on a three-axis translation stage. (b) The diamond is placed on a goniometric stage. The diamond top facet is a [110] facet. The NV centers orientations with respect to this facet, the laser beam and the RF antenna are also reported. The three coloured arrows represent the translation axis of the stage (blue arrow), the magnet magnetization axis, which is the optical post axis (green arrow), and the NV centers axis (red arrow).

field generated by a spherical magnet is less homogeneous than the one generated by a cylindrical magnet (section 2.1.3). However, this is not a limitation if a sphere of sufficiently large radius is chosen. In our particular case, we chose a spherical magnet of radius 6.35 mm, which is one order of magnitude larger than the diamond sensing area. The ground state NV center resonance frequencies at different distances from the surface of the magnet are plotted in (fig. 3.4). Tuning the diamond-magnet distance, it is possible to shift the NV center resonance frequencies up to 27 GHz.
To preserve a good ODMR contrast and avoid the quenching of the NV PL (section 2.5), the magnetic field needs to be aligned with the NV center axis. In addition, the alignment needs to be preserved while the magnet is moved close to or further away from the diamond to tune the NV center resonance frequencies.

3.2.1 Alignment procedure

The alignment procedure is realized with the help of a three-axis translation stage which is used to fine control the spatial position of the magnet. A schematic of the experimental setup is reported in fig. 3.5. The magnet is glued on an L-shaped optical post assembly which is then fixed on a three-axis translation stage. The optical post (green arrow in fig. 3.5) is aligned by eye to one axis of the translation stage (blue arrow) and this one is then coarsely aligned, always by eye considering geometric arguments, to one NV center family (red arrow). After this preliminary alignment, a finer alignment is performed in three steps:

- at low static magnetic field
- at the ESLAC
- at the GSLAC

At low static magnetic field, the transverse component of the static magnetic field is negligible with respect to the NV center ground state zero field splitting ($D = 2.87$ GHz) and therefore, independently of their orientation, the four NV center families show a good contrast (section 2.3). When the static magnetic field is well aligned with one NV center family, the other threes are equivalently oriented with respect to it and hence undergo the same Zeeman shift. Therefore the alignment procedure at low field consists

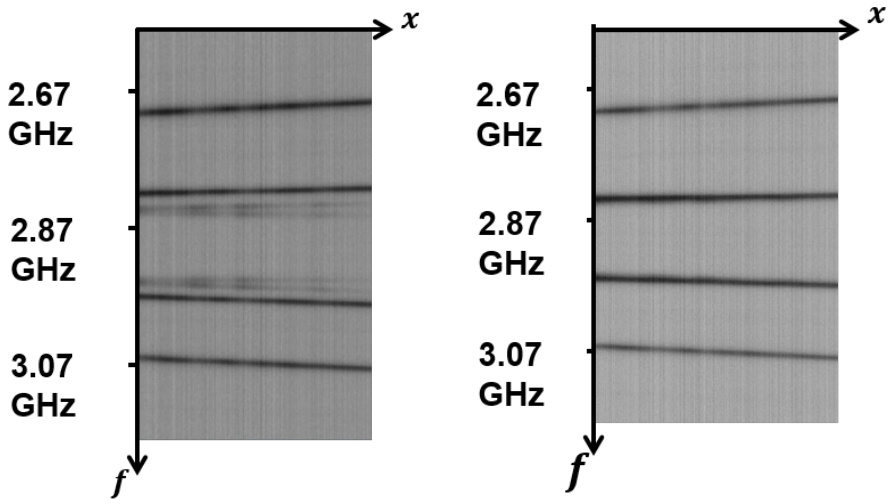

(a) *Mis-aligned static magnetic field* (b) *Aligned static magnetic field*

Figure 3.6: Far field alignment procedure. (a) The static magnetic field is not completely aligned with respect to one NV center family. The four NV families undergo a different Zeeman shift and eight ODMR lines, two for each NV centers family, are visible in the x-f plane (section 2.3). (b) The static magnetic field is aligned to one NV centers family. The three not-aligned families undergo the same Zeeman shift and therefore only four ODMR lines are visible in the x-f plane, two for the aligned family and two for the three not-aligned families. The ODMR lines associated with the well-aligned family are those which undergo the stronger Zeeman shift.

in changing the magnet position until the CW-ODMR lines of the three non-aligned families are superposed (fig. 3.6).
Increasing the static magnetic field, this alignment procedure is not efficient because the three not-aligned families are difficult to detect (section 2.8) due to the decrease of the contrast induced by the transverse component of the static magnetic field.

The alignment procedure at the level anticrossing is based on the contrast decrease induced by the spin state mixing both at the ground state (GSLAC) and the excited state (ESLAC) (section 2.5). Hence, the magnet is displaced until the contrast of the ODMR line is maximized (fig. 3.7). At the GSLAC a second criteria to improve the alignment consists in minimizing the energy gap in correspondence of the level anti-crossing (fig. 3.7d) (section 2.5).

It is important to observe that, after having performed the alignment procedure at low static magnetic field, a new fine alignment is required in proximity of the ESLAC. The same happens at the GSLAC after having performed the alignment procedure at the ESLAC. That means that the alignment between the NV centers and the static magnetic field is slightly lost during the translation of the magnet. This is understandable looking at the experimental setup in fig. 3.5. During the alignment procedure, the magnetic field is aligned with respect to the NV center axis. However, since the magnetic field generated by a spherical magnet in proximity of the pole has, in first approximation, a radial distribution, it is possible that the NV center is well aligned with the static magnetic field but not with the magnet magnetization axis. Moreover, the magnet is translated along the translation stage axis that may not exactly be parallel to the optical post and therefore to the magnet magnetization axis. These sources of misalignment cause, during magnet translation, a small loss of alignment that is most noticeable near the level anti-crossing, where the system is more sensitive to it section 2.7. For

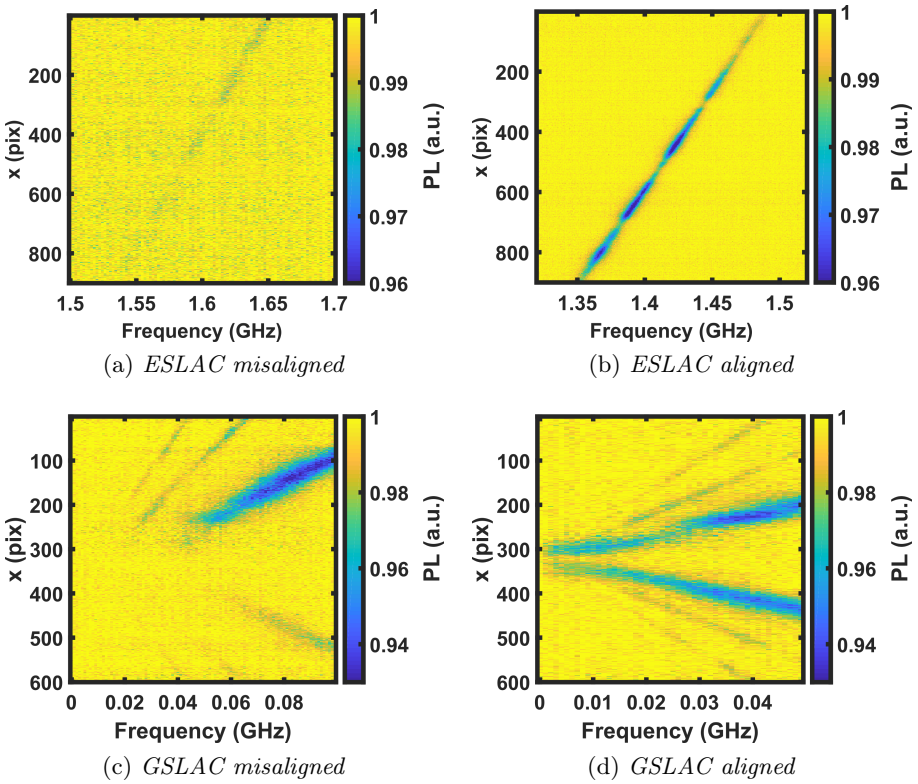

(a) *ESLAC misaligned* (b) *ESLAC aligned*

(c) *GSLAC misaligned* (d) *GSLAC aligned*

Figure 3.7: Alignment procedure at the level anti-crossing. (a-b) ODMR spectrum of the ground state $|0\rangle \rightarrow |-1\rangle$ transition in proximity of the ESLAC in case of misaligned (a) and aligned (b) static magnetic field. At the ESLAC the gorund state $|0\rangle \rightarrow |-1\rangle$ transition is resonant at 1.45 GHz. In case of a misaligned magnetic field, the loss of contrast makes impossible the detection of the $|0\rangle \rightarrow |-1\rangle$ transition also for resonance frequencies hundreds of MHz lower or higher than 1.45 GHz. Since at the ESLAC the system is extremely sensitive to magnetic field alignment (section 2.7), in (b) the resonance line is very well visible at 1.42 GHz but not at 1.5 GHz. This happens because the static magnetic field is better aligned with the NV centers at the bottom of the image ($x = 900$) than with those at the top. (c-d) ODMR spectra of the ground state $|0\rangle \rightarrow |-1\rangle$ transition in proximity of the GSLAC respectively when the magnet is misaligned (c) and well aligned (d) with the NV centers axis. The misalignment causes a reduction in contrast and an increase in the energy gap at the level anti-crossing, which is 50 MHz in (c) and less than 5 MHz in (d). The additional ODMR lines are due to the harmonics of the RF generator (section 2.8).

those reasons, all three alignment procedures are usually required while the magnet is translated toward the diamond. Further increasing the static magnetic field, namely for magnetic field stronger than the one required for the GSLAC, the system becomes less sensitive to small angles of misalignment. In this case, according to our experience, improving the alignment does not result in a real improvement of the contrast (this is true for small angles of misalignment, of the order of some degrees). Anyway, using the procedure described in section 2.8, that is checking that the frequency gap between the $|0\rangle \rightarrow |-1\rangle$ and the $|0\rangle \rightarrow |+1\rangle$ resonance frequencies is twice the zero field splitting (eqs. (2.23) and (2.24)), it is always possible to control the status of the alignment and eventually refine it.

Once the alignment procedure has been done, the magnet-diamond distance can be tuned in order to tune the resonance frequency of the NV centers and explore their behaviour under different regimes of static magnetic field (paragraph 3.4) and static magnetic field gradient (paragraph 3.5). However, before investigating the feasibility and the performance of the RF spectral analysis over a large frequencies range, we want to detail the calibration procedure necessary to spatially encode the NV centers resonance frequencies.

3.3 The calibration procedure

For a given magnet-diamond distance, the calibration procedure consists in associating each pixel to the resonance frequency of the NV centers it images. As already described in section 2.3, looking at the ODMR spectra in the x-f plane[1], for a given value of $y = y_0$, the frequency information is spatially coded by means of magnetic field gradient component along x (fig. 3.8a). Therefore it is possible to create a one-to-one calibration map that associates each frequency to a single pixel (x, y_0).
However, instead of considering a single row of pixels (single value of y), we can take advantage of the widefield imaging mode and sum over all the pixels that resonate at the same frequency, namely summing over the iso-B of the static magnetic field (fig. 3.8b). In this way, we create a one-to-one calibration map that associates each frequency to a set of pixels, increasing the SNR of the measurement (section 2.1.5)

From an experimental point of view, the calibration procedure consists in defining, for each frequency, a mask. The mask is a matrix that has the same dimension as the image captured by the camera. It is zero everywhere except on the pixels which resonate at the frequency associated with the mask; for those pixels, the mask has a value equal to one. The easiest way to define which pixels resonate at a given frequency would consist in defining a contrast threshold, so that, at a given frequency, all pixels whose contrast is above the threshold are defined as resonant at that frequency. However, this method is not applicable because of the inhomogeneous distribution of the NV centers families in our sample (section 2.3), which makes the contrast dependent on the diamond area which is considered. Therefore the mask is defined in a different way.
Looking at fig. 3.8b, the ODMR line in the x-y plane is, in first approximation, a straight line. In order to obtain the mathematical expression of this line, at least two pixel positions are necessary. The y position of these pixels is arbitrarily chosen and for those chosen values of y, the PL along the x axis is fitted by a Gaussian curve to find the position for which the contrast is maximum (fig. 3.8c). Finally, the ODMR line equation is found by a linear fit of the position of the pixels. The mask is then defined by setting the value of pixels laying on the linear fit equal to one (fig. 3.8d). In the mask, the linewidth along the x direction is chosen of the same order of the FWHM

[1]The reference frame is the laboratory reference frame where z is the optical axis and x is the laser beam propagation axis.

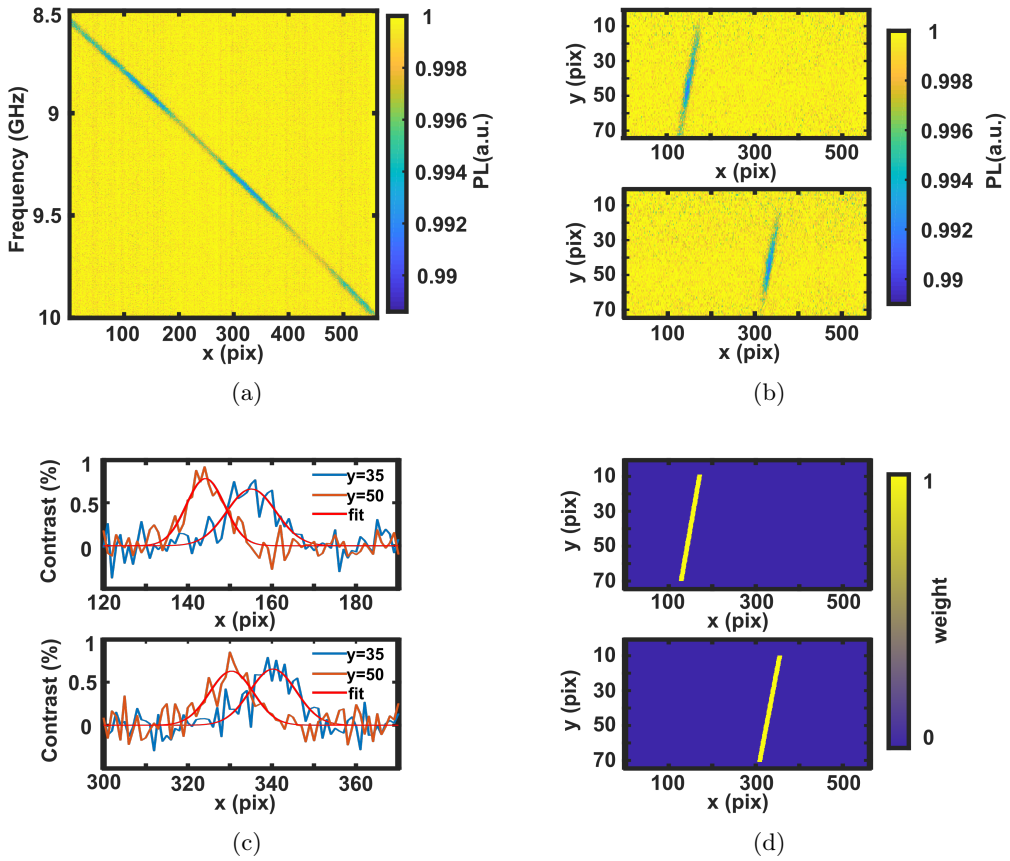

Figure 3.8: Calibration procedure. (a) Ground state $|0\rangle \rightarrow |-1\rangle$ ODMR spectrum . (b) ODMR of an ensemble of NV center at f = 9 GHz (top) and f = 9.5 GHz (bottom). (c) Contrast evolution along the x axis for two different y positions: at f=9 GHz (top) and f=9.5 GHz (down). (d) Masks at f =9 GHz (top) and f=9.5 GHz (down).

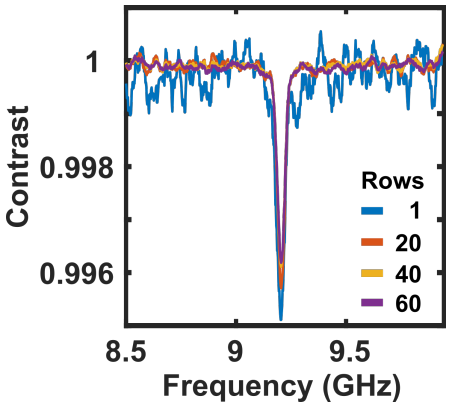

Figure 3.9: Spectrum of a monochromatic RF signal acquired considering a different numbers of rows to realize the mask.

of the previous Gaussian fit (fig. 3.8c). Along the y direction, the pixels are chosen according to the size of the beam waist. This procedure could be repeated for each frequency in the frequency range detectable on the AOI or, in an easier way, assuming that the slope of the ODMR line in the x-y plane changes slowly tuning the frequency, the procedure is repeated only for some frequency values in the frequency range and then an interpolation method is used to define the masks for all the other frequencies.

Once the masks have been defined, the spectrum of an unknown RF signal is given by:

$$S(\nu) = \sum_{(x,y)} D(x,y) M_\nu(x,y) \tag{3.3}$$

where M_ν is the mask associated with the frequency ν and D is the image acquired by the camera when the unknown signal is sent on the diamond.

In order to show the SNR improvement after the calibration procedure and the advantages in summing over several pixels, the comparison between the spectra acquired considering only one row of pixel ($y = 45$) and several rows is reported in fig. 3.9. The contrast is higher for a single-row spectrum because it has been considered the row where the contrast is maximum. On the contrary, summing over several rows, the final contrast is the mean value of the contrast over the different rows. The SNR is evaluated for four different configurations and is equal to 14 for a single row, 51 for 20 rows, 65 for 40 rows, and 60 for 60 rows. As expected from section 2.1.5, due to the different pumping conditions, the SNR does not scale linearly with the square root of the number of pixels. However, the sum over several pixels still remains a valid technique to increase the SNR of the measurement. A more refined masking procedure would consist in weighting pixels proportionally to their contrast, and therefore instead of considering a mask made of zeros and ones, define a more complex mask which accounts for differences in the laser pumping parameter, in the spatial distribution of the NV centers preferential orientation, etc.

Once the calibration is done, the system can work as a spectrum analyzer. The only signal processing needed to retrieve the spectral components of an unknown RF signal is a sum over several pixels (eq. (3.3)), which is fast and frequency-independent. In the following paragraphs, the performance of our experimental architecture is discussed with respect to the main parameters of interest for the spectral analysis of RF signals: frequency range, bandwidth, frequency resolution, dynamic range and time resolution.

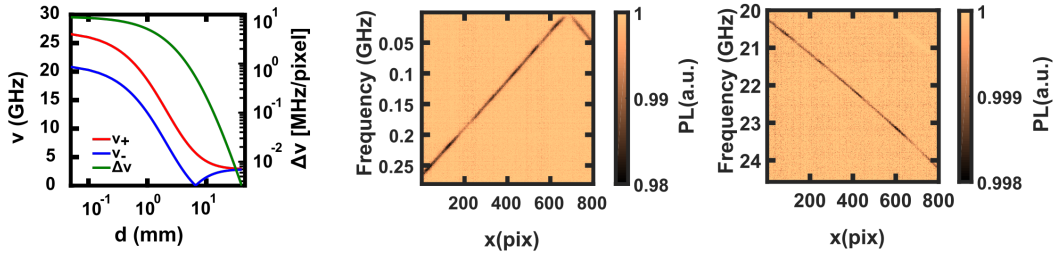

(a) (b) (c)

Figure 3.10: Frequency range and frequency bandwidth. (a) NV center resonance frequencies and frequency gradient per pixel for different magnet-diamond distance. (b) Lower limit of the frequency range. (c) Upper limit of the frequency range.

3.4 Frequency range and real-time bandwidth

Our system works as a tunable microwave frequency detector in a typical range from 10 MHz to 25 GHz (fig. 3.10). The tuning of the frequencies range is simply achieved by changing the magnet-diamond distance.

The lower part of the spectrum is covered when the resonance frequency of the $|0\rangle \rightarrow |-1\rangle$ ground state transition becomes very small, that is near the GSLAC (fig. 3.10b). Therefore, the minimum detectable frequency corresponds to the frequency gap between the $|0\rangle$ and the $|-1\rangle$, which, for a well-aligned system, is of the order of 10 MHz.

The upper limit is related to the maximum strength of the static magnetic field we are able to achieve using our magnet and therefore to the highest resonance frequency of the $|0\rangle \rightarrow |+1\rangle$ transition we are able to detect. According to fig. 3.10a, the maximum detectable frequency is approximately 27 GHz. This frequency is the resonance frequency of the $|0\rangle \rightarrow |+1\rangle$ transition when the magnet and the diamond are at contact. In order to detect the CW-ODMR of the NV centers close to the magnet surface, the RF antenna is displaced from its usual position (fig. 3.11a) and the NV centers are excited by the RF field generated outside the current loop (fig. 3.11b). The ODMR spectra of the NV centers imaged between the antenna and the magnet are reported in fig. 3.11c. The measurement demonstrates that the NV centers electron spin resonance can be detected up to 27 GHz using a single, room-temperature neodymium magnet. The experimental configuration in fig. 3.11b is disadvantageous for sensing because the amplitude of the RF field fast decreases outside the antenna (section 2.1.2). For this reason, the upper limit of the RF spectral analysis is approximately 25 GHz, which is the highest frequency that it is possible to detect considering the AOI inside the loop antenna (figs. 3.10c and 3.11a).

Concerning the frequency range, it is important to emphasize that while the lower limit is a physical limit, the upper limit is a technical limit and it could be extended by means of stronger magnetic fields, for example using cryogenic magnets.

Comparing fig. 3.10b and fig. 3.10c, for the same AOI, we have approximately 300 MHz of total bandwidth for a central frequency of 150 MHz and approximately 4 GHz of bandwidth for a central frequency of 22 GHz. This is because while the central frequency depends on the amplitude of the static magnetic field, the bandwidth depends on the magnetic field gradient. Since in a single-magnet configuration these two parameters are related (fig. 3.10a), the bandwidth depends on the central frequency.

At this point, it is important to make a comment about the magnetic field gradient per pixel. The magnetic field B is oriented along the NV center axis, which forms an

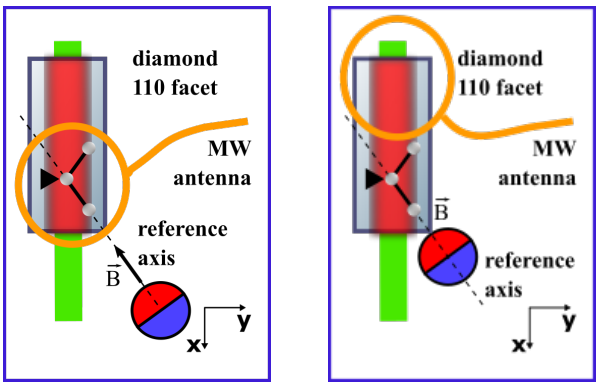

(a) (b)

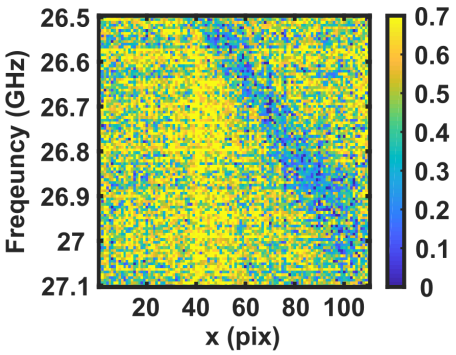

(c)

Figure 3.11: Maximum frequency detectable using our neodymium magnet. (a) Experimental configuration to perform the spectral analysis. The diamond area useful for sensing is the one inside the loop antenna. (b) Experimental setup to measure the strongest Zeeman shift possible with our neodymium magnet. The antenna is shifted so that we can put the magnet in contact with the diamond and collect the PL emitted by the NV centers closest to the magnet. (c) ODMR in the xf plane using the experimental configuration in (b).

angle of approximately 35° with the diamond {110} axis and 55° with the diamond {100} axis, which are respectively the x and y axis of the laboratory frame (fig. 3.11a). Given the small size of the AOI ($\approx$ 500 µm) with respect to the magnet, in first approximation it can be assumed that the static magnetic field is oriented along the NV center axis all along the AOI. Under this approximation, using eq. (3.1), it is possible to evaluate the static magnetic field gradient per pixel along the NV center axis and therefore its components along the x and y axis of the laboratory frame.

The magnetic field gradient per pixel (∇B) along the magnet magnetization axis is plotted in fig. 3.10a. The bandwidth $\Delta\nu$ for a given central frequency (f_c) can be estimated as:

$$\Delta\nu(f_c) = \gamma \nabla B(f_c) \cdot \cos(35) \cdot N_p \tag{3.4}$$

where N_p is the AOI length, in pixel unit, along the x direction. Considering the central frequencies and the AOI in fig. 3.10, we found $\Delta\nu(150\ MHz) = 307\ MHz$ and $\Delta\nu(22\ GHz) = 3.6\ GHz$, in good agreement with the experimental results.
In order to increase the bandwidth, both the AOI and the magnetic field gradient per pixel can be increased.

3.5 Frequency Resolution

The frequency resolution of our system is related to the ODMR linewidth of the NV centers ensemble. It depends on four main contributions:

- NV center intrinsic linewidth
- Optical and RF power broadening
- Magnetic field gradient
- Magnetic field amplitude fluctuations

In our optical grade diamond sample, the intrinsic linewidth is attributed to the decoherence induced by the interaction between the NV centers and the ^{13}C nuclear spins bath [128], and it is of the order of 500 kHz. That is the physical limit of the frequency resolution of the system and can be improved working with ultra-pure diamond samples (section 1.2.4).

The optical and RF power broadening are well described by the NV center model presented in section 1.2.5. According to eq. (1.35), the FWHM of the NV centers ODMR spectrum is given by:

$$\Delta\nu = \Gamma_c^\infty \sqrt{\left(\frac{s}{s+1}\right)^2 + \frac{\Omega_R^2}{\Gamma_p^\infty \Gamma_c^\infty}} \tag{3.5}$$

where $s = P_{laser}/P_{sat}$ accounts for the optical pumping process, the Rabi frequency Ω_R accounts for the power of the RF field which drives the spin transition, and Γ_p^∞ and Γ_p^∞ are the spin decoherence rates induced by the optical pumping at saturation. The optical pumping induces a power broadening of the ODMR line because of the relaxation of the spin coherence during the optical cycle. Therefore the higher is the pumping rate, the faster is the spin coherence relaxation and the broader is the ODMR line. (fig. 3.12).
The power broadening induced by the driving field (the RF field in our case) is a well-known phenomenon of any two-level system (section 1.2.3). This is well depicted in fig. 3.13a, where the ODMR spectrum for different RF powers is plotted. At low RF power the three peaks of the NV center hyperfine structure are well distinguishable, unlike at high power. In fact, increasing the RF power, the FWHM of each resonance

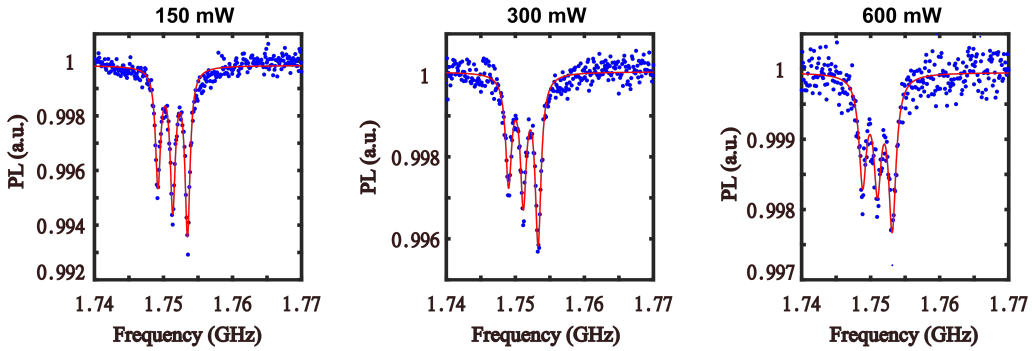

(a) (b) (c)

Figure 3.12: Optical power broadening. Comparison of spectra acquired under different laser powers, reported as the title of each plot. The RF power is set to a nominal value of -5 dBm in order to suppress the RF power broadening. From (a) to (c) the FWHM and the contrast are respectively: FWHM = (0.90 ± 0.04 MHz, 1.04 ± 0.05 MHz and 1.3 ± 0.1 MHz); contrast=(0.60 ± 0.03, 0.4 ± 0.02, 0.21 ± 0.02)

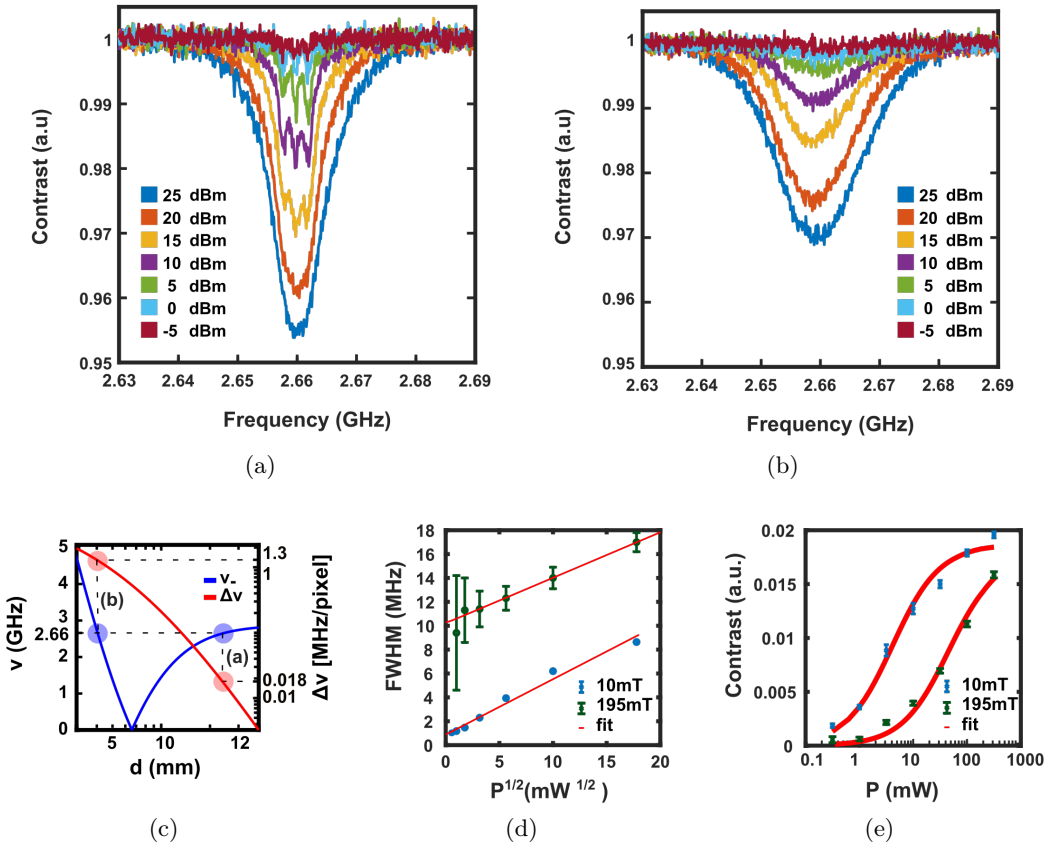

(a) (b) (c) (d) (e)

Figure 3.13: Comparison of the ODMR spectra in the range [2.63 GHz, 2.69 GHz] for different magnetic fields and magnetic field gradients (10 mT and 20 KHz/μm (a) – 195 mT and 1.5 MHz/μm (b)) . The different colours correspond to different nominal powers of the MW generator. The curves are fitted by the sum of three identical Lorentzians shifted by 2.14 MHz. The contrast and the linewidth obtained from the fit are reported in $(c-d)$. In (c) the fit is realized using a fit function of the form of eq. (3.5); in (d) the fit is realized using a fit function of the form of eq. (3.11) for (d).

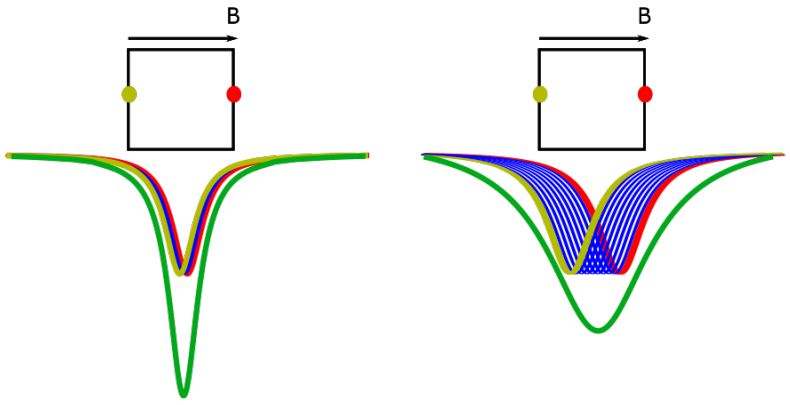

(a) (b)

Figure 3.14: Schematic of the effect of the magentic field gradient per pixel in the case of (a) small magnetic field gradient and (b) strong magnetic field gradient. Assuming the black square to be a pixel, in red and gold are reported the ODMR spectra of the NV centers located at two opposite sides of the pixel. In blue are represented the ODMR spectra of the NV centers located inside the pixel. In green is reported the ODMR spectrum associated with the pixel, that is the sum of the ODMR spectra of all the NV centers imaged by the pixel.

line increases until the hyperfine structure is completely lost. The RF power broadening effect is visible in fig. 3.13b as well.
Both fig. 3.13a and fig. 3.13b show the ODMR spectra of an ensemble of NV centers resonant at 2.66 GHz. In the first case, the magnetic field applied to NV centers is equal to 10 mT; in the second case, it is 195 mT (fig. 3.13c). Comparing figs. 3.13a and 3.13b we can observe that in the second case the hyperfine structure of the NV center is not resolved, not even at low RF power, and the ODMR spectrum is broader and less contrasted with respect to the ODMR spectrum obtained at the same power but under a lower static magnetic field (fig. 3.13d and fig. 3.13e). These differences are caused by the different magnetic field gradients present in the two configurations: in the first case 20 kHz/μm and in the second case 1.5 MHz/μm.
The magnetic field gradient at the pixel scale induces NV centers imaged by the same pixel to undergo a different Zeeman shift and therefore to be resonant at different frequencies for the same transition (Figure 3.14). If the resonance frequency distribution at the pixel scale is small compared to the intrinsic linewidth of the NV center (fig. 3.13a), the effect of the magnetic field gradient is negligible and all the NV centers imaged by the same pixel are approximately resonant at the same central frequency (fig. 3.14a). On the contrary, if the resonance frequency distribution is comparable or larger than the NV center intrinsic linewidth (fig. 3.13a), NV centers imaged by the same pixel do not resonate at the same frequency and therefore the ODMR line results broaden and less contrasted (fig. 3.14b).

The effect of the static magnetic field gradient can be modelled assuming a linear magnetic field at the pixel scale. The ODMR spectrum $S(\nu)$ associated with a single pixel can then be written as:

$$S(\nu) \propto \int_{\nu_1}^{\nu_2} P(\nu_0) L(\nu - \nu_0)\, d\nu_0 \tag{3.6}$$

The integration interval $[\nu_1, \nu_2]$ corresponds to the frequency range of the resonance frequencies of the NV centers imaged by the pixel (red and gold spectra in fig. 3.14);

$P(\nu_0)$ is the probability distribution of the NV center resonance frequency in the pixel; $L(\nu)$ is the spectrum of a single NV center whose resonance frequency is ν_0. Considering the NV center spectrum as a Lorentzian with a full width at half maximum equals to a, we can write:

$$L(\nu) = L_0(\nu) = \frac{(\frac{a}{2})^2}{(\frac{a}{2})^2 + (\nu - \nu_0)^2} \tag{3.7}$$

Under the reasonable assumption of a linear magnetic field, the probability distribution $P(\nu_0)$ is uniform in the integration range and therefore it results:

$$\begin{aligned} S_0(\nu) \propto \int_{\nu_1}^{\nu_2} L_0(\nu - \nu_0)\, d\nu_0 = \int_{\nu_1}^{\nu_2} \frac{(\frac{a}{2})^2}{(\frac{a}{2})^2 + (\nu - \nu_0)^2}\, d\nu_0 = \\ = \frac{a}{2}(\arctan\frac{\nu - \nu_2}{a} - \arctan\frac{\nu - \nu_1}{a}) \end{aligned} \tag{3.8}$$

Taking into account the hyperfine interaction, the NV center spectrum is described by three Lorentzians frequency shifted by $b = 2.14\ MHz$ (section 2.7). Therefore

$$L(\nu) = L_{Hyp}(\nu) = \frac{(\frac{a}{2})^2}{(\frac{a}{2})^2 + (\nu - \nu_0 + b)^2} + \frac{(\frac{a}{2})^2}{(\frac{a}{2})^2 + (\nu - \nu_0)^2} + \frac{(\frac{a}{2})^2}{(\frac{a}{2})^2 + (\nu - \nu_0 - b)^2} \tag{3.9}$$

and the single pixel spectrum can be written as

$$\begin{aligned} S_{Hyp}(\nu) \propto \frac{a}{2}\left(\arctan\frac{\nu - \nu_2 + b}{a} - \arctan\frac{\nu - \nu_1 + b}{a}\right) + \\ \frac{a}{2}\left(\arctan\frac{\nu - \nu_2}{a} - \arctan\frac{\nu - \nu_1}{a}\right) + \frac{a}{2}\left(\arctan\frac{\nu - \nu_2 - b}{a} - \arctan\frac{\nu - \nu_1 - b}{a}\right) \end{aligned} \tag{3.10}$$

As we can observe, the ODMR line has not anymore a lorentzian shape under a strong magnetic field gradient.
A comparison between the ODMR spectra under different magnetic field gradient regimes is reported in figs. 3.15 and 3.16.
The theoretical simulation (fig. 3.15) is realized considering NV centers with a central frequency uniformly distributed in a frequency range $[-\Delta\nu/2\ +\Delta\nu/2]$, where $\Delta\nu = \gamma\Delta B$, γ=28 GHz/T is the NV center gyromagnetic ratio and ΔB is the variation of the static magnetic field at the single pixel scale. Thus eq. (3.10) is solved for different values of ΔB (from 0.01 MHz/pixel to 11 MHz/pixel) considering as parameters $\nu_2 = -\nu_1 = \Delta\nu/2$ and $a = 1$ MHz, which is the FWHM of the experimental ODMR spectrum obtained at 5 dBm in fig. 3.13a.

To experimentally measure the effect of the magnetic field gradient on the ODMR spectra, we sum the ODMR spectra obtained on adjacent pixels. This summing procedure is equivalent to increasing the magnetic field gradient per pixel but, instead of increasing the magnetic field gradient, we increase the size of the pixel. In this way, by considering only a single experimental measurement, it is possible to study the behaviour of the ODMR spectra under different magnetic field gradients per pixel. In particular, we consider the measurement realized when a magnetic field gradient of 20 kHz/μm and a magnetic field of 10 mT are applied to the NV centers (fig. 3.13a) so that, summing over the entire area of the AOI along the laser beam direction, we can investigate a magnetic field gradient per pixel from 13 kHz/pixel to 10 MHz/pixel (sum-

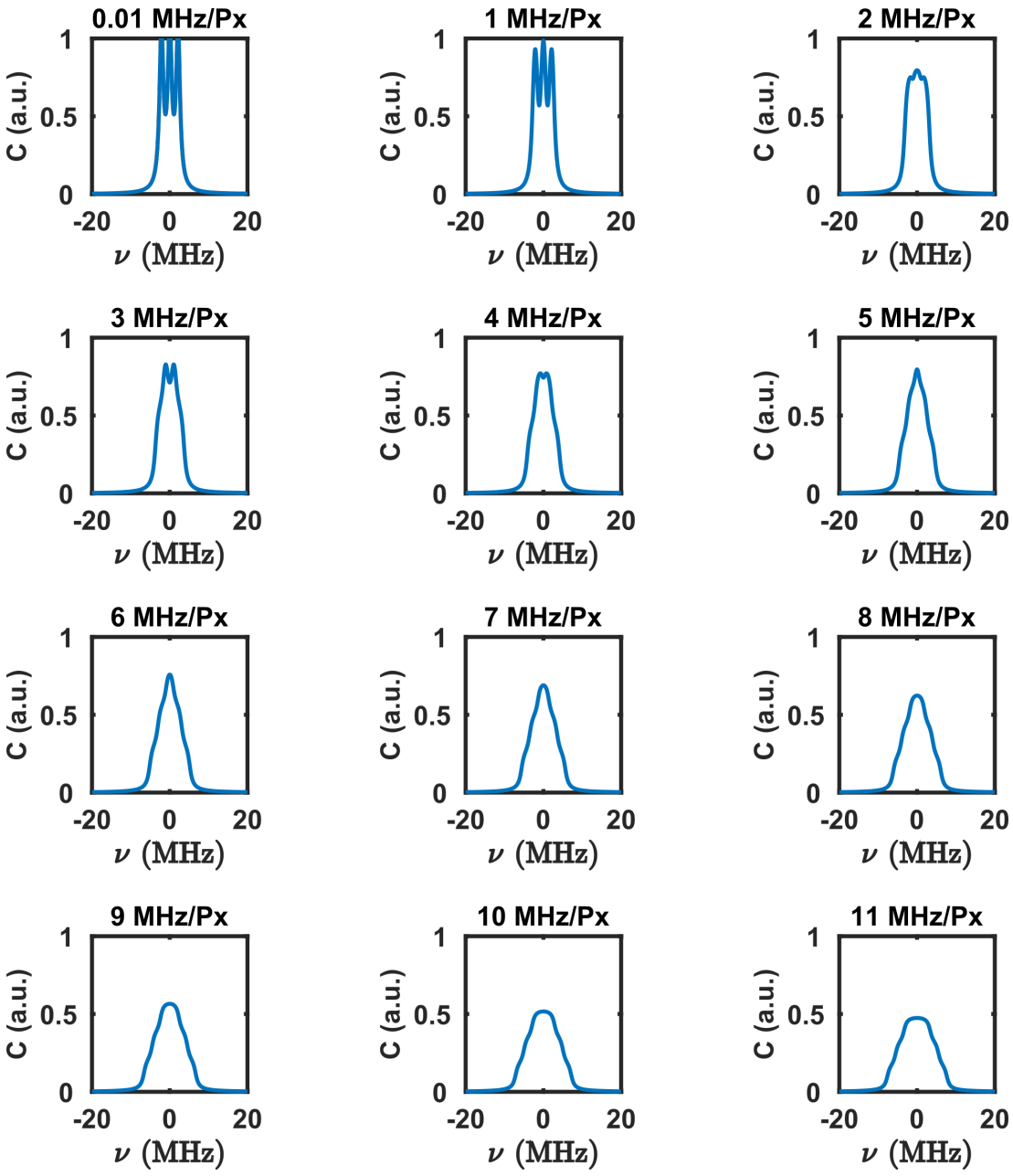

Figure 3.15: Simulation of the linewidth broadening caused by the static magnetic field gradient per pixel. In abscissa the detuning with respect to the frequency of the central hyperfine peak. In the title of each plot is reported the magnetic field gradient used for the simulation in MHz per pixel.

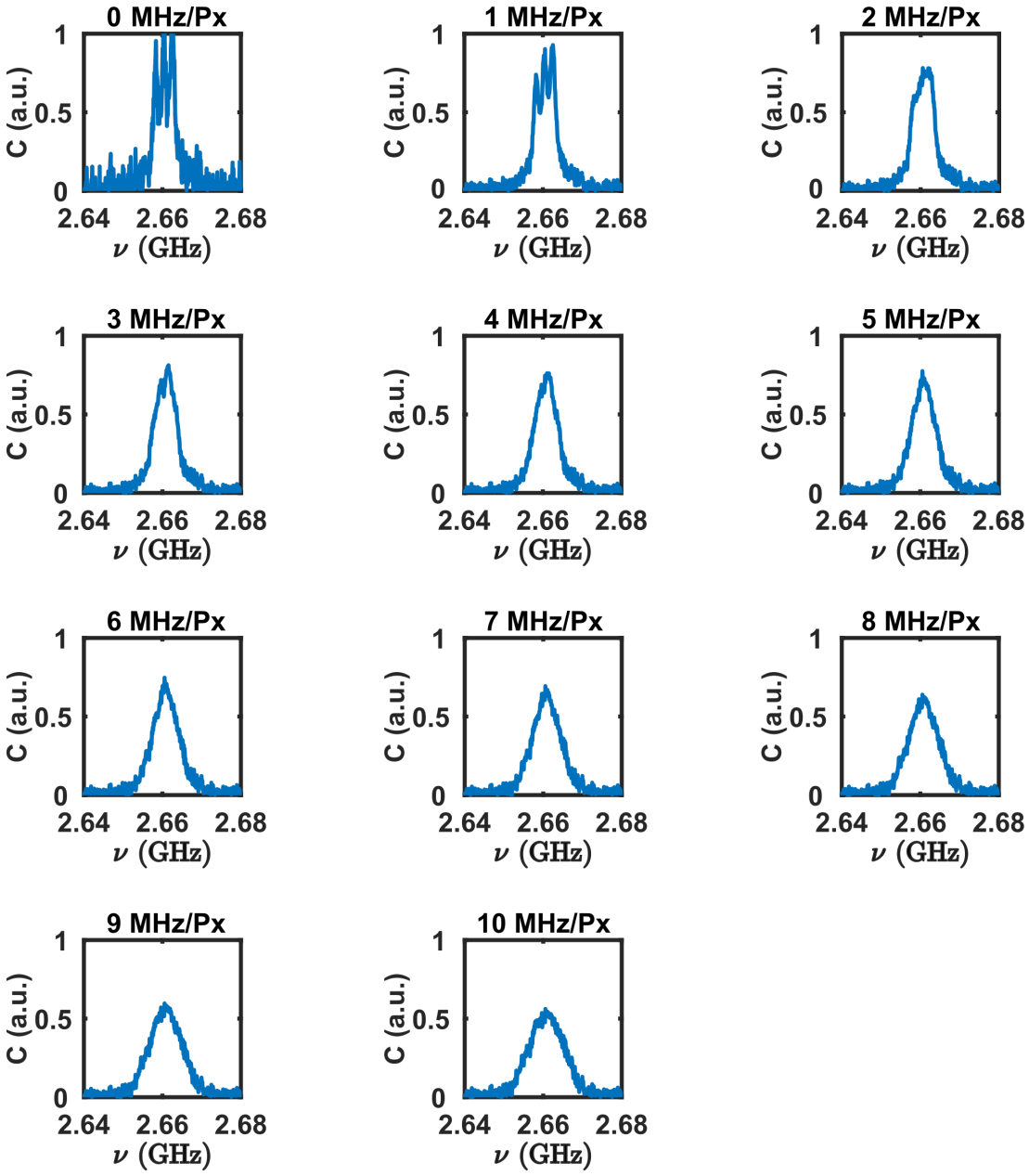

Figure 3.16: Measurement of the linewidth broadening caused by the static magnetic field gradient per pixel. In order to investigate the effect of the magnetic field gradient per pixel we summed the spectra of adjacent pixels along the beam propagation axis after having normalized their contrast. The magnetic field gradient over the integration area is reported in the title of each plot in MHz per pixel.

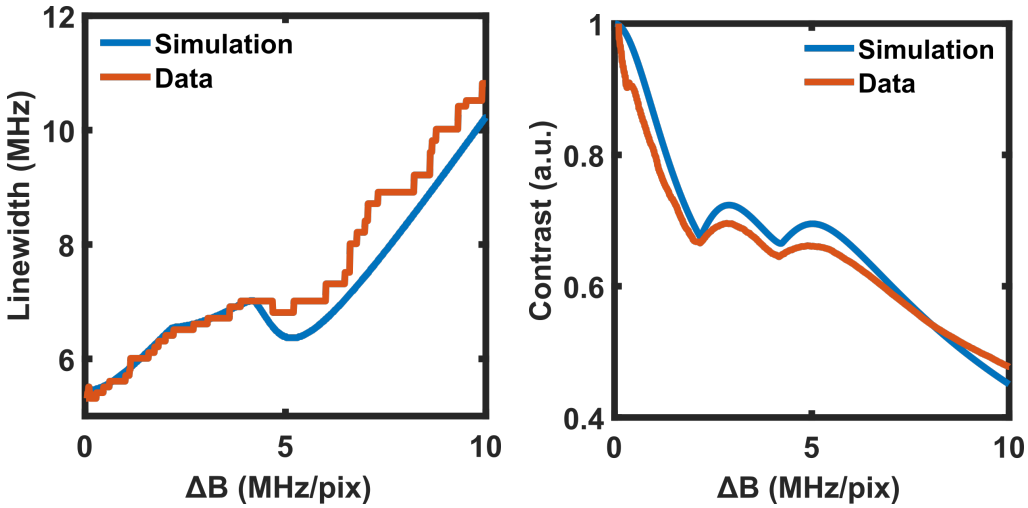

(a) *Linewidth* (b) *Contrast*

Figure 3.17: ODMR linewidth and ODMR contrast evolution under different static magnetic field gradients per pixel. The contrast is evaluated as the maximum value of the spectrum while the FWHM is evaluated as the frequency range for which the contrast is higher than half of the maximum value. The simulation and the experimental results are compared showing a good agreement.

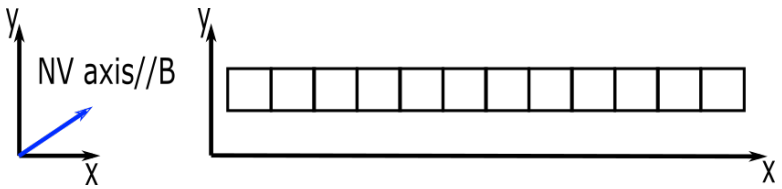

Figure 3.18: The NV center axis and the magnetic field (blue arrow) form an angle of $\approx 35°$ with respect to the beam propagation axis (x). Integrating over several pixels along the beam propagation axis (x), the magnetic field gradient over the integrated area is defined as: $\Delta B = dB/dx \cdot l_{pixel} \cdot N_{pixel}$, where dB/dx is the magnetic field gradient along the beam propagation axis, l_{pixel} is the side of the area imaged by a single pixel and N_{pixel} is the number of pixels summed. Therefore, the magnetic field gradient is evaluated not considering the components along y and z, the two directions perpendicular to the beam propagation axis.

ming over ≈ 800 pixels).
The results are reported in fig. 3.16. The shape of the spectra is in good agreement with the theoretical model and we can notice that, increasing the gradient, the three peaks of the hyperfine structure are not visible anymore. The contrast and the FWHM of the peaks are reported in fig. 3.17 and show a good agreement between the experimental results and the simulation. Concerning the FWHM (fig. 3.17a), the data are in agreement with the simulation for small magnetic field gradients. The small disagreement at high magnetic field gradients is likely due to the way we integrate the ODMR spectra over a large number of pixels. In fact, in order to preserve the same pumping parameter, the integration is done along the beam propagation axis, which is not the magnet magnetization axis. Therefore, the magnetic field gradient reported in fig. 3.17 is the magnetic field gradient along the beam propagation axis and it does not take into account the magnetic field gradient in the two other directions perpendicular to the beam propagation axis (section 3.4 and fig. 3.18). On the contrary, the simulation assumes a magnetic field gradient along the magnet magnetization axis, that is the NV center axis. As a consequence, the experimental results are evaluated underestimating the magnetic field gradient and that can explain the small disagreement with the simulation.
Using the results of the simulation, it is possible to estimate the ODMR linewidth expected for the measurement realized under a static magnetic field of 195 mT and a magnetic field gradient of 1.5 MHz/μm (1 MHz/pixel): it should be approximately 6 MHz at 5 dBm, the RF power considered to choose the NV center linewidth in the simulation. The experimental result is (11.5 $\pm$ 1.5) MHz, almost twice the expected value (fig. 3.13d).
The difference between the experimental result and the simulation can be attributed to fluctuations of the magnetic field amplitude. These fluctuations can be caused by both mechanical vibrations, which change the magnet-diamond distance (section 2.7), and temperature fluctuations, which change the magnet remanent magnetization of $\approx -0,1\%/^\circ$ (section 4.6.2) and therefore the amplitude of the static magnetic field. In both cases, the effect of these fluctuations is more evident for strong static magnetic fields and thus strong magnetic field gradients.

After having investigated the different contributions to the ODMR line broadening, we can conclude that, as expected, in our setup the frequency resolution depends on the frequency set-point and it is better at low frequencies (1 MHz at 2.6 GHz) than at high frequencies (50 MHz at 21 GHz). However, it is important to emphasize that the frequency resolution is ultimately limited by the NV center intrinsic linewidth, which is independent of its resonance frequency, and that different experimental architectures can be implemented in order to improve this parameter.

3.6 Dynamic range and power detection threshold

The quantitative measurement of the MW field amplitude can be realized exploiting the ODMR contrast of an ensemble of NV centers [129] which, according to eq. (1.36) reads as:

$$C = \vartheta \frac{(\Omega_R^2)}{\Omega_R^2 + \Gamma_p^\infty \Gamma_c^\infty \left(\frac{s}{s+1}\right)^2} \tag{3.11}$$

ϑ accounts for the different PL rate of the NV center when it is in $|0\rangle$ or $|\pm 1\rangle$, Ω_R is the Rabi angular frequency and accounts for the RF power, s is the laser power saturation parameter and Γ_p^∞ and Γ_c^∞ account for the longitudinal and transverse spin decoherence induced by the laser pump. Equation (3.11) describes both the laser power

dependence of the contrast (fig. 3.12), showing that it increases reducing the optical pumping parameter, and the RF power dependence of the contrast (fig. 3.13), showing that it linearly increases with respect to the MW power[2] before saturating. The linear dynamic range (the range of power for which the contrast is proportional to the RF power) and the saturation value both depend on the laser power regime.
A parameter of interest for the RF spectral analysis is the power detection threshold, that is the weakest RF field detectable or, equivalently, the RF power for which the SNR of the measurement is equal to one. Defining the PL spectrum of a single NV center as:

$$PL(\nu) = R_0 \left(1 - C\frac{\Delta\nu^2}{\Delta\nu^2 + (\nu - \nu_0)^2}\right) \tag{3.12}$$

where R_0, ν_0, $\Delta\nu$ and C are respectively the PL rate emission, the resonance frequency, the linewidth and the contrast of the NV center, and assuming to sum the PL over N_P, on resonance ($\nu = \nu_0$), photon shot noised and identical pixels (sections 3.3 and 2.1.5), the SNR of the measurements can be written as:

$$SNR = \frac{PL(\nu) - PL(\nu_0)}{\sqrt{PL(\nu)}} = \sqrt{nVN_pR_0\zeta\Delta t}C \tag{3.13}$$

where n is the NV center concentration in the sample, V is the volume imaged per pixel,ζ is the system collection efficiency and Δt is the integration time of the measurement. The RF power is related to the square of the RF magnetic field amplitude and thus to the angular Rabi frequency Ω_R. Considering SNR=1 and replacing eq. (3.11) in eq. (3.13), we can evaluate which parameters are related to the power detection threshold P_{th}:

$$P_{th} \propto \Omega_R^2(SNR = 1) = \frac{\Gamma_p\Gamma_c\left(\frac{s}{s+1}\right)^2}{\vartheta\sqrt{nVN_pR_0\zeta\Delta t} - 1} \tag{3.14}$$

The power detection threshold depends on the diamond (n,Γ_p^∞,Γ_c^∞), on the imaging system (ζ,N_P,V), on the integration time of the measurement (Δt) and on the pumping parameter (s).

The contrast dependence on the RF power can be observed in fig. 3.19, where we report the spectrum of the non-linearity of a MW generator (SMA100A, RS) at 37 MHz and a nominal power of 25 dBm. The measurement performed with our system is compared to the one realized with a commercial electronic spectrum analyzer. Considering the noise floor of our measurement, we are able to detect a signal over a MW power range from 23 dBm to -17 dBm, with a dynamic of approximately 40 dB and a power detection threshold of at least 20 μW.
Equations (3.11) and (3.14) do not take into account the static magnetic field gradient and the static magnetic field amplitude fluctuations, whose effects on the contrast have been anticipated in the previous paragraph and are visible in (fig. 3.13). These effects can be taken into account by performing a contrast calibration which associates, for every frequency, a value of contrast to each RF power. Moreover, the calibration procedure allows accounting for two other effects: the contrast spatial inhomogeneity intrinsic to our sample, for example caused by the presence of a spatial-dependent NV centers preferential orientation, and the frequency-dependent performance of the RF chain. The first aspect has already been discussed in section 2.3 and it is sample dependent, on the contrary the second aspect, that is the frequency dependence of the RF chain (section 2.1.2), is more general and deserves some comments.

[2]The MW power is proportional to the square of the MW field amplitude and thus to the square of the Rabi frequency: $P_{MW} \propto \Omega_R^2$

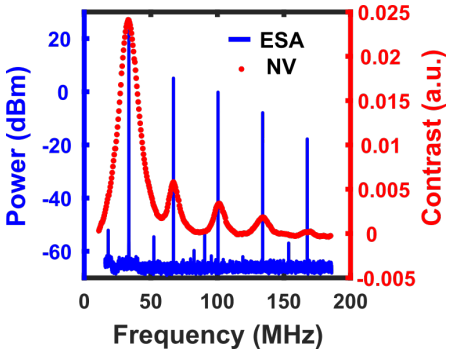

Figure 3.19: Comparison between the measurement realized using a commercial electronic spectrum analyzer (ESA) and the NV centers. The signal analysed is generated by the RF generator set to a frequency of 37 MHz and a nominal power of 25 dBm. Four harmonics of the main frequencies are well visible.

The frequency-dependent performance of the RF chain can be observed in figs. 3.20 and 3.21, where images in the x-y plane acquired at different RF frequencies and different RF powers are reported. The NV center transition investigated is the $|0\rangle \rightarrow |-1\rangle$ transition. Taking advantage of the ground state level anti-crossing, the spectra are acquired at the same resonance frequency but under different static magnetic fields and different magnetic field gradients (see insets figs. 3.20 and 3.21). For simplicity, we will say that the spectra are acquired before or after the GSLAC if NV centers undergo a static magnetic field respectively lower or higher than the one required for the GSLAC (≈ 102 mT). As expected, comparing the spectra acquired at the same frequency before and after the GSLAC, the contrast is higher for the formers because the magnetic field gradient is lower. However, it is interesting to observe that a stronger contribution to the contrast is given by the performance of the RF chain. In fact, comparing the images acquired at different frequencies before the GSLAC, by increasing the static magnetic field, the resonance frequency of the $|0\rangle \rightarrow |-1\rangle$ transition decreases, the magnetic field gradient increases, but the contrast increases. A similar result is reported in fig. 3.22 where the RF power detection threshold is evaluated up to 5 GHz and it is shown that it increases when the frequencies increase. In order to figure out this behaviour, in the next paragraph the RF chain is analysed from an electrical point of view.

3.6.1 Electrical model of the RF antenna

In our experiments, the antenna that brings the RF field close to the NV centers is a small wire-loop which short-circuits the RF chain (fig. 3.23a). The amplitude of the RF field generated near the loop depends on the electric current flowing in the wire and can be studied with the help of an equivalent electric circuit (fig. 3.23b). The RF generator is modelled as an ideal RF generator connected to a 50 Ω impedance. Since the MW frequencies we are interested in are of the order of some GHz, i.e. wavelengths of some cm (e.g. if $\nu = 1$ GHz, $\lambda = 30$ cm), we can neglect the propagative effects in our mm-size antenna and approximate the latter to a load impedance (Z_L) connected to the RF generator by means of an SMA cable whose impedance (50 Ω) matches the output impedance of the generator (50 Ω). The SMA cables insertion losses are low (< 2 dB/m) for frequencies lower than 18 GHz and so they are neglected.

The load impedance (Z_L) is evaluated by modelling the antenna as two parallel copper wires which end in a perfect circle. The equivalent electric circuit is composed of the mutual inductance of the two parallel wires (L_{wire}), the self-inductance of the

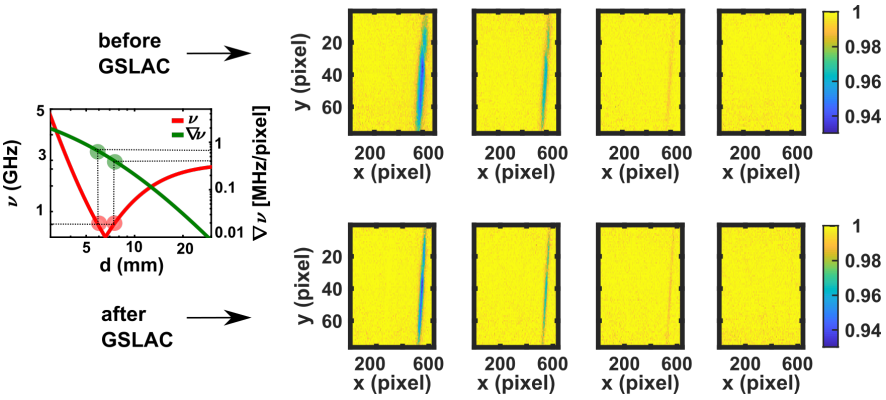

(a)

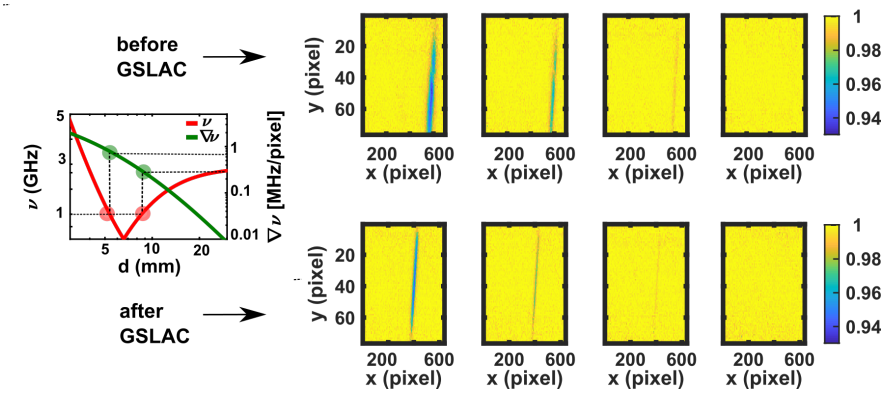

(b)

Figure 3.20: ODMR of the ground state $|0\rangle \rightarrow |-1\rangle$ transition resonant at 500 MHz (a) and 1000 MHz (b). The insets represent the resonance frequency and the frequency gradient per pixel at different distance form the magnet. The measurement is realized both for magnetic field lower and higher than the magnetic field necessary for the level anti-crossing (102 mT), see insets. For each value of the static magnetic field the measurement is repeated at four different RF nominal powers (from left to right): 25 dBm, 15 dBm, 5 dBm, -5 dBm.

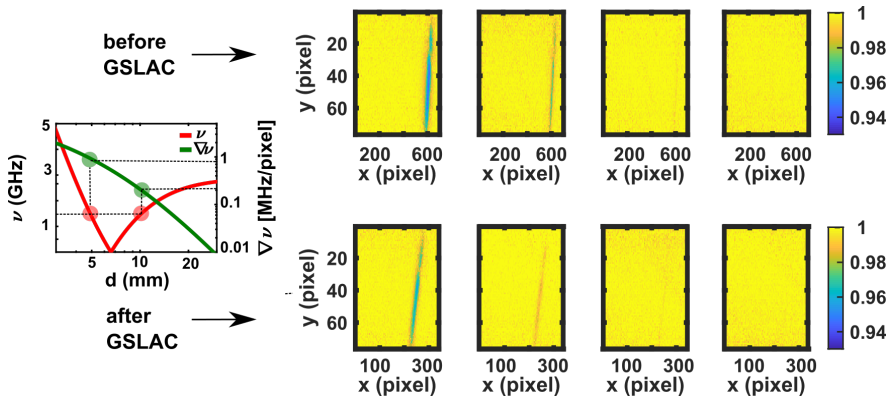

(a)

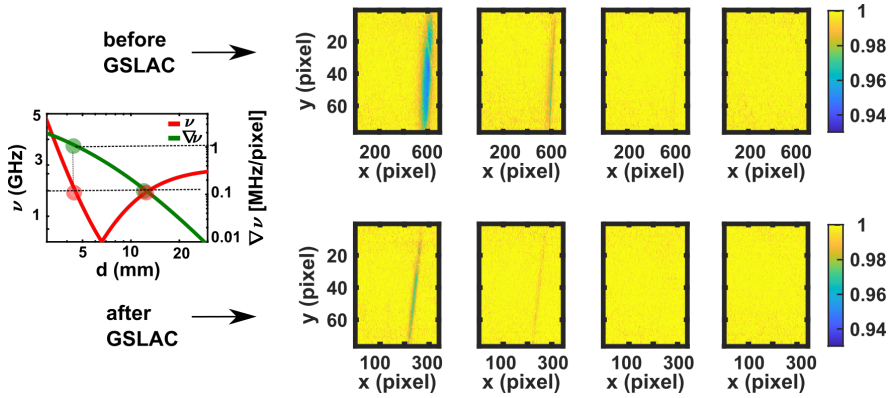

(b)

Figure 3.21: ODMR of the ground state $|0\rangle \rightarrow |-1\rangle$ transition resonant at 1500 MHz (a) and 2000 MHz (b). The measurement is realized both for magnetic field lower and higher than the magnetic field necessary for the level anticrossing (102 mT), see insets. For each value of the static magnetic field, the measurement is repeated at four different RF nominal powers (from left to right): 25 dBm, 15 dBm, 5 dBm, -5 dBm.

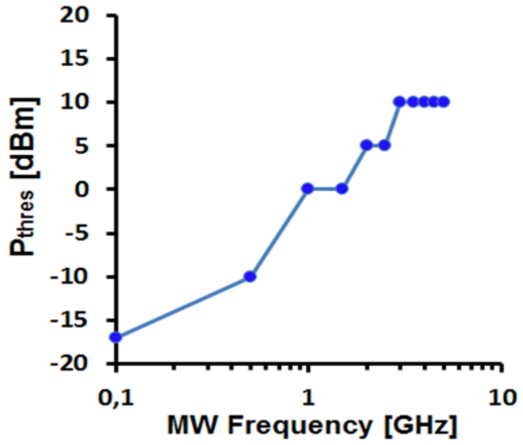

Figure 3.22: Power detection threshold at different RF frequencies.The experiment is carried out considering the same RF nominal power and camera exposure time, and summing over the same number of images for each frequency.

loop (L_{loop}), a capacitance that accounts for the capacitive coupling between the two wires (C_{wire}), and a capacitance which accounts for the capacitive coupling between the wires and the optical table (C_{ground}), assuming the latter is a ground plane.
Due to the skin effect, which is the tendency of an alternate current propagating in a conductor to be more concentrated near the surface than inside the conductor, the electric current flows near the surface of the wires. The skin effect is quantified by the skin penetration depth, that is the distance from the conductor surface for which the current is decreased by $1/e$. The skin penetration depth δ is frequency dependent:

$$\delta = \sqrt{\frac{2\varrho}{\omega\mu}} \tag{3.15}$$

where μ and ϱ are respectively the magnetic permeability ($1.26 \cdot 10^{-6}$ H/m) and the resistivity ($1.7 \cdot 10^{-8}$ $\Omega\cdot$ m) of the copper and $\omega = 2\pi\nu$ is the RF field angular frequency. At 1 GHz it results $\delta = 2$ μm, which is two orders of magnitude smaller than the radius of the wire. As a consequence, the current flows only on the surface of the wire and the inductances and the capacitances of the equivalent circuit of the loop antenna can be calculated as [130, 131]:

$$L_{wire} = \frac{\mu_0 D_{wire}}{\pi} cosh^{-1}(\frac{S_{wire}}{\Phi_{wire}}) \tag{3.16}$$

$$L_{coil} = \mu_0 r_{coil}(\ln\frac{16 r_{coil}}{\Phi_{wire}} - 2) \tag{3.17}$$

$$C_{wire} = \frac{\pi\varepsilon_0 D_{wire}}{cosh^{-1}(\frac{S_{wire}}{\Phi_{wire}})} \tag{3.18}$$

$$C_{ground} = \frac{2\pi\varepsilon_0 D_{wire})}{cosh^{-1}(\frac{2H_{wire}}{\Phi_{wire}})} \tag{3.19}$$

where μ_0 and ε_0 are respectively the vacuum magnetic permittivity and electric permeability, D_{wire} and Φ_{wire} are the length and the diameter of the two wires connecting the SMA cable to the loop (fig. 3.23a); S_{wire} is the distance between the two wires and H_{wire} is the distance between the two wires and the ground plane (optical table); r_{coil} is the radius of the antenna. Assuming $D_{wire} = 1$ cm, $\Phi_{wire} = 200$ μm, $S_{wire} = 3$ mm, $H_{wire} = 15$ cm and $r_{coil} = 250$ μm , it results: $L_{wire} = 13.6$ nH, $L_{coil} = 0.3$ nH and $C_{total} = C_{wires} + C_{ground} = 0.27$ pF. Solving the circuit, it is possible to evaluate the total impedance of the antenna (Z_L):

$$Z_L(\omega) = j\omega(L_{wire} + L_{coil})\frac{1 - \omega^2\frac{L_{wire}L_{coil}}{L_{wire}+L_{coil}}C_{total}}{1 - \omega^2 L_{coil}C_{total}} \tag{3.20}$$

where j is the imaginary unit.
Figure 3.24a shows the module of Z_L versus the frequency. We can observe that at frequencies of some GHz, the impedance of the antenna is one order of magnitude larger than the SMA cable impedance (50 Ω), therefore our assumption to have a short-circuit at the end of the cable is not correct.
In the estimation of the total impedance (eq. (3.20)) we neglected the resistive contribution. This is because, taking into account the skin effect, the electrical resistance of the loop coil is given by:

$$R = \frac{\varrho}{\delta}\frac{D_{wire}}{\pi\Phi_{wire}} \tag{3.21}$$

and, at 1 GHz, it is approximately 0.1 Ω, which is two order of magnitude smaller than

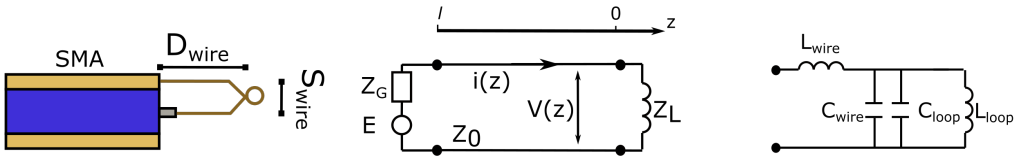

(a) (b) (c)

Figure 3.23: Electric model of the RF antenna. (a) Sketch of the end of the coaxial cable and the RF antenna made by connecting the core of the coaxial cable with the ground by means of a copper wire. The geometry of the antenna is approximated to a two parallel coils with a loop at the end. (b) Equivalent circuit of the RF chain. E and Z_G are an ideal generator and its 50Ω internal resistance. The four black points delimit the coaxial cable of impedance $Z_0 = 50\Omega$. The antenna is represented by a load inductance Z_L. The zero of the z axis is in correspondence of the load. (c) Equivalent circuit of the RF antenna. L_{wire} is the mutual inductance of the two parallel wires and C_{wire} their capacitive coupling, L_{loop} is the auto-inductance of the coil loop and C_{gorund} the capacitive coupling between the wires and the ground plane.

the inductive contribution.
Always in fig. 3.24a, the impedance of the antenna (Z_L) is compared to the inductance of the wires $Z_{wire} = j\omega L_{wire}$. For frequencies lower than 10 GHz, the antenna can be approximated to a simple inductance. It is important to notice that for frequencies higher than 10 GHz our initial hypothesis of neglecting the propagative effect of the RF field is not valid anymore since the RF wavelength becomes comparable to the size of the antenna.

The current and the potential along the transmission line can be evaluated solving the telegrapher's equations [81] for the system in fig. 3.23b. Considering $Z_L = j\omega L_{wire}$, it results:

$$V(z) = -jE\sin(\beta z + \varphi/2)e^{j\varphi/2}e^{-j\beta l} \tag{3.22}$$

$$I(z) = \frac{E}{Z_0}\cos(\beta z + \varphi/2)e^{(j\varphi/2)}e^{-j\beta l} \tag{3.23}$$

where $\varphi = -2\arctan(L_{wire}\omega/Z_0)$, $\beta = \frac{2\pi}{c}\omega\sqrt{\mu\varepsilon}$, μ and ε are the copper magnetic permeability and electric permittivity, c is the speed of light in vacuum and the z axis is defined as in fig. 3.23b. In correspondence of the load ($z = 0$), the module of the current is given by:

$$I(0) = \frac{E}{Z_0}\cos\left(\tan^{-1}\left(\frac{\omega L_{wire}}{Z_0}\right)\right) \tag{3.24}$$

and its frequency dependence is plotted in fig. 3.24b. We can observe a fast decrease of current in the frequency range [100 MHz - 5 GHz] which can explain the experimental results concerning the RF power detection threshold fig. 3.22. In fig. 3.24b it is also plotted the current at the end of the transmission line assuming a loop antenna of radius 500 μm and no parallel wires. In this case, the current starts decreasing at higher frequencies than the previous case, but still in the GHz range.

From an experimental point of view, three different antenna geometries have been tested (fig. 3.25). The first consists of two parallel wires ending in a small loop; the second consists of two twisted wires ending in a small loop; the third is just a small loop. The reflection coefficient S_{11} of the antennas, defined as the ratio between the incident and the reflected voltage wave [81], is measured by an electrical network analyser (VNA).

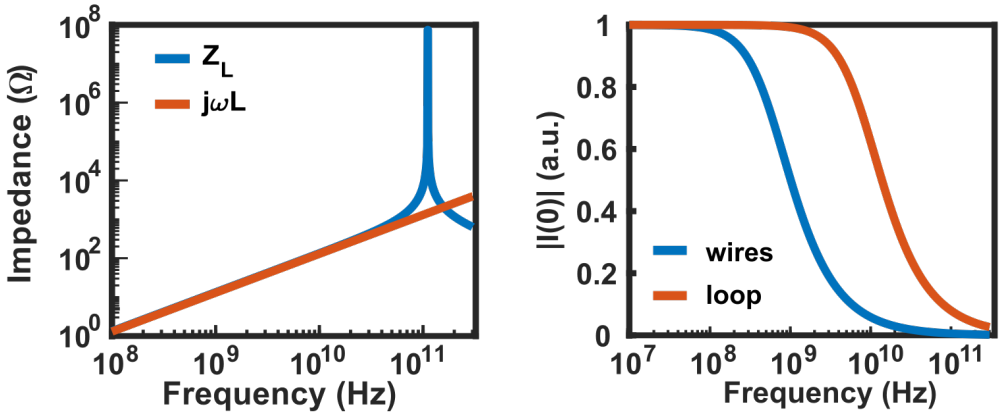

(a) (b)

Figure 3.24: (a) Comparison between the impedance calculated using eq. (3.20) and the impedance induced by the inductance of the two parallel wires. For frequencies lower than 30 GHz the RF antenna has essentially an inductive behaviour due to the two wires. (b) Module of the electric current at the load calculated by using the telegrapher's equations and assuming that the load impedance is given by either the two wires inductance (blue curves) or the loop inductance.

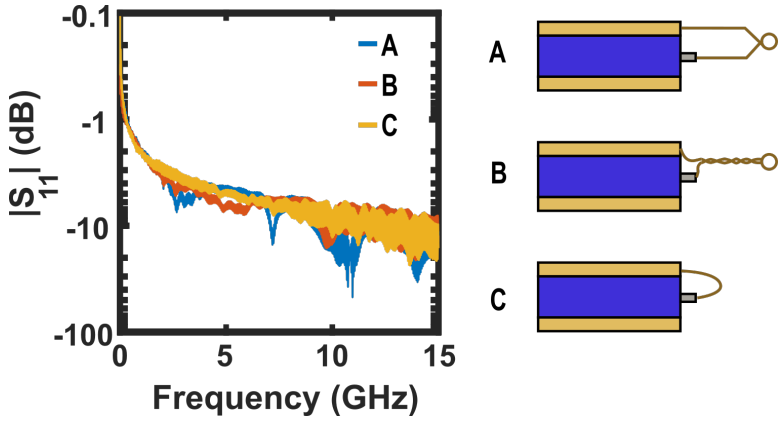

Figure 3.25: S_{11} parameter for three different antenna geometries: (A) two parallel wires ending in a small loop; (B) two twisted wires ending in a small loop; (C) just a small loop.

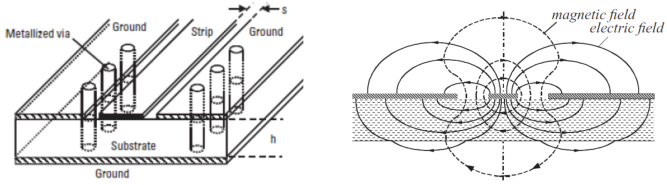

(a) (b)

Figure 3.26: (a) Schematic of a CPW. (b) Electric and magnetic field lines of a quasi-TEM mode propagating in the CPW. Images from [132].

.

The results, reported in fig. 3.25, show the presence of several resonances, especially at high frequencies. These resonances are extremely hard to predict using the electrical model described above, both because the real geometry of the antenna is not easy to define and because the several capacitive and inductive couplings between the antenna and the environment are almost impossible to predict.

To conclude, the electrical analysis and the VNA measurements, although allow partially explaining the frequency-dependent behaviour of the RF chain, principally show that even a very small inductive or capacitive coupling can fast deteriorate the performance of the RF chain. Taking into account all of these couplings is extremely hard. Moreover, the antenna is usually displaced and put in contact with the diamond using a three-axis translation stage. During these displacements, the contact between the diamond and the wires tends to deform the latter, thus altering the electrical properties of the RF chain. Given the difficulties in mastering the behaviour of the antenna, a new RF chain architecture based on a coplanar wave guide (CPW) is proposed.

3.6.2 A CPW-based RF chain

A CPW consists of a central conducting line and two lateral ground planes over a dielectric substrate (fig. 3.26a). Usually a second ground plane is realized on the opposite side of the dielectric substrate to provide mechanical stability and electrical isolation. This ground plane is commonly connected by means of metallic vias to the two lateral ground planes in order to have the same ground potential and prevent the propagation of undesired electromagnetic modes [133].
The principal propagating mode in a CPW is a quasi-TEM[3] mode (fig. 3.26b) with a zero cut-off frequency, and therefore well suited for broadband applications. The electric field lines move from the central strip to the lateral ground planes, while the magnetic field lines turn around the central strip line.
The size, the geometry and the dielectric material of the CPW define the effective dielectric constant, the attenuation and the characteristic impedance of the line [134].
The main advantage of CPWs over homemade antennas is the possibility to correctly simulate their behaviour and to customize the design to the application. In our case, implementing a simulation with the software COMSOL, we found the optimal CPW parameters to maximize the magnetic field amplitude and preserve a 50 Ω impedance over a large frequency range [1 GHz; 20 GHz].
The frequency behaviour of the transmission line is estimated by simulating the scattering parameters of the CWP. In the simulation it has been assumed as input of the

[3]TEM stands for transverse electromagnetic wave, which is an electromagnetic wave whose magnetic and electric components in the propagation direction are equal to zero (e.g. a plane wave). A quasi-TEM mode is a propagation mode whose longitudinal component is very small compared to the transverse component.

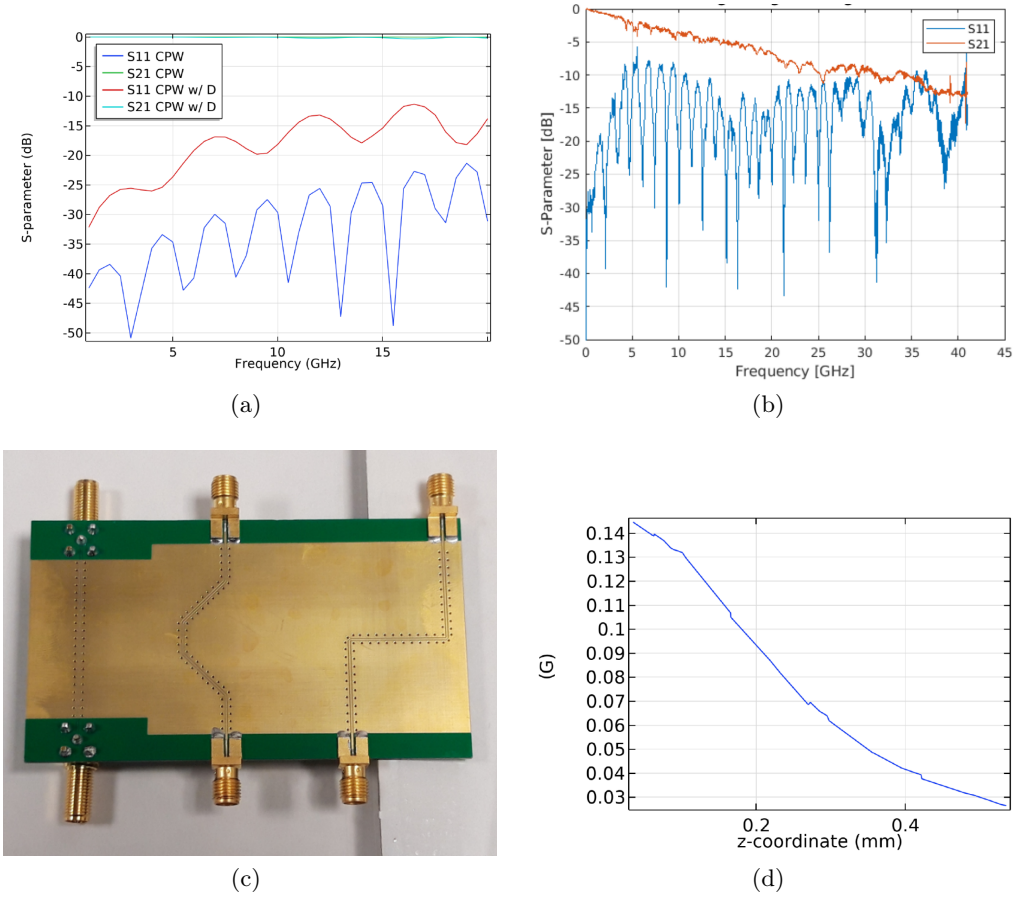

(a) (b)

(c) (d)

Figure 3.27: Comparison between the simulation (a) and the measurement (b) of the scattering parameters for the CPW realized, whose photograph is reported in (c). (d) Magnetic field amplitude versus the distance form the CPW at the center of the strip line.

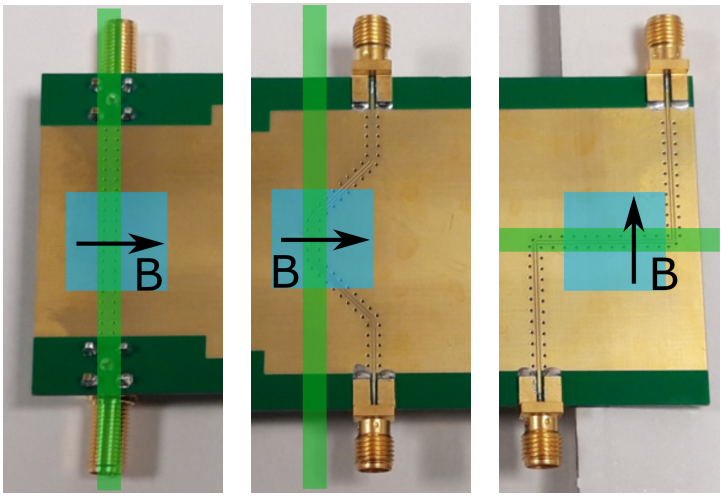

(a) (b) (c)

Figure 3.28: Three CPWs configurations. The green rectangle represents the laser beam, the light blue square represents the diamond. The direction of the RF field generated by the CPW at the middle of the central line is also reported.

ε_r	$H(\mu m)$	$W(\mu m)$	$S(\mu m)$	$t(\mu m)$
3.55	200	345	150	35

Table 3.1: CPW parapmeters. ε_r is the electric permittivity of the dielectric, H the height of the dielectric substrate, W is the width of the central line, S the distance between the central line and the lateral ground plane, t the thickness of the central line and the metallic plate.

line a 50 Ω impedance generator and as output a 50 Ω load. The reflection coefficient S_{11} accounts for eventual impedance mismatching and the transmission coefficient S_{12}, defined as the ratio between the incident and the transmitted voltage waves, accounts for the transmission losses. The simulation is run for two different cases: in the first case only the CPW is considered, in the second case a 0.5 mm thick dielectric plate ($\varepsilon_r = 5.5$) is placed on top of the CPW to simulate the contribution of the diamond plate. In both cases, the results of the simulation (fig. 3.27b) show low (some dB) transmission losses and a good impedance matching (low reflections ≈ -20 dB) over the entire frequency range.

In order to maximize the coupling between the NV center and both the optical and RF field, the laser beam has to be parallel to the NV center axis and the RF field perpendicular to it. To test different experimental configurations, we realized on the same printed circuit board (PCB) three CPWs having different shapes (fig. 3.27c). Their features are reported in Table 3.1. The first configuration consists of a straight CPW guide with the connectors plugged in from the bottom of the line, allowing the propagation of the laser beam parallel to the CPW (fig. 3.28a). The second and third configuration use a different and more versatile approach which consists in misaligning the CPW area used for exciting the NV centers from the connectors axis figs. 3.28b and 3.28c. In this case, additional vias are added near the curvatures of the line to reduce losses. In the second configuration (fig. 3.28b) we tried to minimize the angle of curvature while, in the third configuration, it is maximum (90°). The scattering parameters have been experimentally measured using a VNA and the results, reported in fig. 3.27b, show a good agreement with the simulation: low transmission losses (less than 5 dB in the range [0 GHz; 15 GHz]) and low reflections (≈ -15 dBm over the entire frequency range).
The next step is the implementation of the CPW in the experimental setup to measure the performance of this new architecture. The major issue expected concerns the rapid decrease of the RF field amplitude increasing the distance from the CPW. In fact, differently from the loop antenna, in this case it is not possible to image the diamond area which is in contact with the PCB. Therefore the collected PL will be emitted by NV centers which are approximately 500 μ m (the thickness of the diamond) far from the CWP. According to the simulation in fig. 3.27d, the magnetic field amplitude at such distance from the CPW is 75% lower than the amplitude in proximity of the PCB.

The simulations and the designs of the CPWs proposed in this paragraph are the results of the Diego Florez Alban internship.

3.7 Temporal resolution and simultaneous detection

The advantage of the CW widefield imaging mode is that all the frequencies in the frequency range are simultaneously detectable without any dead time except the one of the camera, opening the way to the real-time frequency detection of complex microwave signals with 100% probability of interception.

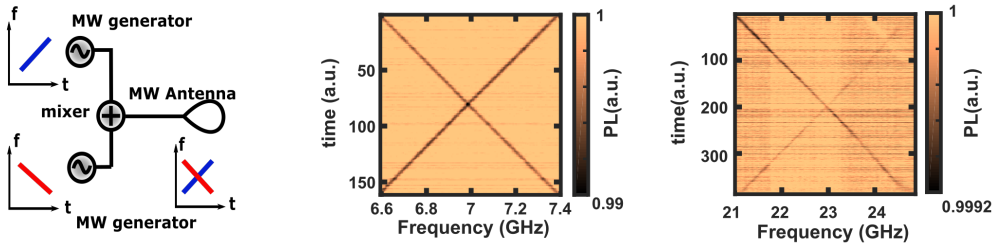

(a) (b) (c)

Figure 3.29: Detection of multi-frequencies signal. A frequency mixer combines the output of two MW generators synchronized to sweep their frequencies in the same frequency range but in a reverse order (a). Time evolution of a two-frequency signal in two different frequency ranges: $7GHz$ (b) and $23GHz$ (c).

To illustrate this point, a time-varying multi-frequencies microwave field is generated combining the signals of two microwave generators and varying their frequencies as a function of time. The frequencies are swept over the entire bandwidth of the image, for two different configurations, around 7 GHz (fig. 3.29b) and around 23 GHz (fig. 3.29c), showing that the simultaneous detection is possible for a number of frequency channels equal to the ratio between the bandwidth and the frequency resolution.

The temporal resolution is the smallest time required to detect the PL variation induced by a resonant MW field. Its physical limit is related to the NV center photodynamics, whose characteristic times are of the order of tens of ns. In our case, the temporal resolution is defined as the lowest camera exposure time needed for a SNR equal to 1, not considering the refreshing time of the camera. Therefore, according to eq. (3.13), assuming $SNR = 1$, the temporal resolution of the system is given by:

$$\Delta t = \frac{1}{nVN_pR_0\zeta}C^2 \tag{3.25}$$

where n is the NV center concentration, V is the diamond volume imaged by a single pixel, N_p is the number of pixels over which the PL is integrated, R_0 is the NV center photoluminescence rate when it is in $|0\rangle$, C is the ODMR contrast and ζ accounts for the PL collection efficiency. Since the contrast and the number of pixels resonating at the same frequency are frequency-dependent parameters, also the temporal resolution is frequency-dependent in our experimental architecture. The frequency dependence of the contrast has been discussed in section 3.6 and essentially depends on the static magnetic field gradient per pixel and the transmission efficiency of the RF chain. The frequency dependence of the number of pixels resonating at the same frequency can be understood considering that, according to the calibration procedure described in section 3.3,

$$N_p = N_{p\parallel} \cdot N_{p\perp} = \frac{\Delta\nu}{\gamma\frac{dB}{dx} \cdot l_{pixel}} \cdot N_{p\perp} \tag{3.26}$$

where $N_{p\parallel}$ and $N_{p\perp}$ are respectively the number of pixels summed parallel and perpendicular to the beam propagation axis, $\frac{dB}{dx}$ is the static magnetic field gradient along x, l_{pixel} is the side of the square area imaged by a single pixel, $\Delta\nu$ is the ODMR linewidth and γ the NV center gyromagnetic ratio. $N_{p\perp}$ is related to the laser beam waist, while $N_{p\parallel}$ to the linewidth, in pixel unit, of the ODMR line in the xy plane. This latter is related both to the static magnetic field gradient along x ($\frac{dB}{dx}$), which is frequency-dependent (section 3.4), and to the linewidth of the ODMR spectrum ($\Delta\nu$) which is frequency-dependent as well (section 3.5).

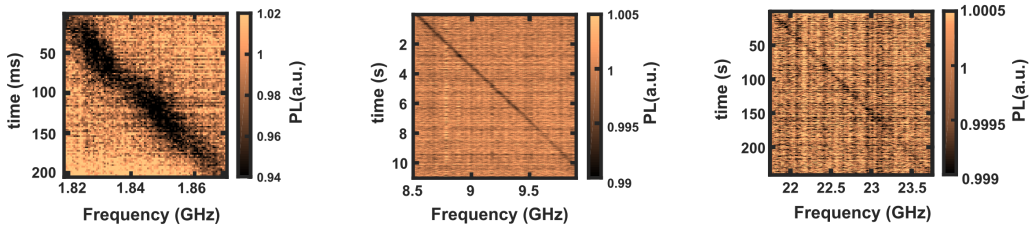

(a) (b) (c)

Figure 3.30: Spectrogram for three different frequency ranges: (a) around 2 GHz, (c) around 9 GHz, (c) around 23 GHz. In order to compare the data, the calibration procedure is done considering the same number of pixels for the three different frequencies.

The linear dependence of the temporal resolution from the number of pixels derives from the assumption that the SNR scales linearly with the square root of it. However, as already described in section 2.1.5, the improvement in the SNR achievable summing over several pixels is finally limited by the PL inhomogeneity and the pixels correlations; for this reason, the contribution of the number of pixels to the SNR and thus to the temporal resolution is difficult to estimate.
We experimentally evaluate the temporal resolution of our system by decreasing the camera exposure time in order to reach values of the SNR close to 1, not considering the refreshing time of the camera. Using a nominal MW power of 25 dBm, we measured a time resolution of 2 ms at 1.8 GHz (C= 6%, SNR= 5), 20 ms at 9 GHz (C= 1%, SNR= 4) and 600 ms at 23 GHz (C= 0.1%, SNR= 1). As expected from eq. (3.25), the temporal resolution is better at low frequency, where the ODMR spectrum shows a better contrast. It should be noted that, for an integration time of 2 ms, using our sample, only a few tens of counts are detected by the camera. Therefore, as discussed in section 2.1.5, the measurement starts to be limited by the intrinsic noise of the camera. In order to increase the SNR and the temporal resolution of the system, several expedients can be adopted: diamonds with a higher NV center concentration (section 1.4), a better PL collection efficiency, different pumping parameters, lower magnetic field gradients, a larger volume per pixels, etc. However, it must be observed that many of these expedients improve the temporal resolution at the cost of other parameters. For example, lowering the static magnetic field gradient reduces the real-time bandwidth, enlarging the volume per pixel reduces the frequency resolution,etc. Therefore, a tradeoff must be made based on the application for which the RF spectral analysis is performed.

3.8 Frequency ambiguity

In this chapter it has been proposed an experimental architecture to use NV centers as a tunable RF spectrum analyzer over a large frequency band [10 MHz, 25 GHz]. However, it may present some frequency ambiguities, namely the presence of more than one resonance frequency associated with the same pixel (section 2.8). Two factors can cause this ambiguity

- the presence of the three non-aligned NV families, which for a given pixel induce the presence of additional resonance frequencies
- the two intrinsic resonance frequencies of the NV center ($|0\rangle \rightarrow |-1\rangle$ and $|0\rangle \rightarrow |+1\rangle$).

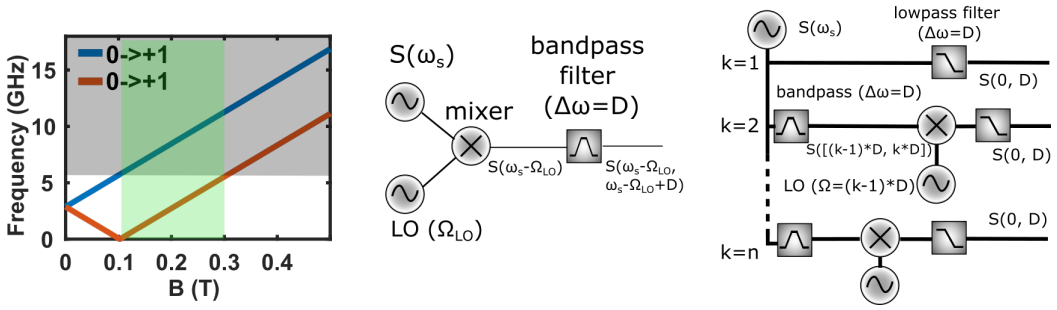

(a) (b) (c)

Figure 3.31: (a) The NV center resonance frequencies versus the amplitude of the static magnetic field. In grey the frequency range filtered by the RF filter. In green the magnetic field range necessary to have a bandwidth of 5.74 GHz with a central frequency of 2.87 GHz and no frequency ambiguity. (b) Working principle of the heterodyne technique. (c) Schematic of a possible heterodyne detection chain to remove the frequency ambiguity and enlarge the frequency range of the NV-center based spectral analysis.

The first source of ambiguity can be suppressed using diamonds with NV centers preferentially oriented along one of the four diamond crystallographic axis (section 1.4). The second source of ambiguity is intrinsic to the single NV center and can be removed by applying a MW filter so that the signal is resonant with only one of the two NV center transitions. This procedure restricts the available bandwidth to a maximum of 5.74 GHz (twice the zero-field splitting), corresponding to the frequency shift between the $|0\rangle \rightarrow |-1\rangle$ and the $|0\rangle \rightarrow |+1\rangle$ transition for magnetic fields stronger than 0.1 T (fig. 3.31a). For example, adding in the RF chain a low pass filter which suppresses all RF signal components at frequencies above 5.74 GHz, allows a non-ambiguous detection over a maximum bandwidth of 5.74 GHz by exploiting the NV center $|0\rangle \rightarrow |-1\rangle$ transition when NV centers undergo a static magnetic field in the range [102 mT, 307 mT] (fig. 3.31a). For the same values of the static magnetic field, the unambiguous RF spectral detection can be achieved using a [5.74 GHz; 11.48 GHz] bandpass filter and exploiting the $|0\rangle \rightarrow |+1\rangle$ transition. More generally, for any static magnetic field stronger than 102 mT it is possible to achieve an unambiguous maximal detection bandwidth of 5.74 GHz by applying a RF filter.

In this configuration, the frequency range can be chosen according to the performance of the MW chain (e.g. corresponding to baseband communication), and any other frequency signal can be brought within this frequency range using heterodyning techniques. The idea behind the heterodyne technique is depicted in fig. 3.31b. The signal of interest (ω_s) is mixed with a local oscillator (Ω_{LO}) by means of a frequency mixer. The mixer output signal contains both a component at frequency $\omega_s + \Omega_L$ and a component at frequency $\omega_s - \Omega_L$. After the mixer, a RF filter whose bandwidth corresponds to the unambiguous real-time bandwidth of the NV centers, suppresses one of the two components, the one at higher frequency in our example.

This way of removing the ambiguity has the disadvantage of limiting the real-time bandwidth to 5.74 GHz but the great advantage of increasing the frequency range, which is now only limited by the heterodyne detection chain. A possible architecture which exploits the heterodyne technique to increase the spectrum analyzer frequency range is presented in fig. 3.31c. The input signal is split in n different channels, each of which is provided by a bandpass filter of bandwidth $D < 5.74$ GHz and lower-passing frequency shifted by D with respect to the previous channel. After the filter, for each channel, a local oscillator downconverts the RF signal in the frequency range $[0; D]$, for which an

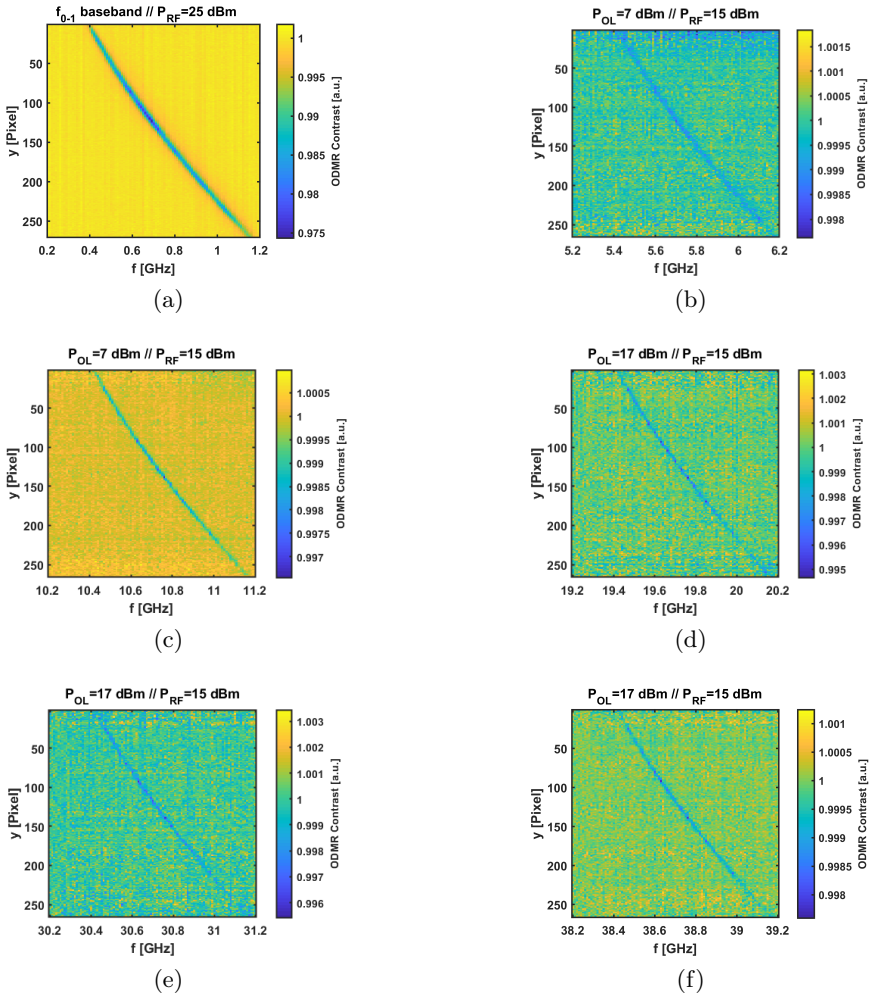

Figure 3.32: Heterodyne detection of RF field up to 40 GHz using an ensemble of NV centers. In the title of each plot are reported the RF power of both the local oscillator and the RF signal.

unambiguous and efficient detection is possible using an ensemble of NV centers.

The experimental demonstration of the RF field detection up to 40 GHz using the heterodyne technique is reported in fig. 3.32. The limit of 40 GHz is due to the maximum frequency of our RF generator. The only difference between the images presented in fig. 3.32 is the frequency of the local oscillator. Therefore, from the point of view of NV centers, the detection and its parameters (frequency resolution, contrast, dynamic range, time resolution) are frequency independent. In fact, independently from the frequency range of the signal, the RF field applied to the NV centers is always in the same frequency range.

3.9 Conclusion and perspectives

In this chapter, we demonstrated that an ensemble of NV centers in a single-crystal diamond can be used to detect a complex microwave signal and resolve its spectral components up to 25 GHz. We investigated the effects of the magnetic field gradient on the key parameters of the RF spectral analysis based on an ensemble of NV centers such as real-time bandwidth, frequency resolution, dynamic range and time resolution. Using our experimental architecture we achieved a MHz frequency resolution and ms

time resolution at low magnetic field gradient and low RF frequencies ($\approx$ 2 GHz), and a few tens MHz of frequency resolution and a few hundreds ms of time resolution at high RF frequencies ($\approx$ 20 GHz). The frequency-dependent performance has been analysed and follows an expected behaviour considering both the effect of the magnetic field gradient and the RF chain. We investigated the frequency ambiguity in the RF spectral analysis based on an ensemble of NV centers and we proposed a solution based on heterodyne techniques which both removes this ambiguity and opens the way to the real-time spectral analysis over a frequency range of several tens of GHz (demonstrated up to 40 GHz).

This work lays the foundation for the application of NV centers for the RF spectral analysis. In particular, we showed how the parameters of interest for the RF spectral analysis are related to each other with respect to the experimental implementation. Following the results presented in this manuscript, it is possible to customize the experimental architecture to optimize its performance according to its application.

Concerning the perspectives of this work, we can identify two main axes of improvement. The first is testing different and new experimental architectures: diamonds with higher NV center concentration and/or preferential orientations, RF chain based on CPWs, higher PL collection efficiency, different pumping parameters or more flexible magnetic field architectures, etc. The second is the implementation of a photoelectrical read-out of the NV centers spin transition (PDMR) [136] which may offer a higher spin detection rate no more limited by the frame rate and the dead time of the camera. Moreover, the electrical read-out interface will allow the realization of a more compact system.

Chapter 4

Imaging of RF field using an ensemble of NV centers

The fast development of RF-based technologies requires proper methods to characterize RF components. In the first chapter we reviewed the most common techniques to perform this kind of analysis showing that there is a need for alternative and complementary techniques which are non-invasive, work at room temperature and offer a high spatial resolution. In this chapter we propose two NV centers-based solutions which fulfill these requirements. The first is described in section 4.1 and consists in exploiting the RF power broadening of the NV centers CW-ODMR spectrum to retrieve information about the amplitude of the microwave field radiated in the near field region by a RF device; in our case the loop antenna used to bring the RF field in proximity of the NV centers. The second technique, described in the rest of this chapter, is based on the widefield detection of NV centers Rabi oscillations. The set-up and the acquisition procedure, which differs from that implemented when an APD-based PL collection system is used, are described in section 4.2. In section 4.3 and section 4.4, the widefield detection of NV center Rabi oscillations is investigated by means of experiments and simulations before being applied to the imaging of the RF near-field generated by a loop antenna (section 4.5), The end of the chapter (section 4.6) is dedicated to the optical detection of the NV center magnetic resonances in pulsed regime (pulsed ODMR) using a widefield imaging system. Some preliminary results are reported.

4.1 Imaging of RF field in CW regime

In section 1.2.5 it has been introduced a mathematical model to describe the NV centers CW-ODMR spectrum and calculate the mathematical expressions for both the CW-ODMR contrast (C, eq. (4.2)) and FWHM linewidth ($\Delta\nu$, eq. (4.1)), here reported [48]:

$$\Delta\nu = \frac{\Gamma_c^\infty}{2\pi}\sqrt{\left(\frac{s}{s+1}\right)^2 + \frac{\Omega_R^2}{\Gamma_p^\infty\Gamma_c^\infty}} \tag{4.1}$$

$$C = \Theta\frac{\Omega_R^2}{\Omega_R^2 + \Gamma_p^\infty\Gamma_c^\infty\left(\frac{s}{s+1}\right)^2} \tag{4.2}$$

where $s = P/P_{sat}$ is the optical saturation parameter, Ω_R is the Rabi angular frequency, Γ_p^∞ and Γ_c^∞ are receptively the longitudinal and transverse spin decoherence rates induced by the laser pumping and ϑ is a parameter which accounts for the spin dependent PL rate. As described in chapter 1, these expressions are valid in the case of a saturation parameter $s > 0.02$.

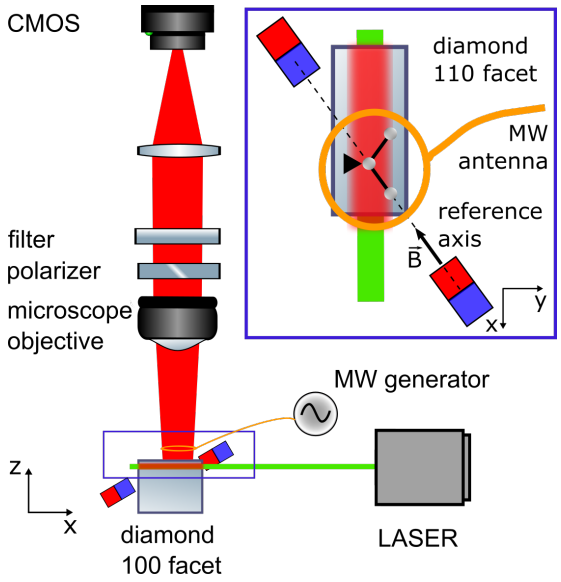

Figure 4.1: Experimental set-up. For a detailed description see section 2.1. The inset shows the top view of the diamond and the two-magnet architecture. The magnets are aligned with respect to one of the two NV center families laying in the diamond [110] plane using the procedure described in section 3.2.1

In order to validate the model for an ensemble of NV centers, the CW-ODMR spectrum is measured for different RF powers and the power dependence of the contrast and the linewidth are evaluated. The experiment is realized using the experimental set-up described in section 2.1 and a two-magnet architecture in order to have a low static magnetic field gradient (fig. 4.1). This is advantageous because, as explained in chapter 3, the magnetic field gradient at the pixel scale broadens the CW-ODMR linewidth and reduces the CW-ODMR contrast. The magnets are carefully aligned to one NV center family (section 3.2.1) and arranged in order to have, at the middle of the two magnets, a static magnetic field amplitude corresponding to ESLAC. In this configuration, the ground state $|0\rangle \rightarrow |-1\rangle$ resonance frequency is approximately 1.4 GHz and only one peak of the hyperfine structure is visible since the nitrogen nuclear spin is optically polarized (section 2.6).
The NV center CW-ODMR spectrum is acquired for different RF nominal powers, ranging from 5 dBm to 25 dBm. For each RF power, the CW-ODMR spectrum is obtained by summing the PL of 25 adjacent pixels to increase the SNR (section 2.1.5). The spectrum is then fitted by a Lorentzian function to evaluate the CW-ODMR contrast and the CW-ODMR FWHM. The measurement is repeated for several pixels and the mean values of the CW-ODMR contrast and the CW-ODMR FWHM are plotted in figs. 4.2c and 4.2d. The error bar is given by the standard deviation. In agreement with the model (eqs. (4.1) and (4.2)), the contrast follows a saturation law while the FWHM increases almost linearly with the magnetic field amplitude.

The power dependence of both the FWHM and the contrast can then be exploited to acquire information about the amplitude of the RF near field emitted by the loop antenna. Comparing the error bars in fig. 4.2c and fig. 4.2d, one can observe that the power-dependence of the contrast is less sensitive than the power-dependence of the FWHM. This is essentially caused by the spatial inhomogeneity of the NV center concentration and the presence of an inhomogeneous NV center preferential orientation in our sample (section 2.3). Moreover, under the optical pumping regime implemented in our experiment, at high RF power the contrast is almost saturated and thus not

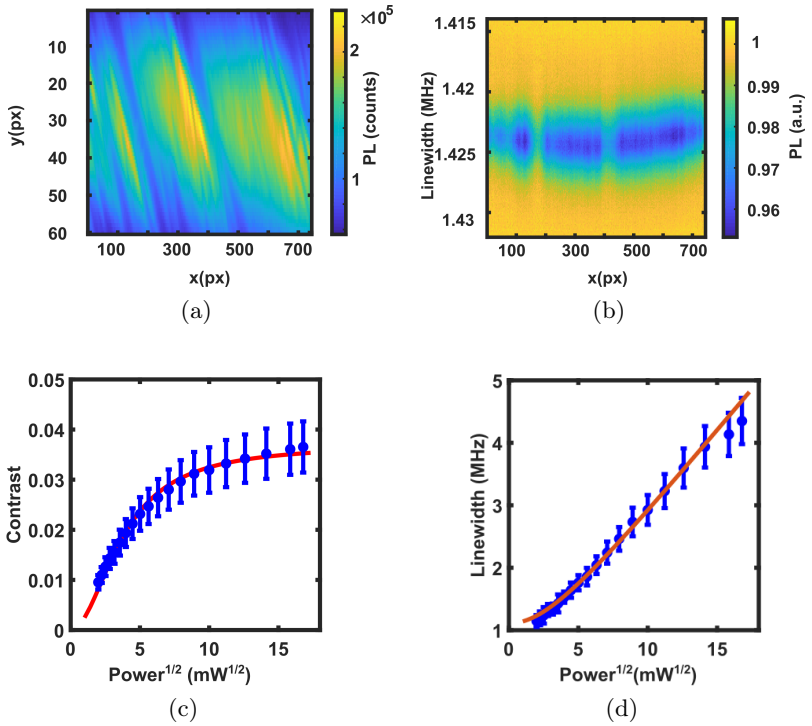

(a) (b) (c) (d)

Figure 4.2: (a) x-y plane image acquired by the camera. (b) CW-ODMR spectrum in the x-f plane. The nominal power of the RF field is set to 25 dBm. (c) Power dependence of the CW-ODMR contrast. The fit is realized using a saturation law: $C = a \cdot P/(P+b)$, where C is the contrast and P is the nominal RF power in mW. (d) Power dependence of the CW-ODMR linewidth. The fit is realized using a saturation law: $L^2 = a \cdot P + b$, where L is the spectral linewidth and P is the nominal RF power in mW.

very sensitive to power fluctuations [129]. For these reasons, in the following of this paragraph, only the FWHM is used to retrieve information about the amplitude of the RF field.
Two different experimental architectures (fig. 4.3) are considered. In the first, the antenna is centred with respect to the camera AOI (fig. 4.3a) and therefore the NV centers imaged by the camera are excited by the RF field generated at the center of the antenna. In the second, the antenna is displaced so that the NV centers are excited by the RF field generated outside the loop (fig. 4.3c). In both cases the RF field is set to a nominal power of 25 dBm. Figures 4.3b and 4.3d show the NV center CW-ODMR linewidth at different positions along the beam propagation axis. At the center of the antenna, (fig. 4.3b) the NV center linewidth is almost homogeneous. Outside the loop, it decreases increasing the distance from the antenna. This observation is in agreement with the evolution of a magnetic field generated by an electric current flowing in a wire loop: a magnetic field almost homogeneous inside the loop and a decreasing behaviour outside the loop. We can approximate the magnetic field generated outside the loop to that generated by a current flowing along an infinite wire: $B(d) \propto 1/d$, where d is the distance from the center of the wire. Hence, the fit in fig. 4.3d is done using the fitting curve:

$$f(d) = \frac{a}{d+b} + c \tag{4.3}$$

where a is a parameter which accounts for the magnetic field amplitude, b is an offset radius which accounts for the fact that the zero of the x axis does not match the center of the wire and c is an offset parameter which accounts for the natural linewidth of the NV centers. From the fit we obtain $b = 140 \pm 7\ \mu m$ which is of the same order of magnitude of the radius of the wire ($50\ \mu m$) and $c = 0.49 \pm 0.03$ MHz, which is comparable to the NV centers linewidth of a CVD optical grade diamond with a nitrogen impurity concentration of 1 ppm (≈ 500 kHz).
The conversion from the pixel unit reported on the abscissa in fig. 4.3b and the SI unit (μm) is done considering that, due to the imaging system implemented in the set-up, each pixel images a 660 nm side diamond square. This is, inter alia, the spatial resolution of our system.
The discrepancy between the value of b and the radius of the wire (which is $50\ \mu m$) may be attributed at several factors. First, fitting the evolution of the FWHM versus the RF power with eq. (4.3), we assume that the RF field is proportional to the CW-ODMR linewidth. This assumption is true for high RF powers, where the optical power broadening is negligible compared to the RF power broadening eq. (4.1). However, outside the wire loop, increasing the distance from the wire, the RF power broadening is expected to be comparable with the optical power broadening, thus making our hypothesis weaker. As a consequence, the FWHM and the amplitude of the RF field have not exactly the same behaviour. Second, the $1/d$ decreasing behavior of the magnetic field amplitude is valid for an infinite straight wire carrying current, whereas, in our case, the radius of curvature of the wire loop is comparable with the distance between the wire and the measurement area. Finally, since the diamond sensing area is not exactly in the plane of the antenna, the angle between the RF field and the NV center axis depends on the distance from the antenna. They can be approximated to be perpendicular for NV centers far from the antenna, but not for those close to it. Since the coupling between the NV centers and the RF field depends on their reciprocal orientation section 1.2.3, this effect can cause a discrepancy between data and theory.

The previous experiment demonstrated that the CW-ODMR linewidth is a useful and simple tool to map the RF near field emitted by a RF device. Moreover, using eq. (4.1) it is possible to estimate the order of magnitude of the Rabi frequency and thus the amplitude of the RF field applied to the NV centers. The values of Γ_p^∞ and

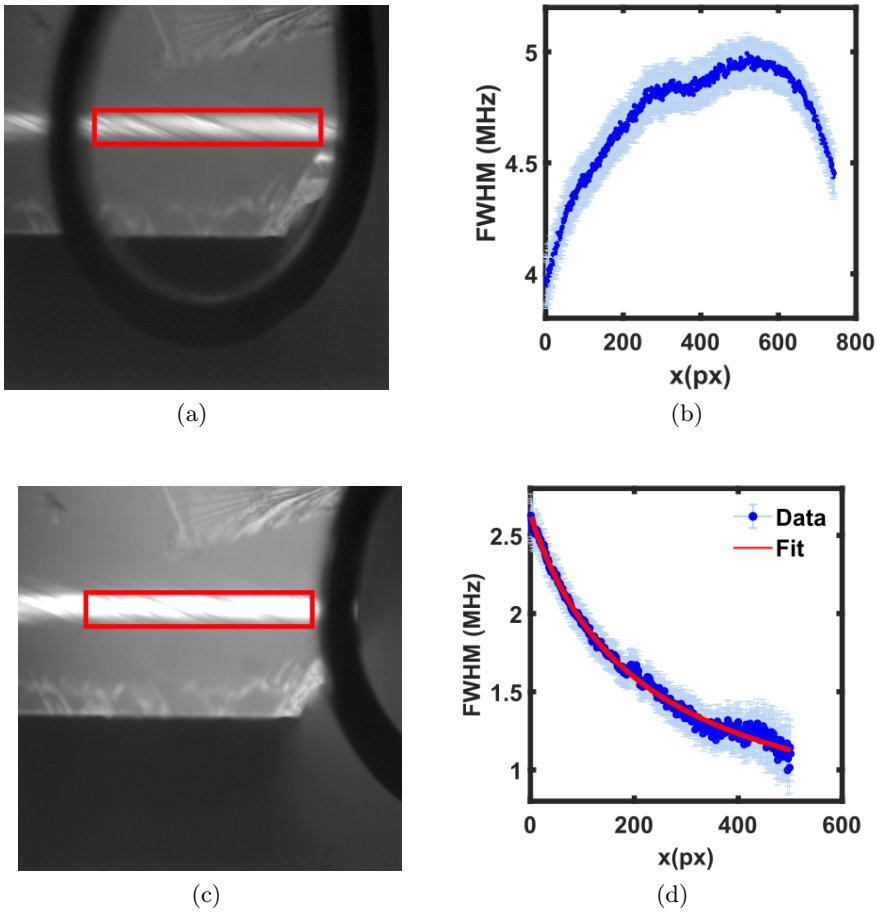

Figure 4.3: CW-imaging of the RF near field emitted by our loop antenna. (a)-(c) Full frame images of the camera for two experimental configurations. We can recognize the diamond (light grey rectangle), the laser beam (white beam) and the shadow of the antenna (black circle in (a) and black arc of circle in (c)). In (a) the NV centers imaged by the camera AOI (red rectangle) are at the center of the antenna (a). In (c) they are outside the antenna (c). (b)-(d) FWHM of the ODMR spectrum of the NV centers embedded in the diamond area imaged by the camera AOI. In (d) the fit is done using eq. (4.3).

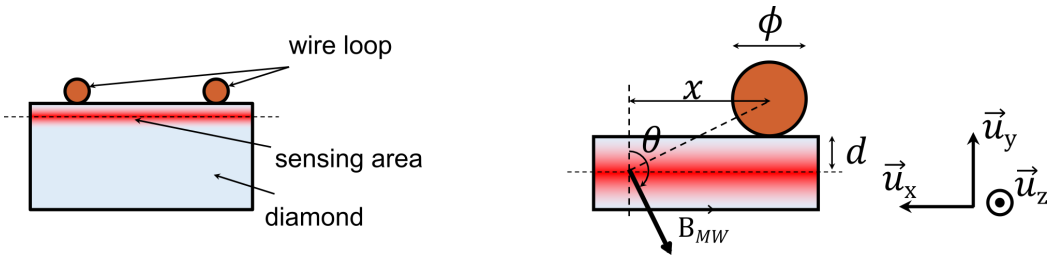

Figure 4.4: Orientation of the MW field with respect to the sensing area. On the left we can observe that the diamond area used for sensing is not exactly in the plane of the antenna, which is posed on the top [110] facet of the crystal. On the right we can observe that the orientation between the MW field and the diamond [110] facet (and thus the two NV center families laying on this plane) depends on the distance from the wire (x).

Γ_c^∞ are chosen in agreement with [48] (see also section 1.2.5): $\Gamma_p^\infty = 5 \cdot 10^6 s^{-1}$ and $\Gamma_c^\infty = 80 \cdot 10^6 s^{-1}$. The parameter $s = P/P_{Sat}$ can be either determined measuring the NV center PL saturation curve or estimated considering the pumping parameter of the experiment. The second way is followed in this manuscript. According to [137], the NV center saturation intensity is: $I_{Sat} \approx 1 - 3$ mW/μm^2. In our experimental set-up, where NV centers are excited by a Gaussian beam of waist $w_0 \approx 35$ μm, the saturation power is achieved at $P_{sat} = \frac{\pi w_0^2}{2} I_{Sat} \approx 2$W. Therefore, using a laser power of 300 mW, the saturation parameter is $s \approx 0.15$. This value confirms the applicability of eq. (4.1), whose expression is valid for $s > 0.02$. From eq. (4.1), the Rabi angular frequency is equal to:

$$\Omega_R = \sqrt{\frac{(2\pi \cdot FWHM)^2 \Gamma_p^\infty}{\Gamma_c^\infty} - \left(\frac{s}{s+1}\right)^2 \Gamma_P^\infty \Gamma_C^\infty} = 7 \cdot 10^6 \; rad \cdot s^{-1} \tag{4.4}$$

Assuming that the RF field generated by a loop antenna is, in first approximation, linearly polarized, it is possible to deduce the amplitude of the RF magnetic field using eq. (1.23):

$$B = \sqrt{2} \frac{\Omega_R}{\gamma \cdot 2\pi} = 56 \; \mu T \tag{4.5}$$

Considering the magnetic field energy density:

$$u = \frac{1}{2} \frac{B^2}{\mu_0} \tag{4.6}$$

where $\mu_0 = 4\pi \cdot 10^{-7}$ H/m is the vacuum permeability, the RF power associated to the RF field measured using eq. (4.5) can be calculated as:

$$P = u \cdot S \cdot c = \frac{1}{2\mu_0} B^2 \pi R^2 c = \frac{R^2 \Omega_R^2 c}{4\pi \mu_0 \gamma^2} \tag{4.7}$$

where c is the speed of light, S is the surface and $R \approx 300$ μm is the radius of the loop antenna. The value of R is estimated from fig. 4.3a considering that each pixel images a square area of side 0.66 μm (section 2.1.4). We obtain: $P \sim 100$ mW (~ 20 dBm), which is of the same order of magnitude as the nominal power set on the RF generator (25 dBm). It is important to remark that this estimation does not take into account neither the spatial distribution of the RF field, which is assumed homogeneous inside the antenna and zero outside it, nor the imperfect shape of the loop, nor the orientation of the RF field with respect to the NV center axis.

To conclude, it has been shown that the CW-ODMR linewidth allows estimating conveniently the RF field emitted in near-field by an antenna. However, in order to quantitatively measure the amplitude of the RF field, a calibration of the system is necessary since, using the simple two-level system model, both the CW-ODMR linewidth and the CW-ODMR contrast are related to the Rabi Frequency by parameters which are not physical constant but depend on the sample and the experimental architecture. For this reason, in the next paragraphs, we investigate a method to directly detect the NV center Rabi oscillations and therefore directly measure the Rabi frequency.

4.2 Rabi oscillations: experimental set-up

The detection of NV center Rabi oscillations using an ensemble of NV centers and a widefield imaging system was introduced in chapter 1. The advantage of this method

with respect to the one described in the previous paragraph is the opportunity to directly measure the angular Rabi frequency Ω_R and therefore the amplitude of the RF field without any calibration procedure.

A schematic of the experimental set-up realized to investigate the NV centers Rabi oscillations is depicted in fig. 4.5. The right side of the image are shows the optical pumping branch and the RF branch of the experimental set-up. The left side of the image shows the imaging system, whose description can be found in section 2.1. The laser pulses are generated by means of an AOM in a double pass configuration while the RF pulses are generated by means of a RF switch. A delay generator controlled by a PC is used to synchronize the laser and the RF pulses.
The laser is focused with a waist of $\sim 15\ \mu m$ on the diamond 100 facet and the PL is collected from the top 110 facet. The AOM specifications set the maximum nominal power of the laser to 500 mW, which corresponds to a power of approximately 250 mW on the diamond. The losses are caused by both the AOM, whose double pass efficiency is 84%, and the several optics along the beam optical path. Considering a beam waist $w_0 \sim 15\mu m$ and an NV saturation intensity $I_{sat} \sim 2$ mW/μm^2, the saturation power in this experimental architecture is given by: $P_{sat} = \frac{\pi w_0^2}{2} \cdot I_{sat} \sim 700$ mW. Therefore using a laser power in the range [75 mW, 250 mW] the saturation parameter s is in the range [0.1 0.3]. For technical reasons, differently from the experimental architecture used until now in this manuscript, in the new architecture depicted in fig. 4.5 the laser beam propagates along the y axis of the laboratory frame and it is focused in the diamond plate through a [100] face.
A schematic of the view from the camera is shown in fig. 4.6. The arrangement of magnets is the same as section 4.1. The image acquired by the camera (xy plane), the widefield ODMR spectrum (yf plane) and two single pixel spectra are reported in fig. 4.7. In the xy plane it is possible to recognize the PL striations (section 2.2) which cause the contrast inhomogeneity visible in the yf plane. The widefield ODMR spectrum in the yf plane shows the presence of a residual magnetic field gradient along the y direction. Looking at the single pixel spectra at the top and the bottom of the image (fig. 4.7c) a frequency shift of 400 kHz is detected for the $|0\rangle \rightarrow |-1\rangle$ transition.

4.2.1 The pulse sequence

As discussed in section 1.3.2, the pulse sequence employed to detect NV center Rabi oscillations by means of a widefield imaging system differs from the one used when the detection is performed by an APD (fig. 4.8). In the second case (fig. 4.8a), a long laser pulse completely polarizes the NV center and, after a waiting time of some hundreds of ns, necessary to empty the metastable state, a RF pulse is used to manipulate the NV center spin state. The spin readout is performed gating the APD for a short time (some hundred of ns) at the beginning and the end of the laser pulse. The PL acquired at the beginning of the laser pulse contains information about the spin state while the PL acquired at the end of the laser pulse, when the NV centers are polarized in $|0\rangle$, constitutes a reference signal. Using this acquisition procedure, the spin readout does not depend on the laser pulse duration.
A similar scheme is unfeasible using a widefield imaging system because the characteristic time of a camera is extremely longer than the APD characteristic time (4-5 orders of magnitude). For this reason, a different pulse sequence is usually implemented when the Rabi oscillations are detected by a camera. (fig. 4.8b).
For the widefield detection of Rabi oscillations a sequence of M laser pulses, each of them followed by a RF pulse of length τ, is sent on the diamond during a single exposure of the camera. The same sequence is repeated with the RF field off, in order to acquire a reference image which is then subtracted from the image acquired with the

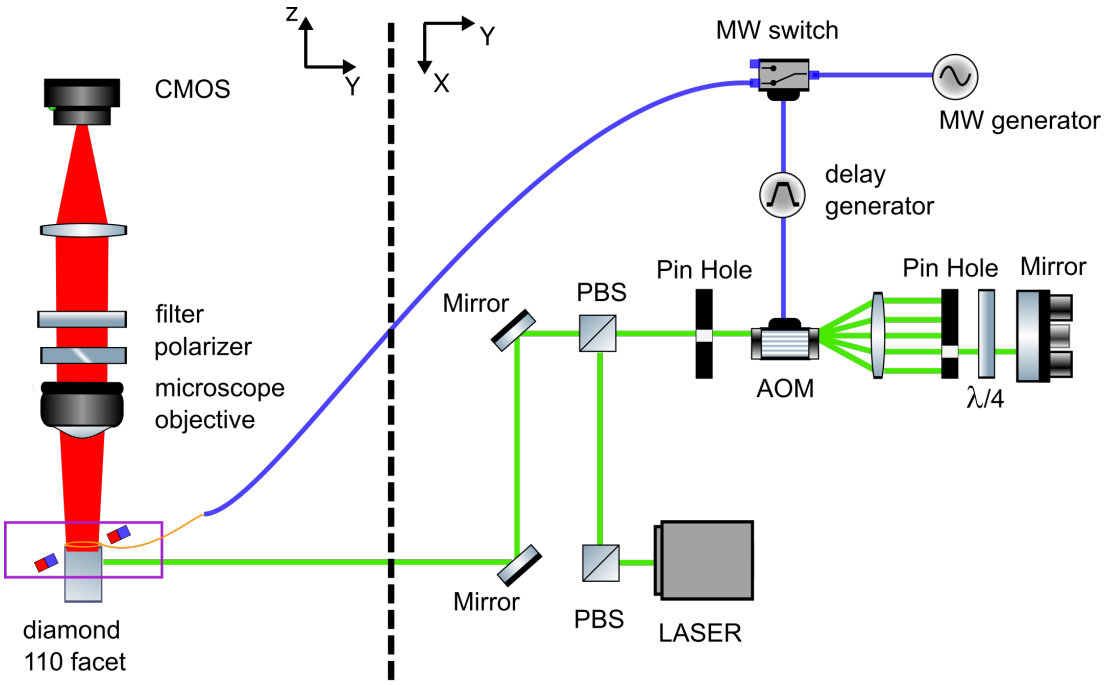

Figure 4.5: Rabi oscillations experimental set-up. At the left of the dashed line is reported the imaging branch of the experimental set-up. The view corresponds to the y-z plane of the laboratory reference frame, being the x-y plane the plane parallel to the optical table. At the right of the dashed line are reported the RF and the optical pumping branches. The view corresponds to the x-y plane. The imaging branch of the experimental set-up is the same as the one described in section 2.1. The only difference is that, in this case, the laser beam is sent on the diamond through a [100] face instead of a [110] facet. In the optical pumping branch of the set-up it is possible to observe the AOM in the double-pass configuration. The laser beam goes through two polarizing beam splitters (PBS) before being diffracted by the AOM. Only the first order of diffraction is back-reflected by a mirror and passes a second time through the AOM. After the second passage through the AOM only the first order of diffraction passes through a pinhole. The second diffraction is not represented to make easier the reading of the image. A quarter-wave plate placed after the AOM turns, after the double pass, the laser linear polarization of 90° so that the beam is transmitted by the PBS and, with the help of some mirrors and lens (here not represented), is focused on the diamond. The RF branch of the system consists of a MW generator connected to a MW switch which is driven by the same delay generator used to drive the AOM. The output signal of the switch is sent in proximity of the NV center by means of a loop antenna.

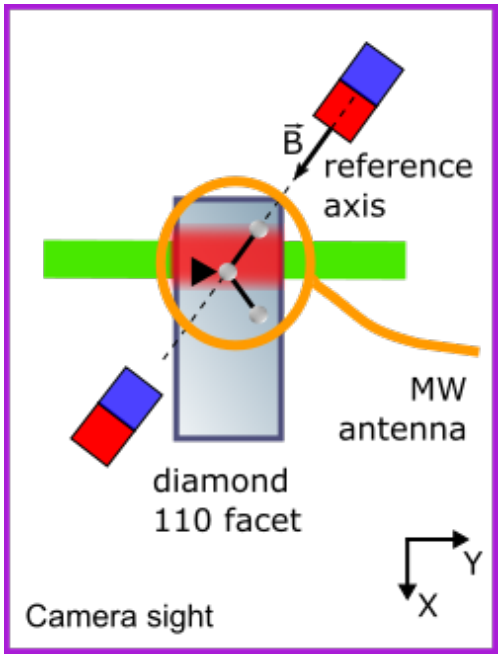

Figure 4.6: View from the camera of the diamond area in the violet rectangle of fig. 4.5. Differently from the experimental set-up reported in fig. 4.1, the beam propagation axis is the y axis. The magnets are arranged in order to minimize the magnetic field gradient. The magnetic field is aligned along one of the two NV center families (reference axis) laying in the diamond [110] plane

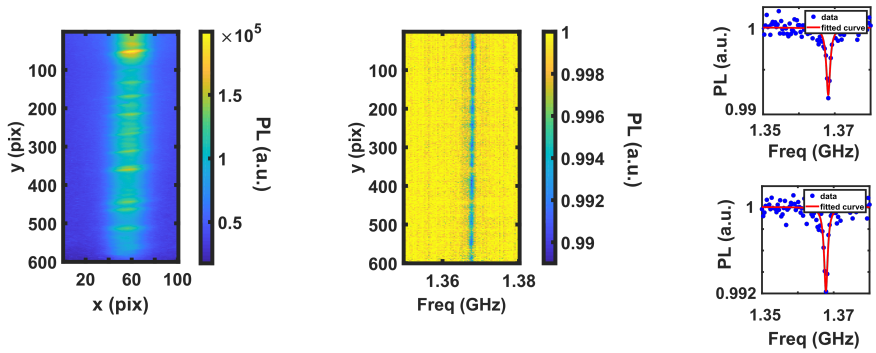

(a) (b) (c)

Figure 4.7: CW-ODMR. (a) x-y plane imaged by the camera. (b) CW-ODMR spectrum in the x-f plane. (c) single pixel spectrum. On the top, the spectrum acquired for the pixel of position (x=100,y=55), at the bottom (x=550,y=55).

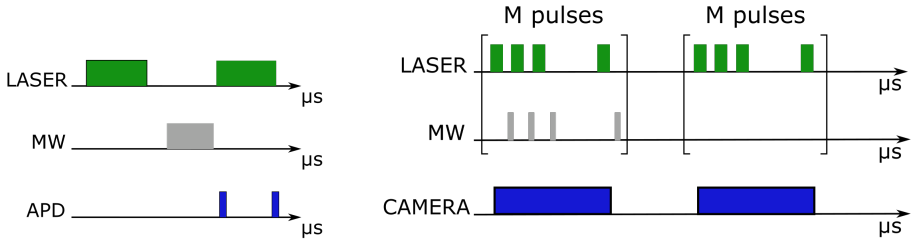

(a) (b)

Figure 4.8: Pulse sequence for the detection of NV centers Rabi oscillations using an APD (a) and a camera (b).

RF on. This procedure is then repeated N times in order to increase the SNR of the measurement (section 2.1.5). Scanning the RF pulse duration τ it is then possible to retrieve the Rabi oscillations.
Using this pulse sequence, differently from the acquisition procedure depicted in fig. 4.8a, the readout process and the polarization process are not independent because the camera detects the PL emitted by the NV centers during all the duration of the laser pulses. For this reason, a compromise must be found in order to use a laser pulse duration sufficiently long to polarize the NV center but sufficiently short to allow the spin state readout (fig. 1.14a). The NV center dynamics during the pulse sequence can be better understood with the help of some simulations, and it is the subject of section 4.4.

The experimental pulse sequence

After having introduced the general pulse scheme used to detect NV center Rabi oscillations by means of a widefield imaging system, we describe in detail the experimental pulse sequence.
We use a laser pulse duration of the order of some μs. The waiting time between the laser pulse and the RF pulse is set to 400 ns and the RF pulse duration is of the order of some μs. The choice of those parameters is discussed in section 4.4. In the following, we refer to the sequence composed by the laser pulse, the waiting time, and the RF pulse as a pulse cycle. Typical exposure times of the camera are several tens of ms. This value is chosen in order to bring the counts of the camera close to their saturation value. Assuming a typical period (T) of 5 μs for each pulse cycle, there are approximately $M(T) = 10^4$ cycles for each exposure of the camera (50 ms). For a given value of RF pulse duration (τ), $N(\tau)$ images are acquired. Since the value of M depends on the period of the cycle and thus on τ, the value of $N(\tau)$ is differently chosen for each RF pulse duration in order to have almost the same number of pulses ($N(\tau) \cdot M(\tau) \approx 10^6$) and so almost the same SNR for each RF pulse duration.
The AOM and the RF switch are synchronized by means of the delay generator and they are continuously triggered during the acquisition. The camera, which is not controlled by the delay generator[1], is turned on and off, independently on the pulse sequence. Therefore, the camera starts the acquisition randomly during the pulse cycle. That has two main consequences. First, the number of pulses captured with the RF on (signal) and the RF off (reference) for a given RF pulse duration is not exactly the same. That

[1]The delay generator used for the experiment has only two independent outputs which are respectively employed for the RF switch and the AOM driver. Therefore, in order to synchronize the camera, more complex synchronisation procedures need to be considered, i.e.using the camera as an external trigger for the delay generator. However, as described in the main text, the synchronisation of the camera is not necessary for our scopes and that simplifies the acquisition.

results in an incertitude on the number of pulses which is, in the worst case, two pulses for camera exposure. However, considering the high number of pulses for each exposure of the camera and the random nature of the camera acquisition process with respect to the pulse sequence, the difference in the number of pulses between the signal and the reference after N acquisitions is assumed negligible (some pulses over 10^6). Second, even if the number of images (N) acquired for a given RF pulse duration is chosen in order to have almost the same number of cycles for each RF pulse duration ($M(\tau) \cdot N(\tau) \approx 10^6$), it is impossible to have exactly the same number of pulses without changing the exposure time of the camera which, on the contrary, in our experiment is fixed. However this condition is not necessary if, instead of simply considering the difference between the images acquired when the RF field is on and the RF field is off, it is considered the contrast of the measurement (section 2.2). In this case, a different number of pulses for different RF pulse durations has, as only consequence, a different SNR for different RF pulse durations. For a sufficiently high number of pulses, this difference is negligible.

After having described the set-up and the pulse sequence for the widefield detection of NV centers Rabi oscillations, in the next paragraph we present the main results achieved.

4.3 Rabi oscillations: Experimental Results

Using the experimental set-up and the pulse sequence described before, it is possible to detect NV center Rabi oscillations using a widefield imaging system (fig. 4.9). The measurement is performed considering a laser pulse duration of 1 μs and a waiting time of 400 ns between the laser pulse and the RF pulse. The RF pulse duration (τ) is swept from 0.5 μs to 4 μs in steps of 20 ns. The RF generator is set to a nominal power of 23 dBm, which is the maximum RF power that is possible to send on the RF switch. The laser nominal power is set to 150 mW. Figure 4.9a shows the contrast evolution versus the RF pulse duration and it is possible to observe the expected oscillating behaviour. The data are fitted using the fit function [94]:

$$a \cdot (1 - e^{-x/b} \cdot \cos[c \cdot x + d]) \tag{4.8}$$

where $b = 1.08 \pm 0.08$ μs is the decay time of the Rabi oscillations [138] and $c = (12.0 \pm 0.2) \cdot 10^6$ rad$\cdot$ s^{-1} is the Rabi angular frequency. $a = 0.0206 \pm 0.0002$ is related to the contrast of the measurement and d is a phase term which accounts for the fact that, for technical reason, the acquisition started at 0.5 μs instead of 0 μs.
The Rabi frequency can also be evaluated using an FFT approach (fig. 4.9b). We obtain a Rabi frequency of $\nu_R^{FFT} = 1.90 \pm 0.09$ MHz in agreement with the Rabi frequency estimated by the fit $\nu_R^{fit} = \frac{\Omega_R}{2\pi} = 1.91 \pm 0.02$ MHz.
Using eq. (4.5), it is possible to calculate the amplitude of the RF field. We obtain: $B = 96 \pm 1$ μT. As we did in section 4.1, we calculate the power associated with the RF field using eq. (4.7). Assuming a radius of 300 μm, we obtain P=25 dBm, which is of the same order of magnitude as the RF nominal power (23 dBm). In fig. 4.10, the measured Rabi angular frequency is plotted for different RF powers. As expected, the Rabi frequency scales linearly with the square root of the RF power which is proportional to the amplitude of the RF field (eq. (4.7)). This measurement confirms that our system is able to measure the amplitude of the RF field emitted in the near-field region by a RF device.
Comparing the data and the fit in fig. 4.9,an unexpected asymmetric sinusoidal shape of the Rabi oscillations can be observed. This shape changes and tends to a well symmetric sine wave increasing the laser pulse duration (fig. 4.11a) or the laser power (fig. 4.11b). Moreover the contrast of the measurement decreases by increasing the laser power or

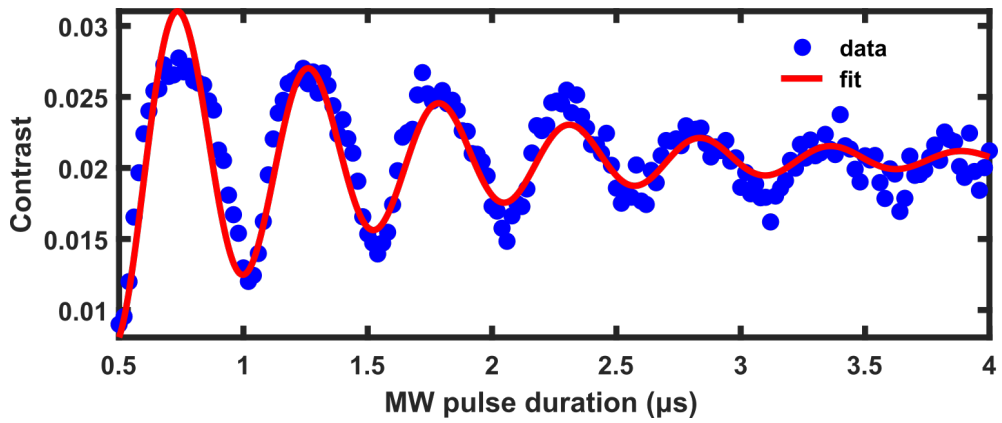

(a)

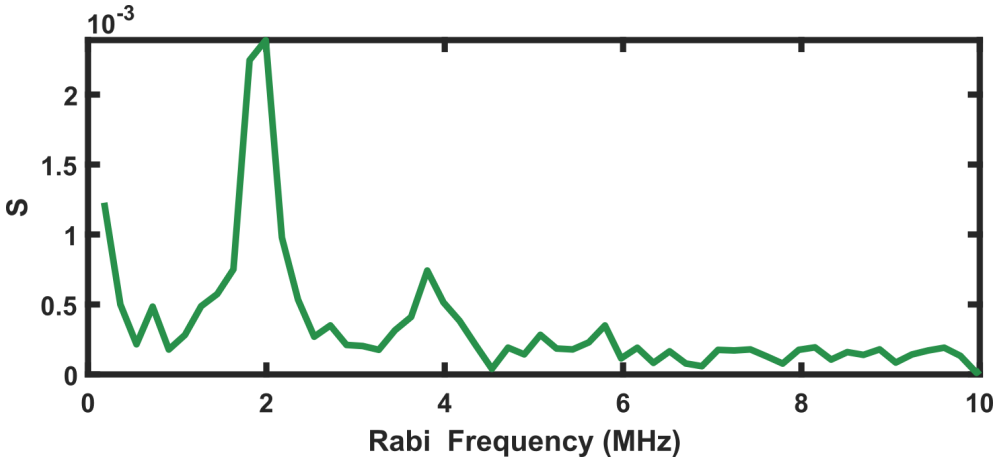

(b)

Figure 4.9: Widefield detection of NV center Rabi oscillations. (a) Contrast evolution versus the RF pulse duration. The fit is realized using eq. (4.8). (b) FFT of the Rabi oscillations plotted in (a). Due to the asymmetry of the Rabi oscillations, in the spectrum of the signal it is possible to recognize the first harmonics.

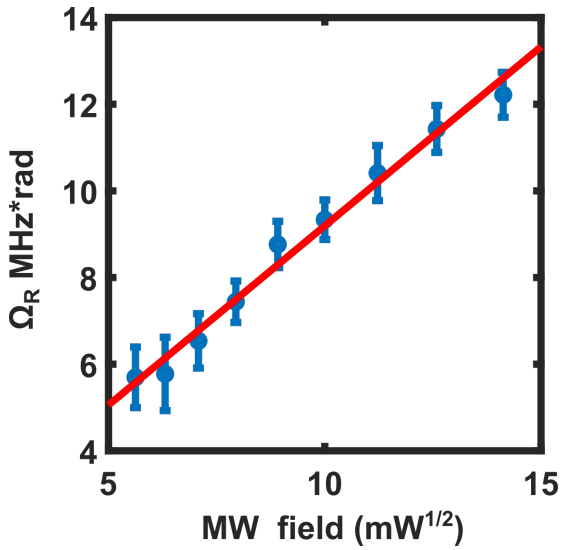

Figure 4.10: Power-dependence of the Rabi angular frequency.

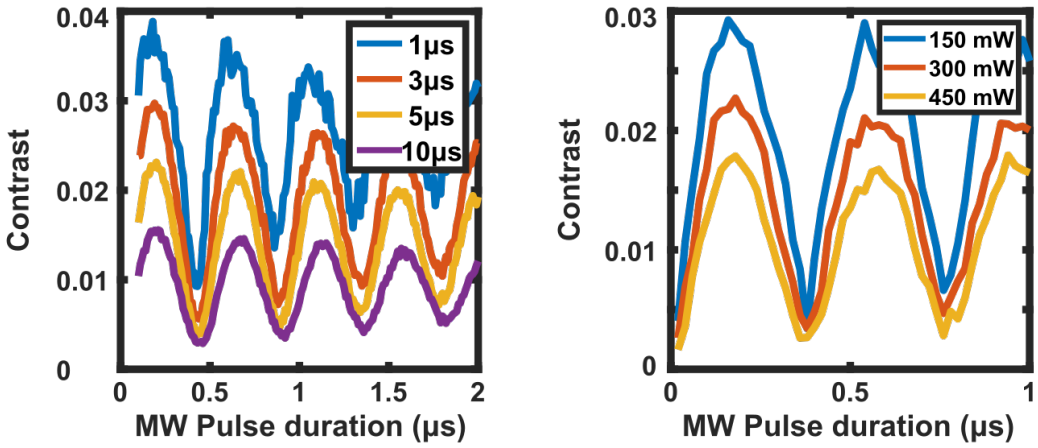

(a) (b)

Figure 4.11: NV centers Rabi oscillations for different laser pulse durations (a) and laser powers (b). (a) The laser power is set to 150 mW and the laser pulse duration is swept. The laser pulse durations are reported in the legend of the plot. (b) The laser pulse duration is set to 2 μs and the laser power is swept. The laser powers are reported in the legend of the plot. (a-b) It is possible to observe a slight detuning between the different curves. It comes from mechanical vibrations and temperature fluctuations of the system which induce fluctuation in the static magnetic field and therefore in the NV center resonance frequency during the measurement time.

Ω_R (MHz)	2	2	0.5	0.5
$\Delta\omega$ (MHz)	2.14	0.3	2.14	0.3
$\frac{\Omega_R^2}{\Omega_R^2+(\Delta\omega)^2}$	0.42	0.97	0.05	0.73
$\sqrt{\Omega_R^2+\Delta\omega^2}$	2.92	2.02	2.16	0.58

Table 4.1: Detuning parameters

the laser pulse duration. This behaviour is investigated in section 4.4 with the help of some simulations.

4.3.1 The effect of the detuning on the Rabi oscillations

The effect of the detuning on the Rabi oscillations has already been discussed in section 1.2.3. Here we report the formula of the Rabi oscillations:

$$P(t,\omega) = \frac{\Omega_R^2}{\Omega_R^2+(\Delta\omega)^2}\sin^2\left[\sqrt{\Omega_R^2+(\Delta\omega)^2}\frac{t}{2}\right] \tag{4.9}$$

The two main effects caused by the detuning ($\Delta\omega$) are: a reduction of the Rabi oscillations amplitude by a factor $\frac{\Omega_R^2}{\Omega_R^2+(\Delta\omega)^2}$, and an increase of the oscillations frequency, which becomes: $(\sqrt{\Omega_R^2+\Delta\omega^2})$. In Table 4.1 we report the effect of the detuning in two different cases:

- for a detuning of 2.14 MHz, which is the frequency shift between the NV center hyperfine peaks;

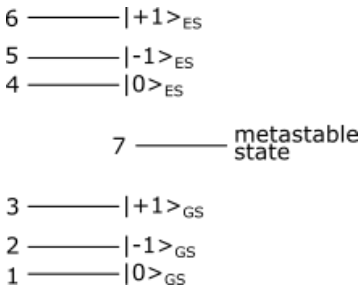

Transition	Transition rate (μs^{-1})
$k_{41} = k_{52} = k_{63}$	64.9
k_{47}	10.6
$k_{57} = k_{67}$	80
k_{71}	2.6
$k_{72} = k_{73}$	3

Figure 4.12: Room temperature NV center transition rates. On the left, the NV center is approximated to a seven-level system. On the right, the NV center rate transitions (k_{ij}) between the level i and the level j [36].

- for a detuning of 300 kHz, which is the order of magnitude of the detuning induced by the static magnetic field gradient on the diamond area imaged by the camera (fig. 4.7).

In table 4.1 we consider two different Rabi frequencies: 2 MHz and 0.5 MHz. For a detuning of 2.14 MHz and a low Rabi frequency (0.5 MHz), the Rabi oscillations show a contrast 95% smaller than the zero-detuning contrast. Instead, at high Rabi frequencies (2 MHz), the contrast is reduced only by a factor 2 and the frequency of the oscillations is increased by almost a factor of $\sqrt{2}$ with respect to the on resonance case. Therefore, assuming to be on resonance with one of the three NV center hyperfine transitions, at high RF power the Rabi oscillations are affected by the NV center hyperfine structure while this is not the case at low RF power. The easiest way to avoid this effect is working, as we do, in proximity of the ESLAC where the nitrogen nuclear spin is polarized.
A detuning of 300 kHz, at high Rabi frequencies, induces neither remarkable contrast losses nor remarkable variations of the oscillation frequencies, confirming the interest in working with a two-magnet architecture to minimize the static magnetic field gradient. On the contrary, at low Rabi frequencies, even a small detuning induced by the static magnetic field gradient tends to reduce the contrast and to alter the frequency of the oscillations.

4.4 Rabi oscillations: simulation

4.4.1 The model

The pulse sequence implemented for the widefield detection of NV center Rabi oscillations (fig. 4.8b) can be essentially divided in three different processes: the NV center optical polarization, the depletion of the NV center metastable state and the NV center ground state spin manipulation.
The first and the second process can be studied solving the NV center rate equations for a seven-level system without considering the coherence of the system. Using the

level notation and the decay rates reported in fig. 4.12, we can write:

$$\frac{dn_1}{dt} = -n_1 W_p + n_4 k_{14} + n_7 k_{17} \tag{4.10a}$$
$$\frac{dn_2}{dt} = -n_2 W_p + n_5 k_{25} + n_7 k_{27} \tag{4.10b}$$
$$\frac{dn_3}{dt} = -n_3 W_p + n_6 k_{25} + n_7 k_{27} \tag{4.10c}$$
$$\frac{dn_4}{dt} = n_1 W_p - n_4 k_{14} - n_4 k_{47} \tag{4.10d}$$
$$\frac{dn_5}{dt} = n_2 W_p - n_5 k_{25} - n_5 k_{57} \tag{4.10e}$$
$$\frac{dn_6}{dt} = n_3 W_p - n_6 k_{14} - n_6 k_{57} \tag{4.10f}$$
$$1 = n_1 + n_2 + n_3 + n_4 + n_5 + n_6 + n_7 \tag{4.10g}$$

The last equation accounts for the fact that we are considering a closed system.
The third process, that is the NV center spin manipulation by means of a RF field, can be studied solving the NV center Bloch equations for the $|0\rangle$ and $|-1\rangle$ (or $|+1\rangle$) NV center ground state levels (eq. (1.30)). To simplify the reading, the Bloch equations are here reported:

$$\frac{d\varrho_{11}}{dt} = \Gamma_1 (\varrho_{00} - \varrho_{11}) + \Omega_R \Im [\varrho_{01}] \tag{4.11a}$$
$$\frac{d\varrho_{00}}{dt} = -\Gamma_1 (\varrho_{00} - \varrho_{11}) - \Omega_R \Im [\varrho_{01}] \tag{4.11b}$$
$$\frac{d\Im [\varrho_{01}]}{dt} = -\frac{\Omega_R}{2} (\varrho_{11} - \varrho_{00}) - \Gamma_2 \Im [\varrho_{01}] - \delta\omega \Re[\varrho_{01}] \tag{4.11c}$$
$$\frac{d\Re [\varrho_{01}]}{dt} = +\delta\omega \Im[\varrho_{01}] - \Gamma_2 \Re[\varrho_{01}] \tag{4.11d}$$

Assuming a RF field on resonance with NV centers, $\delta\omega \sim 0$ (or more generally $\delta\omega << \Gamma_2$), eq. (4.11d) is independent from the first three equations and it can be neglected.

The rate equations (eq. (4.10)) and the Bloch equations (eq. (4.11)) can be merged to obtain a single set of equations which describes the entire pulse cycle. To do this, the RF pumping process and the coherence terms of the Bloch equations are added in the rate equations model. Since in the experiment the degeneracy between the $|-1\rangle$ and $|+1\rangle$ states is removed by a static magnetic field and it is possible to address only one of the two NV center transitions, in the model we assume that the RF field only drives the $|0\rangle \rightarrow |-1\rangle$ transition. Moreover, in first approximation, the spin-lattice relaxation process can be neglected since its characteristic time ($T_1 \approx$ ms) is more than two orders of magnitude larger than the characteristic time of the pulse cycle ($<10\ \mu s$). Therefore,

from eq. (4.10) and eq. (4.11) we can write:

$$\frac{dn_1}{dt} = -n_1 W_p + n_4 k_{14} + n_7 k_{17} + \Omega_R \cdot n_c \tag{4.12a}$$
$$\frac{dn_2}{dt} = -n_2 W_p + n_5 k_{25} + n_7 k_{27} - \Omega_R \cdot n_c \tag{4.12b}$$
$$\frac{dn_3}{dt} = -n_3 W_p + n_6 k_{25} + n_7 k_{27} \tag{4.12c}$$
$$\frac{dn_4}{dt} = n_1 W_p - n_4 k_{14} - n_4 k_{47} \tag{4.12d}$$
$$\frac{dn_5}{dt} = n_2 W_p - n_5 k_{25} - n_5 k_{57} \tag{4.12e}$$
$$\frac{dn_6}{dt} = n_3 W_p - n_6 k_{14} - n_6 k_{57} \tag{4.12f}$$
$$1 = n_1 + n_2 + n_3 + n_4 + n_5 + n_6 + n_7 \tag{4.12g}$$
$$\frac{dn_c}{dt} = -\Gamma_2 \cdot n_c + \frac{\Omega_R}{2} \cdot (n_2 - n_1) \tag{4.12h}$$

where, in order to uniform the notation, we define $n_c = \Im[\varrho_{01}]$ and we assume the RF transition on resonance with the $|0\rangle \rightarrow |-1\rangle$ transition ($\delta\omega = 0$).
The PL emitted by the system is given by:

$$PL \propto n_4 + n_5 + n_6 \tag{4.13}$$

and the NV center ground state optical polarization in $|0\rangle$ is given by:

$$P_{GS} = \frac{n_1}{n_1 + n_2 + n_3} \tag{4.14}$$

4.4.2 The results

The saturation parameter

In the model (eqs. (4.12) and (4.10)) the laser power is taken into account by the pumping parameter W_p. In order to relate W_p to the NV center saturation parameter $s = P/P_{sat}$, the NV center PL saturation curve is simulated and fitted by a saturation law:

$$PL = a\frac{\frac{W_p}{b}}{1 - \frac{W_p}{b}} \tag{4.15}$$

The NV center PL saturation curve is simulated solving the NV center rate equation (eq. (4.10)) in the steady state condition for different values of W_p. For each value of W_p the NV center PL is evaluated according to (eq. (4.13)). The results are plotted in fig. 4.13 and fitted by the saturation law in eq. (4.15). From the fit it is obtained: $b = W_p^{sat} = 2 \cdot 10^7\ s^{-1}$. Since the saturation parameter used in the experiment is in the range s=[0.1 0.3] (section 4.2) and more in particular a saturation parameter of s=0.15 is used for the detection of the Rabi oscillations reported in fig. 4.9, in the simulation it is considered a pumping parameter $W_p = W_p^{sat} \cdot s = 3 \cdot 10^6\ s^{-1}$.

The ground-state polarization time

The NV center rate equations (eq. (4.10)) allow evaluating the time needed to optically polarize the NV centers assuming they are initially in the thermal equilibrium state. Figure 4.14a reports the time-evolution of the ground state polarization (eq. (4.14)) for different pumping parameters. The initial condition is set to the thermal equilib-

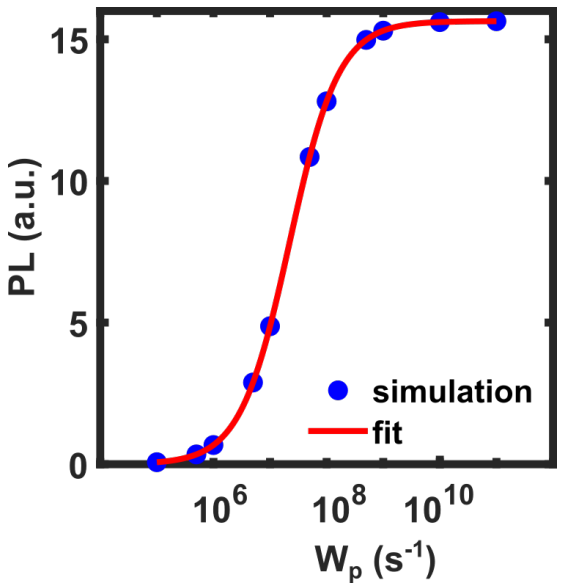

Figure 4.13: Simulation of the NV center PL saturation curve. The fit is realized using eq. (4.15).

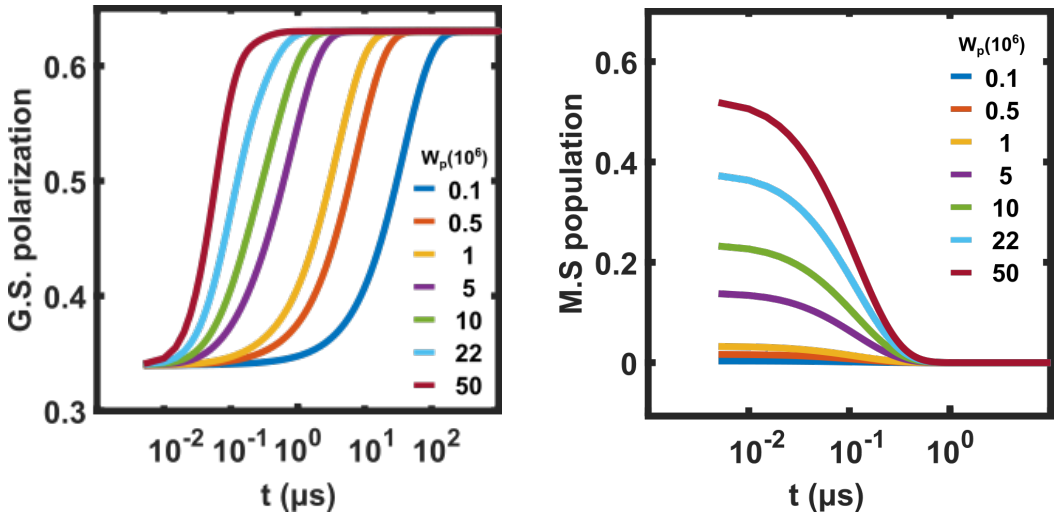

(a) (b)

Figure 4.14: (a) Time evolution of the NV center ground state polarization under different laser pumping parameters. (b) Time evolution of the NV center metastable state population for different laser pumping parameters.

rium condition: $n = (n_1, n_2, n_3, n_4, n_5, n_6) = (1/3, 1/3, 1/3, 0, 0, 0)$. Increasing W_p, the laser pulse duration necessary to polarize the NV center decreases. For a pumping parameter of the order of $W_p = 10^6\ s^{-1}$, the system is polarized after approximately 10 µs.

The metastable state depletion time

Using the NV center rate equations (eq. (4.10)) and setting $W_p = 0$ after having completely polarized the NV center, it is possible to evaluate the metastable state depletion time. The time-dependent metastable state population is plotted in fig. 4.14b, for different values of the pumping parameter. This figure shows two interesting results. First, the metastable population depends on the pumping parameter and is higher at high pumping rate. Second, the time needed to completely empty the metastable state is of the order of 400 ns. Therefore, this is usually the waiting time left between the laser pulse and the RF pulse.

The simulation of the Rabi oscillations

Now that the laser pulse duration necessary to polarize the NV centers and the waiting time necessary to empty the metastable state are known, it is possible to simulate the behaviour of an ensemble of NV centers under the pulse sequence described in fig. 4.8b. The simulation is done using the model in (eq. (4.12)) and consists in three steps: the simulation of the laser pulse, the simulation of the waiting time to empty the metastable state and the simulation of the RF pulse. For each step the rate equations are solved using as initial condition the final condition of the previous step. The initial condition of the first step is the thermal equilibrium state $n = (n_1, n_2, n_3, n_4, n_5, n_6, n_c) = (1/3, 1/3, 1/3, 0, 0, 0, 0)$.
To simulate the laser pulse, the rate equations (eq. (4.12)) are solved over a time interval equal to the laser pulse duration. Since during the laser pulse the RF field is off, Ω_R is set to 0. The pumping parameter W_p is set, if not differently specified, to $3 \cdot 10^6\ s^{-1}$, which corresponds to a saturation parameter $s = W_p/W_p^{sat} = 0.15$. To take into account the decoherence introduced by the laser pumping process, the relaxation rate Γ_2 is set equals to $\Gamma_c = \Gamma_c^{\infty} \frac{s}{s+1} = 5 \cdot 10^6\ s^{-1}$ [48].
To simulate the waiting time between the laser pulse and the RF pulse, both Ω_R and W_p are set to 0 and Γ_2 is set to $5 \cdot 10^5\ s^{-1}$, corresponding to a T_2^* of 2 µs. The rate equations are then solved for a time interval of 400 ns.
Finally, to simulate the RF pulse, we set: $\Omega_R = 10 \cdot 10^6$ rad$\cdot s^{-1}$, $W_p = 0$ and $\Gamma_2 = 5 \cdot 10^5\ s^{-1}$.
The duration of the RF pulse is swept in order to simulate the acquisition procedure of the Rabi oscillations and, for each RF pulse duration, the PL is evaluated.
In order to simulate the behaviour of the system when the RF field is off and acquire a reference image, the entire simulation is repeated setting $\Omega_R = 0$ for all the three steps. After having evaluate the PL for both the simulation with the RF on ($PL_{ON}(\tau)$) and the RF off ($PL_{OFF}(\tau)$), the contrast is calculated as: $C(\tau) = \frac{PL_{OFF}(\tau) - PL_{ON}(\tau)}{PL_{OFF}(\tau)}$.

It is interesting to observe that the model described in eq. (4.12) is almost equivalent to a hybrid model in which the rate equations (eq. (4.10)) are applied to solve the first two steps of the pulse cycle and the Bloch equations (eq. (4.11)) are applied to solve the last step. In fact, substituting the model parameters (W_p, Ω_R, Γ_2) in eq. (4.12) it is possible to obtained both eq. (4.10) when $\Omega_R = 0$, that is during the first two steps of the cycle, and eq. (4.11) when $W_p = 0$, that is during the last step of the cycle. Nevertheless, two main differences can be remarked.
First, in the model described by eq. (4.12), the coherence of the system is taken into

account during the laser pulse, whereas this is not the case in the rate equations (eq. (4.10)). However, since during the laser pulse $\Omega_R = 0$, the coherence term (n_c) does not alter the spin polarization process. The coherence term plays a role during the spin manipulation of the system. If the system was solved using the Bloch equations (eq. (4.11)), the initial condition of the coherence term would be equal to zero. Using the model described in eq. (4.12), for $W_p = 3 \cdot 10^6$ s^{-1}, the spin coherence relaxation time is $1/\Gamma_c = 0.2\mu s$ (one order of magnitude shorter than $T_2^* \approx 2$ µs). Therefore after sufficiently long laser pulses (longer than the T_2^*), n_c is almost equal to 0, as it would have been if the system had been solved using the Bloch equations in eq. (4.11).
Second, using eq. (4.12) instead of eq. (4.11) the density matrix is not normalized to one. However, if the metastable state is completely empty and no spin-lattice phenomena are considered ($1/T_1 = 0$), the density matrix of eq. (4.12) preserves its trace. This is equivalent to saying that before applying a RF pulse, the density matrix is multiplied by a normalization factor, and after the RF pulse it is divided by the same normalization factor. This is, by the way, the procedure which is followed when the hybrid model is used to simulate the pulse cycle. Therefore we choose the model described by eq. (4.12) only because it is more compact and easier to handle from a programming point of view. Probably, from a computational point of view, the hybrid model (rate equation and Bloch equations) is more advantageous because a system with fewer differential equations needs to be solved.

Using the model in eq. (4.12), we evaluate the time evolution of the population of NV center energy levels during the pulse sequence implemented for the widefield detection of the Rabi oscillations (fig. 4.15). The green, blue and pink areas of the plot correspond to the three steps of the simulation; respectively the laser pulse of duration 20 μs, the waiting time to empty the metastable state of duration 1 μs and the RF pulse of duration 5 μs. Here a waiting time of 1 μs has been chosen to make easier the reading of the plot. The pulse cycle has been repeated five times and figs. 4.15c and 4.15d show a zoom of the first cycle. During the laser pulse the NV centers are optically polarized in $|0\rangle$ (n_1 and n_4). During the waiting time between the laser pulse and the RF pulse, it is possible to observe firstly the fast depletion of the excited state (n_4, n_5, n_6) and then the depletion of the metastable state, characterized by an increase of the NV center population in the ground state (n_1, n_2, n_3). Finally, during the RF pulse, it is possible to observe the system oscillating between $|0\rangle$ and $|-1\rangle$ (Rabi oscillations) and the coherence term oscillating as well (n_c). After the RF pulse, the pulse cycle starts again with a laser pulse which re-polarizes the NV centers and erases the coherence.

Looking at fig. 4.15a and fig. 4.15b we can observe that, except for the first cycle, the NV center dynamics during the remaining four cycles is the same. For the first cycle, in fact, the initial condition is the population of the NV centers energy levels at the thermal equilibrium while for the other cycles it is related to the duration of the RF pulse. Since during the experiment for a given exposure of the camera hundreds of cycles are performed, the contribution of the first pulse can be neglected. For this reason, in the simulation, the PL is evaluated only during the last cycle, that is when the system is at the equilibrium. The PL is evaluated, for different RF pulse durations, both with the RF field on and the RF off. The contrast is plotted in fig. 4.16a and it is possible to observe the oscillating behaviour typical of the Rabi oscillations. The fit is realized using eq. (4.8) and a Rabi angular frequency of $9.9969 \pm 0.0003 \cdot 10^6$ rad$\cdot s^{-1}$ is measured, in agreement with the value set for the simulation ($10 \cdot 10^6$ rad$\cdot s^{-1}$).

In order to simulate the experimental pulse sequence used in section 4.3, the simulation is repeated using the same parameters, except for the laser pulse duration, which is set to 1 μs. The contrast of the Rabi oscillations is reported in fig. 4.16b. Comparing fig. 4.16a and fig. 4.16b it is possible to observe, in the second case, a higher contrast and an asymmetry in the shape of the Rabi oscillations. This behaviour is in agree-

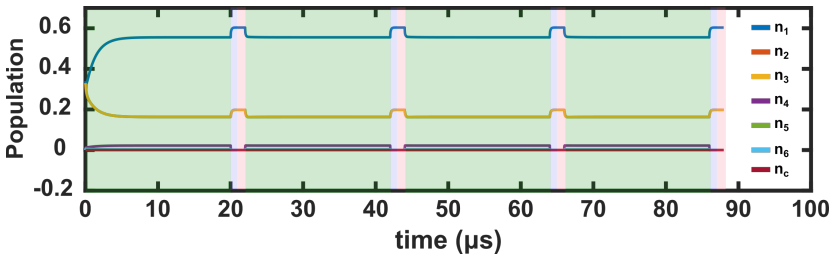

(a)

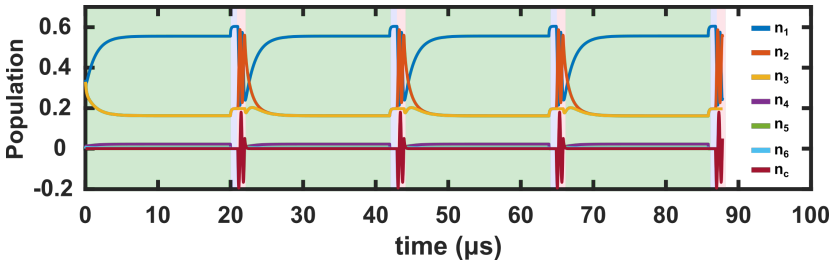

(b)

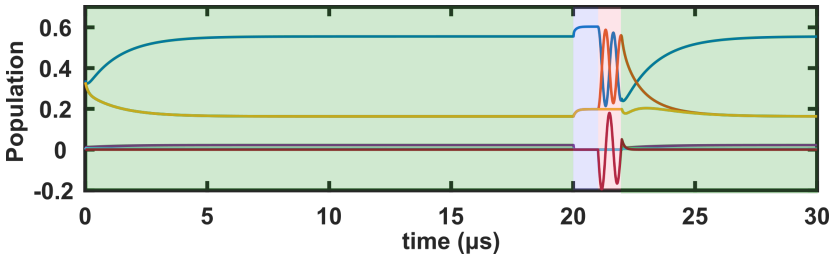

(c)

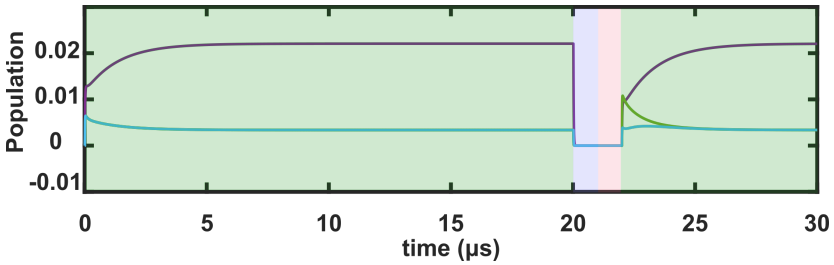

(d)

Figure 4.15: Time evolution of the NV centers levels population during the pulse sequence used to detect the Rabi oscillations both with the RF field OFF (a) and ON (b-d).(c-d) represents a zoom of the first cycle of (b) in order to better analyse the behaviour of the NV center ground state (c) and excited state (d). The green areas correspond to the laser pulse, the light blue areas correspond to the waiting time between the laser pulse and the RF pulse, the pink areas correspond to the RF pulse; When not visible, the plot of the $|-1\rangle$ states is superposed to the plot of the $|+1\rangle$ states

.

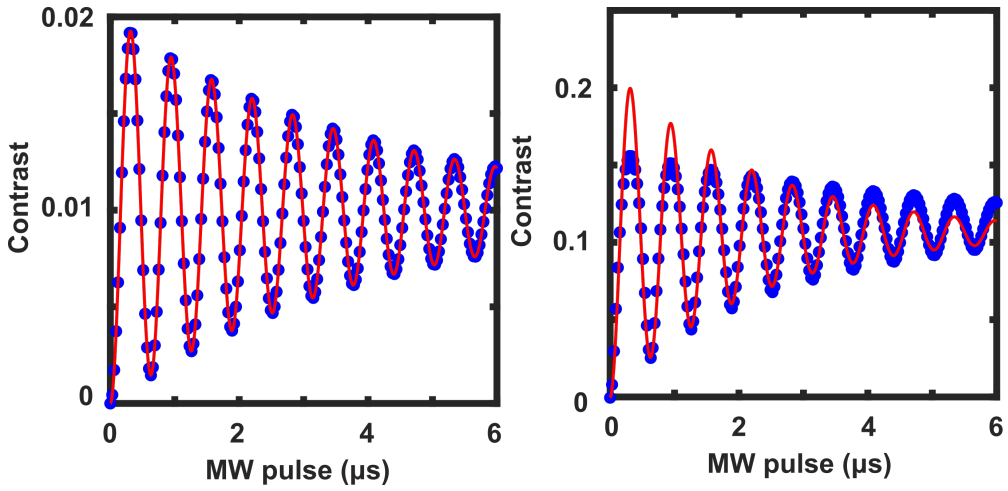

(a) (b)

Figure 4.16: Simulation of the NV centers contrast for different values of RF pulse duration. The simulation is realized using a pumping parameter $W_p = 3 \cdot 10^6\ s^{-1}$, a Rabi angular frequency $\Omega_R = 10 \cdot 10^6$ rad$\cdot s^{-1}$ and a $\Gamma_2 = 0.5 \cdot 10^6\ s^{-1}$. The RF pulse duration is swept in steps of 30 ns. The laser pulse is 20 μs in (a) and 1 μs in (b).

ment with the experimental results. From the fit (eq. (4.8)) we obtain a Rabi angular frequency equal to $9.99 \pm 0.04 \cdot 10^6$ rad$\cdot s^{-1}$, in agreement with the value set for the simulation ($10 \cdot 10^6$ rad$\cdot s^{-1}$). As expected the asymmetry of the oscillations results in a higher uncertainty on the fit parameters with respect to the previous case.
To figure out the asymmetric shape of the Rabi oscillations, we compare the NV center level populations for a laser pulse of duration 20 μs (fig. 4.17) and a laser pulse of duration 1 μs (fig. 4.18). The comparison is done at both a π pulse and a 2π pulse.

A laser pulse duration of 20 μs (fig. 4.17) is sufficiently long to completely re-polarize the NV centers after a RF pulse and thus the Rabi oscillations have always the same initial conditions and the same amplitude, independently of the RF pulse duration. As a consequence, the contrast evolution versus the RF pulse duration has a symmetric sinusoidal shape. A laser pulse duration of 1 μs (fig. 4.18) is not long enough to completely re-polarize the NV centers and therefore the initial condition and the amplitude of the Rabi oscillations depends on the RF pulse duration (fig. 4.18). As a consequence, the contrast evolution versus the RF pulse duration has an asymmetric shape.
Using a more intuitive point of view, we can imagine that a short laser pulse is able to re-polarize the NV center after a 2π pulse but not after a π pulse. In fact, in the first case the majority of the NV centers are already in $|0\rangle$ before the laser pulse, whereas in the second case they are essentially in $|-1\rangle$. When the NV centers are better polarized (e.g. after a 2π) the population difference between the $|0\rangle$ and the $|-1\rangle$ is higher than when they are not completely polarized (e.g. after a π) and, as a consequence, the amplitude of the Rabi oscillations is bigger in the first case (fig. 4.18b) than in the second case (fig. 4.18a). This effect causes the detection of asymmetric Rabi oscillations. The asymmetry is less evident for long RF pulse (e.g. 6 μs) because, due to the spin-spin relaxation, the population difference between the $|0\rangle$ and the $|-1\rangle$ states after a 9π pulse and a 10π pulse is lower than the one we have between a π pulse and a 2π pulse. In order to restore the symmetric shape of the Rabi oscillations, it is necessary a laser pulse which is able to completely re-polarize the NV centers, independently of the RF pulse duration. That is accomplished by increasing the laser pulse or the laser power

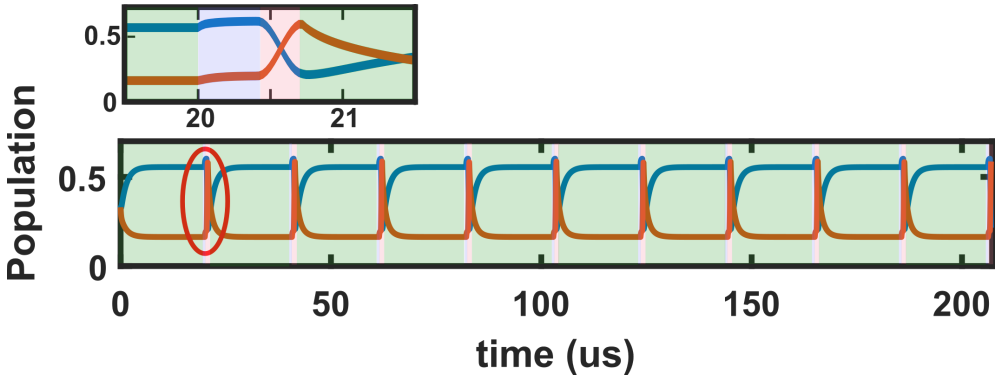

(a)

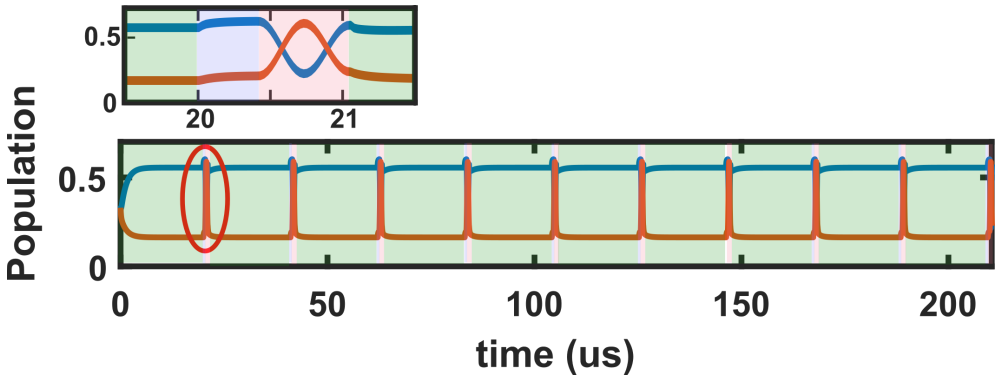

(b)

Figure 4.17: Time evolution of the population of the NV centers ground state $|0\rangle$ (blue curve) and $|-1\rangle$ (orange curve) levels during the Rabi oscillations pulse sequence. The laser pulse duration is 20 μs. (a) RF pulse duration correspondent to a π pulse (b) RF pulse duration correspondent to a 2π pulse. The laser pumping parameter is set to $W_p = 3 \cdot 10^6\ s^{-1}$. The green areas correspond to the laser pulse, the light blue areas correspond to the waiting time between the laser pulse and the RF pulse, the pink areas correspond to the RF pulse. The small plot at the top of the larger one is a zoom of the area in the red circle.

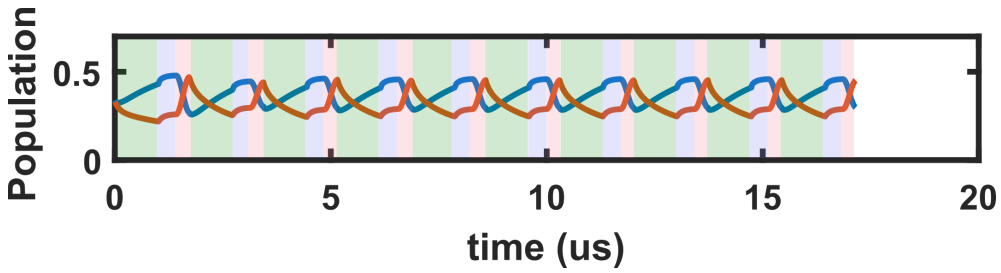

(a)

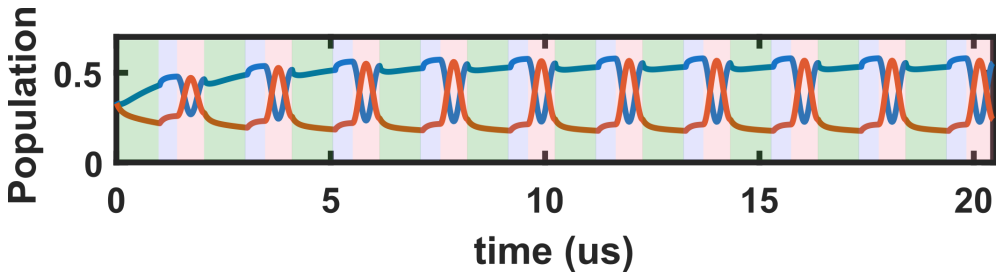

(b)

Figure 4.18: Time evolution of the population of the NV centers ground state $|0\rangle$ and $|-1\rangle$ levels during the Rabi oscillations pulse sequence. The laser pulse duration is 1 μs. (a) RF pulse duration correspondent to a π pulse (b) RF pulse duration correspondent to a 2π pulse. The laser pumping parameter is set to $W_p = 3 \cdot 10^6\ s^{-1}$. The green areas correspond to the laser pulse, the light blue areas correspond to the waiting time between the laser pulse and the RF pulse, the pink areas correspond to the RF pulse.

(pumping parameter), at the cost of a lower contrast, as shown in fig. 4.19. These results are in agreement with the experimental observations presented in the previous paragraph.

To conclude, the model presented in eq. (4.12) allows explaining the experimental results and, in particular, the asymmetric shape of the Rabi oscillations. Moreover it confirms that, despite the asymmetric shape due to an incomplete re-polarization of the NV centers, the contrast oscillates at the Rabi frequency, making possible the measurement of the RF field amplitude. This aspect is extremely interesting for the widefield imaging of RF field. In fact, the size of the diamond area useful for sensing is finally limited by the laser beam waist. Increasing this one without changing the laser power results in reducing the pumping parameter s, which means that a longer laser pulse is necessary to completely polarize the NV centers. The consequence is a longer acquisition time. On the other hand, especially for compact and easy-to-use devices, the augmentation of the laser power ($>$ some Watts) is not a suitable solution. For this reason, the detection of NV centers Rabi oscillations without a complete re-polarization of the system is advantageous for widefield applications and, furthermore, allows a better contrast of the measurement.

4.5 Widefield imaging of RF near field

In section 4.3 we reported the detection of the NV center Rabi oscillations using a camera and an appropriate acquisition procedure, but we limited our discussion to the PL contrast acquired by some pixels of the camera. In this paragraph, measuring pixel by pixel the NV centers Rabi frequency, we map the RF near field emitted by our loop antenna.

As it has been done in section section 4.1, two different experimental configurations

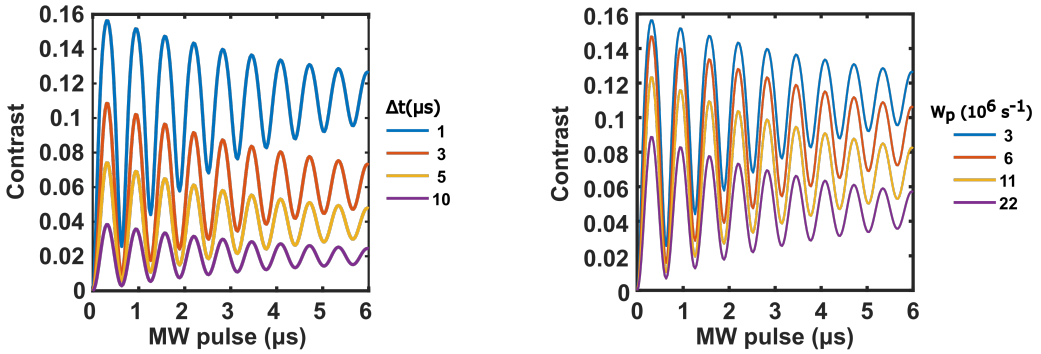

(a) (b)

Figure 4.19: Contribution of the pumping parameter to the contrast of the NV center Rabi oscillations. (a) Simulation results obtained considering different laser pulse durations and a pumping parameter $W_p = 3 \cdot 10^6\ s^{-1}$. (b) Simulation results obtained using different laser pumping parameters and a laser pulse duration of 1 μs.

are considered. In the first, the antenna is centred with respect to the camera AOI so that the NV centers imaged by the camera are excited by the RF field generated inside the wire loop (fig. 4.20a). In the second, the antenna is displaced so that the NV centers imaged by the camera are excited by the RF field generated outside the wire loop (fig. 4.20b).
The NV center Rabi oscillations are then driven and detected using the pulse sequence in fig. 4.8b. The laser pulse duration is set to 2 μs in the first configuration and 5 μs in the second configuration. The RF pulse duration is swept from 0.1 μs to 10 μs in steps of 20 ns.
Figures 4.20c and 4.20d show the contrast of the Rabi oscillations along the beam propagation axis. For each value of x, the contrast is evaluated as the mean value of the contrast of the 10 pixels centred with respect to the center of the laser beam in the y direction. The large horizontal line showing an almost homogeneous contrast at the top of fig. 4.20d is the shadow of the antenna. The several thin horizontal lines which show a very low level of contrast both in fig. 4.20c and fig. 4.20d correspond to the diamond position where there are the PL striations and where, as described in section 2.2, the ODMR contrast is lower. On the rest of the image the value of the contrast oscillates as a consequence of the NV centers Rabi oscillations. The oscillation frequency depends on the diamond position and it is the sign that the antenna is emitting an inhomogeneous RF field. Using the FFT approach described in Section section 4.3, the rabi frequency is measured for each value of x and the results are plotted in figs. 4.20e and 4.20f. Inside the antenna (fig. 4.20e), the Rabi frequency, and thus the amplitude of the RF field is almost homogeneous. Outside the antenna (fig. 4.20f) the amplitude of the magnetic field decreases increasing the distance from the antenna. The data in fig. 4.20f are fitted by eq. (4.3) and a value of $b = 154 \pm 24\ \mu m$ is obtained. This value is of the same order of magnitude of the radius of the wire (50 μm) and the discrepancy is probably due to the same reason discussed in section 4.1.

The measurement of the RF field amplitude done exploiting the Rabi oscillations is in agreement with the measurement done exploiting the power broadening of the NV CW-ODMR spectrum. The two measurements were done using two different antennas having almost the same radius and realized with the same type of wire. Comparing the two measurements, it is possible to recognize the same profile for the magnetic field generated inside and outside the wire loop. The main difference between the two

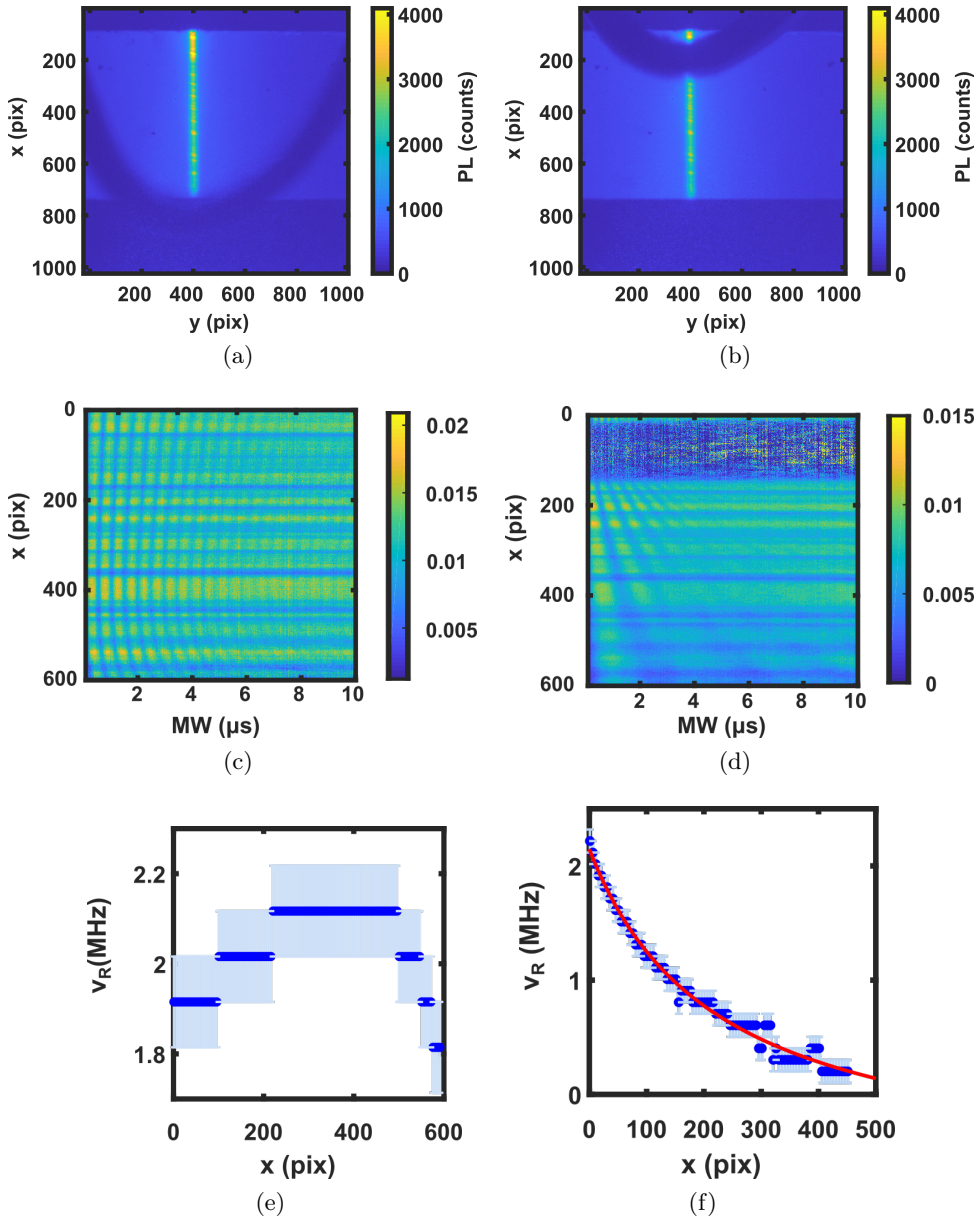

Figure 4.20: Widefield imaging of the RF field emitted by a loop antenna in the near-field region. (a-b) Antenna position. The pictures are the full-frame images acquired by the camera. The laser beam (yellow beam in the picture), the shadow of the antenna (dark blue semi-circle) and the diamond (light blue rectangle) are visible. During the detection of the NV center Rabi oscillations, the AOI of the camera is reduced to the diamond area pumped by the laser beam. In the first configuration (a) the AOI is inside the wire-loop of the antenna while in the second configuration (b) the AOI is outside the wire-loop. (c-d) Rabi oscillations contrast along the beam propagation axis (y) for the first (c) and second (d) antenna configuration. (e-f) Rabi frequency along the beam propagation axis obtained by the FFT of the Rabi oscillations for the first (e) and the second (f) antenna position. The fit in (f) is done using eq. (4.3)

techniques is that the one exploiting the RF power broadening requires a calibration procedure to measure the real value of the magnetic field amplitude whereas the one exploiting Rabi oscillations does not. On the contrary, the first procedure is easier to implement and faster to realize (some minutes instead of some hours) since no pulse sequence is required.
To conclude, both procedures represent a useful tool to image the RF near field emitted by RF devices. In our case, the image has been limited to only one spatial direction, the beam propagation axis direction, because of the size of the beam waist with respect to the RF device. A larger waist will enable the two-dimensional imaging of the RF near field emitted by RF devices ([13]).

4.6 Widefield pulsed-ODMR

The set-up depicted in fig. 4.5 can be employed to optically detect the NV centers magnetic resonances in pulsed regime (pulsed-ODMR). As it is for the Rabi oscillations, the widefield pulsed-ODMR protocol differs from the classic pulsed-ODMR protocol which is implemented when an APD is used as detector [139].

The APD-based pulsed-ODMR protocol is similar to the APD-based Rabi oscillation protocol (fig. 4.8a) with the difference that in this case the frequency of the RF field is swept around the NV center resonance frequency while the RF pulse duration is set to: $\tau = \frac{\pi}{\Omega_r}$ (on resonance π-pulse). When the RF field is detuned with respect to the NV center resonance frequency, the π pulse is not able to completely bring the NV centers from $|0\rangle$ to $|-1\rangle$ or to $|+1\rangle$ thus reducing the contrast of the measurement (eq. (1.14)). Measuring the contrast for different values of detuning it is possible to retrieve the spectrum of the NV centers.
The pulsed-ODMR lineshape [48, 3] is given by the convolution between the Fourier transform of the RF π pulse, which for a rectangular pulse is a sinc function [140], and the NV center intrinsic lineshape. The FWHM of the Fourier transform of a rectangular pulse of length τ is equal to:

$$FWHM_{sinc} = \frac{1.2}{\pi\tau} \tag{4.16}$$

The NV center intrinsic linewidth, assuming a lorentzian lineshape typical of NV centers ensemble [141, 142], is equal to

$$FWHM_{NV} = \frac{1}{\pi T_2^*} \tag{4.17}$$

Therefore, choosing a π pulse duration of the order of the T_2^* of the sample, the pulsed-ODMR linewidth corresponds to the NV center intrinsic linewidth. Moreover, since the RF spin manipulation and the optical spin readout happen in two different moments, the laser power and the APD acquisition time can be optimized to maximize the contrast, which is usually better than the CW-ODMR contrast. Therefore, the NV centers pulsed-ODMR spectrum is not affected by neither optical nor RF power broadening allowing a higher magnetic sensitivity[2] than the CW-ODMR one [48]. The theoretical expressions of the pulsed-ODMR and CW-ODMR sensitivity are here reported from [139]:

$$\eta_{CW} = \frac{4}{3\sqrt{3}} \frac{1}{\gamma} \frac{\Delta\nu}{C_{CW}\sqrt{(N)}} \sqrt{(t_R)} \tag{4.18}$$

[2]The magnetic sensitivity is defined as the smallest variation of static magnetic field detectable by the system. It is measured in $T/\sqrt{Hz}$ [143]

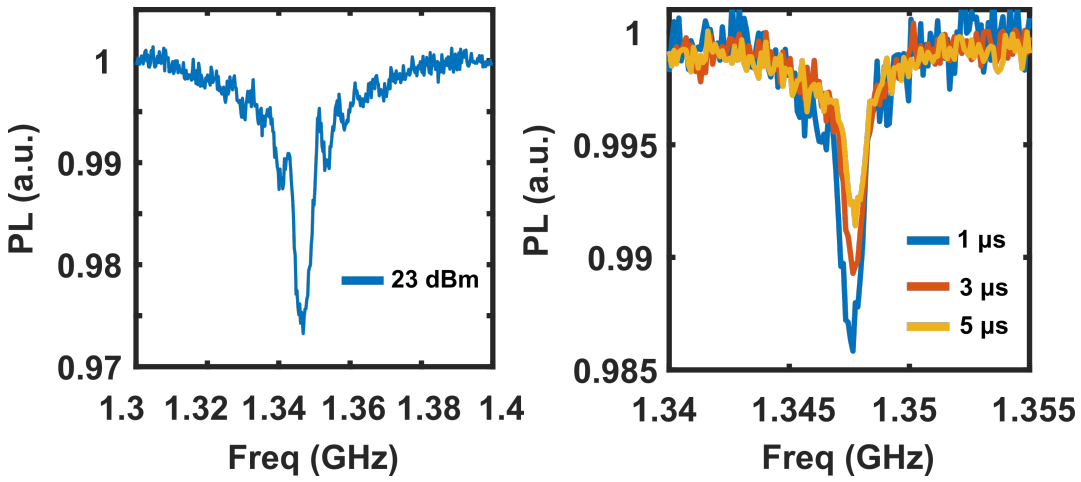

(a) (b)

Figure 4.21: Pulsed ODMR at 23 dBm (a) and 5 dBm (b). In (b) measurements realized using different laser pulse durations are compared.

Laser Pulse duration (μs)	Contrast	FWHM
1	1.5	1.3
3	1.2	1.05
5	0.9	1.09

Table 4.2

$$\eta_{Pulsed} = \frac{4}{3\sqrt{3}} \frac{1}{\gamma} \frac{1}{C_{Pulsed}\sqrt{(N)}\pi T_2^*} \sqrt{(t_M)} \tag{4.19}$$

where γ is the NV center gyromagnetic ratio, $\Delta\nu$ is the CW-ODMR linewidth, C_{CW} and C_{Pulsed} are respectively the CW-ODMR and the Pulsed-ODMR contrast, N is the number of photons collected by the detector, t_R is the PL detection time and t_M is the acquisition time of the measurement. We can also write $t_M = t_R + t_I + \tau = t_R + t_I + T_2^*$, where t_I is the initialization time of the measurement (laser pulse duration plus the waiting time between the laser pulse duration and the RF pulse duration minus t_R) and τ is the pi pulse duration, which is usually chosen equal to T_2^*.

The acquisition procedure for the widefield detection of the NV centers pulsed-ODMR is similar to the one adopted for the Rabi oscillations (fig. 4.8b). In this case the RF pulse corresponds to a π-pulse and the RF frequency is swept around the NV centers resonance frequency. Preliminary results are reported in fig. 4.21. Figure 4.21a shows the pulsed-ODMR spectrum obtained for a RF power of 23 dBm and a π pulsed duration of 200 ns. Since the π pulse duration is shorter than the NV center T_2^* time, which is of the order of 1 μs, the pulsed-ODMR spectrum has a sinc shape. On the contrary, fig. 4.21b shows the pulsed-ODMR spectra obtained for a RF power of 5 dBm, a π pulse duration of 1.1 μs and three different laser pulse durations. In this case the spectra have a Lorentzian shape since the π pulse duration is comparable with the T_2^* of the sample. The ODMR contrast and the ODMR linewidth (Table 4.2) depend on the laser pulse duration because, as already explained in Section section 4.4, the π pulse contrast depends on the laser pulse duration.

The contrast and the linewidth dependence from the laser pulse duration is a re-

markable difference between the widefield pulsed-ODMR acquisition procedure and the APD-based pulsed ODMR acquisition procedure and may call into question the advantages of the pulsed-ODMR with respect to the CW-ODMR when a widefield detection of the NV centers PL is performed. At the moment, an exhaustive analysis to understand if the pulsed-ODMR is still advantageous with respect to the CW-ODMR using a widefield detector has not been conducted and it is one of the perspectives of this work.

4.6.1 Modelisation of the NV centers widefield pulsed-ODMR

The widefield detection of the NV centers pulsed ODRM can be simulated using the model described in section 4.4. In this case, the detuning between the RF field and the NV center resonance frequency must be taken into account and the rate equations of the model (eq. (4.12)) become:

$$\frac{dn_1}{dt} = -n_1 W_p + n_4 k_{14} + n_7 k_{17} + O_R \cdot n_C \tag{4.20a}$$
$$\frac{dn_2}{dt} = -n_2 W_p + n_5 k_{25} + n_7 k_{27} - O_R \cdot n_C \tag{4.20b}$$
$$\frac{dn_3}{dt} = -n_3 W_p + n_6 k_{25} + n_7 k_{27} \tag{4.20c}$$
$$\frac{dn_4}{dt} = n_1 W_p - n_4 k_{14} - n_4 k_{47} \tag{4.20d}$$
$$\frac{dn_5}{dt} = n_2 W_p - n_5 k_{25} - n_5 k_{57} \tag{4.20e}$$
$$\frac{dn_6}{dt} = n_3 W_p - n_6 k_{14} - n_6 k_{57} \tag{4.20f}$$
$$1 = n_1 + n_2 + n_3 + n_4 + n_5 + n_6 + n_7 \tag{4.20g}$$
$$\frac{dn_c}{dt} = -\Gamma_2 \cdot n_c + \frac{O_R}{2} \cdot (n_2 - n_1) \tag{4.20h}$$
$$\frac{dn_d}{dt} = -\Gamma_2 \cdot n_d + \delta\omega n_c \tag{4.20i}$$

where $n_d = \Re[\varrho_{01}]$, according to eq. (4.11). The pulsed-ODMR spectrum is thus obtained repeating, for different values of the detuning, the simulation done in section 4.4 assuming a RF pulse duration equal to 1 μs and a Rabi angular frequency equals to $\pi \cdot 10^6$ rad$\cdot s^{-1}$. The results are reported in fig. 4.22. The lineshape of the spectra is essentially lorentzian since in the simulation we set the π-pulse duration equal to the T_2^*. The plots in fig. 4.22 show that both the pulsed-ODMR contrast and the pulsed-ODMR linewidth depend on the laser pulse duration, in agreement with the experimental results.

4.6.2 Temperature dependent static magnetic field fluctuations

The widefield pulsed-ODMR has been employed to investigate the temperature fluctuations of the magnet remanent magnetization. The experiment consists in tracking the NV center resonance frequency while, at the same time, the temperature of the laboratory is measured in proximity of the diamond by means of a temperature sensor. The set-up is the one reported in fig. 4.5. The pulsed-ODMR measurement is done using a RF power of 2 dBm corresponding to a π pulse duration of 2 μs. It is repeated every 15 minutes and the resonance frequency of the NV center ground state $|0\rangle \rightarrow |-1\rangle$ transition is measured each time. The results are plotted in fig. 4.23 and they clearly show that the frequency shift of the NV center resonance frequency follows the temperature fluctuations. This effect is caused by the temperature dependence of the magnet remanent magnetization (B_R) which, for Neodymium magnets, is: $\Delta B_r \approx -0.1\%/^\circ$.

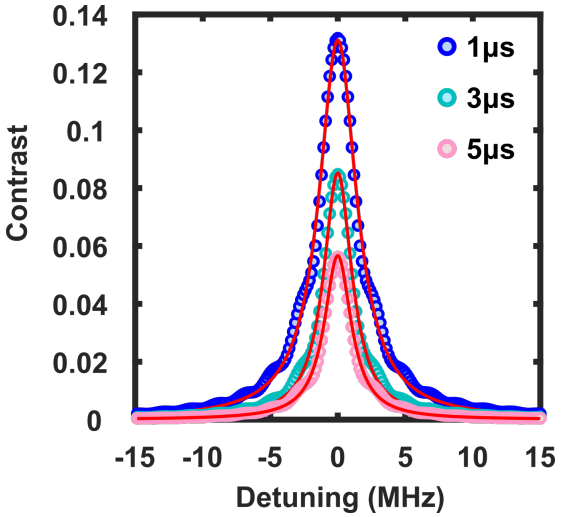

Figure 4.22: Simulation of pulsed ODMR spectra using different laser pulse durations. The fit is realized using a lorentzian curve.

The static magnetic field applied to the NV centers during the measurement can be calculated as:

$$B = \frac{D - f_{|0\rangle\rightarrow|-1\rangle}}{\gamma} = 54\ mT \tag{4.21}$$

The fluctuations of the magnet remanent magnetization induce fluctuations of the same order in the static magnetic field (eq. (3.1)). The static magnetic field fluctuations are thus given by:

$$\Delta B = B \cdot \Delta B_R = 0.054\ mT/^\circ \tag{4.22}$$

which corresponds to a frequency fluctuation of the $|0\rangle \rightarrow |-1\rangle$ transition of

$$\Delta f = \gamma \cdot \Delta B = 1.5\ MHz/^\circ \tag{4.23}$$

which is of the same order of magnitude of the frequency fluctuation experimentally measured (≈ 1.3 MHz/°).

The static magnetic field fluctuations due to temperature fluctuations of the magnets are proportional to the amplitude of the static magnetic field itself eq. (4.22). Therefore, at high static magnetic field, the magnetic field fluctuations and thus the frequency fluctuations are more important than at low static magnetic field. This effect plays a role when NV centers are employed for the spectral analysis of RF field. In this case, in fact, NV centers undergo static magnetic field of the order of hundreds of mT and therefore, as anticipated in chapter 3, temperature fluctuations of the magnets can induce a line broadening during the long calibration procedure. To get rid of this effect, temperature stabilization of the magnets is required.

4.7 Conclusions and perspectives

In this chapter, we investigated two NV center-based techniques to image the RF field emitted by a RF device and we employed them to map the RF near-field generated inside and outside a loop antenna. The results were in agreement with the magnetic field profile theoretically expected: inside the loop an almost homogeneous RF field, and outside the loop a decreasing magnetic field amplitude as the distance from the antenna increases. The first technique presented, based on the RF power broadening

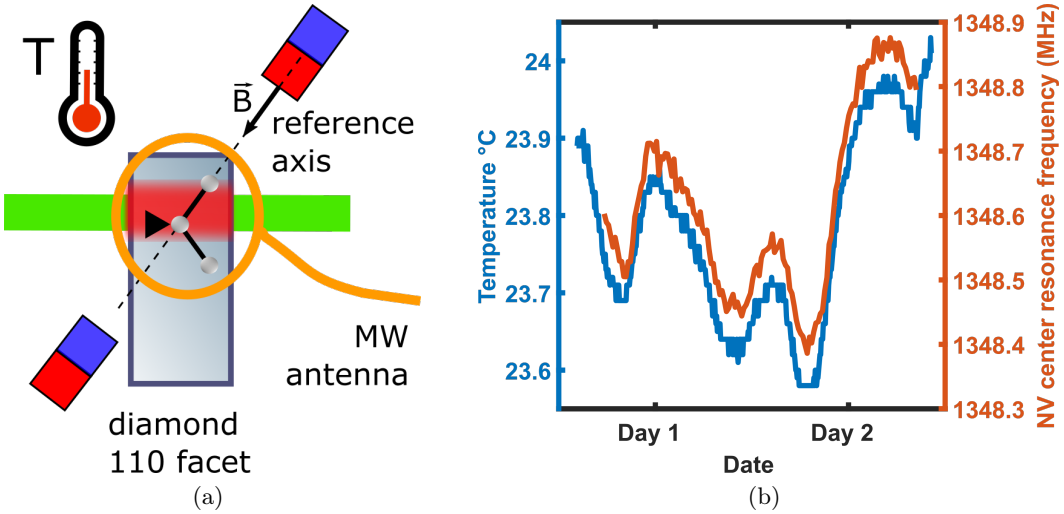

(a) (b)

Figure 4.23: Temperature fluctuations of the magnet remanent magnetization . (a) Schematic of the set-up, viewed from the camera. (b) Shift of the NV centers resonance frequency due to temperature fluctuations of the magnet remanent magnetization. The NV center transition considered for the measurement is the ground state $|0\rangle \rightarrow |-1\rangle$ transition. The temperature of the room is measured near the diamond using a temperature detector and it is plotted in blue on the graph. The NV center resonance frequency is evaluated fitting the pulsed-ODMR spectrum with a lorentzian curve and considering the central frequency of the fit function as the NV center resonance frequency. The results are plotted in orange on the graph.

of the NV center CW-ODMR spectrum, works in continuous-wave regime. It is easy to implement and handle but requires a calibration procedure to measure the amplitude of the RF field. On the contrary, the second technique, based on the widefield detection of NV center Rabi oscillations, allows a direct measurement of the amplitude of the RF field but requires a pulsed excitation. In this chapter, the imaging of the RF field has been demonstrated in one spatial dimension. One of the perspectives of this chapter is to extend the field of view of our experimental architecture to realize two-dimensional maps of the RF field emitted by real RF devices.

The widefield detection of Rabi oscillations requires a different pulse sequence respect from the one used when the detection is performed by APD-based system. By implementing this pulse sequence, we detected Rabi oscillations that showed an asymmetric shape. In order to figure out this shape, we implemented a model which, merging the rate equations and the Bloch equations approaches, is able to simulate the NV centers behaviour during the pulse sequence and provides results in agreement with data. In particular, we demonstrated that the Rabi oscillations asymmetric shape is caused by an incomplete re-polarization of the NV centers during the pulse sequence. Increasing the laser pulse duration or the laser power, it is possible to obtain more symmetric but less contrasted Rabi oscillations. The Rabi frequency does not depend on the laser power or on the duration of the laser pulse. These results show the opportunity to drive NV center Rabi oscillations without completely re-polarizing the NV centers spin and, at the same time, without losing information on the amplitude of the RF field. That is advantageous for widefield imaging systems where, in order to image a large diamond area by means of a large beam waist, the NV centers are excited by low optical powers. Moreover, short laser pulses enable faster acquisitions. From a more general point of view, the simple model developed in this chapter is a powerful tool to study and visualize the coherent evolution of an ensemble of NV centers. One of the perspectives of

this chapter is indeed to use this model to optimize the pulse sequence implemented in the widefield Rabi oscillations detection and investigate the NV center properties under unusual optical pumping conditions.

The last interesting result we want to report concerns the opportunity to use a widefield imaging system to measure NV centers pulsed-ODMR spectra. Specifically, we demonstrated that, differently from an APD-based pulsed-ODMR measurement, in the widefield pulsed-ODMR scheme the laser pulse duration plays a central role. Further experiments and simulations are required to figure out if and within what limits the pulsed-ODMR can improve the magnetic sensitivity of an ensemble of NV centers when a widefield detection is performed. This is certainly one of the perspectives of this chapter.

Conclusions and perspectives

In this manuscript we proposed two applications based on an ensemble of NV centers in diamond for the RF signal analysis and we investigated their working principle and performance. That also made it possible to study NV centers from a more general point of view, obtaining interesting results not only in view of the two proposed applications.

Concerning the general aspects of the NV centers ODMR widefield detection, we showed its main features offering a guideline to its experimental implementation and data analysis. An original contribution of this work is the introduction of a polarizer in the NV centers PL detection system. In particular we employed it to characterize our sample and recognize the presence of an inhomogeneous NV center preferential orientation. More generally, we demonstrated that the use of a polarizer is a wise trick to easily improve the contrast and thus the sensitivity of the system.
We showed the great advantage of working with a widefield imaging system in combination with a magnetic field gradient. Indeed that allows visualizing the frequency evolution of the NV centers spin transitions under a static magnetic field and helps their identification. Specifically, we detected the NV centers resonance spectrum over a broad frequency range (several GHz) with a high spectral resolution. The achieved results turn out to be extremely useful for an in-depth understanding of the behaviour of an ensemble of NV centers under a static magnetic field and a static magnetic field gradient, which is the starting point for several NV centers applications.
Exploring the behaviour of an ensemble of NV centers over a broad spectral range, we demonstrated the opportunity to optically polarize the NV center nuclear spin over a frequency range larger than 4 GHz and with a high polarization efficiency: better than 80% in proximity of the GSLAC and ESLAC and however better than 50% over the entire range. This result is encouraging for NV-based quantum information applications which exploit nuclear spins in diamond as qubits.

The first of the two applications investigated in this thesis is a room temperature, real-time, RF spectrum analyzer based on an ensemble of NV centers in a single diamond crystal. Its working principle relies on the spatial encoding of the NV center resonance frequencies by means of a controlled magnetic field gradient. We studied the main physical features of NV centers considered as MW detectors and we implemented an experimental architecture which allows realizing the real-time spectral analysis of complex MW signal over a tunable frequency range from 10 MHz to 25 GHz. We investigated the performance of our architecture and in particular the effects of the magnetic field gradient on the key parameters of the RF spectral analysis: real-time bandwidth, frequency resolution, dynamic range and time resolution. We achieved a MHz frequency resolution and ms time resolution at low frequencies ($\approx$ 2 GHz), and a few tens of MHz frequency resolution and a few hundreds of ms time resolution at high frequencies ($\approx$ 20 GHz). The frequency-dependent performance of our device was investigated and we showed that it is caused both by the magnetic field gradient at the pixel scale and by the RF chain transmission efficiency. We discussed the frequency ambiguity which may arise during the RF spectral analysis based on an ensemble of NV centers and we proposed an architecture based on heterodyne techniques which allows

an unambiguous real-time RF spectral analysis over a frequency range of several tens of GHz (demonstrated up to 40 GHz) with a 5.74 GHz of maximum real-time bandwidth. More generally we discussed how the parameters of interest for the RF spectral analysis are related to each other with respect to the experimental implementation. Therefore, the results presented in this manuscript can serve as a guideline for the experimental implementation of a RF spectrum analyzer based on an ensemble of NV centres whose performance is set to meet the requirements of a well-defined application.

The second application based on an ensemble of NV centers presented in this thesis is the imaging of the RF field radiated by a RF device in the near-field region. We proposed two complementary techniques which allowed a good reconstruction of the RF field generated inside at outside a loop antenna. The first technique, based on the microwave power broadening of the NV center CW-ODMR spectrum, works in continuous-wave regime, it is easy both to implement and to handle but requires a calibration procedure to measure the amplitude of the RF field. Complementary, the second technique, based on the widefield detection of the NV center Rabi oscillations, allows a direct measurement of the amplitude of the RF field but works in pulsed regime. We proposed a model to study the dynamics of the NV center during the pulse sequence implemented for the widefield detection of the Rabi oscillations. In fact, differently from the APD-based acquisition procedure, during the widefield detection of NV centers Rabi oscillations the optical spin polarization and the optical spin readout cannot be separated. Therefore, a compromise needs to be found in order to sufficiently repolarize the NV centers without losing information about their spin state. With the help of simulations, we demonstrated that short or low-power laser pulses are not able to completely repolarize the NV centers after each RF pulse but optimize the spin readout. As a consequence, the detected Rabi oscillations have a high-contrast asymmetric sinusoidal shape. On the contrary, long or high-power laser pulses allow a complete repolarization of the NV centers spin and therefore the detected Rabi oscillations have a symmetric but less contrasted sinusoidal shape. The Rabi frequency is independent of the laser power and the laser pulse duration. These results show the opportunity of driving NV center Rabi oscillations without completely repolarizing the NV centers spin and, at the same time, without losing information on the amplitude of the RF field. This is advantageous for widefield imaging systems where, in order to image a large diamond area, a large beam waist is required and thus the NV centers are excited by low optical powers. Moreover, short laser pulses make the detection faster.

This work of thesis opens up several challenging perspectives that we can group into three blocks. First, improve the performance of the spectrum analyzer based on an ensemble of NV centers by testing alternative experimental architectures and the recently discovered photoelectrical readout of the NV center spin transitions. Second, optimize the pulse sequence parameters and the experimental architecture to image more efficiently and over a larger area the RF field radiated by real RF devices. This technique may prove to be extremely useful for a non-disturbing characterization of RF components with a high spatial resolution. Moreover, it may result a useful tool for those scientific domains which investigate the magnetic properties of materials (e.g. spintronics, solid-state physics, etc...) since it allows probing quite large areas with high spatial resolution while being in proximity of the sample under test. Third, exploit the potentiality of the simple model developed in this manuscript to investigate the widefield detection of an ensemble of NV centers in pulsed regime. For example, it may reveal itself useful to investigate the widefield detection of NV centers pulsed-ODMR. Moreover, it can be employed, supported by some optimal control techniques, to study complex pulse sequences which could improve the performance of NV centers as both quantum sensors and qubits.

To conclude, in this manuscript we demonstrated the potentiality of an ensemble of NV centers and we proposed two applications which are promising candidates, in a near future, to become real quantum sensors.

Bibliography

[1] Jonathan P. Dowling and Gerard J. Milburn. Quantum technology: the second quantum revolution. *Philosophical Transactions of the Royal Society of London. Series A: Mathematical, Physical and Engineering Sciences*, 361(1809):1655–1674, 2003.

[2] David P. DiVincenzo. The physical implementation of quantum computation. *Fortschritte der Physik*, 48(9-11):771–783, 2000.

[3] C. L. Degen, F. Reinhard, and P. Cappellaro. Quantum sensing. *Rev. Mod. Phys.*, 89:035002, Jul 2017.

[4] L Rondin, J-P Tetienne, T Hingant, J-F Roch, P Maletinsky, and V Jacques. Magnetometry with nitrogen-vacancy defects in diamond. *Reports on Progress in Physics*, 77(5):056503, may 2014.

[5] Ashok Ajoy and Paola Cappellaro. Stable three-axis nuclear-spin gyroscope in diamond. *Phys. Rev. A*, 86:062104, Dec 2012.

[6] G Kucsko, PC Maurer, NY Yao, M Kubo, HJ Noh, PK Lo, H Park, and MD Lukin. Nanometre-scale thermometry in a living cell. *Nature*, 500(7460):54—58, August 2013.

[7] Margarita Lesik, Thomas Plisson, Loïc Toraille, Justine Renaud, Florent Occelli, Martin Schmidt, Olivier Salord, Anne Delobbe, Thierry Debuisschert, Loïc Rondin, et al. Magnetic measurements on micrometer-sized samples under high pressure using designed nv centers. *Science*, 366(6471):1359–1362, 2019.

[8] Edward H. Chen, Hannah A. Clevenson, Kerry A. Johnson, Linh M. Pham, Dirk R. Englund, Philip R. Hemmer, and Danielle A. Braje. High-sensitivity spin-based electrometry with an ensemble of nitrogen-vacancy centers in diamond. *Phys. Rev. A*, 95:053417, May 2017.

[9] Federal communications commission office of engineering, technology policy, and rules division.

[10] Rohde & Schwarz. *Implementation of Real-Time Spectrum Analysis. White Paper.*

[11] Xihua Zou, Bing Lu, Wei Pan, Lianshan Yan, Andreas Stöhr, and Jianping Yao. Photonics for microwave measurements. *Laser & Photonics Reviews*, 10(5):711–734, 2016.

[12] M. Chipaux, L. Toraille, C. Larat, L. Morvan, S. Pezzagna, J. Meijer, and T. Debuisschert. Wide bandwidth instantaneous radio frequency spectrum analyzer based on nitrogen vacancy centers in diamond. *Applied Physics Letters*, 107(23):233502, 2015.

[13] Andrew Horsley, Patrick Appel, Janik Wolters, Jocelyn Achard, Alexandre Tallaire, Patrick Maletinsky, and Philipp Treutlein. Microwave device characterization using a widefield diamond microscope. *Phys. Rev. Applied*, 10:044039, Oct 2018.

[14] Pascal Bohi, Max F. Riedel, Theodor W. Hänsch, and Philipp Treutlein. Imaging of microwave fields using ultracold atoms. *Applied Physics Letters*, 97(5):051101, 2010.

[15] National Research Council. *Status and Applications of Diamond and Diamond-Like Materials: An Emerging Technology*. The National Academies Press, Washington, DC, 1990.

[16] A.M. Zaitsev. *Optical Properties of Diamond. A Data Handbook*. Springer, Berlin, Heidelberg, 2001.

[17] N. W. Ashcroft and N. D. Mermin. *Solid State Physics*. Holt-Saunders, 1976.

[18] F. P. BUNDY, H. T. HALL, H. M. STRONG, and R. H. WENTORFJUN. Man-made diamonds. *Nature*, 176(4471):51–55, Jul 1955.

[19] R S Balmer, J R Brandon, S L Clewes, H K Dhillon, J M Dodson, I Friel, P N Inglis, T D Madgwick, M L Markham, T P Mollart, N Perkins, G A Scarsbrook, D J Twitchen, A J Whitehead, J J Wilman, and S M Woollard. Chemical vapour deposition synthetic diamond: materials, technology and applications. *Journal of Physics: Condensed Matter*, 21(36):364221, aug 2009.

[20] William G. Eversole. Synthesis of diamond, 1961.

[21] Paul S. DeCarli and John C. Jamieson. Formation of diamond by explosive shock. *Science*, 133(3467):1821–1822, 1961.

[22] K. Turcheniuk and V. N. Mochalin. Biomedical applications of nanodiamond (review). *Nanotechnology*, 28(25):252001, jun 2017.

[23] Efthimios Kaxiras John D. Joannopoulos. *Quantum theory of materials*. Cambridge university press, 2019.

[24] Yoshimi Mita. Change of absorption spectra in type-ib diamond with heavy neutron irradiation. *Phys. Rev. B*, 53:11360–11364, May 1996.

[25] Akib Karim, Igor Lyskov, Salvy P. Russo, and Alberto Peruzzo. Bright ab-initio photoluminescence of nv+ in diamond, 2021.

[26] Anna Maria Ferrari, Maddalena D'Amore, Khaled E. El-Kelany, Francesco Silvio Gentile, and Roberto Dovesi. The nv0 defects in diamond: A quantum mechanical characterization through its vibrational and electron paramagnetic resonance spectroscopies. *Journal of Physics and Chemistry of Solids*, 160:110304, 2022.

[27] P. Delaney L.C.L. Hollenberg M. W. Doherty, N. B. Manson. The negatively charged nitrogen-vacancy centre in diamond: the electronic solution. *New Journal of Physics*, 13(2):025019, feb 2011.

[28] E. Togan Y. Chu A. Trifonov E. Kaxiras J. R. Maze, A. Gali and M D Lukin. Properties of nitrogen-vacancy centers in diamond: the group theoretic approach. *New Journal of Physics*, 13(2):025025, feb 2011.

[29] E. Kaxiras A.Gali, M. Fyta. Ab initio supercell calculations on nitrogen-vacancy center in diamond: Electronic structure and hyperfine tensors. *Phys. Rev. B*, 77:155206, Apr 2008.

[30] A. Gali. Ab initio theory of the nitrogen-vacancy center in diamond. *Nanophotonics*, 8(11):1907–1943, 2019.

[31] H.F. Wilson F.M. Hossain, M.W. Doherty and L.C.L. Hollenberg. Ab initio electronic and optical properties of the $N - V^-$ center in diamond. *Phys. Rev. Lett.*, 101:226403, Nov 2008.

[32] M.J. Sellars L.J. Rogers, S. Armstrong and N.B. Manson. Infrared emission of the nv centre in diamond: Zeeman and uniaxial stress studies. *New Journal of Physics*, 10(10):103024, 2008.

[33] E. Bauch V.M. Acosta, A. Jarmola and D. Budker. Optical properties of the nitrogen-vacancy singlet levels in diamond. *Phys. Rev. B*, 82:201202, Nov 2010.

[34] L.J. Zipp M.P. Ledbetter E. Bauch V.M. Acosta, A. Jarmola and D. Budker. Broadband magnetometry by infrared-absorption detection of diamond nv centers and associated temperature dependence. In *Advances in Photonics of Quantum Computing, Memory, and Communication IV*, volume 7948, page 79480W. International Society for Optics and Photonics, 2011.

[35] V. Jacques F. Treussart Y. Dumeige, M. Chipaux, J. Roch, T. Debuisschert, V. Acosta, A. Jarmola, K. Jensen, P. Kehayias, and D. Budker. Magnetometry with nitrogen-vacancy ensembles in diamond based on infrared absorption in a doubly resonant optical cavity. *Physical Review B*, 87:155202, 2013.

[36] Lucio Robledo, Hannes Bernien, Toeno Van Der Sar, and Ronald Hanson. Spin dynamics in the optical cycle of single nitrogen-vacancy centres in diamond. *New Journal of Physics*, 13(2):025013, 2011.

[37] Nabeel Aslam, Gerhald Waldherr, Philipp Neumann, Fedor Jelezko, and Joerg Wrachtrup. Photo-induced ionization dynamics of the nitrogen vacancy defect in diamond investigated by single-shot charge state detection. *New Journal of Physics*, 15(1):013064, 2013.

[38] Carlo Bradac, Torsten Gaebel, and James R. Rabeau. *Nitrogen-Vacancy Color Centers in Diamond: Properties, Synthesis, and Applications*, chapter 5, pages 143–175. John Wiley & Sons, Ltd.

[39] Franck Laloë Claude Cohen-Tannoudji, Bernard Diu. *Quantum Mechanics, Volume 1: Basic Concepts, Tools, and Applications*. Wiley, 2019.

[40] Phila Rembold, Nimba Oshnik, Matthias M. Müller, Simone Montangero, Tommaso Calarco, and Elke Neu. Introduction to quantum optimal control for quantum sensing with nitrogen-vacancy centers in diamond. *AVS Quantum Science*, 2(2):024701, 2020.

[41] J Kölbl, M Kasperczyk, B Bürgler, A Barfuss, and P Maletinsky. Determination of intrinsic effective fields and microwave polarizations by high-resolution spectroscopy of single nitrogen-vacancy center spins. 21(11):113039, nov 2019.

[42] Thiago P. Mayer Alegre, Charles Santori, Gilberto Medeiros-Ribeiro, and Raymond G. Beausoleil. Polarization-selective excitation of nitrogen vacancy centers in diamond. *Phys. Rev. B*, 76:165205, Oct 2007.

[43] Johannes Herrmann, Marc A. Appleton, Kento Sasaki, Yasuaki Monnai, Tokuyuki Teraji, Kohei M. Itoh, and Eisuke Abe. Polarization- and frequency-tunable microwave circuit for selective excitation of nitrogen-vacancy spins in diamond. *Applied Physics Letters*, 109(18):183111, 2016.

[44] Anais Dréau. *Spins individuels dans le diamant pour l'information quantique.* PhD thesis, 2013. Thèse de doctorat dirigée par Roch, Jean-François Sciences physiques Cachan, Ecole normale supérieure 2013.

[45] Daniel Manzano. A short introduction to the lindblad master equation. *AIP Advances*, 10(2):025106, 2020.

[46] D. Sugny, C. Kontz, and H. R. Jauslin. Time-optimal control of a two-level dissipative quantum system. *Phys. Rev. A*, 76:023419, Aug 2007.

[47] Gilbert Grynberg Claude Cohen-Tannoudji, Jacques Dupont-Roc. *Processus d'interaction entre photons et atomes.*

[48] A. Dreau, M. Lesik, L. Rondin, P. Spinicelli, O. Arcizet, J.-F. Roch, and V. Jacques. Avoiding power broadening in optically detected magnetic resonance of single nv defects for enhanced dc magnetic field sensitivity. *Phys. Rev. B*, 84:195204, Nov 2011.

[49] www.qzabre.com.

[50] www.qnami.ch.

[51] John F. Barry, Matthew J. Turner, Jennifer M. Schloss, David R. Glenn, Yuyu Song, Mikhail D. Lukin, Hongkun Park, and Ronald L. Walsworth. Optical magnetic detection of single-neuron action potentials using quantum defects in diamond. *Proceedings of the National Academy of Sciences*, 113(49):14133–14138, 2016.

[52] Sandra Claveau, Jean-Rémi Bertrand, and François Treussart. Fluorescent nanodiamond applications for cellular process sensing and cell tracking. *Micromachines*, 9(5), 2018.

[53] Giulia Petrini, Ekaterina Moreva, Ettore Bernardi, Paolo Traina, Giulia Tomagra, Valentina Carabelli, Ivo Pietro Degiovanni, and Marco Genovese. Is a quantum biosensing revolution approaching? perspectives in nv-assisted current and thermal biosensing in living cells. *Advanced Quantum Technologies*, 3(12):2000066, 2020.

[54] King Yau Yip, Kin On Ho, King Yiu Yu, Yang Chen, Wei Zhang, S Kasahara, Y Mizukami, T Shibauchi, Y Matsuda, Swee K Goh, et al. Measuring magnetic field texture in correlated electron systems under extreme conditions. *Science*, 366(6471):1355–1359, 2019.

[55] S Hsieh, P Bhattacharyya, C Zu, T Mittiga, TJ Smart, F Machado, B Kobrin, TO Höhn, NZ Rui, Mehdi Kamrani, et al. Imaging stress and magnetism at high pressures using a nanoscale quantum sensor. *Science*, 366(6471):1349–1354, 2019.

[56] D. R. Glenn, R. R. Fu, P. Kehayias, D. Le Sage, E. A. Lima, B. P. Weiss, and R. L. Walsworth. Micrometer-scale magnetic imaging of geological samples using a quantum diamond microscope. *Geochemistry, Geophysics, Geosystems*, 18(8):3254–3267, 2017.

[57] E. Farchi, Y. Ebert, D. Farfurnik, G. Haim, R. Shaar, and N. Bar-Gill. Quantitative vectorial magnetic imaging of multi-domain rock forming minerals using nitrogen-vacancy centers in diamond. *SPIN*, 07(03):1740015, 2017.

[58] Qi-Chao Sun, Tiancheng Song, Eric Anderson, Andreas Brunner, Johannes Förster, Tetyana Shalomayeva, Takashi Taniguchi, Kenji Watanabe, Joachim Gräfe, Rainer Stöhr, et al. Magnetic domains and domain wall pinning in atomically thin crbr 3 revealed by nanoscale imaging. *Nature communications*, 12(1):1–7, 2021.

[59] David A. Broadway, Sam C. Scholten, Cheng Tan, Nikolai Dontschuk, Scott E. Lillie, Brett C. Johnson, Guolin Zheng, Zhenhai Wang, Artem R. Oganov, Shangjie Tian, Chenghe Li, Hechang Lei, Lan Wang, Lloyd C. L. Hollenberg, and Jean-Philippe Tetienne. Imaging domain reversal in an ultrathin van der waals ferromagnet. *Advanced Materials*, 32(39):2003314, 2020.

[60] Lucas Thiel, Zhe Wang, Märta A Tschudin, Dominik Rohner, Ignacio Gutiérrez-Lezama, Nicolas Ubrig, Marco Gibertini, Enrico Giannini, Alberto F Morpurgo, and Patrick Maletinsky. Probing magnetism in 2d materials at the nanoscale with single-spin microscopy. *Science*, 364(6444):973–976, 2019.

[61] Maximilian Ruf, Noel H. Wan, Hyeongrak Choi, Dirk Englund, and Ronald Hanson. Quantum networks based on color centers in diamond. *Journal of Applied Physics*, 130(7):070901, 2021.

[62] I. A. Khramtsov, M. Agio, and D. Yu. Fedyanin. Electrical excitation of color centers in diamond: Toward practical single-photon sources. *AIP Conference Proceedings*, 2359(1):020015, 2021.

[63] Sébastien Pezzagna and Jan Meijer. Quantum computer based on color centers in diamond. *Applied Physics Reviews*, 8(1):011308, 2021.

[64] Nizovtsev A.P. Wrachtrup J., Kilin S.Y. Quantum computation using the 13c nuclear spins near the single nv defect center in diamond. *Opt. Spectrosc.*, 91,(1):429–437, 2001.

[65] C. E. Bradley, J. Randall, M. H. Abobeih, R. C. Berrevoets, M. J. Degen, M. A. Bakker, M. Markham, D. J. Twitchen, and T. H. Taminiau. A ten-qubit solid-state spin register with quantum memory up to one minute. *Phys. Rev. X*, 9:031045, Sep 2019.

[66] Agilent. *Spectrum Analysis Basics. Application Note 150.*

[67] Luis Romero Cortés, Daniel Onori, Hugues Guillet de Chatellus, Maurizio Burla, and José Aza na. Towards on-chip photonic-assisted radio-frequency spectral measurement and monitoring. *Optica*, 7(5):434–447, May 2020.

[68] Shilong Pan and Jianping Yao. Photonics-based broadband microwave measurement. *Journal of Lightwave Technology*, 35(16):3498–3513, 2017.

[69] Hengyun Jiang, David Marpaung, Mattia Pagani, Khu Vu, Duk-Yong Choi, Steve J. Madden, Lianshan Yan, and Benjamin J. Eggleton. Wide-range, high-precision multiple microwave frequency measurement using a chip-based photonic brillouin filter. *Optica*, 3(1):30–34, Jan 2016.

[70] Lam Anh Bui. Recent advances in microwave photonics instantaneous frequency measurements. *Progress in Quantum Electronics*, 69:100237, 2020.

[71] Xihua Zou, Wangzhe Li, Bing Lu, Wei Pan, Lianshan Yan, and Liyang Shao. Photonic approach to wide-frequency-range high-resolution microwave/millimeter-wave doppler frequency shift estimation. *IEEE Transactions on Microwave Theory and Techniques*, 63(4):1421–1430, 2015.

[72] Chongjia Huang, Hao Chen, and Erwin H. W. Chan. Simple photonics-based system for doppler frequency shift and angle of arrival measurement. *Opt. Express*, 28(9):14028–14037, Apr 2020.

[73] Ivan Lorgeré, Loïc Ménager, Vincent Lavielle, Jean-Louis Le Gouët, Daniel Dolfi, Sylvie Tonda, and Jean-Pierre Huignard. Demonstration of a radio-frequency spectrum analyser based on spectral hole burning. *Journal of Modern Optics*, 49(14-15):2459–2475, 2002.

[74] Perrine Berger, Yoann Attal, Muriel Schwarz, Stéphanie Molin, Anne Louchet-Chauvet, Thierry Chanelière, Jean-Louis Le Gouët, Daniel Dolfi, and Loïc Morvan. Rf spectrum analyzer for pulsed signals: Ultra-wide instantaneous bandwidth, high sensitivity, and high time-resolution. *J. Lightwave Technol.*, 34(20):4658–4663, Oct 2016.

[75] Kristian D. Merkel, Scott H. Bekker, Aaron S. Traxinger, Colton R. Stiffler, Alex J. Woidtke, Michael D. Chase, Wm. Randall Babbitt, Cal H. Harrington, and Zeb W. Barber. Extreme bandwidth spectrum analysis. In *2016 IEEE Photonics Conference (IPC)*, pages 487–488, 2016.

[76] Nilesh Kumar Tiwari, Surya Prakash Singh, and M. Jaleel Akhtar. Near field planar microwave probe sensor for nondestructive condition assessment of wood products. *Journal of Applied Physics*, 123(22):224502, 2018.

[77] R. Joffe, E. O. Kamenetskii, and R. Shavit. Novel microwave near-field sensors for material characterization, biology, and nanotechnology. *Journal of Applied Physics*, 113(6):063912, 2013.

[78] E. C. Greenawald, L. J. Levenberry, N. Qaddoumi, A. McHardy, R. Zoughi, and C. F. Poranski. Microwave nde of impact damaged fiberglass and elastomer layered composites. *AIP Conference Proceedings*, 509(1):1263–1268, 2000.

[79] Tristan Dubois, Sylvie Jarrix, Annick Penarier, Philippe Nouvel, Daniel Gasquet, Laurent Chusseau, and Bruno Azais. Near-field electromagnetic characterization and perturbation of logic circuits. *IEEE Transactions on Instrumentation and Measurement*, 57(11):2398–2404, 2008.

[80] J. C. Weber, J. B. Schlager, N. A. Sanford, A. Imtiaz, T. M. Wallis, L. M. Mansfield, K. J. Coakley, K. A. Bertness, P. Kabos, and V. M. Bright. A near-field scanning microwave microscope for characterization of inhomogeneous photovoltaics. *Review of Scientific Instruments*, 83(8):083702, 2012.

[81] David M. Pozar. *Microwave Engineering*. Wiley, 2011.

[82] Bjorn T. Rosner and Daniel W. van der Weide. High-frequency near-field microscopy. *Review of Scientific Instruments*, 73(7):2505–2525, 2002.

[83] S. Sayil, D.V. Kerns, and S.E. Kerns. Comparison of contactless measurement and testing techniques to a all-silicon optical test and characterization method. *IEEE Transactions on Instrumentation and Measurement*, 54(5):2082–2089, 2005.

[84] S. K. Dutta, C. P. Vlahacos, D. E. Steinhauer, Ashfaq S. Thanawalla, B. J. Feenstra, F. C. Wellstood, Steven M. Anlage, and Harvey S. Newman. Imaging microwave electric fields using a near-field scanning microwave microscope. *Applied Physics Letters*, 74(1):156–158, 1999.

[85] Yingjie Gao and I. Wolff. A new miniature magnetic field probe for measuring three-dimensional fields in planar high-frequency circuits. *IEEE Transactions on Microwave Theory and Techniques*, 44(6):911–918, 1996.

[86] R. L. Fagaly. Superconducting quantum interference device instruments and applications. *Review of Scientific Instruments*, 77(10):101101, 2006.

[87] R. C. Black, F. C. Wellstood, E. Dantsker, A. H. Miklich, D. T. Nemeth, D. Koelle, F. Ludwig, and J. Clarke. Microwave microscopy using a superconducting quantum interference device. *Applied Physics Letters*, 66(1):99–101, 1995.

[88] R. C. Black, F. C. Wellstood, E. Dantsker, A. H. Miklich, D. Koelle, F. Ludwig, and J. Clarke. Imaging radio-frequency fields using a scanning squid microscope. *Applied Physics Letters*, 66(10):1267–1269, 1995.

[89] Vladimir V Talanov, Nesco M Lettsome Jr, Valery Borzenets, Nicolas Gagliolo, Alfred B Cawthorne, and Antonio Orozco. A scanning SQUID microscope with 200 MHz bandwidth. *Superconductor Science and Technology*, 27(4):044032, mar 2014.

[90] Andrew Horsley. *High resolution field imaging with atomic vapor cells*. PhD thesis, University of Basel, 2015.

[91] M. M. Dong, Z. Z. Hu, Y. Liu, B. Yang, Y. J. Wang, and G. X. Du. A fiber based diamond rf b-field sensor and characterization of a small helical antenna. *Applied Physics Letters*, 113(13):131105, 2018.

[92] *Radio Frequency and Microwave Power Measurement*. Institution of Engineering and Technology, 1990.

[93] D.C. Paulusse, N.L. Rowell, and A. Michaud. Accuracy of an atomic microwave power standard. *IEEE Transactions on Instrumentation and Measurement*, 54(2):692–695, 2005.

[94] Patrick Appel, Marc Ganzhorn, Elke Neu, and Patrick Maletinsky. Nanoscale microwave imaging with a single electron spin in diamond. *New Journal of Physics*, 17(11):112001, nov 2015.

[95] M. Wahnschaffe, H. Hahn, G. Zarantonello, T. Dubielzig, S. Grondkowski, A. Bautista-Salvador, M. Kohnen, and C. Ospelkaus. Single-ion microwave near-field quantum sensor. *Applied Physics Letters*, 110(3):034103, 2017.

[96] Giacomo Mariani, Shuhei Nomoto, Satoshi Kashiwaya, and Shintaro Nomura. System for the remote control and imaging of mw fields for spin manipulation in nv centers in diamond. *Scientific reports*, 10(1):1–10, 2020.

[97] Shintaro Nomura, Koki Kaida, Hideyuki Watanabe, and Satoshi Kashiwaya. Near-field radio-frequency imaging by spin-locking with a nitrogen-vacancy spin sensor. *Journal of Applied Physics*, 130(2):024503, 2021.

[98] J. Achard, V. Jacques, and A. Tallaire. Chemical vapour deposition diamond single crystals with nitrogen-vacancy centres: a review of material synthesis and technology for quantum sensing applications. *Journal of Physics D: Applied Physics*, 53(31):313001, may 2020.

[99] J. Botsoa, T. Sauvage, M.-P. Adam, P. Desgardin, E. Leoni, B. Courtois, F. Treussart, and M.-F. Barthe. Optimal conditions for nV^- center formation in type-1b diamond studied using photoluminescence and positron annihilation spectroscopies. *Phys. Rev. B*, 84:125209, Sep 2011.

[100] S Pezzagna, B Naydenov, F Jelezko, J Wrachtrup, and J Meijer. Creation efficiency of nitrogen-vacancy centres in diamond. *New Journal of Physics*, 12(6):065017, jun 2010.

[101] A. Tallaire, L. Mayer, O. Brinza, M. A. Pinault-Thaury, T. Debuisschert, and J. Achard. Highly photostable nv centre ensembles in cvd diamond produced by using n2o as the doping gas. *Applied Physics Letters*, 111(14):143101, 2017.

[102] J. R. Rabeau, A. Stacey, A. Rabeau, S. Prawer, F. Jelezko, I. Mirza, and J. Wrachtrup. Single nitrogen vacancy centers in chemical vapor deposited diamond nanocrystals. *Nano Letters*, 7(11):3433–3437, nov 2007.

[103] Takehide Miyazaki, Yoshiyuki Miyamoto, Toshiharu Makino, Hiromitsu Kato, Satoshi Yamasaki, Takahiro Fukui, Yuki Doi, Norio Tokuda, Mutsuko Hatano, and Norikazu Mizuochi. Atomistic mechanism of perfect alignment of nitrogen-vacancy centers in diamond. *Applied Physics Letters*, 105(26):261601, 2014.

[104] Takahiro Fukui, Yuki Doi, Takehide Miyazaki, Yoshiyuki Miyamoto, Hiromitsu Kato, Tsubasa Matsumoto, Toshiharu Makino, Satoshi Yamasaki, Ryusuke Morimoto, Norio Tokuda, Mutsuko Hatano, Yuki Sakagawa, Hiroki Morishita, Toshiyuki Tashima, Shinji Miwa, Yoshishige Suzuki, and Norikazu Mizuochi. Perfect selective alignment of nitrogen-vacancy centers in diamond. *Applied Physics Express*, 7(5):055201, apr 2014.

[105] A. M. Edmonds, U. F. S. D'Haenens-Johansson, R. J. Cruddace, M. E. Newton, K.-M. C. Fu, C. Santori, R. G. Beausoleil, D. J. Twitchen, and M. L. Markham. Production of oriented nitrogen-vacancy color centers in synthetic diamond. *Phys. Rev. B*, 86:035201, Jul 2012.

[106] M. Lesik, T. Plays, A. Tallaire, J. Achard, O. Brinza, L. William, M. Chipaux, L. Toraille, T. Debuisschert, A. Gicquel, J.F. Roch, and V. Jacques. Preferential orientation of nv defects in cvd diamond films grown on (113)-oriented substrates. *Diamond and Related Materials*, 56:47–53, 2015.

[107] www.e6.com.

[108] www.femm.info.

[109] Thomas J. Fellers and Michael W. Davidson. Ccd noise sources and signal-to-noise ratio.

[110] www.photometrics.com. Control of noise and background in scientific cmos technology.

[111] G. Davies, M. F. Hamer, and William Charles Price. Optical studies of the 1.945 ev vibronic band in diamond. *Proceedings of the Royal Society of London. A. Mathematical and Physical Sciences*, 348(1653):285–298, 1976.

[112] RJ Epstein, FM Mendoza, YK Kato, and DD Awschalom. Anisotropic interactions of a single spin and dark-spin spectroscopy in diamond. *Nature physics*, 1(2):94–98, 2005.

[113] Kiyoshi Kobayashi Motoichi Ohtsu. *Optical Near Fields*.

[114] L. M. Pham, N. Bar-Gill, D. Le Sage, C. Belthangady, A. Stacey, M. Markham, D. J. Twitchen, M. D. Lukin, and R. L. Walsworth. Enhanced metrology using preferential orientation of nitrogen-vacancy centers in diamond. *Phys. Rev. B*, 86:121202, Sep 2012.

[115] Marcus W. Doherty, Neil B. Manson, Paul Delaney, Fedor Jelezko, Jörg Wrachtrup, and Lloyd C.L. Hollenberg. The nitrogen-vacancy colour centre in diamond. *Physics Reports*, 528(1):1–45, 2013. The nitrogen-vacancy colour centre in diamond.

[116] Péter Udvarhelyi, V. O. Shkolnikov, Adam Gali, Guido Burkard, and András Pályi. Spin-strain interaction in nitrogen-vacancy centers in diamond. *Phys. Rev. B*, 98:075201, Aug 2018.

[117] Marcis Auzinsh, Andris Berzins, Dmitry Budker, Laima Busaite, Ruvin Ferber, Florian Gahbauer, Reinis Lazda, Arne Wickenbrock, and Huijie Zheng. Hyperfine level structure in nitrogen-vacancy centers near the ground-state level anticrossing. *Phys. Rev. B*, 100:075204, Aug 2019.

[118] Xing-Fei He, Neil B. Manson, and Peter T. H. Fisk. Paramagnetic resonance of photoexcited n-v defects in diamond. ii. hyperfine interaction with the ^{14}N nucleus. *Phys. Rev. B*, 47:8816–8822, Apr 1993.

[119] F. Poggiali, P. Cappellaro, and N. Fabbri. Measurement of the excited-state transverse hyperfine coupling in nv centers via dynamic nuclear polarization. *Phys. Rev. B*, 95:195308, May 2017.

[120] JP Tetienne, L Rondin, P Spinicelli, M Chipaux, T Debuisschert, JF Roch, and V Jacques. Magnetic-field-dependent photodynamics of single nv defects in diamond: an application to qualitative all-optical magnetic imaging. *New Journal of Physics*, 14(10):103033, 2012.

[121] V. Jacques, P. Neumann, J. Beck, M. Markham, D. Twitchen, J. Meijer, F. Kaiser, G. Balasubramanian, F. Jelezko, and J. Wrachtrup. Dynamic polarization of single nuclear spins by optical pumping of nitrogen-vacancy color centers in diamond at room temperature. *Phys. Rev. Lett.*, 102:057403, Feb 2009.

[122] Laima Busaite, Reinis Lazda, Andris Berzins, Marcis Auzinsh, Ruvin Ferber, and Florian Gahbauer. Dynamic ^{14}N nuclear spin polarization in nitrogen-vacancy centers in diamond. *Phys. Rev. B*, 102:224101, Dec 2020.

[123] Mayeul Chipaux, Alexandre Tallaire, Jocelyn Achard, Sébastien Pezzagna, Jan Meijer, Vincent Jacques, Jean-François Roch, and Thierry Debuisschert. Magnetic imaging with an ensemble of nitrogen-vacancy centers in diamond. *The European Physical Journal D*, 69(7):1–10, 2015.

[124] E. Arimondo. Dark resonances in quantum optics. *Acta Physica Polonica A - ACTA PHYS POL A*, 112, 11 2007.

[125] Thierry Debuisschert Christian Larat Loïc Morvan Jan Meijer Sébastien Pezzagna Mayeul Chipaux, Loïc Toraille. Systeme d'analyse d'un signal hyperfrequence par imagerie, 2016.

[126] Viktor Stepanov, Franklin H. Cho, Chathuranga Abeywardana, and Susumu Takahashi. High-frequency and high-field optically detected magnetic resonance of nitrogen-vacancy centers in diamond. *Applied Physics Letters*, 106(6):063111, 2015.

[127] R. A. Babunts, D. D. Kramushchenko, A. Gurin, A. P. Bundakova, M. V. Muzafarova, A. G. Badalyan, N. G. Romanov, and P. Baranov. Features of high-frequency epr/ese/odmr spectroscopy of nv-defects in diamond. *Physics of the Solid State*, 62:2024–2032, 2020.

[128] J. R. Maze, J. M. Taylor, and M. D. Lukin. Electron spin decoherence of single nitrogen-vacancy defects in diamond. *Phys. Rev. B*, 78:094303, Sep 2008.

[129] Linbo Shao, Ruishan Liu, Mian Zhang, Anna V. Shneidman, Xavier Audier, Matthew Markham, Harpreet Dhillon, Daniel J. Twitchen, Yun-Feng Xiao, and Marko Lončar. Wide-field optical microscopy of microwave fields using nitrogen-vacancy centers in diamonds. *Advanced Optical Materials*, 4(7):1075–1080, 2016.

[130] David J. Griffiths. *Introduction to Electrodynamics*. Cambridge University Press, 4 edition, 2017.

[131] Frederick W. Grover. *Inductance Calculations*. Dover, 1952.

[132] Iulian Rosu. Microstrip, stripline, cpw, and siw design.

[133] *Conductor-Backed Coplanar Waveguide*, chapter 3, pages 87–111. John Wiley and Sons, Ltd, 2001.

[134] Franco Di Paolo. *Networks and devices using planar transmissions lines*. CRC Press, 2018.

[135] Robert Staacke, Roger John, Max Kneiß, Christian Osterkamp, Séverine Diziain, Fedor Jelezko, Marius Grundmann, and Jan Meijer. Method of full polarization control of microwave fields in a scalable transparent structure for spin manipulation. *Journal of Applied Physics*, 128(19):194301, 2020.

[136] E Bourgeois, A Jarmola, P Siyushev, M Gulka, J Hruby, Fedor Jelezko, D Budker, and M Nesladek. Photoelectric detection of electron spin resonance of nitrogen-vacancy centres in diamond. *Nature Communications*, 6(1):1–8, 2015.

[137] Tse-Luen Wee, Yan-Kai Tzeng, Chau-Chung Han, Huan-Cheng Chang, Wunshain Fann, Jui-Hung Hsu, Kuan-Ming Chen, and Yueh-Chung Yu. Two-photon excited fluorescence of nitrogen-vacancy centers in proton-irradiated type ib diamond. *The Journal of Physical Chemistry A*, 111(38):9379–9386, Sep 2007.

[138] Hans De Raedt, Bernard Barbara, Seiji Miyashita, Kristel Michielsen, Sylvain Bertaina, and Serge Gambarelli. Quantum simulations and experiments on rabi oscillations of spin qubits: Intrinsic vs extrinsic damping. *Phys. Rev. B*, 85:014408, Jan 2012.

[139] Yang Zhang, Zhonghao Li, Yuanyao Feng, Hao Guo, Huanfei Wen, Jun Tang, and Jun Liu. High-sensitivity dc magnetic field detection with ensemble nv centers by pulsed quantum filtering technology. *Opt. Express*, 28(11):16191–16201, May 2020.

[140] Tony J. Rouphael. Chapter 2 - common analog modulation and pulse-shaping methods. In Tony J. Rouphael, editor, *RF and Digital Signal Processing for Software-Defined Radio*, pages 7–24. Newnes, Burlington, 2009.

[141] Erik Bauch, Connor A. Hart, Jennifer M. Schloss, Matthew J. Turner, John F. Barry, Pauli Kehayias, Swati Singh, and Ronald L. Walsworth. Ultralong dephasing times in solid-state spin ensembles via quantum control. *Phys. Rev. X*, 8:031025, Jul 2018.

[142] E. R. MacQuarrie, T. A. Gosavi, A. M. Moehle, N. R. Jungwirth, S. A. Bhave, and G. D. Fuchs. Coherent control of a nitrogen-vacancy center spin ensemble with a diamond mechanical resonator. *Optica*, 2(3):233–238, Mar 2015.

[143] John F. Barry, Jennifer M. Schloss, Erik Bauch, Matthew J. Turner, Connor A. Hart, Linh M. Pham, and Ronald L. Walsworth. Sensitivity optimization for nv-diamond magnetometry. *Rev. Mod. Phys.*, 92:015004, Mar 2020.

université PARIS-SACLAY

ÉCOLE DOCTORALE
Ondes et matière
(EDOM)

Titre: Ensemble de centres azote-lacune dans le diamant pour l'analyse de signaux radiofréquences

Mots clés: Centres NV, spectroscopie,Capteur Quantique, Radiofréquence, ODMR

Résumé: Le centre azote-lacune (NV) est un défaut de spin du diamant constitué d'un atome d'azote et d'une lacune de carbone dans deux positions adjacentes du réseau cristallin du diamant. Il possède de remarquables propriétés optiques dépendant du spin qui en font une piste prometteuse pour les applications d'information quantique ou comme capteur quantique. Dans le présent manuscrit, deux applications basées sur un ensemble de centres NV dans le diamant sont étudiées: un analyseur de spectre radiofréquence (RF) ainsi qu'une technique de microscopie à champ large pour l'imagerie en champ proche du rayonnement RF émis par des dispositifs RF. Le premier chapitre expose les propriétés des centres NV du diamant ainsi que les motivations des deux applications basées sur celles-ci. En particulier, les solutions disponibles et l'état de l'art des techniques pour l'analyse spectrale RF et l'imagerie en champ proche RF sont passées en revue et l'intérêt d'une solution alternative basée sur les centres NV est discuté. Dans le deuxième chapitre, un montage expérimental permettant la détection optique en champ large de la résonance de spin des centres NV est présenté et utilisé pour étudier les principales propriétés de ce défaut du diamant. Les résonances de spin électronique des centres NV sont étudiées sur une large bande de fréquences (plus de 10 GHz) et différents phénomènes sont étudiés : le comportement d'un ensemble de centres NV auquel on applique un champ magnétique statique, les propriétés de polarisation de la photoluminescence émise par les centres NV et comment elles peuvent être exploitées pour reconnaître les orientations des centres NV dans le diamant, la polarisation du spin nucléaire de l'azote des centres NV sur une large gamme de fréquences (plus de 2 GHz). Le troisième chapitre est consacré à la mise en œuvre d'un analyseur de spectre RF en temps réel basé sur un ensemble de centres NV. Les principales caractéristiques physiques d'un ensemble de centres NV considéré comme un détecteur radiofréquence sont étudiées. Une architecture expérimentale qui permet une analyse spectrale RF en temps réel sur une gamme de fréquence accordable (10 MHz – 25 GHz), une largeur de bande jusqu'à 4GHz, une résolution en fréquence jusqu'au MHz et une résolution temporelle jusqu'à la milliseconde est proposée. La mise en place de ce dispositif a nécessité une analyse sur le comportement d'un ensemble de centres NV sous fort gradient de champ magnétique (plusieurs dizaines de Tesla par mètre) qui est aussi détaillée dans le chapitre. Le quatrième et dernier chapitre traite de l'imagerie en champ large des champs RF basée sur un ensemble de centres NV. Deux techniques sont proposées. La première est basée sur l'élargissement en puissance RF de la résonance de spin des centres NV et la seconde utilise la détection en champ large des oscillations de Rabi des centres NV. Ces deux techniques ont permis de reconstruire le champ proche magnétique radiofréquence émis par une antenne boucle. La première technique nécessite une calibration pour retrouver l'amplitude du champ RF alors que la seconde permet sa mesure directe. La détection champ large des oscillations de Rabi des centres NV a donc été étudiée à la fois expérimentalement et par des simulations. En particulier, les oscillations de Rabi des centres NV détectées expérimentalement à l'aide d'un système d'imagerie en champ large ont une forme asymétrique. Afin de comprendre cette forme, le comportement du centre NV pendant la séquence d'impulsions utilisée pour piloter l'oscillation de Rabi a été modélisé. Les résultats des simulations, en accord avec les résultats expérimentaux, permettent finalement d'avoir une meilleure compréhension de la polarisation optique et de la lecture du spin du centre NV pendant la séquence.

université PARIS-SACLAY

ÉCOLE DOCTORALE
Ondes et matière
(EDOM)

Title: Ensemble of nitrogen-vacancy centers in diamond for radiofrequency signal analysis

Keywords: NV centers, Sensors, Spectroscopy, ODMR, Quantum Sensing, ESR

Abstract: The nitrogen-vacancy center (NV) is a diamond spin defect consisting of a nitrogen atom and a carbon vacancy in two adjacent positions of the diamond lattice. Its remarkable spin-dependent optical properties make it a promising platform for quantum sensing and quantum information applications. In the present manuscript, two applications involving an ensemble of NV centers in diamond are investigated: a radio frequency (RF) spectrum analyser and a widefield imaging technique of the RF radiation emitted in near field by microwave devices. In the first chapter, the NV centers in diamond, their properties and the motivations behind the two NV centers based applications proposed in this manuscript are presented. The available solutions and the state-of-the-art techniques for both RF spectral analysis and near field imaging of RF radiation are reviewed and the potential of alternative solutions using NV centres are discussed. In the second chapter, a set-up for the widefield optical detection of the NV centers spin resonances is presented and used to investigate the main properties of this diamond defect. The NV center electron spin resonances are detected over a large frequency range (more than 10 GHz) and different phenomena are investigated: the behaviour of an ensemble of NV centers under a static magnetic field, the polarization properties of the NV center photoluminescence (PL) and how they can be exploited to recognise the NV centers orientations, the NV's nitrogen nuclear spin polarization over a large frequency range (more than 2 GHz). The third chapter is devoted to the implementation of a real-time RF spectrum analyser based on an ensemble of NV centers. The main physical features of NV centers considered as MW detectors are investigated and an experimental architecture which allows a real-time RF spectral analysis over a tunable frequency range (10 MHz to 25 GHz), 4 GHz bandwidth, a MHz frequency resolution and a ms time resolution is demonstrated. The implementation of this device required an interesting analysis of the behaviour of an ensemble of NV centers under strong magnetic field gradients (tens of Tesla per meter) which is detailed in the chapter. The fourth and last chapter deals with the widefield imaging of RF field based on an ensemble of NV centers. Two techniques are proposed. The first is based on the RF power broadening of the NV center spin resonances in the continuous regime domain while the second is based on the widefield detection of NV centers Rabi oscillations in a pulsed regime. Both techniques allowed reconstructing the magnetic near field RF field emitted by a loop antenna. However, while the first technique requires a calibration to retrieve the amplitude of the RF field, the second allows a direct measurement of it. The widefield detection of the NV centers Rabi oscillations has thus been investigated both by means of experiments and simulations. Since the NV centers Rabi oscillations detected using our widefield experimental set-up showed an asymmetric shape, a model has been realized to figure out the NV centers behaviour during the pulse sequence employed to drive the Rabi oscillation. The results of the simulations, in agreement with the experimental results, enable to have a better insight of the NV center spin optical polarization and readout during the widefield detection of the Rabi oscillations.